The Physics and Chemistry of Oxygen-rich Circumstellar Envelopes as Traced by Simple Molecules

Dissertation

zur

Erlangung des Doktorgrades (Dr. rer. nat.)

der

Mathematisch-Naturwissenschaftlichen Fakultät

der

Rheinischen Friedrich–Wilhelms–Universität Bonn

vorgelegt von

Ka Tat Wong

aus

Hongkong

Bonn, 2017

Angefertigt mit Genehmigung der Mathematisch-Naturwissenschaftlichen Fakultät der Rheinischen Friedrich–Wilhelms–Universität Bonn.

Prepared with the permission from the Faculty of Mathematics and Natural Sciences of the University of Bonn.

1. Referent / *First Referee*:	Prof. Dr. Karl M. Menten
2. Referent / *Second Referee*:	Prof. Dr. Norbert Langer
Tag der Promotion / *Conferral Date*:	30.01.2018
Erscheinungsjahr / *Year of Publication*:	2018

Abstract

The physics and chemistry of the circumstellar envelopes (CSEs) of evolved stars are not fully understood despite decades of research. This thesis addresses two issues in the study of the CSEs of oxygen-rich (O-rich) evolved stars. In the first project, the ammonia (NH_3) chemistry of O-rich stars is investigated with multi-wavelength observations; in the second project, the extended atmosphere and inner wind of the archetypal asymptotic giant branch (AGB) star *o* Ceti (Mira) is studied with high-angular resolution observations.

One of the long-standing mysteries in circumstellar chemistry is the perplexing overabundance of the NH_3 molecule. NH_3 in O-rich evolved stars has been found in much higher abundance, by several orders of magnitude, than that expected in equilibrium chemistry. Several mechanisms have been suggested in the literature to explain this high NH_3 abundance, including shocks in the inner wind, photodissociation of nitrogen by interstellar ultraviolet radiation, and nitrogen enrichment in stellar nucleosynthesis; however, none of these suggestions can fully explain the abundances of NH_3 and various other molecular species in the CSEs of O-rich stars.

In order to investigate the distribution of NH_3 in O-rich CSEs, observations of the spectral lines of NH_3 from a diverse sample of evolved stars and in different wavelength regimes are necessary. In this thesis, the NH_3 line emission and absorption from four O-rich stars are studied. These targets include the AGB star IK Tauri, the pre-planetary nebula OH 231.8+4.2, the red supergiant VY Canis Majoris, and the yellow hypergiant IRC +10420. The amount of NH_3 observational data has increased drastically thanks to the recent advancement of instrumentation. Observations of NH_3 rotational line emission at submillimetre/far-infrared wavelengths were possible with the *Herschel* Space Observatory (2009–2013). The new wideband correlator in the upgraded Karl G. Janksy Very Large Array (VLA) provided data of multiple radio inversion lines of NH_3. Furthermore, mid-infrared absorption of NH_3 has been observed by the NASA Infrared Telescope Facility (IRTF) for IK Tau and VY CMa.

Full radiative transfer modelling including mid-infrared pumping to the first vibrationally excited state ($v_2 = 1$) has been carried out to reproduce the observed emission and absorption spectra and to retrieve the NH_3 abundances in the targets. It is found that the NH_3 emission in the CSEs of the targets arises from localised spatial-kinematic structures in which the gas density may be higher than in the surrounding gas. Circumstellar shocks may contribute to, but cannot fully account for, the formation of the molecule.

Besides circumstellar chemistry, our understanding of the dust formation and wind-driving mechanisms of oxygen-rich evolved stars is still incomplete. One of the obstacles in the past was the difficulty in imaging the dust condensation and wind acceleration zones due to the lack of high-angular resolution instruments. Thanks to the Atacama Large Millimeter/submillimeter Array (ALMA), which has the longest baseline of about 15 km, we are now able to produce high-fidelity images at unprecedented angular resolutions of tens of milliarcseconds (mas) in the (sub)millimetre regime. Such angular resolutions, which are compa-

rable to the stellar radii of nearby objects, are necessary to understand the gas dynamics and chemical evolution in the pulsating atmosphere and dust formation zone of nearby AGB stars.

The eponymous Mira-type long-period variable, *o* Cet, was observed as a Science Verification target during the first ALMA Long Baseline Campaign that took place in 2014. The observations produced images of the stellar radio photosphere and the molecular transitions of SiO and H_2O at an angular resolution of about 30 mas near 220 GHz (1.3 mm). The millimetre stellar disc of *o* Cet was resolved and modelled. More importantly, this is the first time that molecular line absorption against the background stellar continuum has been clearly imaged in the (sub)millimetre wavelength regime.

Through radiative transfer modelling of the SiO and H_2O line absorption and emission, it is found that during the ALMA observations, the extended atmosphere of the star exhibited infall motions in general with a shock front of velocity $\lesssim$12 km s^{-1} beyond the radio photosphere of *o* Cet. Gas-phase SiO starts to deplete beyond 4 stellar radii at the temperature of $\lesssim$600 K. Comparisons between the physical structures of the inner wind derived from the imaging and those predicted from hydrodynamical calculations found that theoretical models are able to reproduce the observations in great detail. Future interferometric observations will reveal more details of the dust condensation processes and wind acceleration, and hence lead to a better understanding of the late stages of stellar evolution.

List of Publications

1. **Circumstellar ammonia in oxygen-rich evolved stars**
   Wong, K. T.; Menten, K. M.; Kamiński, T.; Wyrowski, F.; Lacy, J. H.; Greathouse, T. K. (2017) A&A, in press.
   DOI: 10.1051/0004-6361/201731873 [arXiv:1710.01027]

   This article corresponds to Chapter 2.

2. **An observational study of dust nucleation in Mira (o Ceti): II. Titanium oxides are negligible for nucleation at high temperatures**
   Kamiński, T.; Müller, H. S. P.; Schmidt, M. R.; Cherchneff, I.; **Wong, K. T.**; Brünken, S.; Menten, K. M.; Winters, J. M.; Gottlieb, C. A.; Patel, N. A. (2017) A&A, 599, A59.
   DOI: 10.1051/0004-6361/201629838 [arXiv:1610.01141]

3. **An observational study of dust nucleation in Mira (o Ceti): I. Variable features of AlO and other Al-bearing species**
   Kamiński, T.; **Wong, K. T.**; Schmidt, M. R.; Müller, H. S. P.; Gottlieb, C. A.; Cherchneff, I.; Menten, K. M.; Keller, D.; Brünken, S.; Winters, J. M.; Patel, N. A. (2016) A&A, 592, A42.
   DOI: 10.1051/0004-6361/201628664 [arXiv:1604.05641]

4. **Resolving the extended atmosphere and the inner wind of Mira (o Ceti) with long ALMA baselines**
   Wong, K. T.; Kamiński T.; Menten, K. M.; Wyrowski, F. (2016) A&A, 590, A127.
   DOI: 10.1051/0004-6361/201527867 [arXiv:1603.03371]

   This article corresponds to Chapter 3.

5. **Probing NH_3 Formation in Oxygen-rich Circumstellar Envelopes**
   Wong, K. T.; Menten, K. M.; Kamiński T.; Wyrowski, F. (2015) in Why Galaxies Care About AGB Stars III: A Closer Look in Space and Time, eds. F. Kerschbaum, R. F. Wing, and J. Hron, ASP Conf. Ser., 497, 141.
   URL: http://aspbooks.org/custom/publications/paper/497-0141.html

Blank Page

Contents

Blank Page

List of Figures

Blank Page

List of Tables

Blank Page

CHAPTER 1

Introduction

1.1. Late stages of stellar evolution

General References: Iben & Renzini (1983); Lattanzio & Wood (2003); Kippenhahn et al. (2012); Karakas & Lattanzio (2014).

1.1.1. Main sequence stars

A star spends most of its lifetime on the main sequence. Main-sequence stars, including the Sun, occupy a densely populated band in the luminosity–temperature plot of stars, i.e. the Hertzsprung–Russell (HR) diagram (Hertzsprung, 1905, 1907, 1911; Russell, 1914a,b). Figure 1.1 shows a highly simplified example of the HR diagram locating a few important phases of stellar evolution. Main-sequence stars are in the state of hydrostatic equilibrium. For each gas element inside the star, the radially inward gravitational force is always balanced by the outward force contributed by the thermal pressure of the gas and radiation pressure of the photons. Stars produce energy by nucleosynthesis at the stellar core (Bethe, 1939; Burbidge et al., 1957), a process which fuses lighter nuclei into heavier ones. During the main-sequence phase, the dominant thermonuclear reaction is the production of helium (^{4}He) from hydrogen (^{1}H). For low-mass stars that are less than 2 solar masses ($M \lesssim 2\,M_\odot$), the dominant H-burning mechanism is the proton-proton (pp) chain. In pp chain reactions, deuterium (^{2}H) is first produced, followed by successive reactions that produce ^{3}He and eventually ^{4}He. For more massive stars, the carbon–nitrogen–oxygen (CNO) cycles take place and produce helium from hydrogen using the isotopes of carbon, nitrogen, and oxygen as catalysts. Massive stars consume hydrogen at much higher rates than lower mass stars. The main-sequence phase ends when hydrogen is depleted in the stellar core. The main-sequence lifetime of a 1-$M_\odot$ star is about 10^{10} yr while that of a massive star with $M = 10\,M_\odot$ is $\sim 10^7$ yr.

1.1.2. Post-main sequence evolution of low- and intermediate-mass stars

When all the hydrogen at the stellar core has been exhausted and has become helium, energy production at the core stops and core contraction follows. Nuclear fusion of hydrogen continues in a thin shell surrounding the helium core. At the same time, the layers beyond the hydrogen burning shell expand and cool. The star therefore appears much more luminous and redder than it was during the main-sequence evolution. In the HR diagram, the star has now transited to the region known as the red giant branch (RGB).

During the RGB phase, the outer layer of the stellar envelope is convective and the hydrogen burning shell moves outwards. At the point when the convective layer is in contact with the

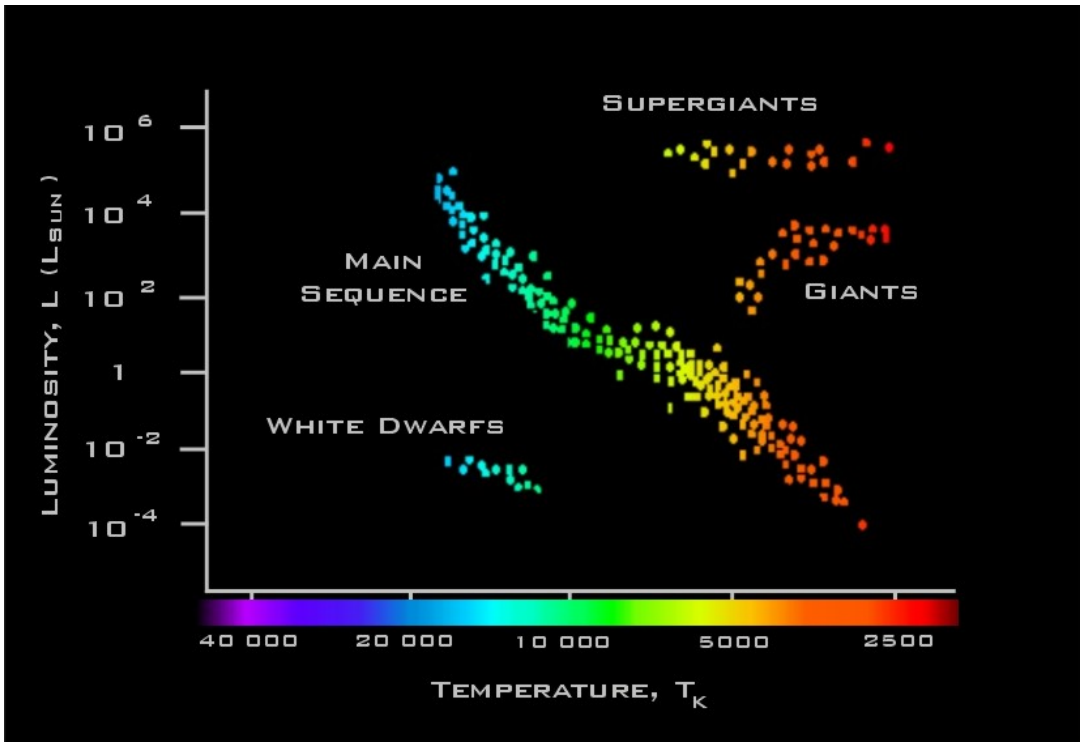

Figure 1.1.: A simplified Hertzsprung–Russell (HR) diagram plotting the stellar luminosity (in solar units) against the surface temperature (in Kelvin). Credit: C. Brinkworth and C. Thomas, University of Leicester (https://www.le.ac.uk/ph/faulkes/web/stars/o_st_overview.html).

layers where hydrogen burning has occurred, products of nucleosynthesis such as ^{4}He, ^{13}C, and ^{14}N are mixed up with the convective layer and brought to the stellar surface. The mixing process is known as the first dredge-up.

When the temperature of the core reaches a temperature of $\sim 10^8$ K, the triple-alpha process becomes possible. Helium-4 nuclei (the α-particle) are first fused to beryllium (^{8}Be) and then carbon (^{12}C). The core of low-mass stars ($0.8\,M_\odot \lesssim M \lesssim 2\,M_\odot$) is degenerate, and hence the pressure of the electron gas remains constant despite the rapid increase in temperature. A positive feedback loop is formed because the rate of energy production and temperature enhance each other. This results in a thermonuclear runaway called helium flash.

After that, the degeneracy is removed, the stellar core expands and cools, and core helium burning occurs at a steady rate. The stellar core becomes convective and the star transits to the horizontal branch in the HR diagram if its metallicity is low (or a red clump star if it is of solar metallicity). Helium burning enriches carbon at the stellar core. As the abundance of ^{12}C increases, the reaction between carbon and helium to form oxygen (^{16}O) also takes place. When helium is exhausted at the core, helium burning will occur in a shell surrounding the core which is dominated by degenerate carbon and oxygen. There is also an outer hydrogen burning shell. The star is now in the asymptotic giant branch (AGB) phase. In the HR diagram, AGB stars are distributed in a narrow zone that appears to be asymptotic to the region occupied by RGB stars.

For intermediate-mass stars ($2\,M_\odot \lesssim M \lesssim 7\,M_\odot$), the core is more massive and hotter than in low-mass stars. Electron degeneracy does not occur during helium burning. Hence, the triple-alpha process takes place steadily and there is no core helium flash. Eventually, a degen-

erate carbon-oxygen core is created, surrounded by a helium-burning shell and a hydrogen-burning shell. The inter-shell helium region expands, therefore reducing the temperature of the hydrogen-burning shell and hence extinguishing hydrogen burning. The outer convective layers penetrate into the region that has been processed by hydrogen burning and is enriched with ^{4}He and ^{14}N. The material is brought up through convection and the process is called the second dredge-up. At the same time, hydrogen is also brought down from the convective envelope. The helium burning shell continues to propagate more outwards and heat up the hydrogen. Hydrogen burning is then restarted in an outer shell.

The helium burning shell eventually becomes very thin compared to the stellar radius. The pressure in the thin burning shell is primarily maintained by gravity and hence does not respond to the increase in temperature due to the triple-alpha burning process. Hence, the thin helium burning shell becomes thermally unstable, resulting in helium shell flash. After that, the intershell region expands and cools, extinguishing the outer hydrogen burning shell again. The luminosity of the star is now dominated by the burning of helium. The outer convective envelope may also invade the intershell region and bring elements (such as ^{12}C) to the upper layers. This process is known as the third dredge-up. After that, the hydrogen burning shell is reactivated and gradually dominates the energy production of the star. The above cycle, known as thermal pulse (TP), can repeat for multiple times and the stars in this cyclic evolutionary phase are called TP-AGB stars.

AGB stars exhibit prodigious mass loss, forming extended circumstellar envelopes (CSEs) around them. The circumstellar material consists of gas and dust particles. Stellar pulsations and radiation pressure on dust grains are thought to be the main drivers of the strong stellar wind from AGB stars. The structure of the CSE of a typical AGB star is further described in Sect. 1.2. The surface temperature of an AGB star increases as mass loss proceeds, the star is then seen to be evolving horizontally leftwards on the HR diagram. The ultraviolet (UV) radiation from the star becomes stronger and may ionize the circumstellar material, forming a planetary nebula (PN). After the stellar envelope is almost completely lost and hydrogen burning is extinguished, the stellar remnant cools and becomes a white dwarf (WD).

1.1.3. Post-main sequence evolution of massive stars

The post-main sequence evolution of massive stars ($M \gtrsim 10\,M_{\odot}$) differs from that of their lower-mass counterparts by the presence of non-degenerate carbon burning at the centre due to higher core temperature and mass. Depending on the core temperature and compositions, further ignitions of neon, oxygen, silicon, etc. will take place at various stages. Furthermore, massive stars are much more luminous than low- and intermediate-mass stars. It is believed that strong radiation pressure, and hence strong outward momentum, on the loosely bound material near the stellar surface leads to high mass-loss rate throughout the main-sequence evolution. These radiation-driven winds have a high degree of ionization and typically do not contain molecules.

Moderately massive stars (up to about 25 $M_{\odot}$; Levesque, 2010) evolve from the upper part of the main sequence to the upper right region of the HR diagram and become red supergiants (RSGs), during which helium is burnt at the core. The physical origins of mass loss in RSGs are still not clearly known. In addition to stellar pulsation and radiation pressure on dust particles, convection and magnetic field may also be the important drivers of mass loss in RSGs (Humphreys, 2016). A significant fraction of the stellar mass can be lost to the circumstellar environment by the end of the stellar evolution. Less massive RSGs would end their evolution as Type II (core-collapse and hydrogen-rich) supernovae. Some RSGs may evolve back to the

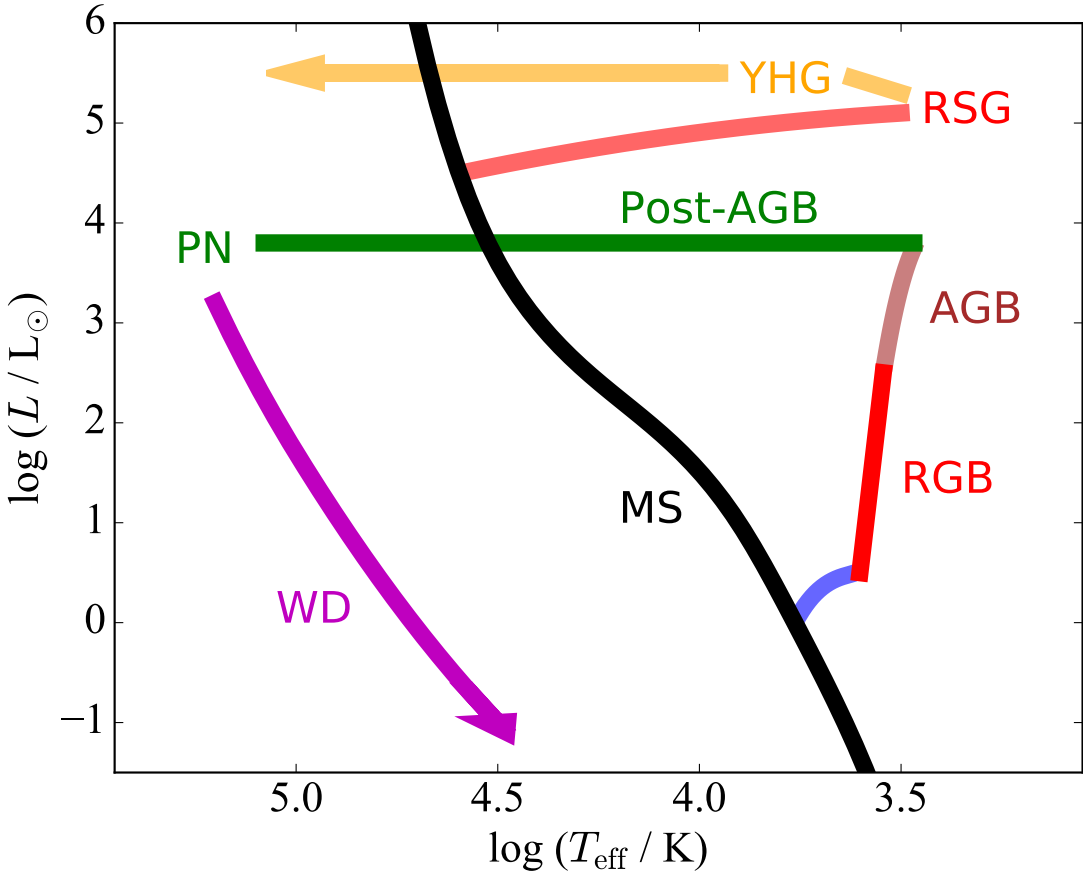

Figure 1.2.: A simplified Hertzsprung-Russell (HR) diagram plotting the stellar luminosity (in terms of solar luminosity) against the surface temperature (in Kelvin). The dark curve shows the main sequence. Example evolutionary tracks for a low-mass and a massive stars are also drawn to indicate a few important phases of the late stages of stellar evolution.

warmer part of the HR diagram and become yellow supergiants or yellow hypergiants (YHGs) (Oudmaijer et al., 2009). Depending on the initial mass and the mass-loss rate, the star may further evolve into a blue supergiant, a Wolf-Rayet star, and then undergo Type II supernova explosion. After that, the remnant may become a neutron star or a black hole.

1.2. Circumstellar envelope

Mass loss from an evolved star is evidenced by the presence of an extended circumstellar envelope (CSE) which produces numerous molecular emission lines and is typically very bright at the infrared (IR) wavelengths. The following parts will describe, in the context of an AGB star, the physics and chemistry of different regions of the circumstellar environment from the stellar surface to the interstellar medium.

1.2.1. Extended atmosphere

General References: Höfner (2015, 2016).

Current mass loss models of AGB stars usually consist of two main elements: (1) the levitation of material from the stellar atmosphere by radial pulsations and convective flows; and (2) radiation pressure on dust grains formed at some radii from the atmosphere. AGB stars exhibiting radial pulsations are classified as Mira-type, semi-regular, or irregular variables. Mira-type variables – named after the archetype *o* Ceti (Mira Ceti; Hevelius, 1662) – typically

have a period of a few hundred days. Stellar pulsations (and probably large-scale convective motions; Schwarzschild, 1975) trigger large-scale shock waves propagating in the upper part of the stellar atmosphere. Convective motions, on the other hand, generate small-scale shocks (Freytag et al., 2017). The shocks of various scales lift the gas in the upper part of the stellar envelope to an extended region beyond the stellar photosphere[1], which is known as the extended atmosphere.

In the extended atmosphere, the chemistry is dominated by shock-induced processes (Millar, 2016; Gobrecht et al., 2016). Depending on the photospheric abundance ratio of carbon and oxygen at that evolutionary phase, an evolved star can be classified as a carbon-rich (C/O > 1), oxygen-rich (C/O < 1), or the intermediate S-type (C/O ≈ 1) star. Chemical models and observations have shown that shocks can trigger chemistry that is not expected under thermal equilibrium conditions, such as carbon-bearing molecules in oxygen-rich winds (Duari et al., 1999; Cherchneff, 2006; Kamiński et al., 2017b). It has also been shown that the optically thick infrared absorption bands can be explained by molecular gas (e.g. H_2O, CO) of temperature $\lesssim$2000 K at the radii of 1–2 $R_\star$ (also known as 'MOLsphere'; e.g. Tsuji, 2000; Ohnaka, 2004; Perrin et al., 2004).

In the radio and (sub)millimetre wavelength regimes, the optically thick region in the line-free (continuum) spectrum has a typical radius of ~2 $R_\star$. It has been proposed that the optically thick free-free emission resulting from the interactions between electrons and hydrogen (in either atomic or molecular form) forms the 'radio photosphere' (Reid & Menten, 1997a, 2007). Figure 1.3 shows a schematic diagram from Reid & Menten (1997a) of the extended atmosphere of a typical Mira variable. Since the size of the radio photosphere is of the order of AU (astronomical unit, i.e. 1.496×10^{13} cm or 215 solar radii), imaging observations require an excellent angular resolution of ~10 mas for the nearest AGB stars ($d \sim 100$ pc) to resolve the stellar continuum disc. In Chap. 3, images of the radio photosphere and extended atmosphere of *o* Ceti as observed by the Atacama Large Millimeter/submillimeter Array (ALMA) will be presented and analysed.

1.2.2. Wind acceleration

Within a distance of ~2 $R_\star$, the radiation pressure from the central star on the gas is not high enough to drive a steady stellar wind. As a result of the interplay between gravitational pull and outward motions driven by pulsations, the movements of the gas in these layers can be away from or towards the star. The outward or inward radial velocity of the inner wind depends on the pulsation phase of the star and can be determined by the infrared absorption spectra of abundant molecules on the stellar surface, such as CO (Nowotny et al., 2010; Liljegren et al., 2017, and references therein).

Beyond the radius of ~2 $R_\star$, dust grains start to grow. By transferring the radiation pressure from the star to the linear outward momentum of the gas, a slowly accelerating outflow is produced. The outflow reaches its terminal expansion velocity at the radius of $\gtrsim$10 $R_\star$. It has been suggested that the oxides of aluminium (Al) or titanium (Ti) may form the first seed particles or clusters on which larger dust grain can grow (Cherchneff, 2013; Kamiński et al., 2016, and references therein). Silicate grains, which are commonly found in the circumstellar dust shells of oxygen-rich evolved stars, form at lower temperatures (<1000 K; outer radii)

[1] The stellar photosphere is determined from the line-free (continuum) regions of the optical or infrared spectrum. Its radius is defined as the stellar radius, $R_\star$. In the following parts of the thesis, the stellar photosphere is referred to as the 'optical/infrared photosphere' in order to distinguish it from other concepts such as the 'radio photosphere' ($R_{\rm continuum}$) and the 'MOLsphere' (cf. Chap. 3).

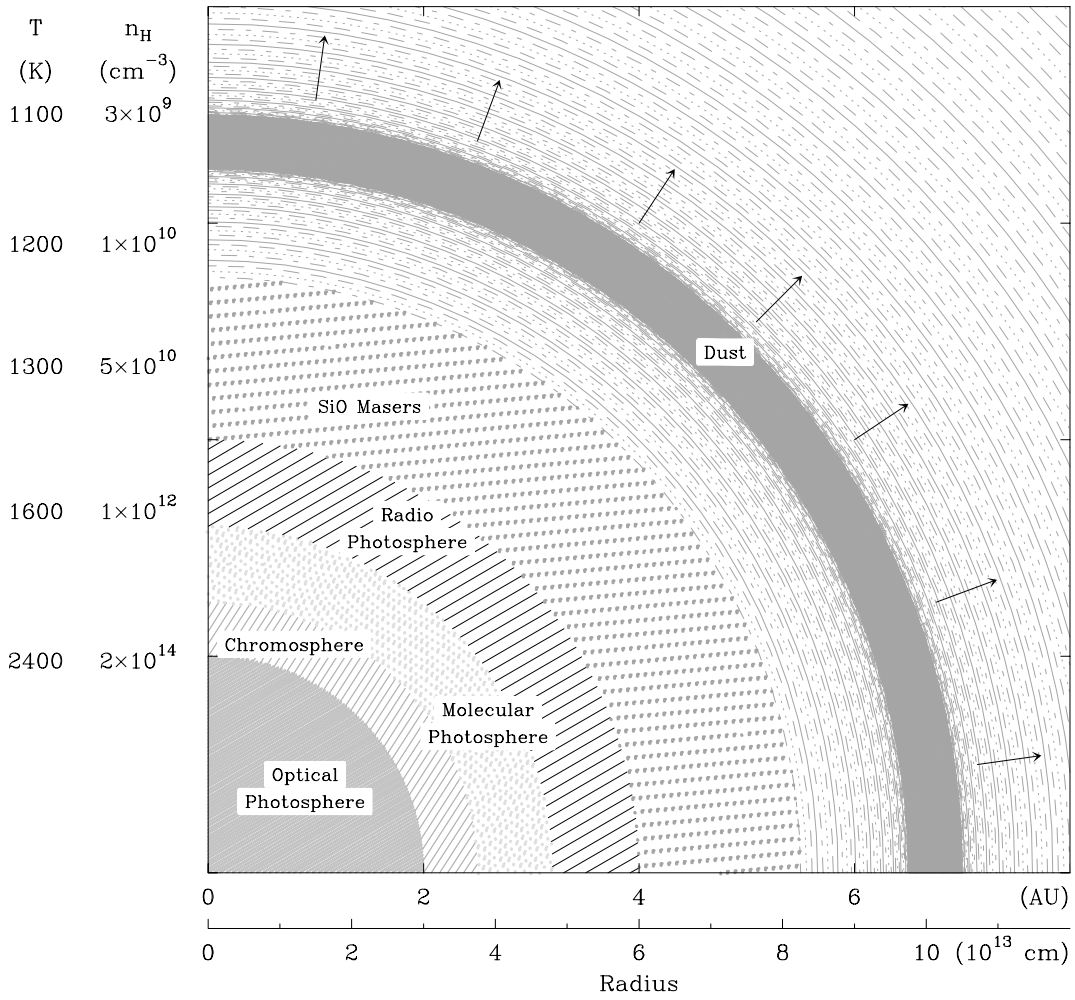

Figure 1.3.: A schematic diagram of the extended atmosphere of a typical Mira variable. Credit: Reid & Menten (1997a).

at the expense of gas-phase SiO. In Chap. 3, high-angular resolution ALMA observations of SiO and H_2O gas within the silicate condensation region will be presented. Detailed literature review and discussions on the physical structure of the extended atmosphere and wind acceleration mechanisms can be found in Sect. 3.5.2.

1.2.3. Outer circumstellar envelope

General References: Willacy & Millar (1997); Li et al. (2014, 2016); Millar (2016).

A fully accelerated CSE consisting of solid dust grains and gaseous molecules is created beyond the dust condensation zone. The extent of the CSE can reach a few thousand stellar radii (~10″ for nearby evolved stars). The circumstellar gas and dust will eventually return to the interstellar medium and feed the future generations of star formation.

Molecules formed in the inner wind become the parent molecules of the chemical networks that determine the molecular composition of the outer CSE. There, the chemical abundances are determined by photodissociation of molecules due to interstellar UV radiation, chemical reactions among neutral species, and reactions between neutral and ionised species. Figure 1.4 summarises the dominant chemistry in different regions of the CSE from the star to the interstellar medium.

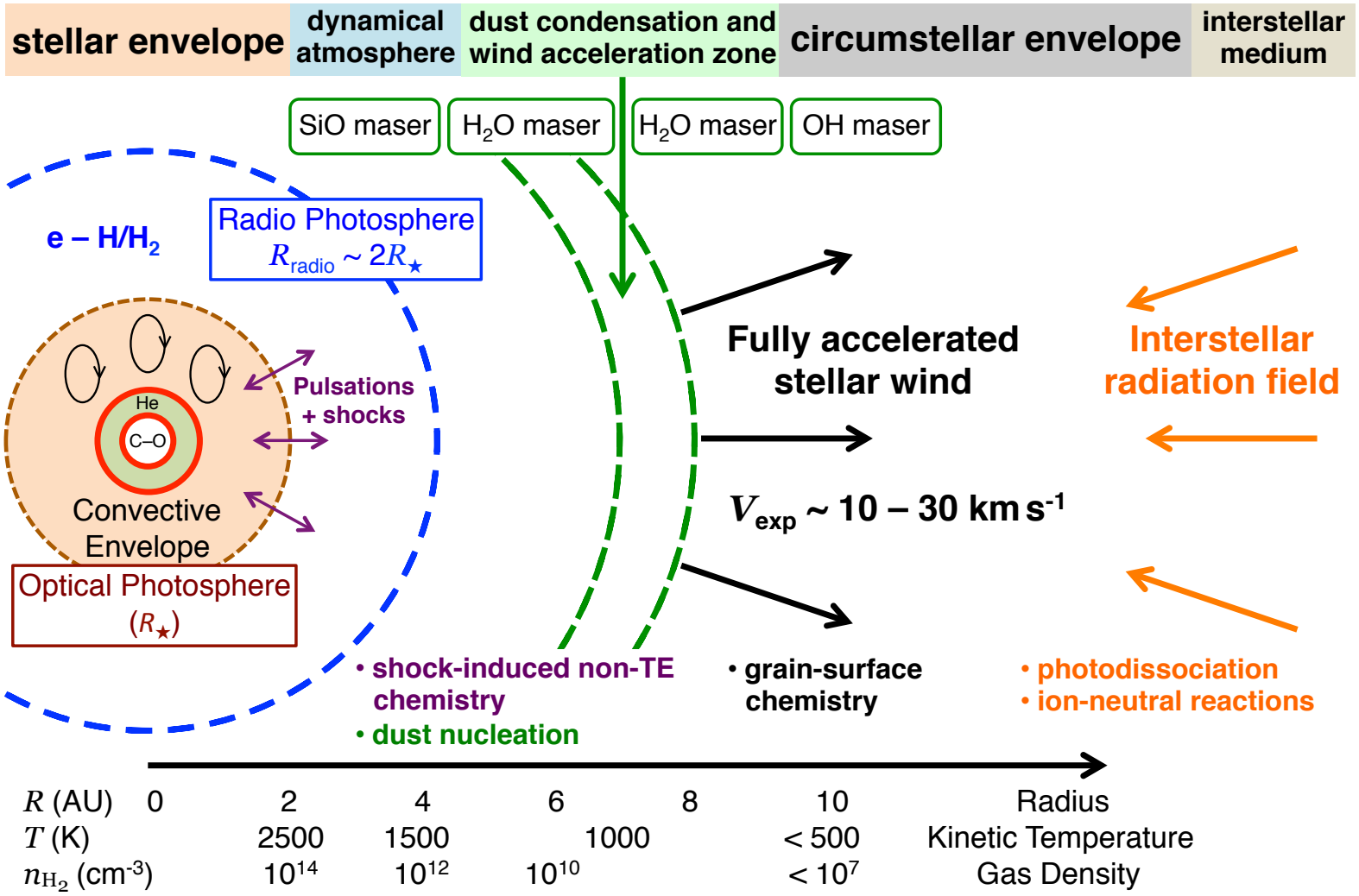

Figure 1.4.: A schematic diagram of the circumstellar envelope (CSE) of a typical oxygen-rich AGB star.

The circumstellar chemical networks can be investigated by two approaches: forward chemical modelling or a retrieval method. In forward chemical modelling (e.g. Millar et al., 2000; Cordiner & Millar, 2009; McElroy et al., 2013), a large chemical network covering a few hundred species and a few thousand chemical reactions is constructed. With the temperature-dependent reaction rate coefficients of these reactions, the rates of photodissociation and photoionization, and the adopted physical conditions of the CSE (i.e. gas density, kinetic temperature, and extinction as functions of the radial distance from the star), the abundances of all included chemical species at different radii can be predicted. Recent examples of chemical models of AGB star CSEs can be found in Li et al. (2014, 2016).

On the other hand, abundances of individual molecules can be retrieved from observations through excitation analysis of their transitions. In a full radiative transfer model, the input physical parameters include gas density, kinetic temperature, molecular abundance, velocity field, and local turbulence (a line-broadening parameter). The populations of individual energy levels of the modelled molecule are computed by solving the coupled equations of statistical equilibrium and radiative transfer iteratively. Synthesised spectral line profiles are produced from the level populations and then compared to the observed spectra. The parameters of the input physical model are then varied until a satisfactory fit is obtained. Details of radiative transfer modelling are described in Appendices A and B. In Chaps. 2 and 3, radiative transfer modelling of NH_3, SiO, and H_2O will be carried out so as to derive these molecule's abundances as a function of radius from the central star.

1.3. Outline of the thesis

This thesis includes two observational studies of the CSEs of oxygen-rich evolved stars. Chapter 2 presents the first project, which is about the long-standing puzzle of the ammonia (NH_3) abundance in the CSE of both oxygen-rich and carbon-rich stars. NH_3 has been detected at a very high abundance in the outer CSE compared to thermal equilibrium abundance at the stellar surface; therefore, H_3 has to be produced efficiently in the inner wind or the outer CSE. However, the origin of NH_3 could not be explained by shock-induced chemistry in the inner wind or chemical models for the outer CSE. Forward chemical models have to assume NH_3 as a parent species and adopt a high abundance (based on observationally retrieved values) to explain the abundance of nitrogen-bearing molecules. The goals of this project are (1) to spatially resolve the distribution of NH_3 in oxygen-rich CSEs and (2) to more accurately characterise the physical conditions of NH_3-carrying gas by detailed radiative transfer modelling.

Chapter 3 presents the high-angular resolution observations of the famous Mira-type AGB star, *o* Cet (Mira), with ALMA. The observations produced images of the photospheric continuum emission of the star at millimetre wavelength and of several transitions of SiO and H_2O in Mira's extended atmosphere and inner wind. One of the highlights of this study is that, for the first time, molecular line absorption against the stellar continuum has been clearly imaged at (sub)millimetre wavelengths. Since SiO and H_2O are among the most abundant molecules within the dust formation zone in an oxygen-rich CSE, the ALMA observations allowed studying the gas dynamics in unprecedented detail.

This thesis also includes five technical appendices. Appendix A explains the theoretical background of radiative transfer modelling. Appendix B describes the extrapolations of the collisional rate coefficients of NH_3 and SiO in the radiative transfer models. Appendix C includes a new derivation of the period of IK Tau for the discussion in Chap. 2. Issues in image reconstruction of Mira's observations (Chap. 3) were identified and are discussed in Appendix D. Finally, Appendix E presents additional spectral line images of Mira for completeness.

CHAPTER 2

Multi-wavelength observations of circumstellar ammonia in oxygen-rich evolved stars

This chapter is adapted from the accepted paper of Wong, K. T., Menten, K.M., Kamiński, T., Wyrowski, F., Lacy, J. H., and Greathouse, T. K. 2017, A&A in press.
DOI: 10.1051/0004-6361/201731873 [arXiv:1710.01027]

Brief summary

The circumstellar ammonia (NH_3) chemistry in evolved stars is poorly understood. Previous observations and modelling showed that NH_3 abundance in oxygen-rich stars is several orders of magnitude above that predicted by equilibrium chemistry.

In order to characterise the spatial distribution and excitation of NH_3 in the oxygen-rich CSEs, we carried out multi-wavelength (radio, submillimetre, and mid-infrared) observations and radiative transfer modelling of NH_3 from four diverse oxygen-rich stars: IK Tau, a long-period variable (LPV) with a high mass-loss rate; OH 231.8+4.2, a bipolar pre-planetary nebula (PPN) around an OH/IR star; VY CMa, a red supergiant (RSG); and IRC +10420, yellow hypergiant (YHG), which is believed to be in the post-RSG phase.

In this study, NH_3 is detected in very high abundance in oxygen-rich evolved stars compared to the predictions from equilibrium chemistry. Modelling results show that the NH_3 abundance relative to molecular hydrogen is generally of the order of 10^{-7}, which is a few times lower than previous estimates that were made without considering mid-infrared vibrational excitation of the molecule and is at least 10 times higher than that in the carbon-rich CSE of IRC +10216. There are also indications that NH_3 may come from localised regions that are denser than the ambient medium. Circumstellar shocks in the accelerated wind may facilitate the formation of NH_3 but cannot fully explain the origin of the molecule.

2.1. Introduction

2.1.1. A ubiquitous molecule

Being the first polyatomic molecule discovered in the interstellar space (Cheung et al., 1968), ammonia (NH_3) is found in a wide variety of astronomical environments. The molecule has been detected in cold and infrared dark clouds (IRDCs; e.g. Cheung et al., 1973; Pillai et al., 2006), molecular clouds (e.g. Harju et al., 1993; Mills & Morris, 2013; Arai et al., 2016), massive star-forming regions (e.g. Urquhart et al., 2011; Wienen et al., 2012), and a protoplanetary disc (Salinas et al., 2016). Recently, NH_3 has also been found in some more complex environments, such as the interacting region between an IRDC and the nebula of a luminous

blue variable candidate (Rizzo et al., 2014) and the stellar merger remnant candidate Nova Vul 1670 (Kamiński et al., 2015). Furthermore, NH_3 is one of the main atmospheric components of gas-giant (exo)planets (e.g. Betz, 1996; Madhusudhan et al., 2016) and is considered to be one of the possible reactants in the synthesis of prebiotic organic molecules (e.g. amino acids) in the ISM (McCollom, 2013, and references therein).

2.1.2. Circumstellar ammonia

NH_3 has also been detected in the CSEs around a variety of evolved stars of different masses, evolutionary phases, and chemistry. The first detection of circumstellar NH_3 was based on mid-infrared (MIR) absorption spectra[1] in the ν_2-band from the carbon-rich AGB star IRC +10216 (Betz et al., 1979) and several oxygen-rich (super)giants (McLaren & Betz, 1980; Betz & Goldhaber, 1985). Radio emission from the inversion transitions in the ground vibrational state have also been detected from AGB stars (IRC +10216 and IK Tauri; Bell et al., 1980; Menten & Alcolea, 1995), (pre-)planetary nebulae (CRL 2688, OH 231.8+4.2, CRL 618; Nguyen-Q-Rieu et al., 1984; Morris et al., 1987; Truong-Bach et al., 1988, 1996; Martin-Pintado & Bachiller, 1992a,b; Martin-Pintado et al., 1993, 1995), and from a massive star (IRC +10420; Menten & Alcolea, 1995). Recent submillimetre observations with space observatories have detected rotational transitions of NH_3 from evolved stars of all chemical types, including C-rich (Hasegawa et al., 2006; Schmidt et al., 2016), O-rich (Menten et al., 2010; Teyssier et al., 2012), and S-type stars (Danilovich et al., 2014).

2.1.3. An enigma in circumstellar chemistry

The detection of NH_3 from such a wide variety of evolved stars, however, is completely unexpected from the chemical point of view. Assuming dissociative and local thermodynamical equilibria (hereafter, equilibrium chemistry), most of the nitrogen nuclei in the photosphere of cool ($T_{\rm eff} \lesssim 3000$ K) giants and supergiants are locked in molecular nitrogen (N_2) and very few are left to form NH_3 or other N-bearing species (e.g. Tsuji, 1964; Dolan, 1965; Fujita, 1966; Tsuji, 1973; McCabe et al., 1979; Johnson & Sauval, 1982). As a result, the photospheric NH_3 abundance predicted by the above-cited chemical models is typically in the range of 10^{-12}–10^{-10} relative to molecular hydrogen (H_2). The abundance derived from observations (Sect. 2.1.2), however, ranges from 10^{-8} to 10^{-6} (e.g. Betz et al., 1979; Kwok et al., 1981; Martin-Pintado & Bachiller, 1992a; Menten & Alcolea, 1995), which is *several orders* of magnitude higher than that predicted by equilibrium chemistry. Furthermore, circumstellar chemical models have to 'inject' a high NH_3 abundance ($\sim 10^{-6}$–10^{-5}; as derived from observations) in the inner CSE ($r < 10^{16}$ cm) in order to explain the observed abundances of NH_3 and other nitrogen-bearing molecules at radii further out from the photosphere (e.g. Nercessian et al., 1989; Willacy & Millar, 1997; Gobrecht et al., 2016; Li et al., 2016). No chemical mechanisms are given to explain the formation of such a large amount of NH_3 in the circumstellar gas of evolved stars.

2.1.4. Previous modelling

Menten & Alcolea (1995) and Menten et al. (2010) have modelled the NH_3 line emission from several O-rich evolved stars. In the former model of Menten & Alcolea (1995), local thermodynamic equilibrium (LTE) excitation was assumed and an NH_3 abundance of 4×10^{-6} was required to explain the radio inversion line emission from IK Tau and IRC +10420. The more recent model of Menten et al. (2010) has conducted detailed statistical equilibrium (non-LTE)

[1] Details of different NH_3 transitions in various parts of the electromagnetic spectrum will be described in Sect. 2.1.5.

calculations and has found a similarly high NH_3 abundance of $\sim 3 \times 10^{-7}$–3×10^{-6} in order to reproduce the submillimetre ground-state rotational line emission from IK Tau, IRC +10420, VY CMa, and OH 26.5+0.6. However, Menten et al. (2010) found that a lower NH_3 abundance (by a factor of ~2.5–3.0) is enough to fit the spectral line profiles of the radio inversion line of IK Tau and IRC +10420. In their model, NH_3 abundance pertains over the accelerated wind from an inner radius of approximately 10–20 $R_\star$ to ~1300 $R_\star$ for IK Tau and ~8600 $R_\star$ for IRC +10420 (Menten et al., 2010).

The non-LTE model of Menten et al. (2010) only included energy levels within the vibrational ground state of NH_3 and did not consider infrared radiative excitation. Radiative excitation by infrared photons, especially at the mid-infrared (MIR) wavelengths near 10 μm for NH_3, may be important in populating the ground-state rotational energy levels. Indeed, Schmidt et al. (2016) found that the discrepancy between the derived NH_3 abundances from rotational and inversion lines can be reconciled by including the MIR ν_2-band transitions between the ground state ($v = 0$) and the first vibrationally excited state ($v_2 = 1$). The results of Schmidt et al. (2016) are based on the C-rich star IRC +10216 only. It would be important to test the effects of MIR pumping in O-rich stars.

In addition, the inclusion of MIR excitation also reduces the derived NH_3 abundance in IRC +10216 from a high value of 1×10^{-6} (Hasegawa et al., 2006) to $\sim 3 \times 10^{-8}$ (Schmidt et al., 2016). This suggests that the past estimates of NH_3 abundances based only on vibrational ground-state energy levels may be overestimated by about one order of magnitude. Hence, new models are needed for O-rich stars in order to correctly characterise the NH_3 abundance in these CSEs.

2.1.5. Molecular physics of ammonia

2.1.5.1. Vibrational modes

In its equilibrium configuration, NH_3 is a symmetric top molecule and the nitrogen atom at one of the equilibrium positions can tunnel through the plane formed by the three hydrogen atoms to the other equilibrium position. The inverting (non-rigid) NH_3 molecule corresponds to the molecular symmetry point group $\boldsymbol{D}_{3h}$ (Longuet-Higgins, 1963). There are six fundamental modes of vibration for such type of molecules, namely, the symmetric stretch (ν_1: near 3.0 μm), the symmetric bend or the 'umbrella' mode (ν_2: near 10.3 μm and 10.7 μm), the doubly degenerate asymmetric stretch ($\nu_3^{\ell_3}$: near 2.9 μm), and the doubly degenerate asymmetric bend ($\nu_4^{\ell_4}$: near 6.1 μm) (Howard & Bright Wilson, 1934; Herzberg, 1945). Schmidt et al. (2016) have recently shown that, in AGB CSEs, only the ground vibrational state ($v = 0$) and the lowest vibrationally excited state ($v_2 = 1$) play dominant roles in populating the most important energy levels in the ground vibrational state. In this study, therefore, we only consider the energy levels in the ground and $v_2 = 1$ states of the molecule as done by Schmidt et al. (2016).

2.1.5.2. Radio inversion transitions

The rotational energy levels of NH_3 are characterised by several quantum numbers, including J and K, which represent the total angular momentum and its projection along the axis of rotational symmetry, respectively. The existence of two equilibria leads to a symmetric (s, +) and an asymmetric (a, −) combination of the wave functions (e.g. Sect. II, 5(d) of Herzberg, 1945). Therefore, each of the rotational (J, K) levels is split into two inversion levels, except for the levels of the $K = 0$ ladder in which half of the energy levels are missing due to the Pauli exclusion principle (e.g. Sect. 3-4 of Townes & Schawlow, 1955). Dipole selection rules dictate a change in symmetric/asymmetric combination, i.e. $+ \leftrightarrow -$ (e.g. Chap. 12 of

Bunker, 1979), in any transition of the NH_3 molecule. In the ground state, transition between the two inversion levels within a (J, K) state (where $K \neq 0$) corresponds to a wavelength of about 1.3 cm (a frequency of around 24 GHz) and many (J, K) inversion lines can be observed in the radio K band. Modern digital technology allows a large instantaneous bandwidth, so that the newly upgraded Karl G. Jansky Very Large Array (VLA) and the Effelsberg 100-m Radio Telescope (Wieching, 2014) allow simultaneous observations of a multitude of NH_3 inversion lines (see, e.g., Fig. A1 of Gong et al., 2015).

2.1.5.3. (Sub)millimetre rotational transitions

Rotational transitions follow the selection rule $\Delta J = 0, \pm 1$, except for $K = 0$ for which $\Delta J = \pm 1$ only. In each K-ladder, energy levels with $J > K$ are known as non-metastable levels because they decay rapidly to the metastable level ($J = K$) via $\Delta J = -1$ transitions at the submillimetre and far-infrared wavelengths. In the ground state, important low-J rotational transitions include $J_K = 1_0$–0_0, 2_K–1_K, and 3_K–2_K near the frequencies of 572 GHz, 1.2 THz, and 1.8 THz, respectively, frequencies that are inaccessible to ground-based telescopes primarily due to tropospheric water vapour absorption (e.g. Yang et al., 2011). Hence these lines can only be observed with space telescopes or airborne observatories. In the $v_2 = 1$ state, the two important transitions at (sub)millimetre wavelengths are $J_K = 0_0$–1_0 at 466.246 GHz and 2_1–1_1 at 140.142 GHz. These two vibrationally excited lines have previously been detected from a few star-forming regions in the Galaxy (Schilke et al., 1990, 1992), but searches had been unsuccessful in the carbon-rich AGB star IRC +10216 (Mauersberger et al., 1988; Schilke et al., 1990).

Since the axis of rotational symmetry is also along the direction of the molecule's electric dipole moment, no torque exists along this axis and the projected angular momentum does not change upon rotations. In other words, rotational transitions follow the selection rule $\Delta K = 0$ (e.g. Oka, 1976) and radiative transitions between different K-ladders of NH_3 are generally forbidden[2]. Transitions between the metastable levels between K-ladders are only possible via collisions (Ho & Townes, 1983).

2.1.5.4. Mid-infrared rovibrational transitions

Absorption of infrared photon leads to radiative vibrational excitation of NH_3 ($v_2 = 1 \leftarrow 0$). The strongest transitions are in the MIR N band near 10 μm. The rovibrational transitions are classified as P, Q, or R branches if $J(v_2 = 1) - J(\text{ground}) = -1$, 0, or +1, respectively (e.g. Herzberg, 1945). Individual transitions are labelled by the lower (ground-state) level and the upper level can be inferred through selection rules (e.g. Tsuboi et al., 1958). For examples, $aR(0, 0)$ represents the transition between $v = 0$ $J_K = 0_0$(a) and $v_2 = 1$ $J_K = 1_0$(s), while $sP(1, 0)$ represents the transition between $v = 0$ $J_K = 1_0$(s) and $v_2 = 1$ $J_K = 0_0$(a). The letters a and s represent the asymmetric and symmetric states, respectively.

2.1.5.5. Ortho- and para-ammonia

Each hydrogen atom in the NH_3 molecule can take the nuclear spin of $+1/2$ or $-1/2$, and hence the total nuclear spin can either be $I = 1/2$ or $3/2$. Since radiation and collisions in interstellar gas in general do not change the spin orientation, transitions between ortho-NH_3 ($I = 3/2$; $K = 0, 3, 6, \ldots$) and para-NH_3 ($I = 1/2$; $K = 1, 2, 4, 5, \ldots$) are highly forbidden (Cheung et al., 1969; Ho & Townes, 1983). Therefore, the energy levels in ortho- and para-NH_3 should

[2] Radiative transitions with $\Delta K = \pm 3$ are weakly allowed due to centrifugal distortion, in which the molecular rotation induces a small dipole moment in the direction perpendicular to the principal axis of NH_3 (Watson, 1971; Oka, 1976). However, these transitions are important only under very low gas density ($\sim 200\,\text{cm}^{-3}$; Oka et al., 1971). In circumstellar environments, $\Delta K = \pm 3$ transitions are dominated by collisions.

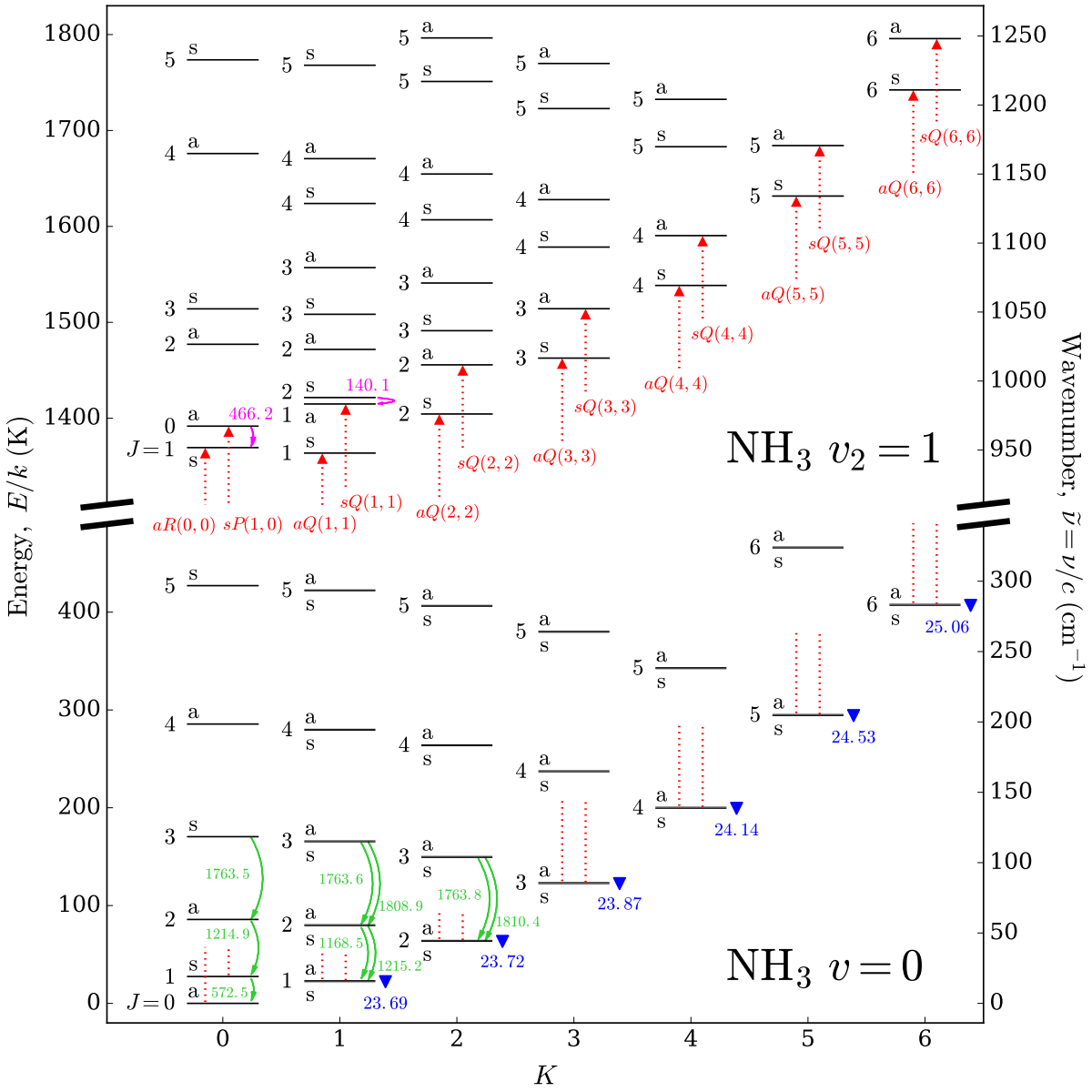

Figure 2.1.: Energy level diagram of NH_3 showing the ground ($v = 0$; *lower half*) and the first excited vibrational ($v_2 = 1$; *upper half*) states. The *truncated* vertical axes on the left and right show the energy from the ground (E/k; K) and the corresponding wavenumber ($\tilde{\nu} = \nu/c$; cm^{-1}), respectively; the horizontal axis shows the quantum number K. The integral value next to each level or inversion doublet shows the quantum number J; the letter 'a' or 's' represents the symmetry of the level. Ground-state inversion doublets ($K > 0$) can only be resolved when the figure is zoomed in due to the small energy differences. Important transitions as discussed in this chapter are labelled: curved green and magenta arrows indicate the (sub)millimetre rotational line emission within the ground and excited states, respectively; blue triangles mark the radio metastable inversion line emission in the ground state; and upward red dotted arrows indicate the absorption in the MIR ν_2 band. These transitions are labelled by their rest frequencies in GHz (see Tables 2.1 and 2.3), except the MIR transitions which are labelled by their transition names (see Table 2.2).

be treated separately in excitation analyses. Faure et al. (2013) found that the ortho-to-para abundance ratio of NH_3 deviates from unity if the molecule was formed in cold interstellar gas of temperature below 30 K. In circumstellar environments where the gas temperatures are generally much higher than 100 K, the ortho- and para-NH_3 abundances are expected to be identical.

Figure 2.1 shows the energy level diagram of NH_3 in the ground ($v = 0$) and first excited vibrational state ($v_2 = 1$). Important transitions in this chapter are annotated with their frequencies or transition names. Observations of these transitions will be discussed in the next section.

2.2. Observations and data reduction

2.2.1. Target selection

We observed various NH_3 transitions towards a diverse set of four different O-rich stars: IK Tau, OH 231.8+4.2, VY CMa, and IRC +10420. The former two objects are in the low-/intermediate-mass regime and the latter two are massive stars. IK Tau and VY CMa are in the earlier phases of post-main sequence stellar evolution while the other two objects are in the later stages. In addition, these targets are among the most chemically rich and the most studied objects of their respective evolutionary phases. These objects also exhibit intense NH_3 emission as revealed by past observations (e.g. Menten & Alcolea, 1995; Menten et al., 2010). Hence, they form an ideal set of samples to study the circumstellar chemistry of O-rich evolved stars.

In the following subsections, we discuss the multi-wavelength observations of NH_3 emission and absorption in the CSEs of these targets.

2.2.2. *Herschel* Space Observatory

General References: Pilbratt et al. (2010); de Graauw et al. (2010).

The *Herschel* Space Observatory was a far-infrared and submillimetre space telescope operated by the European Space Agency (ESA). It was launched in May 2009 and ceased to operate in April 2013 when its liquid helium coolant has been exhausted. *Herschel* orbited around the second Lagrangian (L_2) point of the Sun–Earth system, which is at about 1.5 million kilometres from Earth. *Herschel* carried a 3.5-m diameter telescope and three science instruments, one of which is the Heterodyne Instrument for the Far-Infrared (HIFI). HIFI consists of seven heterodyne receivers covering the frequency ranges of 480–1250 GHz and 1410–1910 GHz. The spectral resolution of the wideband spectrometer (WBS) is 1.1 MHz and that of the high resolution spectrometer (HRS) is between 0.125 and 1.0 MHz. The velocity resolution is much better than 1 km s^{-1}, allowing the complex spectral line profiles of CSEs to be spectrally resolved.

In this study, we include all the available NH_3 spectra of the four selected O-rich stars from the *Herschel* Science Archive (HSA; v8.0)[3]. These spectra include the rotational transitions of the molecule from $J = 1$–0 up to $J = 3$–2. Table 2.1 summarises the list of covered NH_3 transitions. The data products from the HSA have been processed with the *Herschel* Standard Product Generation (SPG) pipeline (v14.1.0). For each data product, we averaged the signals from the H and V polarisation channels and stitched the spectrometer subbands together. The spectra in antenna temperature (T_A^*) scale were then exported to CLASS[4] of the GILDAS pack-

[3] http://archives.esac.esa.int/hsa/whsa/
[4] Continuum and Line Analysis Single-dish Software.

age[5] (Pety, 2005) for further data processing, such as polynomial baseline removal, main-beam efficiency correction, and noise-weighted averaging of spectra from different observations.

We converted the scale of the spectra from antenna temperature to main-beam temperature ($T_{\rm mb}$) with the following equation:

$$T_{\rm mb} = T_{\rm A}^{*} \frac{\eta_{\rm l}}{\eta_{\rm mb}}, \tag{2.1}$$

where $\eta_{\rm l} = 0.96$ is the forward efficiency (Roelfsema et al., 2012) and $\eta_{\rm mb}$ is the main-beam efficiency. The main-beam efficiency for each NH_3 line frequency is the average of $\eta_{\rm mb,\,H}$ and $\eta_{\rm mb,\,V}$ for both polarisations, which are evaluated from the parameters reported by Mueller et al. (2014).

By combining the calibration error budget in Roelfsema et al. (2012) in quadrature, we estimate the calibration uncertainties to be about 10% for NH_3 $J = 1$–0 and 15% for $J = 2$–1 and $J = 3$–2. The sizes of the NH_3-emitting regions of our targets as constrained by imaging observations are $\lesssim 4''$, much smaller than the FWHM of the telescope beam ($12''$–$37''$).

Table 2.1.: List of $^{14}NH_3$ lines at submillimetre wavelengths as observed by *Herschel*/HIFI.

Transition J_K(sym)	Rest frequency[a] MHz	Energy[a,b] K	Ref. for line freq.
1_0(s)–0_0(a)	572 498.160(2)	27.48	1
2_1(s)–1_1(a)	1 168 452.39(2)	79.34	2
2_0(a)–1_0(s)	1 214 852.94(2)	85.78	2
2_1(a)–1_1(s)	1 215 245.71(2)	80.45	2
3_0(s)–2_0(a)	1 763 524.4(1)	170.42	3
3_1(s)–2_1(a)	1 763 601.2(1)	165.09	3
3_2(s)–2_2(a)	1 763 823.2(1)	149.10	3
3_1(a)–2_1(s)	1 808 934.6(1)	166.16	3
3_2(a)–2_2(s)	1 810 380.0(1)	150.19	3

References. (1) Cazzoli et al. (2009); (2) Winnewisser et al. (1996); (3) Yu et al. (2010).

Notes. [(a)] The NH_3 experimental line frequencies and upper-level energies are retrieved the calculations and compilations by Yu et al. (2010). The original references are given in the last column. These values are the same as those in the Jet Propulsion Laboratory (JPL) catalogue (Pickett et al., 1998). The numbers shown in brackets are the uncertainties corresponding to the last digit(s) of the quoted frequencies. [(b)] $E_{\rm up}/k$, the upper energy level in K.

2.2.3. IRAM 30-metre Telescope

General References: Wild (1999); Carter et al. (2012); Kramer et al. (2013).

The IRAM 30m Telescope near Pico Veleta, Spain was used to search for the rotational transition within the vibrationally excited state of NH_3 at 140.142 GHz (2.14 mm; $v_2 = 1$ $J_K = 2_1$–1_1). We performed deep integration on the target IK Tau with the Eight MIxer Receiver (EMIR) system in the 2 mm (E150) band in August 2015 (project: 052-15; PI: K. T. Wong).

Observations were done in the wobbler switching mode, in which the telescope beam is moved, by shifting the secondary reflector of the telescope, between the target and two reference positions that are free of emission/absorption and are symmetrical about the target. Subtractions are then performed to eliminate the background radiation and to retain the target

[5] Grenoble Image and Line Data Analysis Software; http://www.iram.fr/IRAMFR/GILDAS/

signals. This method results in flat baselines in the target spectra. During the observations, pointing was checked regularly every ~1 hour with a nearby object with strong flux density at 2-mm wavelength. Focus was checked with the planet Uranus approximately every 3 hours and after sunrise, when the temperature could have changed. The total integration time on IK Tau is about 10 hours. Calibration was done with the MIRA[6] software in GILDAS. Characteristic values for the main-beam and forward efficiencies were adopted, which are $\eta_{\rm mb} = 0.74$ and $\eta_{\rm l} = 0.93$, respectively. The rms noise near 140 GHz in $T_{\rm mb}$ scale is 0.61 mK at the velocity resolution of 5.0 km s^{-1}.

2.2.4. NASA Infrared Telescope Facility (IRTF)

General Reference: Lacy et al. (2002).

The ν_2 excitation of ammonia absorbs MIR radiation near 10.5 μm from the central star and the surrounding dust. There were only a handful of published observations of NH_3 in the MIR, most of which targeted the carbon-rich AGB star IRC +10216 (see Table 2.2 for a summary of past observations). In order to obtain a substantial number of ν_2 absorption lines for the excitation analysis of NH_3, we performed new MIR observations of *o* Cet, IK Tau, and VY CMa with the NASA Infrared Telescope Facility (IRTF) under the programme number 2016B064 (PI: K. T. Wong).

The NASA Infrared Telescope Facility (IRTF) is a 3-metre infrared telescope at the summit of Mauna Kea, Hawai'i, USA. One of its instruments is the Texas Echelon Cross Echelle Spectrograph (TEXES), a mid-infrared (MIR; 5–25 μm) spectrograph offering a resolving power up to $R = \lambda/\Delta\lambda \approx 100\,000$. TEXES consists of two dispersing elements in the high-resolution mode, which are both reflective diffraction gratings. The first one is a high-resolution grating (the echelon; Michelson, 1898); and the second one is another dispersion grating rotated by 90° (the cross-disperser) in order to separate overlapping diffraction orders and achieve high spectral resolution.

We obtained spectra in four wavelength (wavenumber) settings near 10.3 (966), 10.5 (950), 10.7 (930), and 11.3 μm (888 cm^{-1}), targeting 16 rovibrational transitions as listed in Table 2.2. The on-source time for each target in each setting was about 10 minutes. The dwarf planet Ceres was observed as the telluric calibrator for the setting near 10.7 μm (930 cm^{-1}) and the asteroid Vesta was observed for the rest in order to remove atmospheric effects in the MIR spectra of the targets.

During our observations, the seeing at optical wavelengths at the telescope site was $\lesssim$1.″0[7], which corresponds to about 0.″6 at 10 μm (e.g. van den Ancker et al., 2016). This value is smaller than the FWHM of the telescope's point-spread function, which is about 0.″9. Therefore, our observations are diffraction-limited.

The data were processed with a procedure similar to the TEXES data reduction pipeline (Lacy et al., 2002), except that telluric lines were removed by a separate fitting routine. In the pipeline, the calibration frame (flat field) was the difference between the black chopper blade and sky measurements, S_ν(black − sky), which partially removes telluric lines (see Eq. (3) of Lacy et al., 2002). In our processing, the data spectra were flat-fielded with the black

[6] Multichannel Imaging and Calibration Software for Receiver Arrays.

[7] From the Mauna Kea Atmospheric Monitor, available at http://mkwc.ifa.hawaii.edu/current/seeing/index.cgi

measurements and the intermediate source intensity is given by

$$I_\nu(\text{target}) \approx \frac{S_\nu(\text{target})}{S_\nu(\text{black})} B_\nu(T_{\text{black}}), \tag{2.2}$$

where S_ν and B_ν are the measured signal and the Planck's law at the frequency ν. Each intermediate spectrum was then normalised and divided by a modelled telluric transmission spectrum. The parameters of the telluric transmission model were chosen to make the divided spectrum as flat as possible and to fit the observed $S_\nu(\text{black} - \text{sky})$, with the atmospheric temperatures and humidities constrained by weather balloon data. Finally, each target spectrum was divided by a residual spectrum smoothed with a Gaussian kernel of 60 km s^{-1} in FWHM. The last division was necessary to remove broad wiggles due to the echelon blaze function and interference fringes, but may also have removed or created broad wings on the observed circumstellar lines.

We verified the wavenumber scale of the calibrated data by comparing the minima of atmospheric transmission with the rest wavenumbers of strong telluric lines in the GEISA spectroscopic database[8] (2015 edition; Jacquinet-Husson et al., 2016). Almost all strong telluric lines are identified as due to CO_2, except for the H_2O line at 948.262881 cm^{-1}. The differences between the transmission minima and telluric lines do not exceed 4 km s^{-1} in radio local standard of rest (LSR) velocity. The uncertainties of the rest wavenumbers of our targeted NH_3 lines (Table 2.2) correspond to velocities of <0.002 km s^{-1}.

Further data processing include (1) converting the wavenumber (frequency) axis from topocentric to LSR frame of reference using the ephemeris software GILDAS/ASTRO[9] and (2) subtracting the baselines of some NH_3 spectra by fitting low-order polynomials in GILDAS/CLASS to remove local wiggles in the normalised spectra of the targets.

We also compare the old $aR(0,0)$ and $aQ(2,2)$ spectra of VY CMa and the $aR(0,0)$ spectrum of IRC +10420 as detected with the Berkeley heterodyne receiver at the McMath Solar Telescope. These spectra were digitised from the scanned paper of McLaren & Betz (1980, © AAS. Reproduced with permission.) with the online application `WebPlotDigitizer`[10] (version 3.10; Rohatgi & Stanojevic, 2016). We did not detect NH_3 absorption from *o* Cet; therefore we only briefly discuss its non-detection in Sect. 2.4.5.

2.2.5. Karl G. Jansky Very Large Array (VLA)

The radio inversion line emission of NH_3 was observed with the NRAO[11] VLA[12] on the Plains of San Agustin, New Mexico, USA. VLA is a radio interferometer consisting of 27 antennae. Each antenna is 25 metre in diameter. Each pair of antennae forms a baseline and there are in total $27 \times 26 \div 2 = 351$ unique baselines in the whole array. The array operates at four fixed configurations in Y-shape with the longest baseline ranging from 1.03 km (D-configuration) to 36.4 km (A-configuration). The angular resolution of the images produced by an interferometer is equivalent to that of an imaginary single-dish telescope of diameter equal to the longest baseline. At the typical frequency (wavelength) of the metastable ($J = K$) NH_3 inversion transitions of ~24 GHz (1.25 cm), VLA can produce images with beam sizes (in full width at half maximum, FWHM) of approximately 0.″4, 1.″3, and 4.″3 in B-, C-, and D-configurations,

[8] *Gestion et Etude des Informations Spectroscopiques Atmosphériques* [Management and Study of Atmospheric Spectroscopic Information], http://ara.abct.lmd.polytechnique.fr/

[9] A Software To pRepare Observations.

[10] http://arohatgi.info/WebPlotDigitizer/

[11] The National Radio Astronomy Observatory is a facility of the National Science Foundation operated under cooperative agreement by Associated Universities, Inc.

[12] Karl G. Jansky Very Large Array.

Table 2.2.: List of MIR NH_3 ν_2 transitions searched with the TEXES instrument at the NASA IRTF under the programme 2016B064 and their previous detection in evolved stars.

Transition	Wavelength (μm)	Wavenumber[a] (cm^{-1})	E_{up}/k (K)	A_{ul}[b] (s^{-1})	Previous detection in evolved stars[c]	Ref. for detection
$sQ(1,1)$	10.33060	967.997763	1414.86	7.94		
$sQ(2,2)$[d]	10.33337	967.738421	1455.67	10.57		
$sQ(3,3)$	10.33756	967.346340	1514.19	11.60		
$sQ(4,4)$	10.34324	966.814717	1590.39	12.67		
$sQ(5,5)$	10.35035	966.151127	1684.27	13.20		
$sQ(6,6)$	10.35890	965.353911	1795.79	13.58		
$aR(0,0)$	10.50667	951.776244	1369.39	5.49	IRC +10420, VX Sgr	1
					VY CMa	1, 2
					NML Cyg	2
					IRC +10216	2, 3, 4, 5
$sP(1,0)$[e]	10.54594	948.232047	1391.77	14.88	NML Cyg	2
$aQ(1,1)$	10.73390	931.627754	1363.67	7.74		
$aQ(2,2)$	10.73730	931.333249	1404.43	10.32	IRC +10216	2, 4, 6, 7
					VY CMa	1, 2, 8
					o Cet	9
$aQ(3,3)$	10.74394	930.757028	1462.69	11.60	VY CMa	2
					IRC +10216	2, 4, 8
$aQ(4,4)$	10.75387	929.898108	1538.44	12.36	IRC +10216	4
$aQ(5,5)$	10.76711	928.754479	1631.64	12.86		
$aQ(6,6)$	10.78373	927.323036	1742.27	13.22	IRC +10216	2, 4, 6
					VY CMa	2, 8

References. (1) McLaren & Betz (1980); (2) Goldhaber (1988); (3) Betz & McLaren (1980); (4) Keady & Ridgway (1993); (5) Fonfría et al. (2017); (6) Betz et al. (1979); (7) Monnier et al. (2000c); (8) Monnier et al. (2000b); (9) Betz & Goldhaber (1985).

Notes. [(a)] The uncertainties of the wavenumbers are smaller than 0.000004 cm^{-1} (~0.0013 km s^{-1}). The wavenumbers and uncertainties are computed from the data in supplementary material 6 of Chen et al. (2006), which is also publicly available at `https://library.osu.edu/projects/msa/jmsa_06.htm`. [(b)] The Einstein *A* coefficient. The values are retrieved from Table S1 of Yu et al. (2010, supplementary material). [(c)] Additional ν_2 transitions have been detected towards the red hypergiants VY CMa and NML Cyg by Goldhaber (1988) and towards IRC +10216 by Holler (1999, quoted in Monnier et al., 2000b). Schrey (1986) also reported detection of $sQ(2,1)$ or $sQ(2,2)$ absorption towards the Mira-type AGB star R Leonis; however, the purported detection had very low S/N ratios in the spectra and the position of the more probable $sQ(2,2)$ line was too far away from the suspected absorption features. [(d)] Potentially blended with telluric CO_2 $R(8)$ absorption at 967.707233 cm^{-1}. [(e)] Potentially blended with telluric o-H_2O $J_{K_a,K_c} = 12_{5,8}$–$11_{0,11}$ absorption at 948.262881 cm^{-1}.

respectively. The high angular resolutions achieved by the interferometer allow us to constrain the spatial distribution of the molecular emission.

The data obtained by the interferometer have to be properly calibrated before they can be imaged. The standard calibration process is outlined below.

1. Removal of bad data points.
2. Prior data corrections based on the latest antenna positions, elevation-dependent gain-curves, and atmosphere opacities.
3. Frequency-dependent corrections of phase and amplitude as derived from a strong bandpass calibrator.
4. Absolute flux calibration based on the scaling factor determined from a well-monitored flux calibrator.
5. Time-dependent (gain) corrections of phase and amplitude interpolated from a nearby gain calibrator.

The radio emission from the science targets usually contains (a) the continuum emission from the star and circumstellar dust shells and (b) the spectral line signals from the circumstellar gas at certain frequency ranges. In the typical data analysis of spectral line data with strong continuum signals, the continuum emission is fitted over the frequency ranges that are free of spectral lines and the fitted continuum model is then removed from the data.

The strongest NH_3 emission in radio frequencies comes from metastable inversion transitions, which are listed in Table 2.3. NH_3 $(J, K) = (1, 1)$ and $(2, 2)$ were observed with the VLA in 2004 for IK Tau and IRC +10420 (project: AM797; PI: K. M. Menten). The absolute flux calibrators during the observations of IK Tau and IRC +10420 were 3C48 (J0137+3309) and 3C286 (J1331+3030), respectively. The flux densities of 3C48 and 3C286 during the observations were 1.10 Jy and 2.41 Jy, respectively (Perley & Butler, 2013). The interferometer phase of IK Tau was referenced to the nearby gain calibrator J0409+1217 and that of IRC +10420 was referenced to J1922+1530. Both gain calibrators are about 4° from the respective targets.

Table 2.3.: Observations of $^{14}NH_3$ lines in the radio wavelengths as observed by the VLA.

Transition J_K(sym)	Rest frequency[a] (MHz)	Energy[a,b] (K)	Ref. for line freq.
1_1(a)–1_1(s)	23 694.4955(2)	23.26	1
2_2(a)–2_2(s)	23 722.6333(2)	64.45	1
3_3(a)–3_3(s)	23 870.1292(2)	123.54	1
4_4(a)–4_4(s)	24 139.4163(2)	200.52	2
5_5(a)–5_5(s)	24 532.9887(2)	295.37	2
6_6(a)–6_6(s)	25 056.03(1)	408.06	3

References. (1) Kukolich (1967); (2) Kukolich & Wofsy (1970); (3) Poynter & Kakar (1975).

Notes. [(a)] The NH_3 experimental line frequencies and upper-level energies are retrieved from the calculations and compilations by Yu et al. (2010). Code for original references are given in the last column. These values are the same as those in the Jet Propulsion Laboratory (JPL) catalogue (Pickett et al., 1998). The numbers shown in brackets are the uncertainties corresponding to the last digit(s) of the quoted frequencies. [(b)] E_{up}/k, the upper energy level in K.

We reduced the data with $\mathcal{AIPS}$[13]. Some of the observations of IK Tau (time ranging between 16:15:00 and 19:16:00) suffered from poor phase stability and had to be discarded.

[13] NRAO Astronomical Image Processing System.

The rest of the calibration and imaging follows the standard manner, except that continuum subtraction was not performed because the radio continuum of IK Tau is well within the noise levels. We imaged the data with the CLEAN algorithm under natural weighting to minimise the rms noise and restored the final images with a circular beam of 3.″7 in FWHM, which is approximately the geometric mean of the FWHMs of the major and minor axes of the raw beam.

In 2011, VLA was upgraded with expanded capabilities. The new wideband correlator, WIDAR[14], allows simultaneous observations of multiple NH_3 inversion lines, particularly around 22–25 GHz. We carried out three 2-GHz K-band surveys towards IK Tau, VY CMa, and OH 231.8+4.2 with different array configurations and frequency coverages. VY CMa and OH 231.8+4.2 were observed in 2013 under the project VLA/13A-325 (PI: K. M. Menten) and IK Tau was observed in 2015–2016 under the project VLA/15B-167 and VLA/16A-011 (PI: K. T. Wong). The detailed list of calibrators and frequency coverages is shown in Table 2.4.

Table 2.4.: VLA observing log.

Target	Date	Config.	Gain calibrator	Flux calibrator	Freq. coverage ((J, K) or GHz)
IK Tau	2004-07-20	D	J0409+1217	3C48	(1, 1), (2, 2)
	2015-10-30 (D1)[a]	D	J0409+1217	3C48	21.12–23.14[c]
	2015-11-05 (D2)[a]	D	J0409+1217	3C48	21.12–23.14[c]
	2015-01-03 (D3)[a]	D	J0409+1217	3C48	21.12–23.14[c]
	2016-01-29 (C1)[a]	C	J0409+1217	3C48	22.12–24.18[d]
	2016-02-06 (C2)[a]	C	J0409+1217	3C48	22.12–24.18[d]
	2016-05-29 (B1)[a]	B	J0409+1217	3C48	22.12–24.18[d]
	2016-06-17 (B2)[a]	B	J0409+1217	3C48	22.12–24.18[d]
	2016-06-19 (B3)[a]	B	J0409+1217	3C48	22.12–24.18[d]
	2016-07-01[b]				
IRC +10420	2004-08-09	D	J1922+1530	3C286	(1, 1), (2, 2)
OH 231.8+4.2	2004-07-26	D	J0735-1735 J0730-1141	3C286	(1, 1), (2, 2)
	2013-04-05	D	J0748-1639	3C147	23.29–25.26[e]
VY CMa	2013-04-05	D	J0731-2341	3C147	23.29–25.26[e]
	2016-01-10	DnC	J0731-2341	3C147	21.12–23.14[c]

Notes. [(a)] Each VLA observation of IK Tau in 2015–2016 is labelled by the array configuration ('D', 'C', or 'B') and an ordinal number. [(b)] This dataset is completely discarded because of poor phase stability and high rms noise. [(c)] Covered NH_3 lines include (J, K) = (5, 3), (4, 2), (3, 1), (5, 4), (4, 3), (6, 5), (3, 2), (7, 6), and (2, 1). [(d)] Covered NH_3 lines include (J, K) = (3, 1), (5, 4), (4, 3), (6, 5), (3, 2), (7, 6), (2, 1), (1, 1), (2, 2), (3, 3), and (4, 4). [(e)] Covered NH_3 lines include (J, K) = (1, 1), (2, 2), (3, 3), (4, 4), (5, 5), and (6, 6).

These new datasets were calibrated with CASA[15] in the standard manner, an example of which can be found in the CASA tutorial[16]. After calibration, the continuum signals were subtracted to make sure that the data only contain spectral line signals (i.e. NH_3 emission). For

[14] Wideband Interferometer Digital Architecture.
[15] Common Astronomy Software Applications; https://casa.nrao.edu/
[16] https://casaguides.nrao.edu/index.php?title=EVLA_high_frequency_Spectral_Line_tutorial_-_IRC%2B10216_-_CASA_4.2&oldid=15543

VY CMa and OH 231.8+4.2, we used natural weighting to image all six inversion lines. The rms noise in each channel map ($\Delta V = 3\,\mathrm{km\,s^{-1}}$) is roughly 0.8 mJy beam^{-1} and the restoring beam is 4.″0 in FWHM. For IK Tau, additional self-calibration[17] has been done using the strong H_2O masers near 22.235 GHz. One dataset of IK Tau suffered from very poor phase stability and was discarded. After calibration, we then subtracted the continuum and imaged the data with a common, circular beam of 0.″45 in FWHM. The images presented in this section are further smoothed to a resultant beam of 0.″83 for better visualisation.

The continuum data of the ~2-GHz windows of IK Tau, VY CMa, and OH 231.8+4.2 were also calibrated and imaged in the similar methods as the spectral line data. The continuum image from each day of observation was fitted with a single Gaussian component. The fitted centres and the integrated fluxes of these fitted components are presented in Table 2.5.

Table 2.5.: Radio continuum measurements.

Target	Date	R.A. (J2000)	Decl. (J2000)	$\nu_{\rm rep}$ (GHz)	$F(\nu_{\rm rep})$ (μJy)
IK Tau	2015-10-30	$03^{\rm h}53^{\rm m}28\overset{\rm s}{.}924(9)$	+11°24′21.″5(1)	22.13	350 ± 31
	2015-11-05	$03^{\rm h}53^{\rm m}28\overset{\rm s}{.}915(5)$	+11°24′21.″50(9)	22.13	271 ± 22
	2016-01-03	$03^{\rm h}53^{\rm m}28\overset{\rm s}{.}926(2)$	+11°24′21.″45(5)	22.13	250 ± 11
	2016-01-29	$03^{\rm h}53^{\rm m}28\overset{\rm s}{.}9236(8)$	+11°24′21.″51(1)	23.21	308 ± 14
	2016-02-06	$03^{\rm h}53^{\rm m}28\overset{\rm s}{.}9230(6)$	+11°24′21.″52(1)	23.21	278 ± 13
	2016-05-29	$03^{\rm h}53^{\rm m}28\overset{\rm s}{.}9255(4)$	+11°24′21.″509(6)	23.21	346 ± 23
	2016-06-17	$03^{\rm h}53^{\rm m}28\overset{\rm s}{.}9244(2)$	+11°24′21.″493(6)	23.21	361 ± 21
	2016-06-19	$03^{\rm h}53^{\rm m}28\overset{\rm s}{.}9253(3)$	+11°24′21.″485(6)	23.21	366 ± 23
VY CMa	2013-04-05	$07^{\rm h}22^{\rm m}58\overset{\rm s}{.}3253(9)$	−25°46′02.″98(3)	24.27	1404 ± 13
OH 231.8+4.2	2013-04-05	$07^{\rm h}42^{\rm m}16\overset{\rm s}{.}943(3)$	−14°42′49.″77(6)	24.27	735 ± 18

Notes. The columns are (from *left* to *right*): target, date of VLA observation, right ascension and declination of the centre of the fitted continuum, representative frequency, $\nu_{\rm rep}$, in GHz, and the continuum flux at $\nu_{\rm rep}$, $F(\nu_{\rm rep})$, in μJy.

2.3. Radiative transfer modelling

We modelled the NH_3 spectra with the 1-D radiative transfer code RATRAN[18] (version 1.97; Hogerheijde & van der Tak, 2000), assuming that the distribution of NH_3 is spherically symmetric. RATRAN solves the coupled level population and radiative transfer equations with the Monte Carlo method and produces an output image cube for each modelled transition. We then convolved the model image cubes with the same telescope point-spread function or restoring beam as that of the observed data. We processed the modelled images and spectra with the Miriad software package[19] (Sault et al., 1995). The theoretical background of radiative transfer modelling is explained in Appendix A. In the following subsections, we explain the molecular data files and input dust temperature profiles. We discuss the input physical models for each target in Sect. 2.4.

[17] See the CASA tutorial at https://casaguides.nrao.edu/index.php?title=VLA_high_frequency_Spectral_Line_tutorial_-_IRC%2B10216-CASA4.6&oldid=20567

[18] https://personal.sron.nl/~vdtak/ratran/frames.html

[19] http://www.atnf.csiro.au/computing/software/miriad/

2.3.1. Molecular data of ammonia

As discussed in Sect. 2.1.5, ortho- and para-NH_3 do not convert to each other easily in interstellar and circumstellar gas; therefore the two species have to be modelled separately.

The molecular data files of ortho- and para-NH_3 are based on those provided by Schmidt et al. (2016). The energy levels and transition line strengths were retrieved from the 'BYTe' hot NH_3 line list[20] (Yurchenko et al., 2011). The files include energy levels up to 3300 cm^{-1} (or 4750 K) in the ground vibrational state and the $v_2 = 1$ state. It is the first time that the modelling of NH_3 in O-rich CSEs includes the first vibrationally excited state ($v_2 = 1$). In total, there are 172 energy levels (up to $J = 15$) and 1579 radiative transitions for ortho-NH_3, and 340 levels and 4434 transitions for para-NH_3. The collisional rate coefficients of NH_3–H_2 are described in Appendix B.1.

2.3.2. Dust continuum emission

The thermal continuum emission from dust is related to the emission and absorption coefficients. In RATRAN, the absorption coefficient is given by

$$\alpha_\nu^{\rm dust} = \kappa_\nu \rho_{\rm dust} = \kappa_\nu \cdot 2.4\,{\rm u} \cdot ({\rm d/g}) \cdot n_{\rm H_2}, \tag{2.3}$$

where u is the atomic mass unit, d/g is the dust-to-gas mass ratio, and $n_{\rm H_2}$ is the number density of molecular H_2 (Hogerheijde & van der Tak, 2000). The code assumes that the gas consists of 80% H_2 and 20% He by number. The emission coefficient can then be computed with the knowledge of the dust temperature, $T_{\rm dust}$,

$$j_\nu^{\rm dust} = \alpha_\nu^{\rm dust} B_\nu\left(T_{\rm dust}\right), \tag{2.4}$$

where $B_\nu(T)$ is the Planck function.

We produce the dust temperature profiles of IK Tau, VY CMa, and IRC +10420 by modelling their spectral energy distributions (SEDs) with the continuum radiative transfer code DUSTY (Ivezić et al., 1999). We constrain the MIR fluxes of IK Tau by the IRAS[21] Low Resolution Spectra corrected by Volk & Cohen (1989) and Cohen et al. (1992) and those of VY CMa and IRC +10420 by the ISO[22] SWS[23] data processed by Sloan et al. (2003). The FIR fluxes of these three stars are constrained by the ISO LWS[24] data processed by Lloyd et al. (2013).

We only modelled the SEDs with cool oxygen-rich interstellar silicates and adopted the optical constants from Ossenkopf et al. (1992). The comparison of Suh (1999) shows that the opacity functions and optical constants of the cool silicates from Ossenkopf et al. (1992) are consistent with those of other silicates in the literature. The optical constants of silicates mainly depend on the contents of magnesium and iron in the assumed chemical composition (Dorschner et al., 1995). The dust emissivity function (and hence the dust opacity, κ_ν) of cool silicates from Ossenkopf et al. (1992) are readily available in the RATRAN package, therefore allowing us to employ a dust temperature profile that describes the SED self-consistently. Our SED models are primarily based on that presented in Maercker et al. (2008, 2016) for IK Tau and those in Shenoy et al. (2016) for VY CMa and IRC +10420. The derived dust temperature

[20] http://www.exomol.com/data/molecules/NH3/14N-1H3/BYTe/
[21] Infrared Astronomical Satellite (Neugebauer et al., 1984).
[22] Infrared Space Observatory (Kessler et al., 1996).
[23] Short Wavelength Spectrometer (de Graauw et al., 1996).
[24] Long Wavelength Spectrometer (Clegg et al., 1996).

profiles of IK Tau and IRC +10420 agree very well with the optically thin model for dust temperature (Sopka et al., 1985),

$$T_{\rm dust}(r) = T_\star \left(\frac{R_\star}{2r}\right)^{2/(4+p)} \tag{2.5}$$

where p has a typical value of 1 (Olofsson, 2003).

MIR images of OH 231.8+4.2 by Lagadec et al. (2011) have revealed a bright, compact core and an extended halo around the star. The MIR-emitting circumstellar material is dusty (Jura et al., 2002; Matsuura et al., 2006). The MIR emission of OH 231.8+4.2 near the wavelengths of silicate bands extends to FWHM sizes of $2\farcs6 \times 4\farcs3$ at 9.7 μm and $5\farcs4 \times 9\farcs9$ at 18.1 μm (Lagadec et al., 2011), covering most if not all of the NH_3-emitting region. Jura et al. (2002) were able to explain the MIR emission from the compact core at 11.7 μm and 17.9 μm by an opaque, flared disc with an outer radius of $0\farcs25$ and outer temperature of 130 K. This temperature is about 45% of that expected from the optically thin dust temperature model as shown in Eq. (2.5). For simplicity, therefore, we scale Eq. (2.5) by a factor of 0.45 and adopt $p = 1$ as the dust temperature profile of OH 231.8+4.2 in the NH_3-emitting region, which is beyond the opaque disc model of Jura et al. (2002).

2.4. Results and discussion

With the VLA, we detect all covered metastable ($J = K$) inversion transitions from all four targets, including $(J, K) = (1, 1)$ to $(4, 4)$ for IK Tau, $(1, 1)$ to $(6, 6)$ for VY CMa and OH 231.8+4.2, and $(1, 1)$ and $(2, 2)$ for IRC +10420. However, no non-metastable inversion emission from IK Tau is securely detected. Ground-state rotational line emission is also detected in all available *Herschel*/HIFI spectra. These include up to $J = 3$–2 towards IK Tau, VY CMa, and OH 231.8+4.2; and up to $J = 2$–1 towards IRC +10420. We do not detect the 140-GHz rotational transition in the $v_2 = 1$ state towards IK Tau from the IRAM 30m observations. In the MIR spectra, all 14 rovibrational transitions from IK Tau and 12 unblended transitions from VY CMa are detected in absorption. Figure 2.2 shows the full IRTF spectra of both stars in three wavelength settings. There are no strong emission components in these spectra. We note that, however, the spectra are susceptible to imperfect telluric line removal and baseline subtraction as mentioned in Sect. 2.2.4.

In Sects. 2.4.1–2.4.4, we shall discuss the observational and modelling results for each target separately; in Sect. 2.4.5, we summarise the modelling results and discuss the possible origin of circumstellar ammonia. We made use of the `IPython` shell[25] (version 5.1.0; Pérez & Granger, 2007) and the Python libraries including `NumPy`[26] (version 1.11.2; van der Walt et al., 2011), `SciPy`[27] (version 0.18.1; Jones et al., 2001), `matplotlib`[28] (version 1.5.3; Hunter, 2007; Matplotlib Developers, 2016), and `Astropy`[29] (version 1.3; Astropy Collaboration et al., 2013) in computing and plotting the results in this chapter.

2.4.1. IK Tau

2.4.1.1. VLA observations of IK Tau

Figure 2.3 shows the integrated intensity maps of all the four metastable inversion lines ($J = K$) over the LSR velocity range between 34 ± 21 km s^{-1}. These images combined the data

[25] https://ipython.org/
[26] http://www.numpy.org/
[27] https://www.scipy.org/
[28] https://matplotlib.org/
[29] http://www.astropy.org/

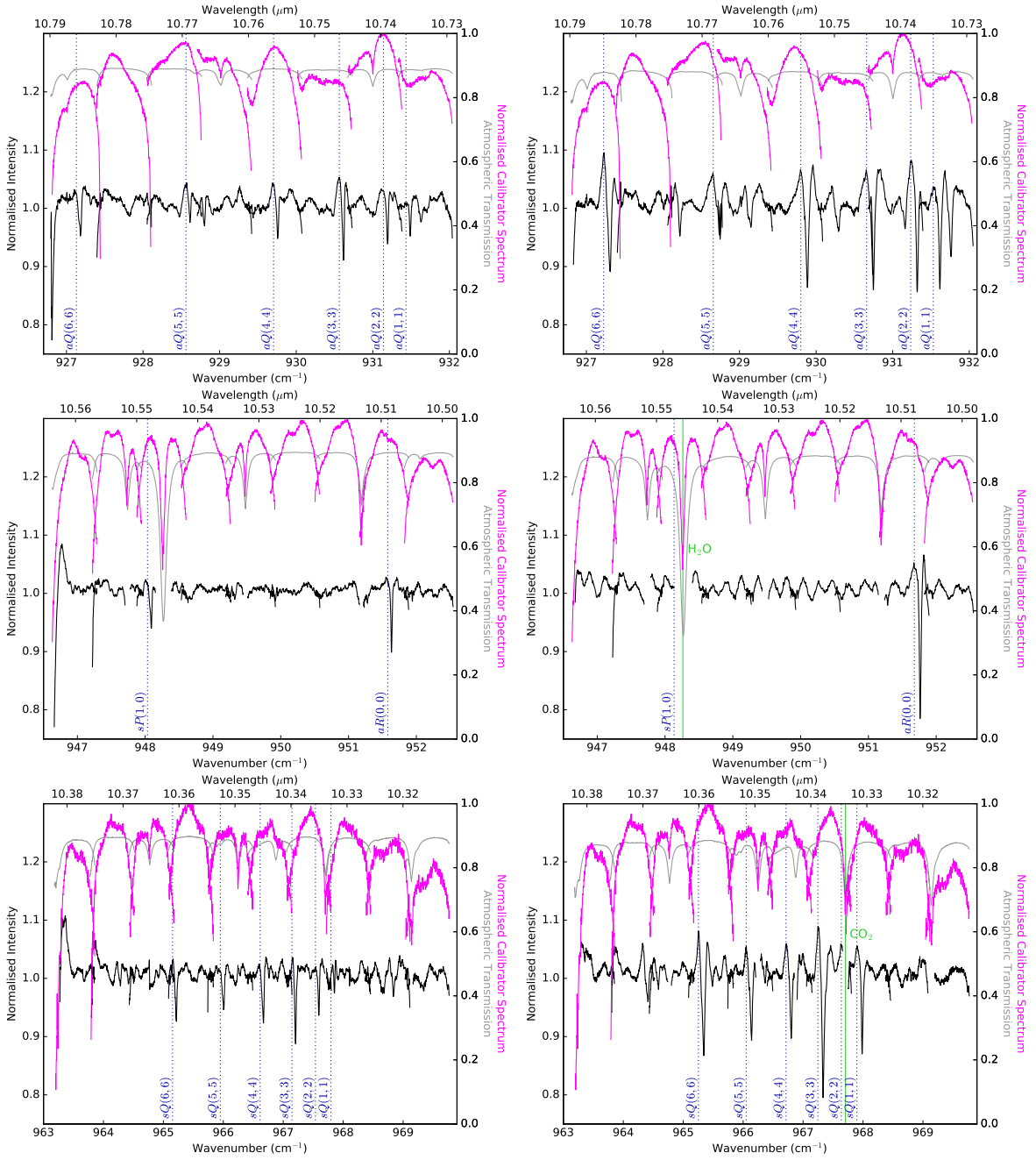

Figure 2.2.: NASA IRTF/TEXES spectra (in black) of IK Tau (*left*) and VY CMa (*right*) near the wavelengths (wavenumbers) of 10.7 μm (930 cm^{-1}; *top*), 10.5 μm (950 cm^{-1}; *middle*), and 10.3 μm (966 cm^{-1}; *bottom*). The wavenumber axes are in the topocentric frame of reference. The target spectra are normalised and zoomed. The normalised calibrator spectra are plotted in magenta and the fractional atmospheric transmissions are shown in grey. Only the target data with atmospheric transmission greater than 0.8 are plotted. The dark blue dotted lines in each spectrum indicate the positions of the labelled NH_3 rovibrational transitions in the stellar rest frame and the green solid lines indicate the telluric lines (in the observatory frame) that blend with the NH_3 lines of VY CMa. We assume the systemic velocities of IK Tau and VY CMa to be 34 km s^{-1} and 22 km s^{-1}, respectively.

from our 2016 observations with the B and C arrays of the VLA. The native resolution was about 0.″45 in FWHM and we smoothed the images to the final resolution of 0.″83 for better visualisation. NH_3 emission is detected at rather low S/N ratio ($\lesssim$6). The images from the D-array observations in 2004 do not resolve the NH_3 emission and are not presented. Figure 2.4 shows the flux density spectra, integrated over the regions specified in the vertical axes, of all VLA observations.

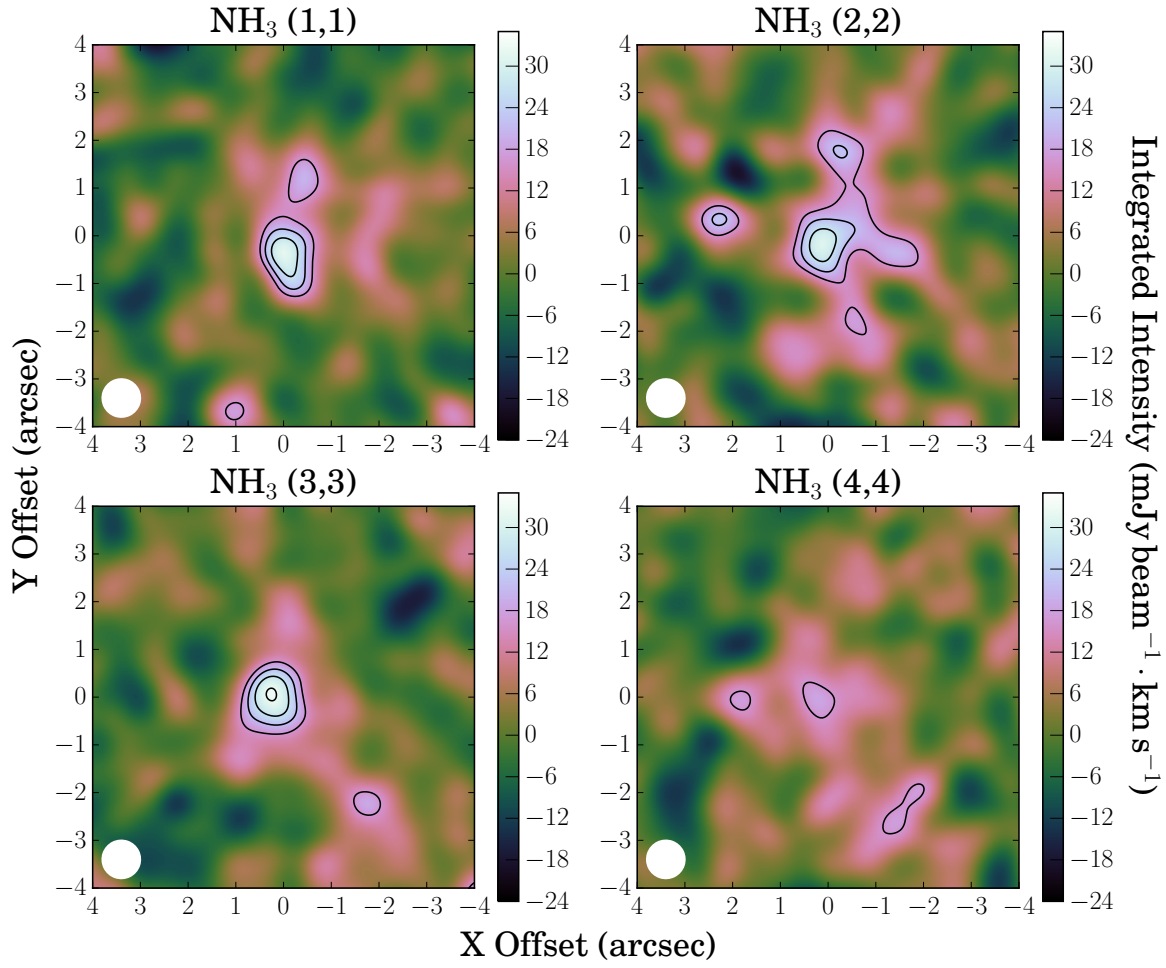

Figure 2.3.: Integrated intensity maps of the four lowest NH_3 inversion lines from IK Tau as observed with the VLA in B and C configurations over the LSR velocity range of [13, 55] km s^{-1} (relative velocity between ±21 km s^{-1} to the systemic). Horizontal and vertical axes represent the offsets (arcsec) relative to the fitted centre of the continuum in the directions of right ascension and declination, respectively. The circular restoring beam of 0.″83 is indicated at the bottom-left corner in each map. The contour levels for the NH_3 lines are drawn at $3, 4, 5, 6\sigma$, where $\sigma = 5.4$ mJy beam^{-1} km s^{-1}.

Comparing the NH_3 (1, 1) (top row) and (2, 2) (middle row) spectra taken at two epochs, the (1, 1) line emission in 2004 was predominantly in the redshifted velocities while that in 2016 was mainly blueshifted. This may indicate temporal variations in the NH_3 emission at certain LSR velocities, but is not conclusive because of the low S/N ratios of the spectra. The total fluxes of the 2004 spectra within a $10'' \times 10''$ box are consistent with those of the 2016 spectra within a 2″-radius aperture centred at the stellar radio continuum. Hence, most of the NH_3 inversion line emission is confined within a radius of ∼2″. In the full-resolution images, the strongest emission is generally concentrated within ∼0.″7 from the star – but not exactly at the

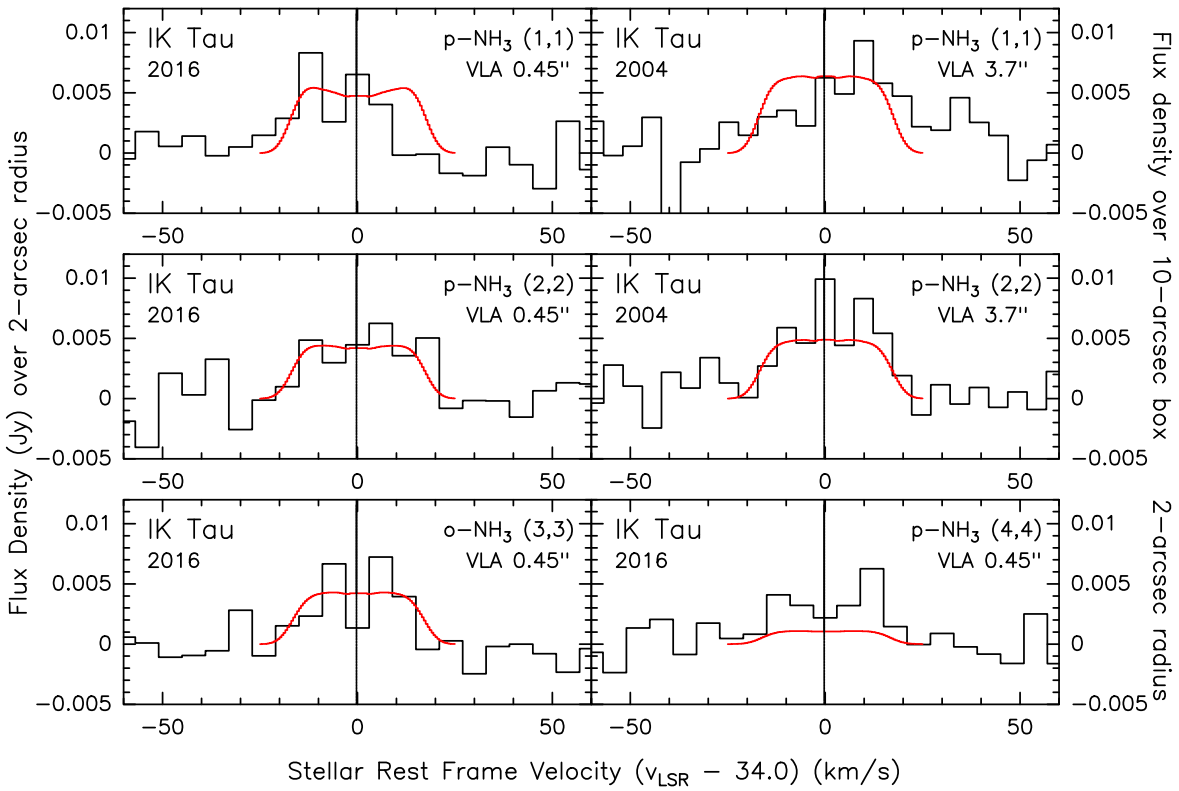

Figure 2.4.: NH_3 inversion line spectra of IK Tau. Black lines show the VLA spectra in flux density and red lines show the modelled spectra. NH_3 (1,1) and (2,2) have been observed in 2004 (*top right* and *middle right*) with D configuration and 2016 (*top left* and *middle left*) with both B and C configurations. The 2004 spectra were integrated over a $10'' \times 10''$ box and the 2016 spectra were integrated over a $2''$-radius circle.

continuum position – and appear to be very clumpy. Individual channel maps show localised, outlying emission up to $\sim 2''$ from the centre.

2.4.1.2. *Herschel*/HIFI observations of IK Tau

The *Herschel*/HIFI spectra of IK Tau are shown in Fig. 2.5. Except for the blended transitions $J_K = 3_0$–2_0 and 3_1–2_1, the rotational spectra appear to be generally symmetric with a weak blueshifted wing near the relative velocity between -21 and $-16\,\mathrm{km\,s^{-1}}$ from the systemic. This weakness of the blueshifted wing may be a result of weak self-absorption. The central part of the profiles within the relative velocity of $\pm 10\,\mathrm{km\,s^{-1}}$ is relatively flat. Since the NH_3-emitting region is unresolved within the *Herschel*/HIFI beams, the flat-topped spectra suggest that the emission only has a small or modest optical thickness. In the high-S/N spectrum of 1_0–0_0, the central part also shows numerous small bumps, suggesting the presence of substructures of various kinematics in the NH_3-emitting regions. Since the line widths of NH_3 spectra resemble those from other major molecular species (e.g. CO, HCN; Decin et al., 2010b), the bulk of NH_3 emission comes from the fully accelerated wind in the outer CSE with a maximum expansion velocity of $17.7\,\mathrm{km\,s^{-1}}$ (Decin et al., 2010b).

2.4.1.3. IRAM observations of IK Tau

We did not detect the rotational transition $v_2 = 1$ $J_K = 2_1$–1_1 near 140 GHz within the uncertainty of 0.61 mK per $5.0\,\mathrm{km\,s^{-1}}$. If we assume the line-emitting region of this transition is also

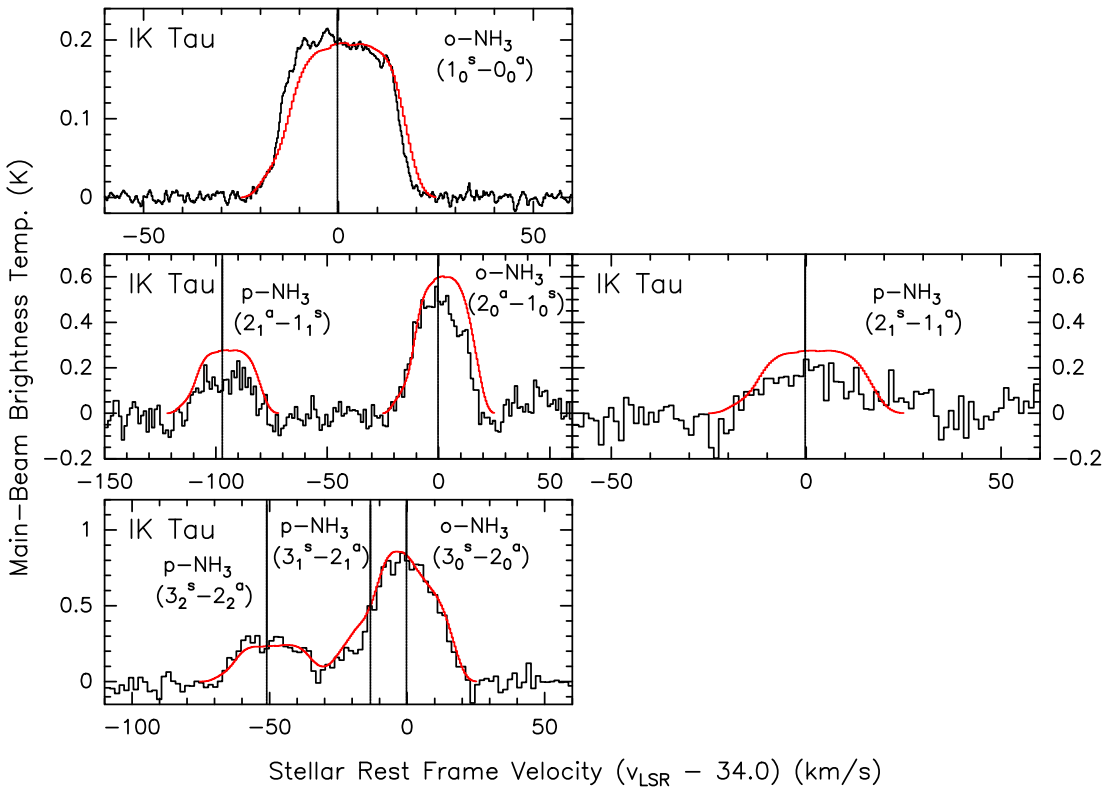

Figure 2.5.: NH_3 rotational line spectra of IK Tau. Black lines show the observed spectra from *Herschel*/HIFI and red lines show the modelled spectra.

located in the fully accelerated wind with an expansion velocity of $V_{exp} = 17.7\,km\,s^{-1}$, as for the ground-state rotational transitions, then the rms noise of the velocity-integrated spectrum would be ~0.24 mK (over $35.4\,km\,s^{-1}$) in T_{mb}.

Our observations repeated the detection of PN near 141.0 GHz (De Beck et al., 2013) and H_2CO near 150.5 GHz (Velilla Prieto et al., 2017) at higher S/N ratios. We also detected NO near 150.18 and 150.55 GHz that were not reported in Velilla Prieto et al. (2017), in which the higher NO transitions near 250.5 GHz were detected. In the context of circumstellar environments and stellar merger remnants, NO has only been detected elsewhere towards IRC +10420 (Quintana-Lacaci et al., 2013), OH 231.8+4.2 (Velilla Prieto et al., 2015), and CK Vulpeculae (Nova Vul 1670; Kamiński et al., 2017a) thus far.

2.4.1.4. IRTF observations of IK Tau

Figure 2.2 shows the normalised IRTF spectra of IK Tau in three wavelength settings prior to baseline subtraction. All 14 targeted NH_3 rovibrational transitions are clearly detected in absorption. Figures 2.6–2.8 present the baseline-subtracted spectra in the stellar rest frame. The maximum absorption of all MIR transitions appear near the LSR velocities in the range of 16–17 $km\,s^{-1}$, which corresponds to the blueshifted velocity between −18 and $-17\,km\,s^{-1}$ and is consistent with the terminal expansion velocity of $17.7\,km\,s^{-1}$ as determined by Decin et al. (2010b). Blueshifted absorption near terminal velocity is consistent with the scenario that the NH_3-absorbing gas is moving towards us in the fully-accelerated outflow in front of the background MIR continuum.

The MIR NH_3 absorption in IK Tau cannot come from the inner wind. First of all, our SED modelling (Sect. 2.3.2) shows that the optical depth of the circumstellar dust is about 1.3

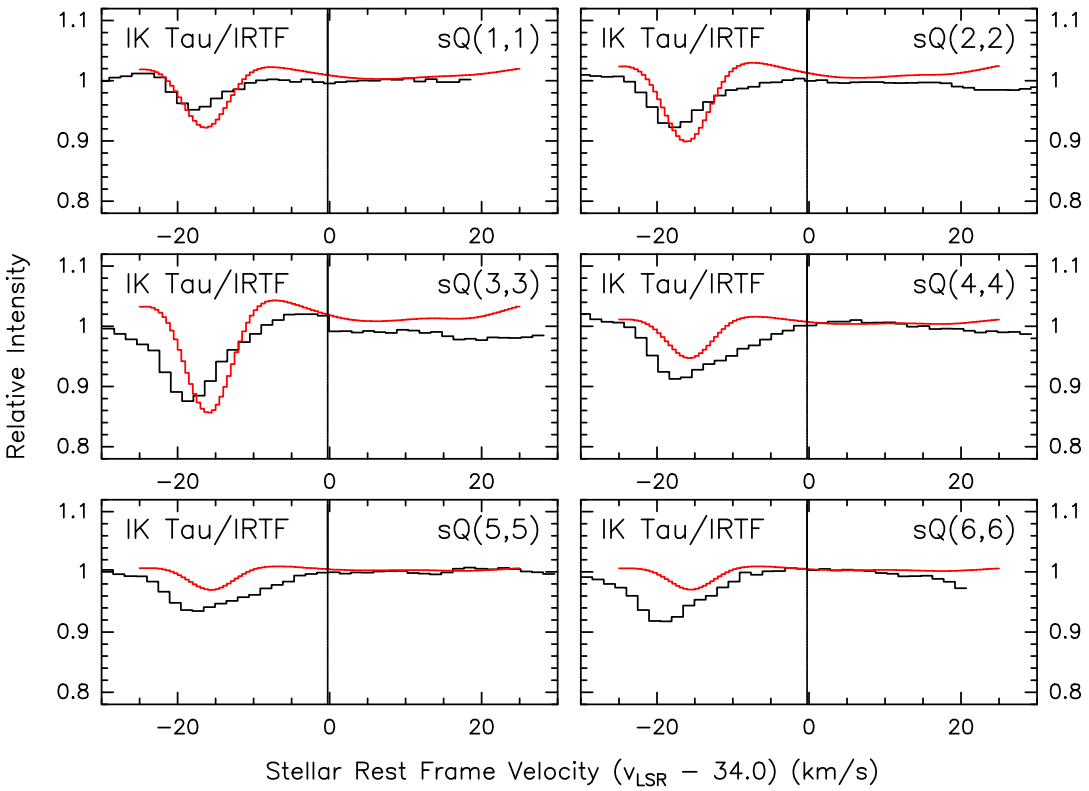

Figure 2.6.: Q-branch NH_3 rovibrational spectra of IK Tau. These transitions connects the lower energy levels of the ground-state inversion doublets and the upper levels in the vibrationally excited state. Black lines show the observed spectra from the NASA IRTF and red lines show the modelled spectra. Each modelled spectrum was divided by a smoothed version of itself as in the real data (see Sect. 2.2.4) in order to induce the similar distortion in the line wings.

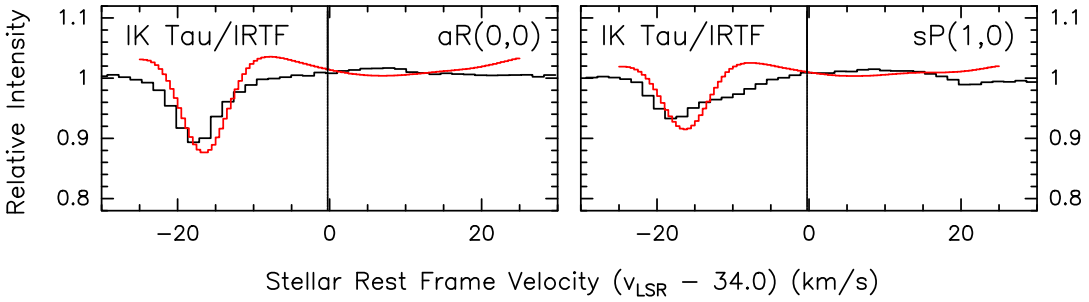

Figure 2.7.: NH_3 rovibrational spectra of IK Tau in the transitions $aR(0,0)$ and $sP(1,0)$. Black lines show the observed spectra from the NASA IRTF and red lines show the modelled spectra. Each modelled spectrum was divided by a smoothed version of itself as in the real data (see Sect. 2.2.4) in order to induce the similar distortion in the line wings.

at 11 μm. Continuum emission from dust grains would probably fill the line absorption near 10.5 μm had it originated beneath the dust shells. Furthermore, the visual phase of IK Tau in our IRTF observations is about 0.35, which is based on our recalculations of its visual light curve using modern photometric data (see Fig. C.2 in Appendix C). Mira variables at this phase, including IK Tau (Hinkle et al., 1997), show CO second overtone ($\Delta v = 3$) absorption,

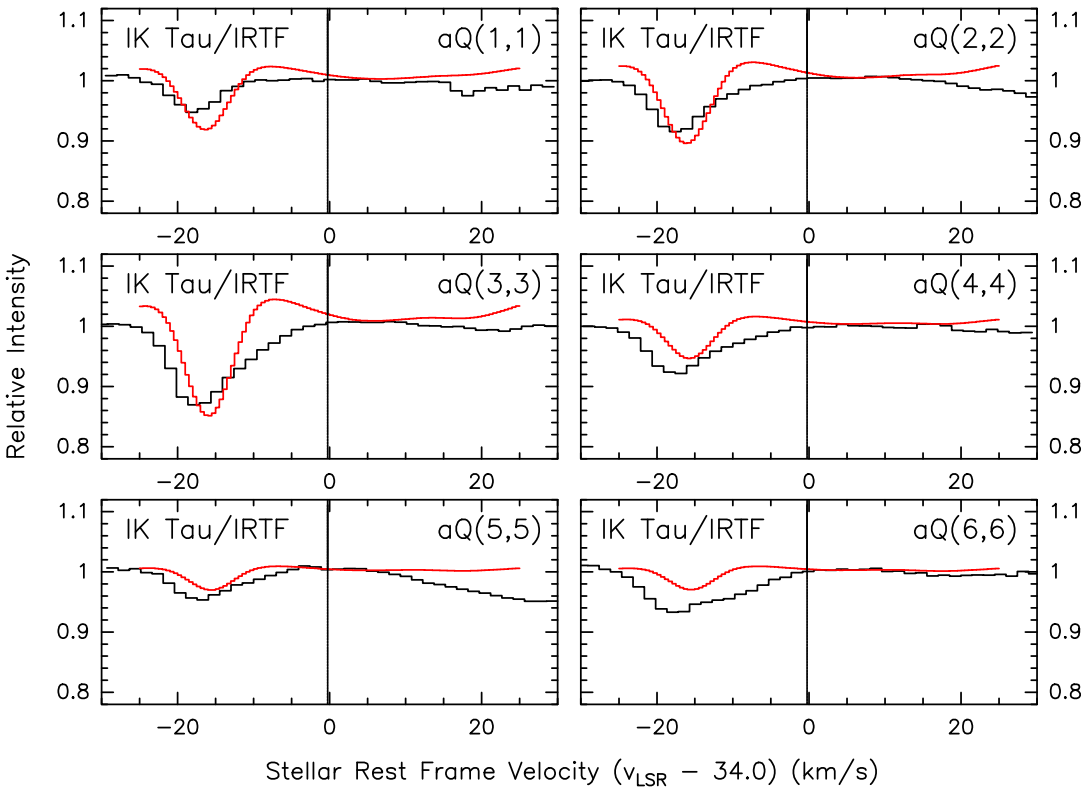

Figure 2.8.: Q-branch NH_3 rovibrational spectra of IK Tau. These transitions connects the upper energy levels of the ground-state inversion doublets and the lower levels in the vibrationally excited state. Black lines show the observed spectra from the NASA IRTF and red lines show the modelled spectra. Each modelled spectrum was divided by a smoothed version of itself as in the real data (see Sect. 2.2.4) in order to induce the similar distortion in the line wings.

which sample the deep pulsating layers down to $\sim 1\,R_\star$, close to the stellar systemic velocity or in the redshifted (infall) velocities (Lebzelter & Hinkle, 2002; Nowotny et al., 2010; Liljegren et al., 2017). If NH_3 was produced in high abundance close to the stellar surface, we would see the absorption features in much redder (more positive) velocities; if it was abundant at the distance of a few stellar radii from the star, the observed velocity blueshifted by about $18\,\mathrm{km\,s^{-1}}$ from the systemic would be too high for the gas in the inner wind of Mira variables (e.g. Höfner et al., 2016; Wong et al., 2016). As a result, we only consider NH_3 in the dust-accelerated regions of the CSE in our subsequent modelling (Sect. 2.4.1.5) even though we cannot exclude the presence of NH_3 gas in the inner wind based on the available MIR spectra.

Among the same series of rotationally elastic transitions (aQ or sQ), the absorption profiles are slightly broader in higher-J transitions. For NH_3, the thermal component of the line broadening is below $1\,\mathrm{km\,s^{-1}}$ when T_{NH_3} is lower than 1000 K, so the observed line widths of several up to $\sim 10\,\mathrm{km\,s^{-1}}$ are mainly contributed by the microturbulent velocity of the circumstellar gas. This suggests that the higher-J levels are more readily populated in more turbulent parts of the CSE.

2.4.1.5. NH_3 model of IK Tau

Decin et al. (2010b) presented detailed non-LTE radiative transfer analysis of molecular line emission from the CSE of IK Tau. In particular, the gas density and thermodynamic structure,

including the gas kinetic temperature and expansion velocity, of the CSE have been constrained by modelling multiple CO and HCN spectra observed by single-dish telescopes. Therefore, we adopt the same density, kinetic temperature and expansion velocity profiles as in model 3 of Decin et al. (2010b). The gas density of the CSE is given by the conservation of mass in a uniformly expanding outflow,

$$n_{\mathrm{H_2}}(r) = \frac{\dot{M}}{4\pi r^2 V(r)}, \tag{2.6}$$

where $\dot{M} = 8 \times 10^{-6}\, M_\odot\,\mathrm{yr}^{-1}$ is the average gas mass-loss rate, $V(r)$ is the expansion velocity at radius r. We use the classical β-law to describe the radial velocity field, i.e.

$$V(r) = V_{\mathrm{in}} + \left(V_{\mathrm{exp}} - V_{\mathrm{in}}\right)\left(1 - \frac{R_{\mathrm{wind}}}{r}\right)^{\beta}, \tag{2.7}$$

where $V_{\mathrm{in}} = 3\,\mathrm{km\,s}^{-1}$ is the inner wind velocity, $V_{\mathrm{exp}} = 17.7\,\mathrm{km\,s}^{-1}$ is the terminal expansion velocity, $R_{\mathrm{wind}} = 12\,R_\star$ is the radius from which wind acceleration begins, and $\beta = 1$ (Decin et al., 2010b).

The gas kinetic temperature is described by two power laws which approximate the profile computed from energy balance equation (Decin et al., 2010b),

$$T_{\mathrm{kin}}(r) = \begin{cases} 40\,\mathrm{K} \cdot {r_{16}}^{-0.68} & \text{if } r \leq 10^{16}\,\mathrm{cm} = 667\,R_\star \approx 2\farcs5 \\ 40\,\mathrm{K} \cdot {r_{16}}^{-0.8} & \text{if } r > 10^{16}\,\mathrm{cm} \end{cases}, \tag{2.8}$$

where

$$r_{16} = \frac{r}{10^{16}\,\mathrm{cm}}. \tag{2.9}$$

We parametrise the radial distribution of NH_3 abundance with a Gaussian function, i.e.

$$f(r) = f_0 \exp\left[-\left(\frac{r}{R_e}\right)^2\right] \quad \text{if } r > R_{\mathrm{in}}, \tag{2.10}$$

where $f(r)$ and f_0 are the fractional abundance of NH_3 relative to H_2 at radius r and at its maximum value, respectively; R_e is the e-folding radius at which the NH_3 abundance drops to $1/e$ of the maximum value presumably due to photodissociation. We did not parametrise the formation of NH_3 in the inner CSE with a smoothly increasing function of radius. Instead, we introduce an inner radius, R_{in}, for the distribution of NH_3 at which its abundance increases sharply from the 'default' value of 10^{-12} to the maximum. We assume the dust-to-gas mass ratio to be d/g = 0.002, a value typical for IK Tau and also AGB stars in general (e.g. Gobrecht et al., 2016). In order to reproduce the broad IRTF rovibrational spectra (Sect. 2.4.1.4), we have to adopt a high Doppler-b parameter of $b_{\mathrm{Dopp}} = 4\,\mathrm{km\,s}^{-1}$.

We are able to fit the spectra with $R_{\mathrm{in}} = 75\,R_\star = 0\farcs3$, $R_e = 600\,R_\star = 2\farcs3$, and $f_0 = 6 \times 10^{-7}$. Both choices of R_{in} and R_e are motivated by the inner and outer radii of the observed inversion line emission from the VLA images (Sect. 2.4.1.1). We note, however, that a smaller R_e ($\sim$500 $R_\star$ = 1\farcs9) and a higher f_0 ($\sim 7 \times 10^{-7}$) can also reproduce fits of similar quality to the available spectra. On the other hand, a very small R_e would reduce the line intensity ratios between higher and lower rotational transitions because the lower transitions come from the outer part of the NH_3 distribution.

The inner radius is not tightly constrained because the small volume of the line-emitting region only contributes to a relatively small fraction of the emission. Although the predicted

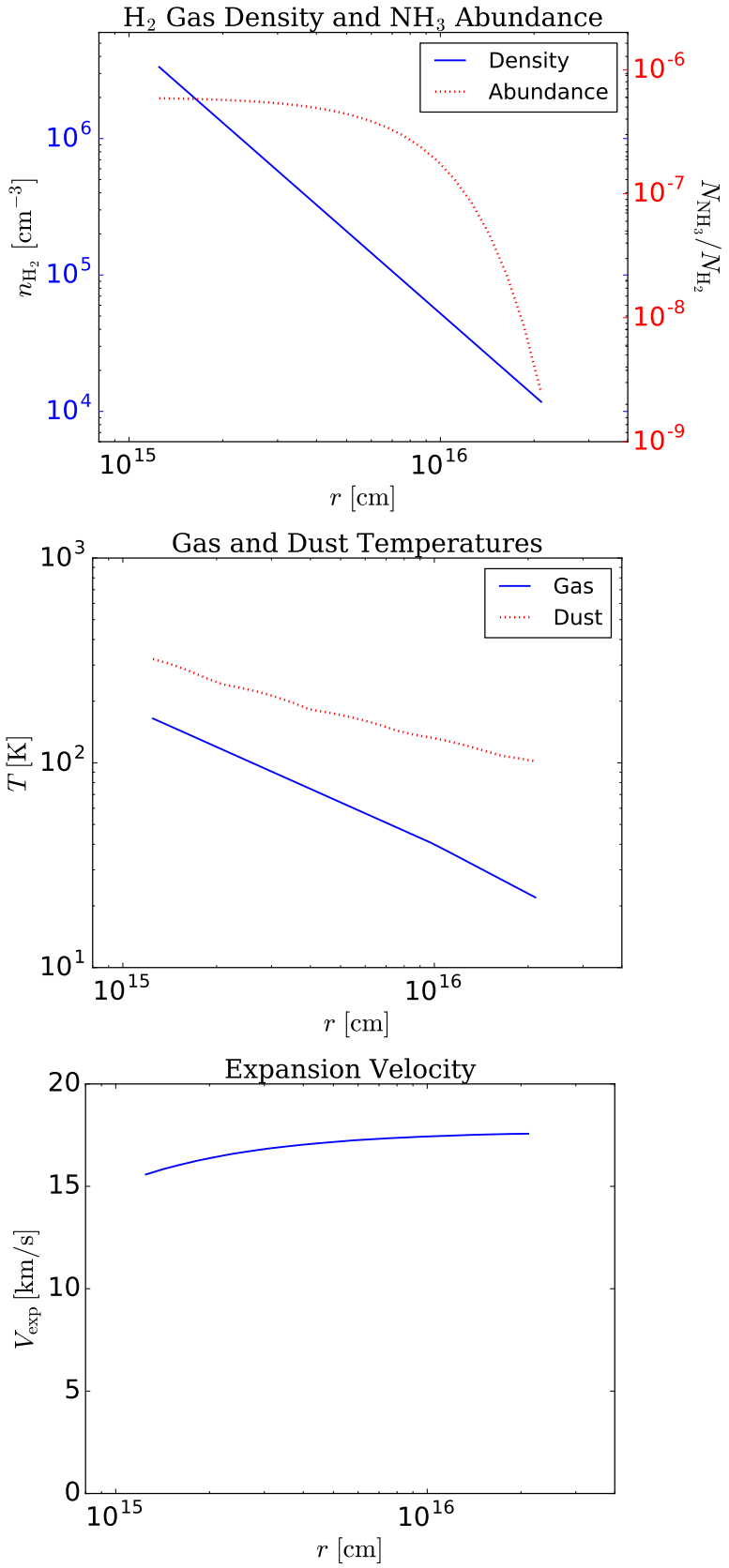

Figure 2.9.: The model for IK Tau. *Left*: Input gas density and NH_3 abundance profiles. Only the radii with abundance $>10^{-10}$ are plotted. *Middle*: Input gas and dust temperature profiles. *Right*: Input expansion velocity profile.

intensities of the rotational transitions within the $v_2 = 1$ state (near 140.1 and 466.2 GHz) are sensitive to the adopted value of $R_{\rm in}$ in our test models, they are very weak compared to the noise levels achievable by (sub)millimetre telescopes with the typical amount of observing time. In the presented model of IK Tau, the peak brightness temperature of the $v_2 = 1$ $J_K = 2_1$–1_1 transition is ~0.03 mK, much lower than the rms noise of our observation (Sect. 2.4.1.3). In this study, we can only conclude that the inner boundary of the NH_3 distribution is $\lesssim 100\,R_\star$. Figure 2.9 shows the radial profiles of the input density, abundance, dust and gas temperatures, and expansion velocity.

2.4.2. VY CMa

2.4.2.1. VLA observations of VY CMa

The radio inversion line emission from the CSE of VY CMa is not clearly resolved by the VLA beam of ~4″. Figures 2.10 and 2.11 shows the integrated intensity maps and flux density spectra, respectively, of all transitions covered in our VLA observation. The strongest emission is detected in NH_3 (3,3) and (2,2), which also show somewhat extended emission up to ~4″–6″ in the maps. Adopting the trigonometric parallax derived distance of 1.14 kpc (Choi et al., 2008, see also Zhang et al., 2012) and the stellar radius of 1420 $R_\odot$ (Wittkowski et al., 2012), NH_3 could maintain a moderate abundance out to ~700 $R_\star$ (4″).

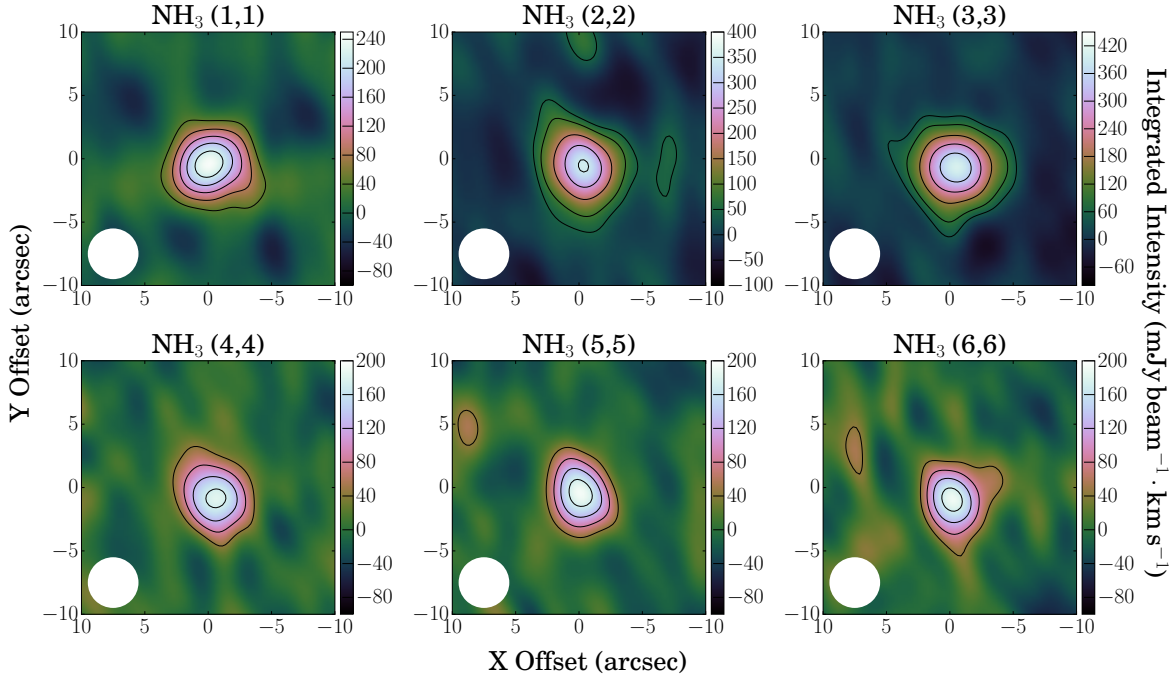

Figure 2.10.: Integrated intensity maps of the six lowest NH_3 inversion lines from VY CMa as observed with the VLA over the LSR velocity range of $[-17, 85]$ km s^{-1} (relative velocity between ±51 km s^{-1}). Horizontal and vertical axes represent the offsets (arcsec) relative to the fitted centre of the continuum in the directions of right ascension and declination, respectively. The circular restoring beam of 4.″0 is indicated at the bottom-left corner in each map. The contour levels for the NH_3 lines are drawn at: $3, 6, 9, 12, 15\sigma$ for (1, 1); $3, 6, 12, 18, 24\sigma$ for (2, 2) and (3, 3); $3, 6, 9, 12\sigma$ for (4, 4) to (6, 6), where $\sigma = 14.2$ mJy beam^{-1} km s^{-1}.

A close inspection on the maps reveals that the emission peaks at $\lesssim 1''$ to the south-west from the centre of the radio continuum, which was determined by fitting the images combining all line-free channels near the NH_3 spectra. This offset in peak molecular emission has also

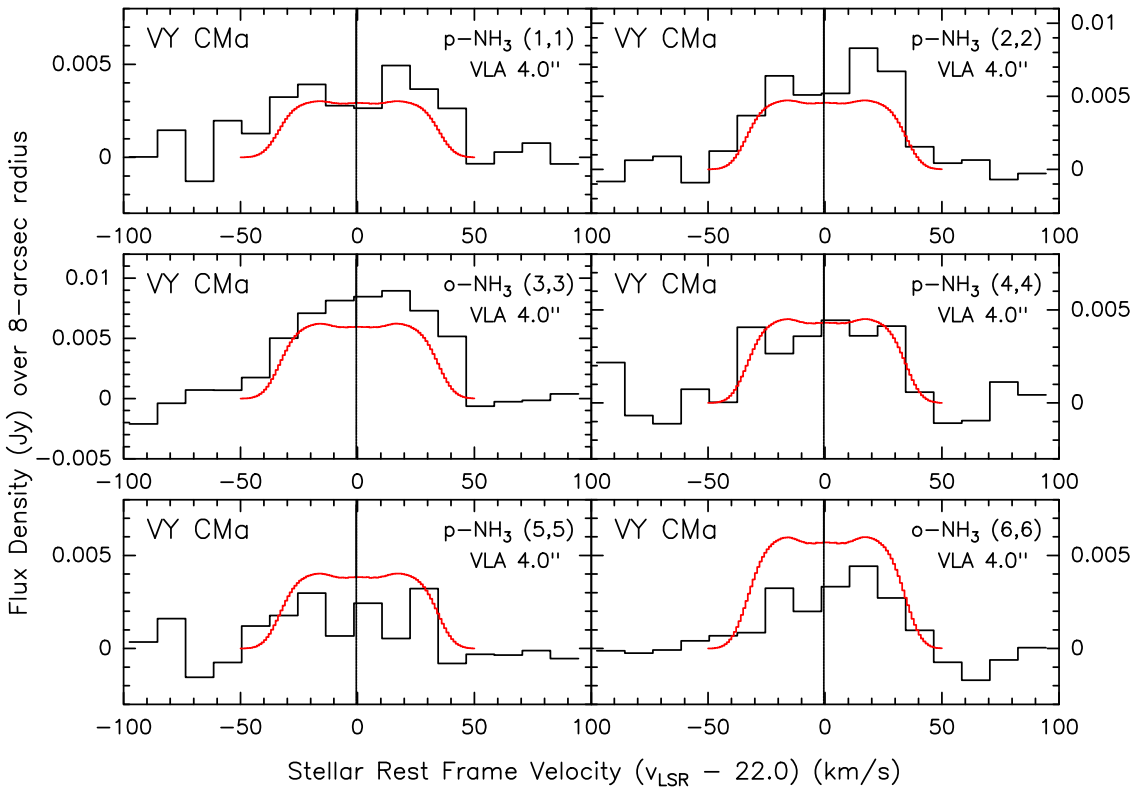

Figure 2.11.: NH_3 inversion line spectra of VY CMa. Black lines show the VLA spectra in flux density and red lines show the modelled spectra. All transitions were observed in 2013 with D configuration. The spectra were integrated over an 8″-radius circle.

been observed under high angular resolution (~0.″9) with the Submillimeter Array (SMA) in multiple other molecules, including dense gas tracers such as CS, SO, SO_2, SiO, and HCN (Fig. 8 of Kamiński et al., 2013). Kamiński et al. (2013) noted that the spatial location of the peak emission may be associated with the 'Southwest Clump' (SW Clump) as seen in the infrared images from the *Hubble* Space Telescope (HST) (Smith et al., 2001; Humphreys et al., 2007). Since SW Clump was only seen in the infrared filter but not in any visible filters, Humphreys et al. (2007) suggested that the feature is very dusty and obscures all the visible light. However, submillimetre continuum emission from SW Clump has never been detected (Kamiński et al., 2013; O'Gorman et al., 2015), which cannot be explained by typical circumstellar grains with a small spectral emissivity index (O'Gorman et al., 2015). From K I spectra near 7700 Å, Humphreys et al. (2007) found that SW Clump is likely moving away from us with a small line-of-sight velocity of ~2.5 km s^{-1}. Molecules from SW Clump, however, do not always emit from the same redshifted velocity. For example, the H_2S and CS emission appears over a wide range of velocities (Sect. 3.1.4 of Kamiński et al., 2013); TiO_2 appears to emit in blueshifted velocities only (Fig. 2 of De Beck et al., 2015); NaCl emission peaks at the redshifted velocity of 3 km s^{-1} (Sect. 3.3 of Decin et al., 2016), similar to the velocity determined from the K I spectra. In our VLA images, we see the south-west offset of NH_3 emission from much higher redshifted velocities between ~9 and 30 km s^{-1} relative to our adopted systemic LSR velocity (22 km s^{-1}). The peak of the south-west emission is seen near 20–25 km s^{-1}. If the peak NH_3 emission is indeed associated with the infrared SW Clump, then NH_3 may trace a distinct kinematic component in this possibly dusty and dense feature.

The spectra show relatively flat profiles, with two weakly distinguishable peaks near the LSR velocities of about −5–0 km s^{-1} and 40–45 km s^{-1}. These features correspond to the relative velocities of roughly −25 km s^{-1} and 20 km s^{-1}, respectively. As we will show in the next subsection, the NH_3 $J_K = 1_0(s)–0_0(a)$ rotational transition, but not the higher ones, also shows similar peaks in its high S/N spectrum. Furthermore, high-spectral resolution spectra of SO and SO_2 also show prominent peaks near the same velocities of the NH_3 features (e.g. Tenenbaum et al., 2010a; Fu et al., 2012; Adande et al., 2013; Kamiński et al., 2013).

2.4.2.2. *Herschel*/HIFI observations of VY CMa

Figure 2.12 shows all rotational spectra of VY CMa. The NH_3 rotational transitions $J_K = 1_0(s)–0_0(a)$ and $J_K = 3_K(s)–2_K(a)$ ($K = 0, 1, 2$) observed under the HIFISTARS programme have already been published by Menten et al. (2010) and Alcolea et al. (2013). Other transitions were covered in the spectral line survey of the proposal ID 'OT1_jcernich_5' (PI: J. Cernicharo). VY CMa is the only target in this study with complete coverage of ground-state rotational transitions up to $J_{up} = 3$.

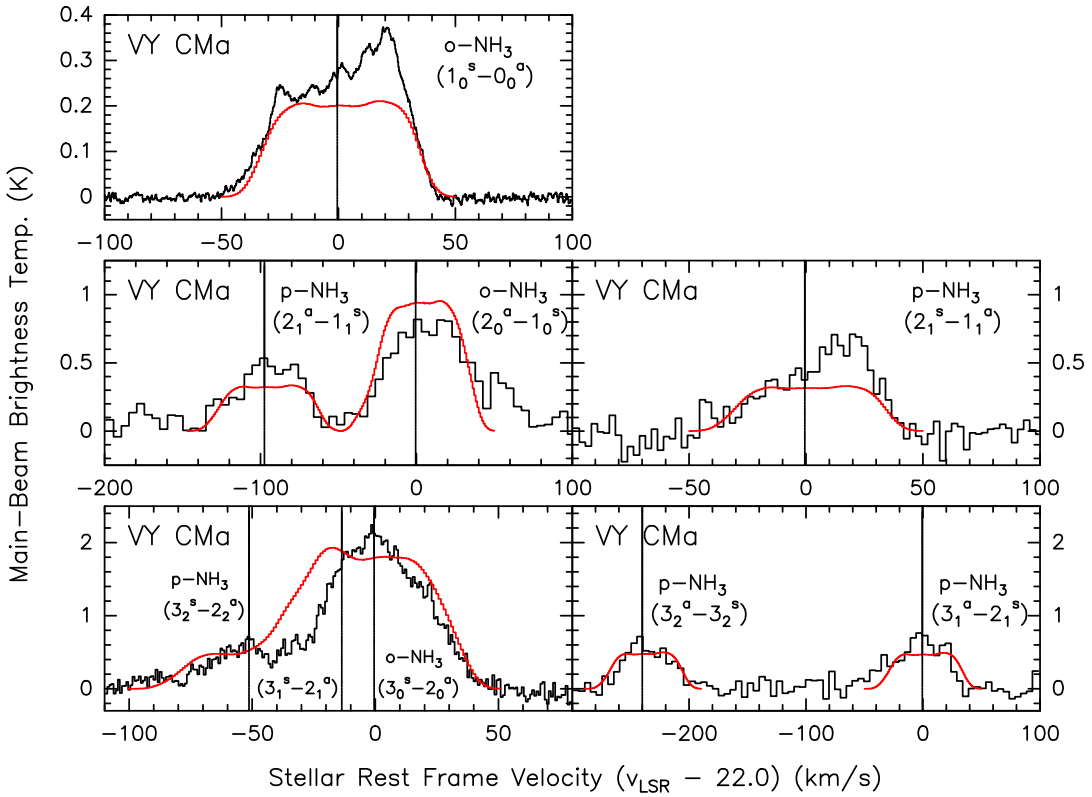

Figure 2.12.: NH_3 rotational line spectra of VY CMa. Black lines show the observed spectra from *Herschel*/HIFI and red lines show the modelled spectra.

The full width (at zero power) of the NH_3 $1_0(s)–0_0(a)$ and $2_0(a)–1_0(s)$ spectra spans the relative velocity range of almost ±50 km s^{-1}. The expansion velocity of the CSE of VY CMa is about 35 km s^{-1} (Decin et al., 2006); and therefore the expected total line width should not exceed 70 km s^{-1} if the NH_3 emission arises from a single, uniformly expanding component of the circumstellar wind. Huge line widths have also been observed in other abundant molecules (e.g. CO, SiO, H_2O, HCN, CN, SO, and SO_2; Tenenbaum et al., 2010a,b; Alcolea et al., 2013; Kamiński et al., 2013). Some of the optically thin transitions even show multiple peaks in the spectra (e.g. Fig. 7 of Kamiński et al., 2013), suggesting the presence of multiple kinematic

components moving at various line-of-sight velocities.

As already discussed by Alcolea et al. (2013, their Sect. 3.3.1), the line profiles of 1_0(s)–0_0(a) and 3_0(s)–2_0(a) are distinctly different, with the former showing significantly stronger emission in the redshifted velocities and the latter showing only one main component at the centre. With the new spectra, which show profiles that are somewhat intermediate between the two extremes, we find that the line shapes mainly depend on the relative intensities between the central component and the redshifted component near +20–21 km s^{-1} relative to the systemic velocity. The redshifted component is stronger than the central in lower transitions, such as 1_0(s)–0_0(a) and 2_1(s)–1_1(a), but becomes weaker and less noticeable in higher transitions. The peak velocity of this redshifted component is also consistent with that of the south-west offset structure as seen in our VLA images, especially in NH_3 (2,2) and (3,3). Therefore, at least part of the enhanced redshifted emission may originate from the local NH_3-emitting region to the south-west of the star.

The 1_0(s)–0_0(a) spectrum, which has the highest S/N ratio, shows five peaks at the relative velocities of approximately −25, −11, 1, 13, and 21 km s^{-1}. Similar spectra showing multiple emission peaks are also seen in CO, SO, and SO_2 (e.g. Muller et al., 2007; Ziurys et al., 2007; Tenenbaum et al., 2010a; Fu et al., 2012; Adande et al., 2013; Kamiński et al., 2013). The most prominent peaks in these molecules occur at LSR velocities of −7, 20–25, and 42 km s^{-1}, corresponding to the relative velocities of −29, −2–+3, and +20 km s^{-1}, respectively. High-angular resolution SMA images and position-velocity diagrams of these molecules show complex geometry and kinematics of the emission; accordingly, dense and localised structures were introduced to explain individual velocity components (Muller et al., 2007; Fu et al., 2012; Kamiński et al., 2013). Except for the high-spectral resolution spectrum of SO $J_N = 7_6$–6_5, which also shows a peak near the relative velocity of 12 km s^{-1} (Fig. 6 in Tenenbaum et al., 2010a), no other molecules seem to exhibit the same peaks at intermediate relative velocities (−11 and 13 km s^{-1}) as in NH_3.

The NH_3 inversion (Sect. 2.4.2.1) and rotational lines show spectral features at similar velocities to the SO and SO_2 lines, suggesting that all these molecules may share similar kinematics and spatial distribution. High-angular resolution SMA images show that SO and SO_2 emission is extended by about 2–3″ (Fig. 8 of Kamiński et al., 2013). Hence, the strongest NH_3 emission is likely concentrated within a radius of ∼2″.

High rotational transitions including $J = 4$–3 (∼125 μm) and $J = 6$–5 (∼84 μm) have been detected by Royer et al. (2010) with the *Herschel*/PACS[30] instrument. However, the spectral resolution of ∼2 GHz (>160 km s^{-1}) is too coarse for detailed analysis.

2.4.2.3. IRTF observations of VY CMa

Figure 2.2 shows the normalised IRTF spectra of VY CMa prior to baseline subtraction. Except for the two transitions blended by telluric lines, all other 12 targeted NH_3 rovibrational transitions are detected in absorption. The normalised spectra in the stellar rest frame are shown in Figs. 2.13–2.15 along with the modelling results. Figure 2.14 additionally shows the old $aR(0,0)$ and $aQ(2,2)$ spectra observed with the McMath Solar Telescope, which are reproduced from Fig. 1 of McLaren & Betz (1980).

The absorption minima of the MIR transitions appear in the LSR velocities between −7 and −4 km s^{-1}, which correspond to the blueshifted velocities of 26–29 km s^{-1}. The positions of our $aR(0,0)$ and $aQ(2,2)$ absorption profiles are consistent with the old heterodyne spectra taken by McLaren & Betz (1980), Goldhaber (1988), and Monnier et al. (2000b) within the spectral

[30] The Photodetector Array Camera and Spectrometer (Poglitsch et al., 2010).

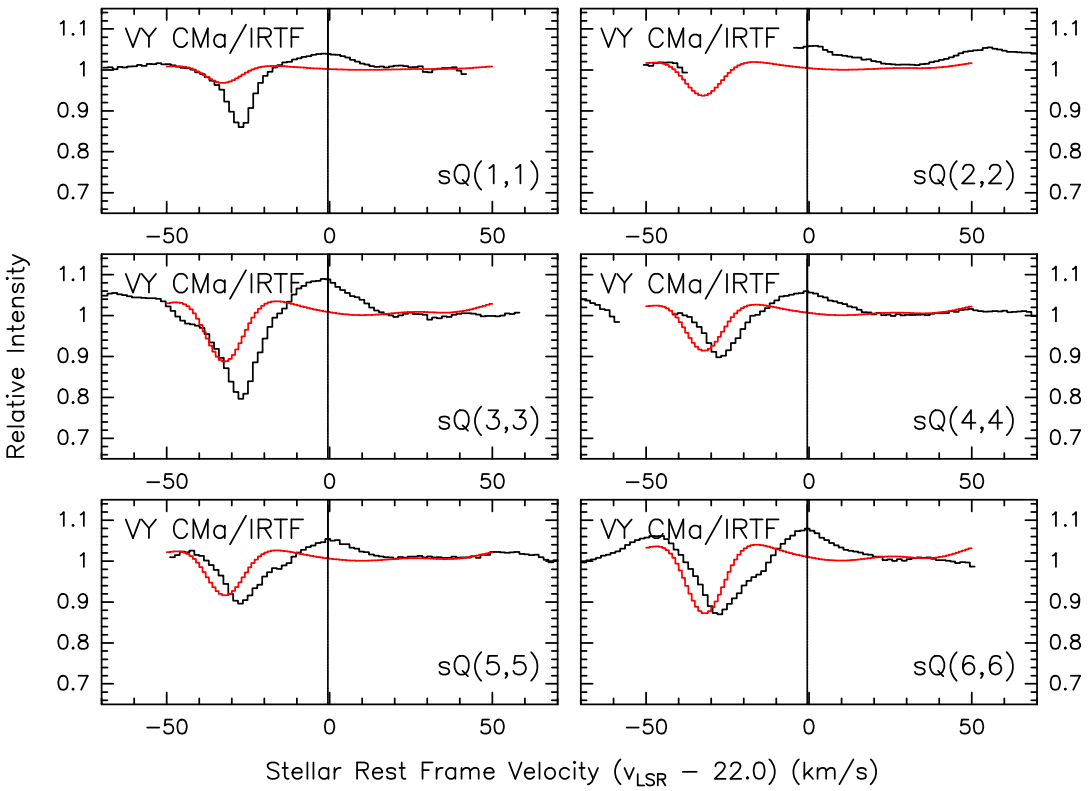

Figure 2.13.: Q-branch NH_3 rovibrational spectra of VY CMa. These transitions connects the lower energy levels of the ground-state inversion doublets and the upper levels in the vibrationally excited state. Black lines show the observed spectra from the NASA IRTF and red lines show the modelled spectra. Each modelled spectrum was divided by a smoothed version of itself as in the real data (see Sect. 2.2.4) in order to induce the similar distortion in the line wings. The transition $sQ(2,2)$ is contaminated by a telluric CO_2 absorption line and therefore a large part of its absorption profile is discarded.

resolution of the TEXES instrument ($\sim$3 km s^{-1}). The velocities of the absorption minima of these MIR spectra are consistent with that of the prominent blueshifted emission peak in the 1_0(s)–0_0(a) spectrum (Fig. 2.12). Assuming the expansion velocity of 35 km s^{-1} (Decin et al., 2006), the bulk of the NH_3-absorbing gas may come from the wind acceleration zone or from a distinct component (along the line of sight through the slit) of which the kinematics is not represented by the presumed uniform expansion.

Similar to IK Tau, we see slightly more broadening of the line profiles towards the less blueshifted wing (i.e. higher LSR velocities) in higher-J transitions. This trend may be indicative of the formation of NH_3 in the accelerating wind where the hotter gas expands at a lower velocity than the outer, cooler gas. In their data of better velocity resolution ($\sim$1 km s^{-1}; Monnier et al., 2000c), Monnier et al. (2000b) found a slight shift in the core of absorption to a lower blueshifted velocity in the higher transition and interpreted – with additional support from the fitting to the visibility data – that NH_3 probably formed near the outer end of the accelerating part of the CSE, i.e. at the radius of $\sim 70\,R_\star$ (460 AU)[31].

[31] The NH_3 formation radius was reported as $40\,R_\star'$ in Monnier et al. (2000b), where $R_\star' = 0\farcs4 = 69.1 R_\star$ (Monnier et al., 2000a).

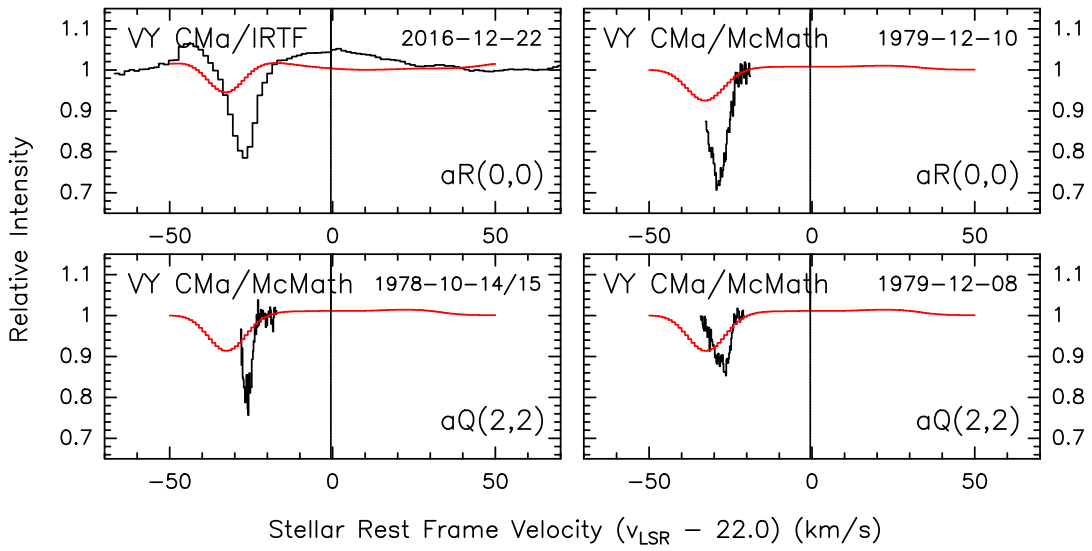

Figure 2.14.: NH_3 rovibrational spectra of VY CMa in the transitions $aR(0,0)$ (*top*) and $aQ(2,2)$ (*bottom*). The black line in the *top-left* panel shows the observed spectrum from the NASA IRTF while those in other panels show the old spectra from the McMath Solar Telescope, as reproduced from Fig. 1 of McLaren & Betz (1980, © AAS. Reproduced with permission.). Red lines show the modelled spectra in all panels. The modelled spectrum in the *top-left* panel was divided by a smoothed version of itself as in the real data (see Sect. 2.2.4) in order to induce the similar distortion in the line wings.

2.4.2.4. NH_3 model of VY CMa

We model the NH_3 emission from VY CMa in the similar manner as for IK Tau (Sect. 2.4.1.5). In our 1-D model, we assume that the bulk of the NH_3-emitting material comes from the fully accelerated wind at the expansion velocity of $35\,\mathrm{km\,s^{-1}}$ with a relatively large turbulence width so as to explain the broad rotational lines (Sect. 2.4.2.2). However, this velocity does not agree with that of the MIR line absorption, which are blueshifted by $\lesssim 30\,\mathrm{km\,s^{-1}}$ (Sect. 2.4.2.3). In addition, our model would not reproduce individual velocity components in the observed spectra. The CSE of VY CMa is particularly complex and inhomogeneous and our simple model is far from being realistic in describing the kinematics of the NH_3-carrying gas.

The gas density of the NH_3-emitting CSE is given by Eq. (2.6) with $\dot{M} \approx 2 \times 10^{-4}\,M_\odot\,\mathrm{yr^{-1}}$ in order to fit the line intensity ratios of the central components of the rotational transitions. The velocity is described by Eq. (2.7) with $V_\mathrm{in} = 4\,\mathrm{km\,s^{-1}}$, $V_\mathrm{exp} = 35\,\mathrm{km\,s^{-1}}$, $R_\mathrm{wind} = 10\,R_\star$, and $\beta = 0.5$ (similar to Decin et al., 2006). The gas temperature is described by a power law,

$$T_\mathrm{kin}(r) = T_\star \left(\frac{r}{R_\star}\right)^{-0.5}, \tag{2.11}$$

where $T_\star = 3490\,\mathrm{K}$ and $R_\star = 1420\,R_\odot = 9.88 \times 10^{13}\,\mathrm{cm}$ are both adopted from Wittkowski et al. (2012).

We assume a typical d/g of 0.002. Assuming that $V_\mathrm{exp} = 35\,\mathrm{km\,s^{-1}}$, we need a very high Doppler-b parameter, of $\sim 7.5\,\mathrm{km\,s^{-1}}$, to explain the broad line profiles as seen in almost all observed spectra (except the high-J rotational lines and a few rovibrational lines). We used the same description of NH_3 abundance as in Eq. (2.10) and found that $R_\mathrm{in} = 60\,R_\star = 0\farcs35$, $R_e = 350\,R_\star = 2''$, and $f_0 = 7 \times 10^{-7}$. The NH_3 inner radius is mainly constrained by the

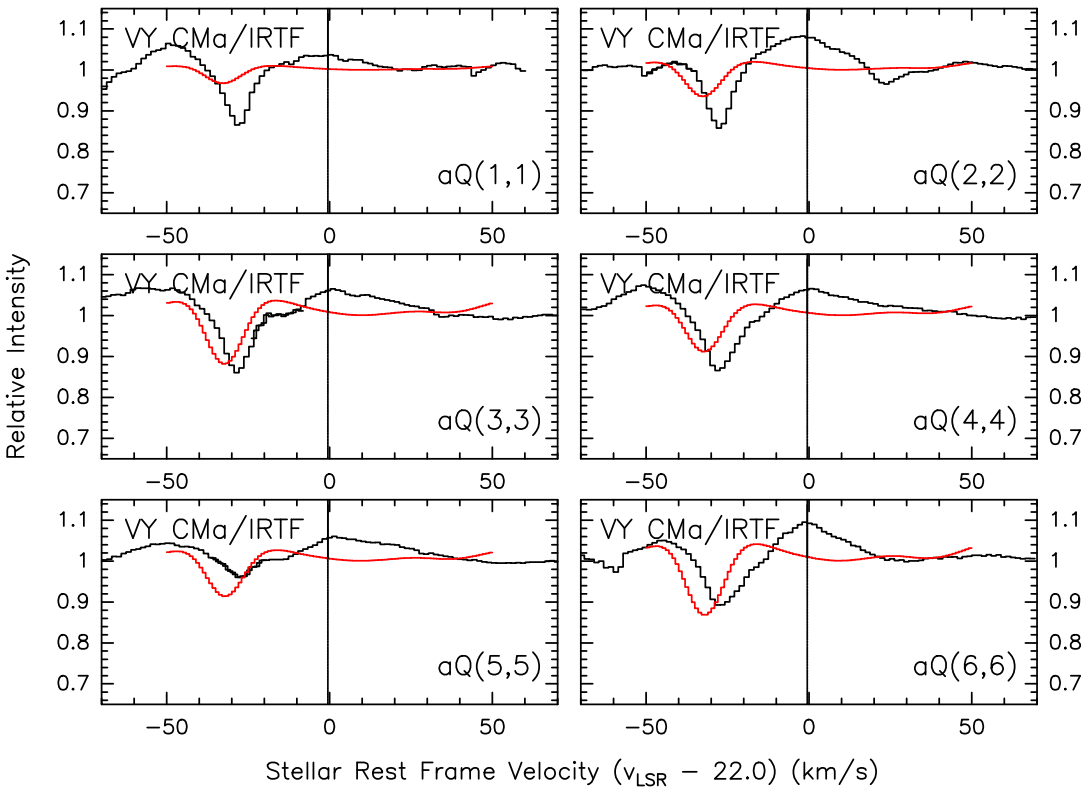

Figure 2.15.: Q-branch NH_3 rovibrational spectra of VY CMa. These transitions connects the upper energy levels of the ground-state inversion doublets and the lower levels in the vibrationally excited state. Black lines show the observed spectra from the NASA IRTF and red lines show the modelled spectra. Each modelled spectrum was divided by a smoothed version of itself as in the real data (see Sect. 2.2.4) in order to induce the similar distortion in the line wings.

relative intensity ratios of the rovibrational transitions. If we adopted a smaller R_{in}, the higher-J absorption profiles would become much stronger than the lower ones. The profiles of gas density, abundance, gas and dust temperatures, and outflow velocity are plotted in Fig. 2.16.

In general, the model is able to fit the central velocity component of most rotational transitions. However, there is a large excess of predicted flux in the spectrum of the blended 3–2 transitions (lower-left panel of Fig. 2.12). In our model, we did not consider radiative transfer between the blended NH_3 transitions. The modelled line flux at each velocity is simply the sum of fluxes contributed from the blending lines. For the inversion transitions (Fig. 2.11), our model tends to overestimate the flux densities of higher transitions. Increasing the adopted R_{in} could reduce the discrepancies, but would also underestimate the line absorption in high-J rovibrational transitions. Better fitting to the MIR absorption profiles (Figs. 2.13–2.15) would have been obtained had we adopted an expansion velocity of $\approx$30 km s^{-1}, which was also the value adopted by Goldhaber (1988, Sect. VII.1.2.B) to fit the MIR lines; however, such velocity cannot explain the broad rotational and inversion spectra with our single-component model (e.g. Figs. 2.11 and 2.12) and is not consistent with the commonly adopted terminal expansion velocity as derived from more abundant molecules (35–45 km s^{-1}; e.g. Decin et al., 2006; Muller et al., 2007; Ziurys et al., 2007). The origin of MIR NH_3 absorption may be close to the end of the wind acceleration as already suggested by Monnier et al. (2000b).

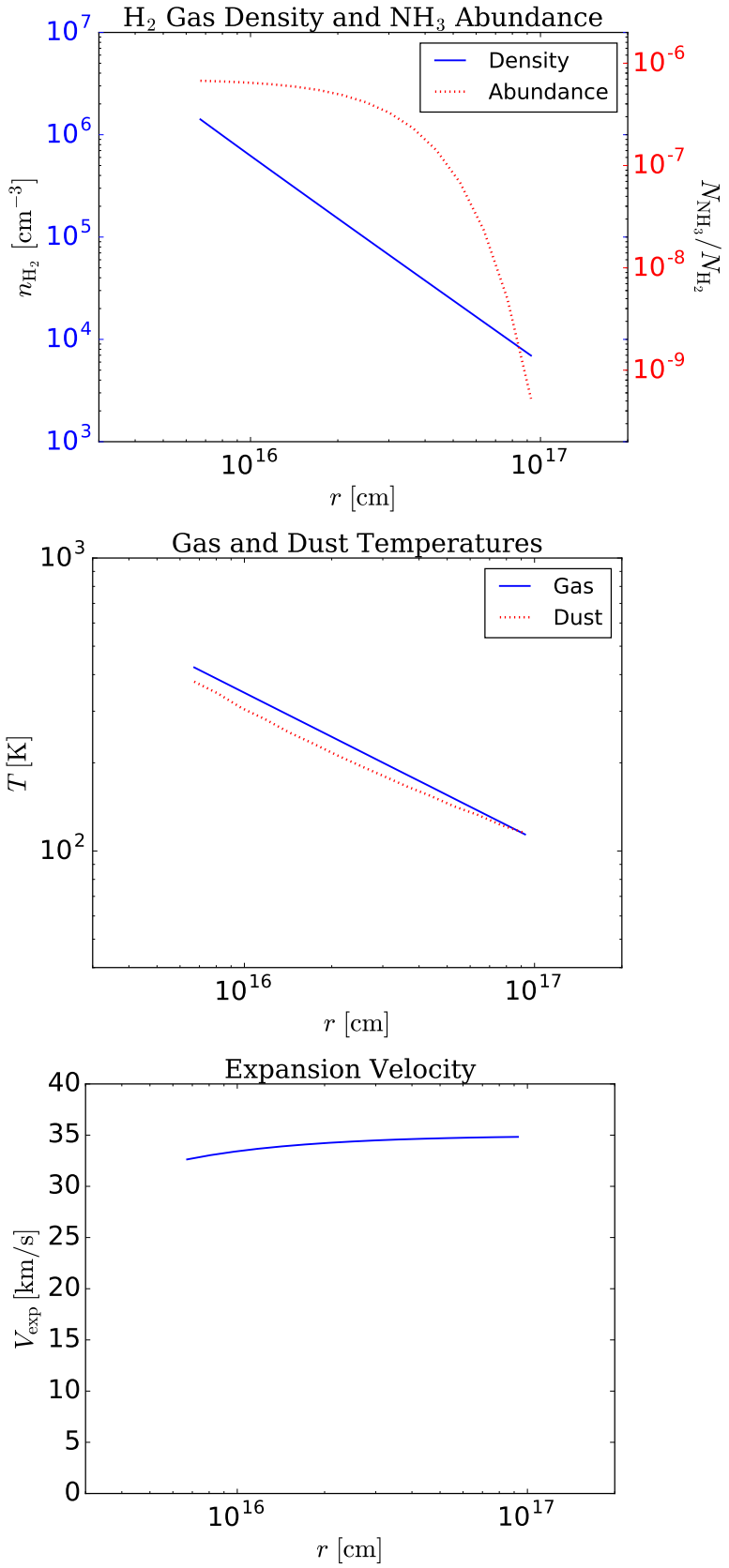

Figure 2.16.: The model for VY CMa. *Left*: Input gas density and NH_3 abundance profiles. Only the radii with abundance $>10^{-10}$ are plotted. *Middle*: Input gas and dust temperature profiles. *Right*: Input expansion velocity profile.

2.4.3. OH 231.8+4.2

OH 231.8+4.2 (also known as Rotten Egg Nebula or Calabash Nebula) is a bipolar pre-planetary nebula (PPN) hosting the Mira-type AGB star QX Pup. This object is believed to be evolving into a planetary nebula (Sánchez Contreras et al., 2004). In this study, we assume a distance of 1.54 kpc (Choi et al., 2012) and a systemic LSR velocity of 34 km s^{-1} (Alcolea et al., 2001). The average estimates of its luminosity and effective temperature are, respectively, $\sim 10^4\,L_\odot$ and ~2300 K(Cohen, 1981; Kastner et al., 1992; Sánchez Contreras et al., 2002). Using the Stefan–Boltzmann law, $L_\star \propto {R_\star}^2 {T_\star}^4$, the stellar radius is estimated to be $\sim 4.4 \times 10^{13}$ cm = 2.9 AU. High-resolution images of molecular emission of the nebula reveal a very clumpy bipolar outflow with a clear axis of symmetry at the position angle (PA) of about 21° and a plane-of-sky-projected, global velocity gradient (∇V) of about 6.5 km s^{-1} arcsec^{-1} from the north-east to the south-west (e.g. Sánchez Contreras et al., 2000; Alcolea et al., 2001). The fact that the CO emission is very compact ($\lesssim 4''$) within each velocity channel of width 6.5 km s^{-1} suggests that the molecular outflow is highly collimated (Alcolea et al., 2001). Most of the mass (~70%) as derived from molecular emission concentrates at the central velocity component, which is known as 'I3', between the LSR velocities of +10 and +55 km s^{-1}. This component spatially corresponds to the central molecular clump within a radius of $\lesssim 4''$ from the continuum centre (Alcolea et al., 1996, 2001). The circumstellar material is thought to have been suddenly accelerated about 770 years ago, resulting in a Hubble-like outflow with a constant velocity gradient, ∇V (Alcolea et al., 2001).

At the core of clump I3, the velocity gradient of SO is opposite in direction (i.e. velocity increasing from the south to the north) to the global ∇V as traced by CO, HCO^+, and $H^{13}CN$ within a radius of about 2″ and up to a velocity of about 10 km s^{-1} relative to our adopted systemic velocity (Sánchez Contreras et al., 2000). In the position-velocity (PV) diagram of SO along the axis of symmetry (Fig. 6 in Sánchez Contreras et al., 2000), there are two regions of enhanced SO emission: one peaks at about 1″ to the north-east and ~5 km s^{-1} redshifted to the systemic and the other peaks around the zero offset and ~5 km s^{-1} blueshifted to the systemic. Sánchez Contreras et al. (2000) suggested that the peculiar velocity gradient of the core SO emission could indicate the presence of a disc-like structure that is possibly expanding.

2.4.3.1. VLA observation of OH 231.8+4.2

Our VLA observations of OH 231.8+4.2 detected all the six covered metastable inversion lines. In each 3 km s^{-1}-wide velocity channel, the NH_3 emission is not resolved by the 4″-beam. This is consistent with the compact channel-by-channel CO emission as observed by Alcolea et al. (2001) assuming that the NH_3 emission also originates from the collimated bipolar outflow or the central clump I3. Figure 2.17 shows the integrated intensity maps of all the inversion lines over the LSR velocity range between 34 ± 54 km s^{-1}. The NH_3 (1,1) transition shows the most extended spatial distribution of typically ~6″ (up to ~9″ along the north-eastern part of the outflow) and the widest velocity range of ±50 km s^{-1} relative to the systemic velocity. All other transitions show emission well within the above limits. Therefore, the vast majority of the ammonia molecules are situated in clump I3 as identified by Alcolea et al. (1996, 2001).

Although the emission is not spatially resolved by channels, we see a systematic shift of the emission centroid from the north-east to the south-west with increasing LSR velocity. In Fig. 2.18, we show the PV diagrams of all six NH_3 transitions extracted along the symmetry axis at PA = 21°. A straight line of ∇V = 6.5 km s^{-1} arcsec^{-1} is also drawn in each diagram to indicate the global velocity gradient as traced by CO (Alcolea et al., 2001). NH_3 (1,1) is the only transition that somehow follows the global ∇V in its extended ($\gtrsim 2''$) emission. Within 2″, however, the intensity of the PV diagram is dominated by a component of enhanced

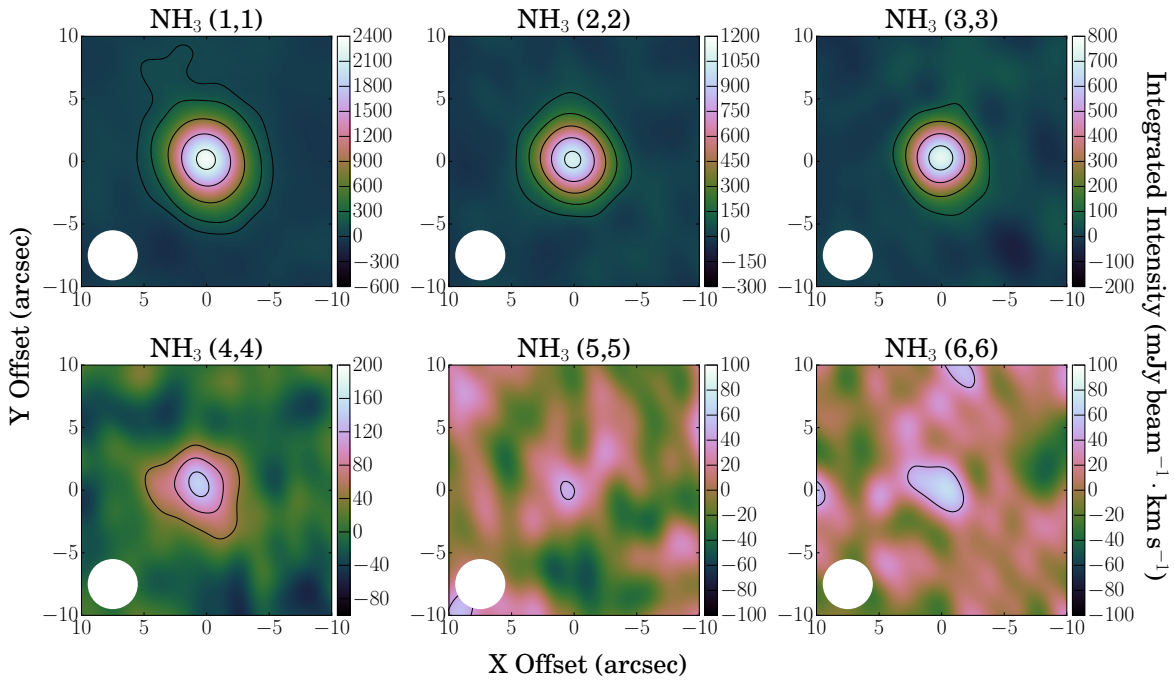

Figure 2.17.: Integrated intensity maps of the six lowest NH_3 inversion lines from OH 231.8+4.2 as observed with the VLA over the LSR velocity range of $[-20, 88]\,\mathrm{km\,s^{-1}}$ (relative velocity between $\pm 54\,\mathrm{km\,s^{-1}}$). Horizontal and vertical axes represent the offsets (arcsec) relative to the fitted centre of the continuum in the directions of right ascension and declination, respectively. The circular restoring beam of 4.″0 is indicated at the bottom-left corner in each map. The contour levels for the NH_3 lines are drawn at: $5, 15, 50, 100, 150\sigma$ for (1, 1); $5, 15, 30, 50, 70\sigma$ for (2, 2); $5, 15, 30, 45\sigma$ for (3, 3); and $3, 6, 9\sigma$ for (4, 4) to (6, 6), where $\sigma = 14.6\,\mathrm{mJy\,beam^{-1}\,km\,s^{-1}}$.

emission at around 0″–1″ north-east and with the redshifted velocities of 0–15 $\mathrm{km\,s^{-1}}$. Even more intriguing is the fact that other inversion lines, from (2,2) to (5,5) (and perhaps also (6,6)), show an enhancement near zero offset and in blushifted velocities; but none of them show the distinct redshifted feature at the same position-velocity coordinates in the diagram of (1,1).

The redshifted and blueshifted components of the NH_3-emitting region probably have different kinetic temperatures. Assuming that all inversion lines are optically thin, we can compute the rotational temperatures using the line ratios of different line combinations by the following formula, i.e. Eq. (1) of Menten & Alcolea (1995):

$$T_{JJ'} = \frac{\dfrac{E_{\mathrm{low}}(J,K)}{k} - \dfrac{E_{\mathrm{low}}(J',K')}{k}}{\ln\left[\dfrac{\int T_{\mathrm{mb}}(J,K)\,\mathrm{d}v}{\int T_{\mathrm{mb}}(J',K')\,\mathrm{d}v}\,\dfrac{J(J+1)}{J'(J'+1)}\,\dfrac{K'^2(2J'+1)}{K^2(2J+1)}\,\dfrac{g_{\mathrm{op}}(K')}{g_{\mathrm{op}}(K)}\right]} \tag{2.12}$$

where $E_{\mathrm{low}}(J,K)/k$ (in Kelvin) is the lower energy level and $\int T_{\mathrm{mb}}(J,K)\,\mathrm{d}v$ is the velocity-integrated main-beam brightness temperature of the inversion line (J,K). The weighting $g_{\mathrm{op}}(K)$ equals 2 for ortho-NH_3 ($K = 3, 6, \ldots$) and equals 1 for para-NH_3 ($K = 1, 2, 4, 5, \ldots$). We compute the rotational temperatures for the redshifted and blueshifted components separately. From the binned spectra presented in the next subsection, we get the main-beam brightness temperature of the two components from the relative velocity ranges of $[7.5, 13.5]\,\mathrm{km\,s^{-1}}$

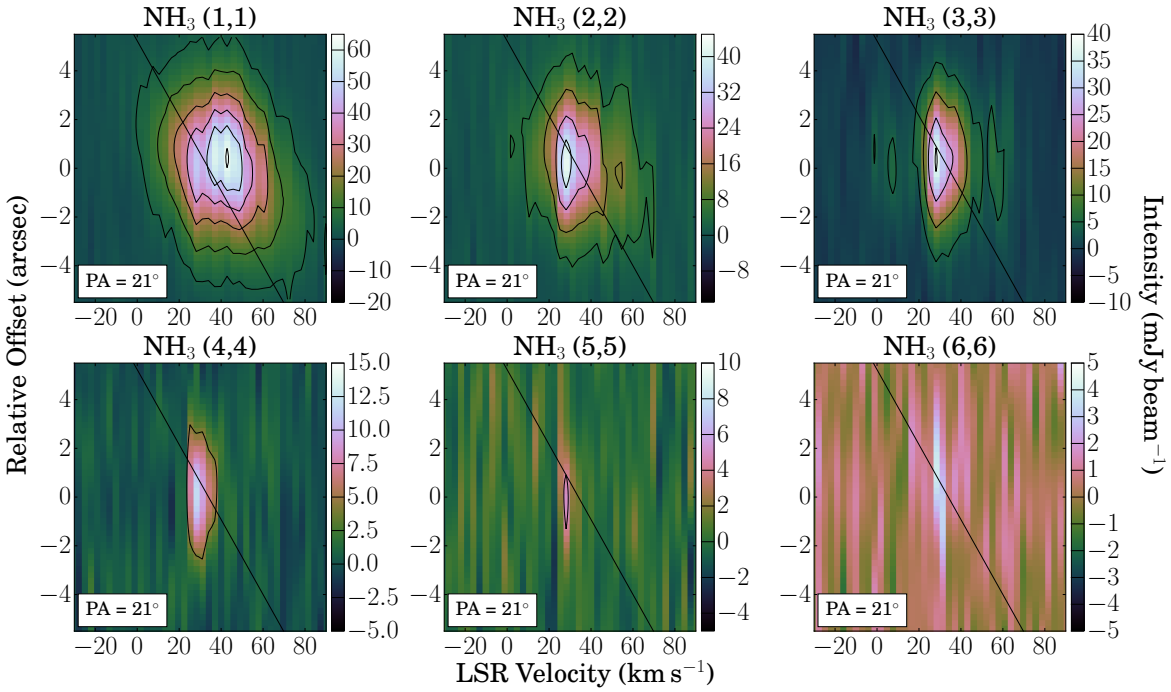

Figure 2.18.: Position-velocity (PV) diagrams of the six lowest NH_3 lines as observed with the VLA cutting along the axis of symmetry of OH 231.8+4.2. Vertical axes represent offsets (arcsec) in the north-east direction at the position angle of 21° and horizontal axes represent the LSR velocity ($km\,s^{-1}$). In each PV diagram, the global velocity gradient of $\nabla V = 6.5\,km\,s^{-1}\,arcsec^{-1}$ is indicated by the straight line passing through the continuum centre (i.e. zero offset) and the systemic LSR velocity ($34\,km\,s^{-1}$) of OH 231.8+4.2.

(where (1,1) peaks) and $[-10.5, -4.5]\,km\,s^{-1}$ (where other lines peak). The rotational temperature T_{12} for the redshifted component is 20 K and that of the blueshifted component is 37 K. The upper limits of T_{14} and T_{24} for the redshifted component (<41 K and <58 K) are also consistently smaller that the derived values for the blueshifted (54 K and 63 K). We do not show the rotational temperatures involving both ortho- and para-NH_3 lines, which are of limited meaning because the conversion between the two species is extremely slow and is not primarily determined by the present temperature (Sect. 2.1.5, see also Ho et al., 1979).

As already predicted by Menten & Alcolea (1995) based on single-dish inversion spectra of NH_3, the (2,2) and (3,3) lines probably exclusively trace the warm material that is close to the central star, while the (1,1) line (among other molecules) traces the cooler part of the circumstellar gas and the high-velocity outflow. From our analysis of the VLA data, we are able to distinguish the spatial and kinematic components that emit at different inversion lines. NH_3 (1,1) emission predominantly comes from the cool material in the bulk of the clump I3, the inner part of the bipolar outflow up to ~6″–9″, and the redshifted component of enhanced emission, which is possibly part of a disc-like structure, as traced by the inner SO emission. On the other hand, most if not all emission of the higher transitions originates from the warm, blueshifted component of the inner SO emission. This component is spatially close to the centre of the radio continuum.

2.4.3.2. *Herschel*/HIFI observations of OH 231.8+4.2

The NH_3 $J_K = 1_0$–0_0 spectrum of OH 231.8+4.2 clearly shows two components: a strong, narrow component within ±20–25 $km\,s^{-1}$ relative to the systemic velocity and a weaker, broad

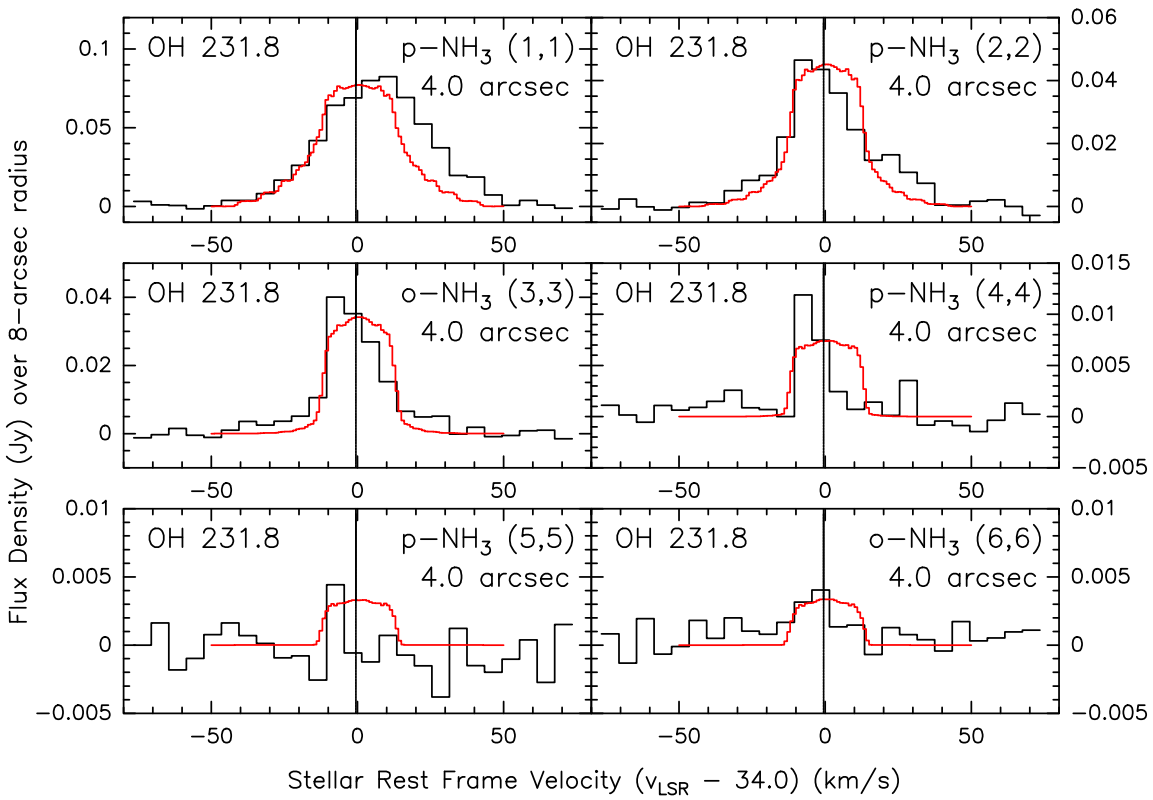

Figure 2.19.: NH_3 inversion line spectra of OH 231.8+4.2. Black lines show the VLA spectra in flux density and red lines show the modelled spectra. All transitions were observed in 2013 with D configuration. The spectra were integrated over an 8″-radius circle.

component that is only apparent in the redshifted velocity range between ~18 km s^{-1} and ~45 km s^{-1}. Both components are asymmetric with signs of self-absorption in blueshifted velocities. Due to poor S/N ratios, higher transitions only show the narrow component but not the broad one. The relative velocity range of the narrow component is consistent with that of the clump I3 (Alcolea et al., 1996), therefore suggesting that most of the rotational line emission originates from this clump within the radius of ~4″.

2.4.3.3. NH_3 model of OH 231.8+4.2

From the above discussion, the NH_3 distribution can be distinguished into at least two parts: (1) a central core containing a possible disc-like structure and (2) an outer outflow following a Hubble-like expansion with a constant velocity gradient. Since the VLA images do not resolve the structure of the possible disc and our code is only one-dimensional, we can only assume spherical symmetry and uniform distribution of the molecule (without any substructures). We adopt the expansion velocity profile as

$$V_{\rm exp}(r) = \begin{cases} 13.0\,{\rm km\,s^{-1}} & \text{if } r \leq 1\farcs5 = 787\,R_\star \\ (8.9\,{\rm km\,s^{-1}\,arcsec^{-1}}) \times r & \text{if } r > 1\farcs5 \end{cases}, \tag{2.13}$$

The gas density distribution of the nebula is not known. We use again Eq. (2.6) to describe the density by assuming the conservation of mass. As in the models of Sánchez Contreras et al. (2015) and Velilla Prieto et al. (2015), we adopt a constant mass-loss rate of $\dot{M} = 1 \times 10^{-4}\,M_\odot\,{\rm yr^{-1}}$ and a characteristic velocity of $\langle V_{\rm exp}\rangle = 20\,{\rm km\,s^{-1}}$. However, we found that such density is too low to reproduce the observed intensities of the rotational lines. We have

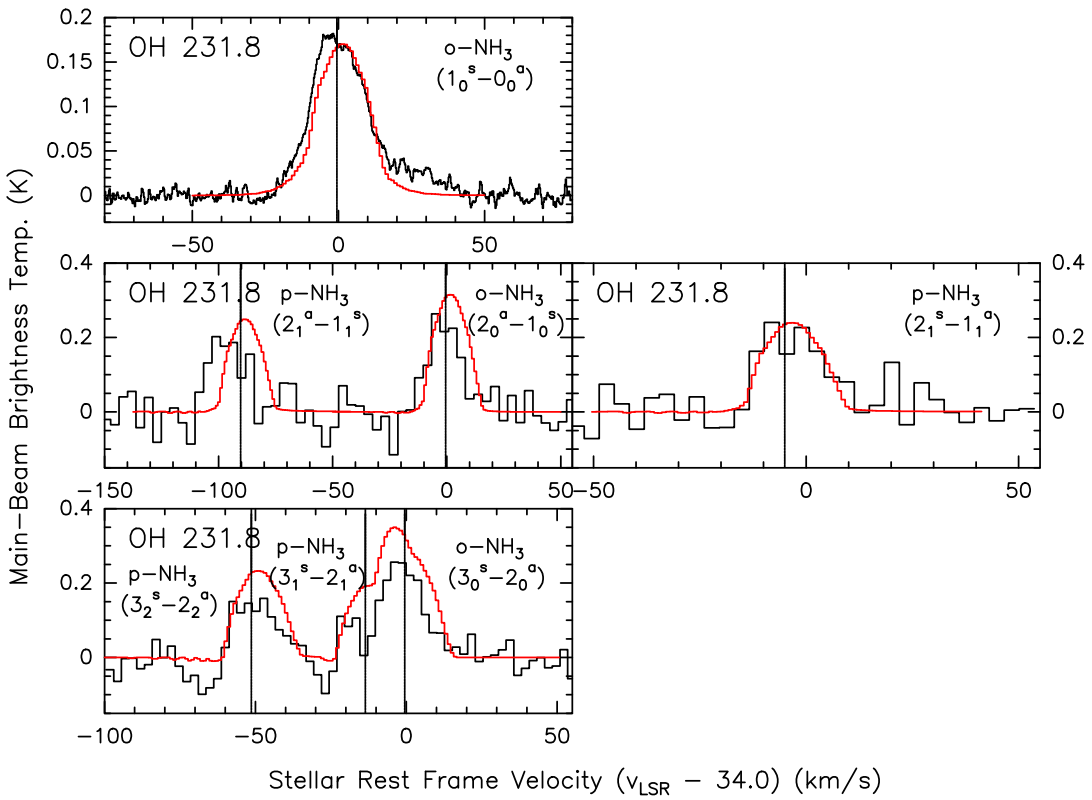

Figure 2.20.: NH_3 rotational line spectra of OH 231.8+4.2. Black lines show the observed spectra from *Herschel*/HIFI and red lines show the modelled spectra.

to introduce a density enhancement factor of 3.5 to fit all the spectra. We use the similar abundance profile as in Eq. (2.10) with $R_{\rm in} = 20\,R_\star$, $R_e = 2100\,R_\star \approx 4''$, and $f_0 = 5 \times 10^{-7}$. The gas temperature in our model is described by a simple power-law

$$T_{\rm kin}(r) = 2300\,{\rm K}\left(\frac{r}{R_\star}\right)^{-0.6}. \tag{2.14}$$

Figures 2.19 and 2.20 show the VLA and *Herschel*/HIFI spectra, respectively; and Fig. 2.21 shows the radial profiles of our input parameters. In general, our model is able to predict the observed emission from all available spectra. However, the fitting to the redshifted part of the spectra is unsatisfactory, especially in the $(J, K) = (1, 1)$ and $J_K = 1_0$–0_0 lines. As discussed in Sect. 2.4.3.1, we speculate that some of the redshifted emission comes from a cool component that is shifted to the north-east of the outflow and predominantly emits in (1,1). Our 1-D model assumes the density of the outflow at those velocities to be $\sim 10^4$–10^5 cm^{-3}, while the critical density of the 1_0–0_0 transition is about 1×10^7 cm^{-3}; therefore, this component is likely to be significantly denser than the ambient gas.

2.4.4. IRC +10420

2.4.4.1. VLA observation of IRC +10420

Figure 2.22 shows the images of NH_3 (1,1) and (2,2) emission from IRC +10420 as observed with the VLA in 2004, before major upgrade of the interferometer. We binned the image cube every 4.9 km s^{-1} to produce the channel maps. We adopt the systemic velocity to be $V_{\rm LSR} = 75$ km s^{-1} (Castro-Carrizo et al., 2007). The two right panels in Fig. 2.23 show the

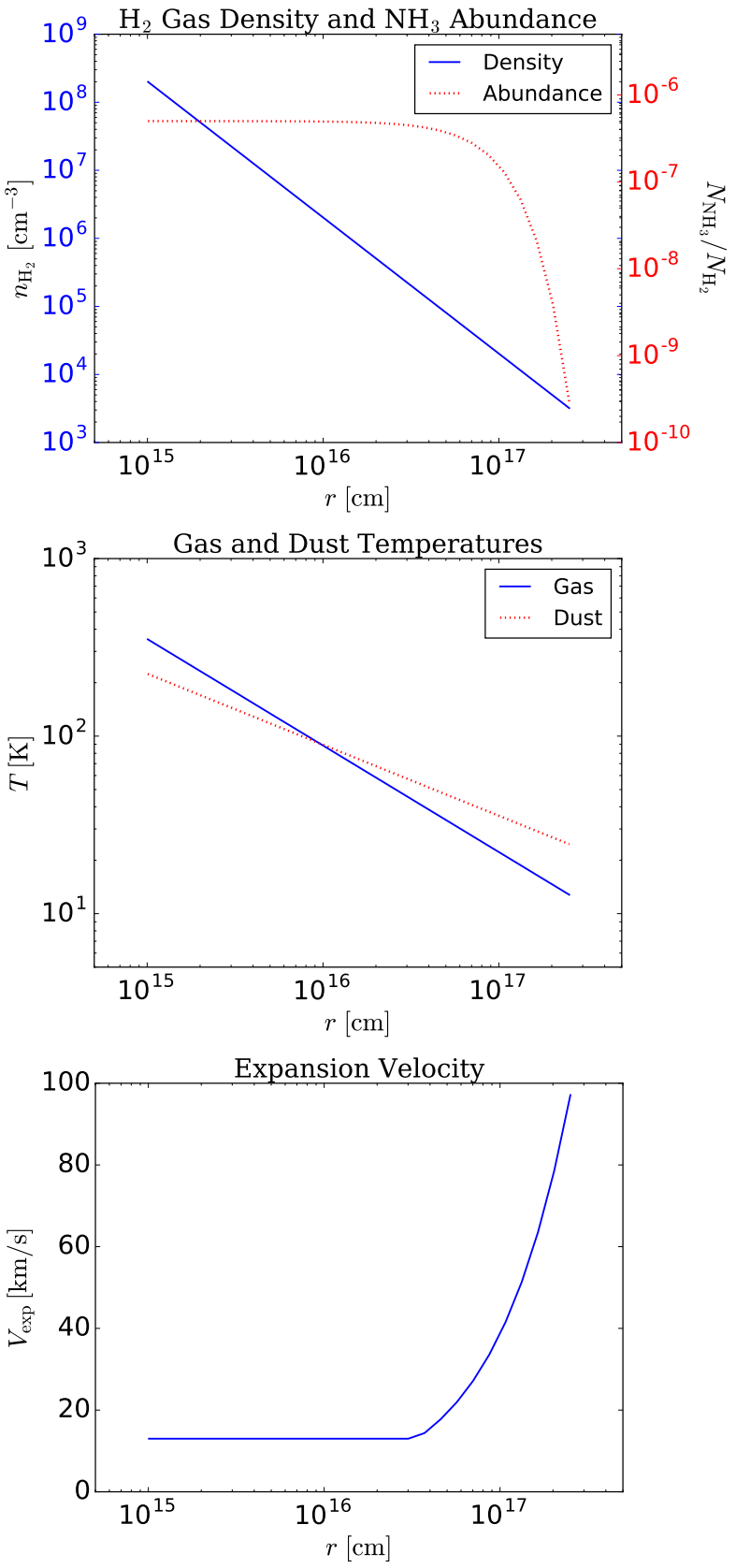

Figure 2.21.: The model for OH 231.8+4.2. *Left*: Input gas density and NH_3 abundance profiles. Only the radii with abundance $>10^{-10}$ are plotted. *Middle*: Input gas and dust temperature profiles. *Right*: Input expansion velocity profile.

observed spectra of the flux density over the same 14″-box as displayed in the VLA images (Fig. 2.22) together with the synthesised spectra as discussed in Sect. 2.4.4.4.

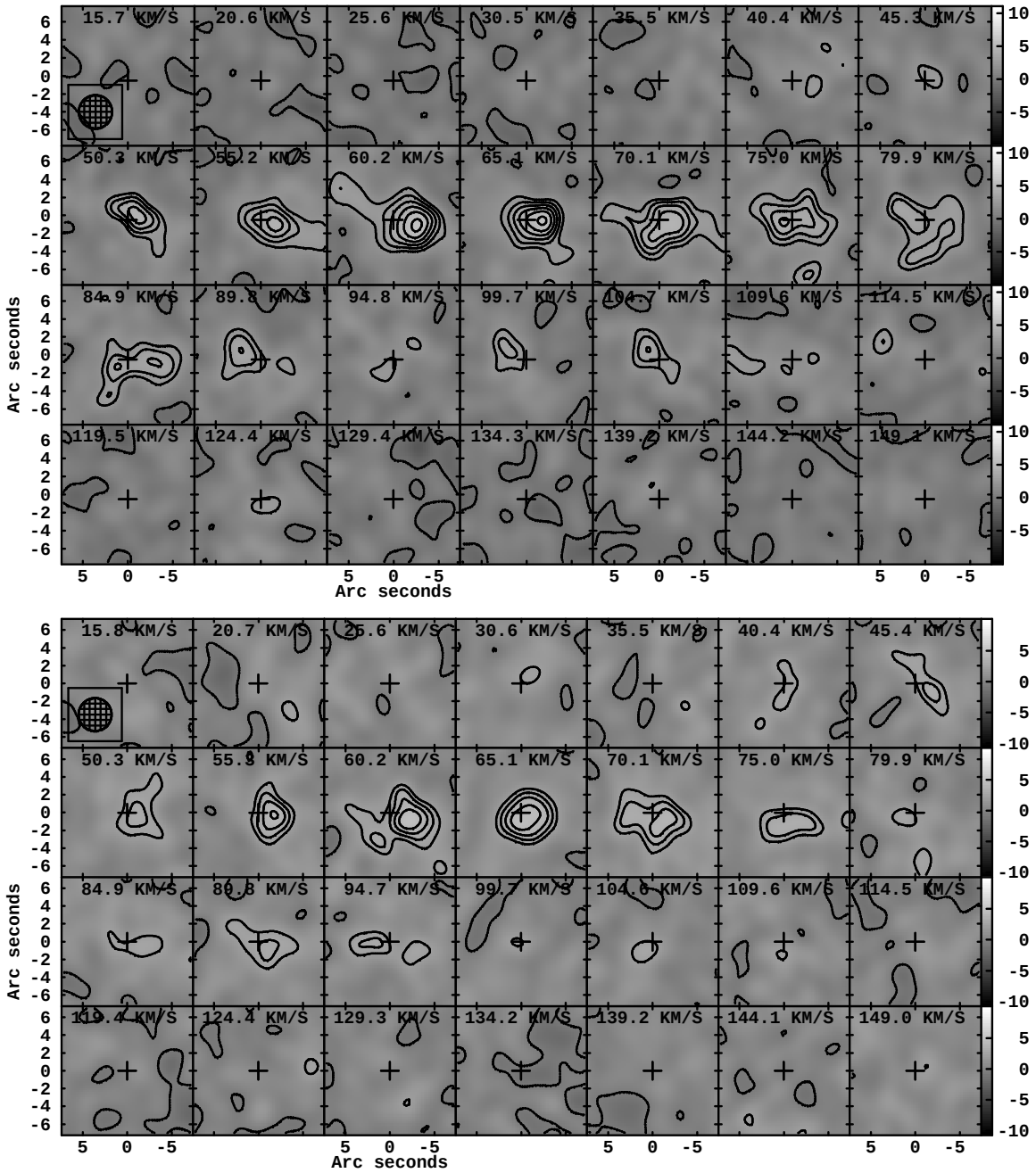

Figure 2.22.: VLA images of NH_3 (1,1) (*top*) and (2,2) (*bottom*) emission from IRC +10420. In each panel, the LSR velocity is shown and the position of IRC +10420 is marked by a cross. The circular restoring beam with a FWHM of 3.″7 is indicated at the bottom left corner of the first panel. The contour levels for the NH_3 lines are drawn at: $3, 4, 5, 6, 7, 8\sigma$, where $\sigma = 0.69$ mJy beam^{-1} for $(1, 1)$ and $\sigma = 0.68$ mJy beam^{-1} for $(2, 2)$.

The NH_3 emission appears to be resolved by the restoring beam of FWHM = 3.″7 and appears to be distributed primarily along the east-west directions. The radius of 3σ detection extends up to about 7″ for (1,1) and 5″ for (2,2). In general, the spatial distributions of the emission from NH_3 (1,1) and (2,2) are very similar, with the (1,1) line being slightly stronger

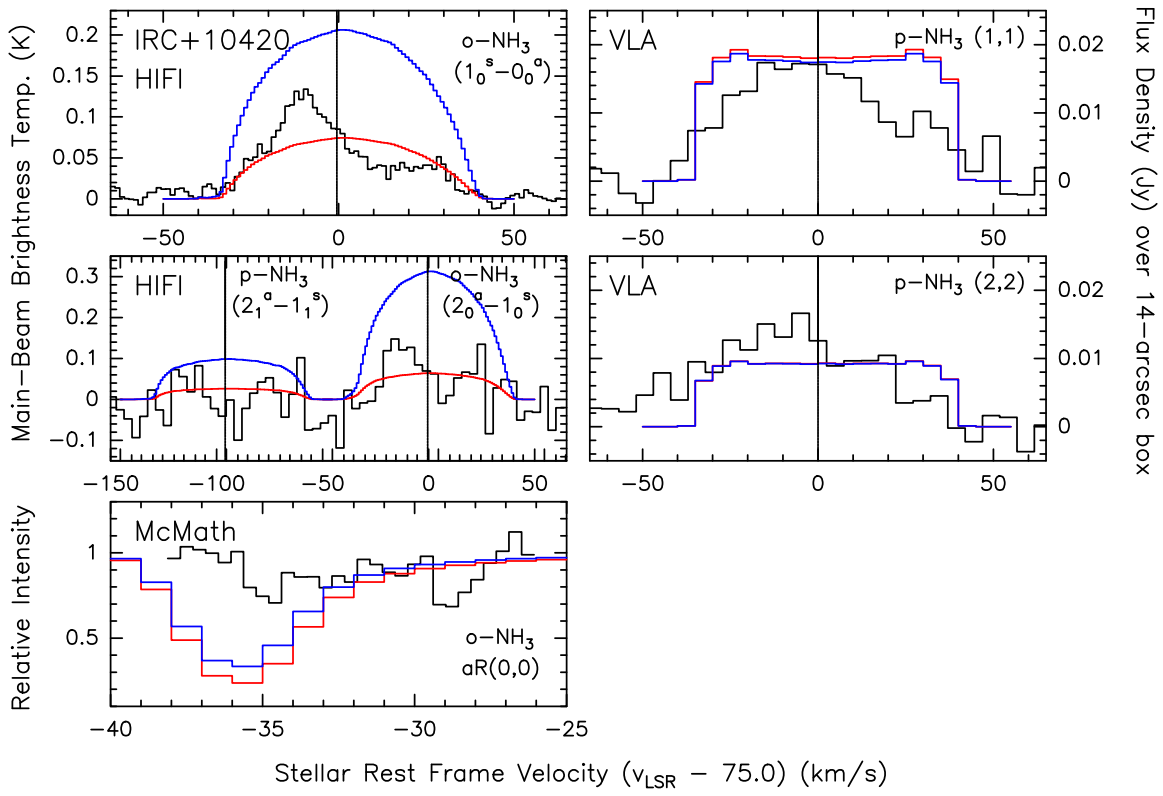

Figure 2.23.: NH_3 spectra of IRC +10420. Black lines show the observed spectra; red and blue lines show the modelled spectra from the first model (low density, high abundance) assuming a dust-to-gas mass ratio of 0.001 and 0.005, respectively. The *top-left* and *middle-left* spectra are *Herschel*/HIFI spectra of IRC +10420. The two spectra on the *right* are VLA spectra showing the flux density integrated over a $14'' \times 14''$ box centred at IRC +10420, i.e. the same region as shown in Fig. 2.22. The black spectrum in the *bottom* panel shows the old $aR(0, 0)$ spectrum from the McMath Solar Telescope, as reproduced from Fig. 3 of McLaren & Betz (1980, © AAS. Reproduced with permission.).

than (2,2). Most of the NH_3 emission is offset to the west/south-west in the V_{LSR} range of ~40–70 km s^{-1}, while the emission is shifted to the east in extreme redshifted velocities near 95–105 km s^{-1}. Similar trend of the velocity gradient is also seen in the rotational emission of ^{13}CO and SO as observed with the SMA by Dinh-V.-Trung et al. (2009b).

A close, channel-by-channel comparison of the interferometric images finds that the spatial distribution of the NH_3 inversion emission, especially that in the (2, 2) line, is strikingly similar to that of rotational emission in SO $J_K = 6_5$–5_4 (Fig. 6 of Dinh-V.-Trung et al., 2009b). Both molecules appear to trace the similar clumpy structures in the CSE at various velocities, suggesting that both molecules share the similar kinematics and abundance distribution. The chemical models of Willacy & Millar (1997) for O-rich AGB stars suggest that SO is produced when S, S^+, or HS is produced from ion-neutral reactions or photodissociation and reacts with OH or O. Therefore, most of the SO molecules form in the gas-phase chemistry of the CSE. If the spatial distribution of NH_3 is similar to that of SO, then NH_3 has to be produced in the CSE rather than the inner wind as presumed in existing chemical models for lower-mass stars. The apparent lack of centrally peaked emission in our VLA images is consistent with such scenario.

There is a bright component emitting in both NH_3 lines at the radius of ∼2″ to the west of the star. This component is the most prominent in the V_{LSR} range of 50–75 km s^{-1}, particularly near 65 km s^{-1}, i.e. a blueshifted velocity of 10 km s^{-1}. The high-resolution CO images of IRC +10420 also show a similar bright component between 60 and 75 km s^{-1}, elongated along a PA of 75° (Fig. 6 of Castro-Carrizo et al., 2007). The peaks of the CO-enhanced component are about 4″ and 1″ south-west of the star in the CO J = 1–0 and J = 2–1 transitions, respectively. At V_{LSR} = 65 km s^{-1}, the brightest CO emission arises from an offset of ∼2″.

2.4.4.2. *Herschel*/HIFI observations of IRC +10420

Herschel/HIFI spectra of IRC +10420 are only available for the $J_K = 1_0(s)–0_0(a)$, $2_0(a)–1_0(s)$, and $2_1(a)–1_1(s)$ transitions. The spectra are shown in the top-left and middle-left panels of Fig. 2.23. The $1_0–0_0$ line has the highest S/N ratio and clearly shows asymmetry. The brightness of this line – and perhaps also that of $2_0–1_0$ – peaks at V_{LSR} = 65 km s^{-1}, which is the same 'peak velocity' as in the VLA data. Therefore, this spectral feature likely corresponds to the bright clump at ∼2″ west of the star in the VLA images. Additionally, there is a weaker, broad spectral component spanning up to the expansion velocity of ∼37 km s^{-1} (e.g. Castro-Carrizo et al., 2007).

By comparing the NH_3 $1_0–0_0$ spectrum with other *Herschel*/HIFI spectra of IRC +10420 in Teyssier et al. (2012), the NH_3 spectral features resemble those of the ortho-H_2O and perhaps OH transitions, especially o-H_2O $J_{K_a,K_c} = 3_{2,1}–3_{1,2}$ and $3_{1,2}–2_{2,1}$. Teyssier et al. (2012) suggested that both water and ammonia abundances may be enhanced by shock-induced chemistry in the CSE of IRC +10420.

2.4.4.3. Old McMath observations of IRC +10420

The bottom panel of Fig. 2.23 shows the MIR $aR(0, 0)$ spectrum reproduced from Fig. 3 of McLaren & Betz (1980). In this spectrum taken in 1979, there are two absorption components at the LSR velocities of ∼40 km s^{-1} and ∼46 km s^{-1}, which correspond to the relative velocities of approximately −35 km s^{-1} and −29 km s^{-1}, respectively, to the systemic velocity. While the more-blueshifted component probably arose from the gas moving towards us at the terminal expansion velocity (as in the cases of IK Tau and VY CMa), the intermediate-velocity component is more intriguing. Owing to the coincidence of their velocities, McLaren & Betz (1980) associated this NH_3 absorption component with the 1612 MHz OH maser spots imaged by Benson et al. (1979). Nedoluha & Bowers (1992) interpreted the 1612 MHz OH masers as coming from a shell of radius ∼8000–9000 AU (∼1.″5), which was slightly smaller than the MIR continuum of IRC +10420 as imaged by Shenoy et al. (2016). Hence, the NH_3 component at V_{LSR} ∼ 46 km s^{-1} could have come from the expanding shell at some offset from the line of sight towards the star, thus causing it to absorb the extended background continuum at a projected line-of-sight velocity.

2.4.4.4. NH_3 model of IRC +10420

IRC +10420 is a yellow hypergiant with an extremely high and variable mass-loss rate (∼10^{-4}–10^{-3} $M_\odot$ yr^{-1}, e.g. Shenoy et al., 2016). The CSE of the IRC +10420 is expanding at a maximum speed of about 37 km s^{-1} (Castro-Carrizo et al., 2007), which is the value we adopt as the constant expansion velocity of the NH_3-carrying gas. The gas density and temperature of the CSE have been studied in detail by modelling multiple CO rotational transitions (Teyssier et al., 2012). The CO emission can be well explained by two distinct mass-loss episodes with a period very low global mass loss in between (Castro-Carrizo et al., 2007; Dinh-V.-Trung et al., 2009b).

In our NH_3 models, however, we found that the gas density profiles derived from such a

mass-loss history are unable to explain the NH_3 emission, especially near the radii of 2″–4″ where there is a low-density 'gap' separating the two dominant gas shells. A higher density in the inter-shell region is required in our model. We assume that the density profile of this region corresponds to a uniformly expanding shell with an equivalent mass-loss rate being the average of the inner and outer shells of the model of Castro-Carrizo et al. (2007), i.e.

$$n_{\mathrm{H_2}}(r) = \begin{cases} 9.37 \times 10^3\ \mathrm{cm^{-3}} \cdot {r_{17}}^{-2} & \text{if } 0.25 \leq r_{17} \leq 1.24 \\ 7.46 \times 10^3\ \mathrm{cm^{-3}} \cdot {r_{17}}^{-2} & \text{if } 1.24 < r_{17} \leq 2.20\ , \\ 5.55 \times 10^3\ \mathrm{cm^{-3}} \cdot {r_{17}}^{-2} & \text{if } 2.20 < r_{17} \leq 5.20 \end{cases} \tag{2.15}$$

where

$$r_{17} = \frac{r}{10^{17}\ \mathrm{cm}}. \tag{2.16}$$

The gas temperature profile is based on that derived by Teyssier et al. (2012). We assume the gas temperature in the inter-shell region to follow the same power-law as the outer shell, i.e.

$$T_{\mathrm{kin}}(r) = \begin{cases} 170\ \mathrm{K} \cdot {r_{17}}^{-1.2} & \text{if } 0.25 \leq r_{17} \leq 1.24 \\ 100\ \mathrm{K} \cdot {r_{17}}^{-0.8} & \text{if } 1.24 < r_{17} \leq 5.20 \end{cases}. \tag{2.17}$$

We found that infrared pumping by dust grains has significant influence on the intensity of the rotational transitions. Assuming a typical dust-to-gas mass ratio of d/g = 0.005 (Oudmaijer et al., 1996), the modelled rotational line intensities are significantly higher than the observed. We had to adopt a lower d/g in order to reduce the contribution of radiative excitation from dust. The following NH_3 abundance distribution is found to be able to reproduce the radial intensity profiles of NH_3(1,1) and NH_3(2,2) at the peak velocity ($V_{\mathrm{LSR}} = 65\ \mathrm{km\ s^{-1}}$):

$$n_{\mathrm{NH_3}}/n_{\mathrm{H_2}} = \begin{cases} 1.0 \times 10^{-6} & \text{if } 0.25 \leq r_{17} \leq 1.24 \\ 2.5 \times 10^{-6} & \text{if } 1.24 < r_{17} \leq 2.20\ . \\ 1.0 \times 10^{-6} & \text{if } 2.20 < r_{17} \leq 5.20 \end{cases} \tag{2.18}$$

Figure 2.23 shows our model fitting to all available spectra with two different d/g ratios based on the above model. Our modelled $aR(0, 0)$ spectrum does not reproduce the absorption component at the intermediate velocity near $-29\ \mathrm{km\ s^{-1}}$ because our model does not consider an extended MIR continuum; therefore, line absorption can only occur along the central line of sight and hence at the blueshifted expansion velocity. The radio inversion lines are not affected by the adopted d/g ratio. Our model predicts the inversion lines to be optically thin and show flat-topped spectra. The observed VLA profiles, however, are far from being flat. The synthesised absorption profile at the terminal blueshifted velocity is much deeper than the observed, so is the emission profile in NH_3(1,1). Since our model adopts the oversimplified assumption of a smooth and uniform distribution of NH_3 in the CSE, the discrepancies are probably due to the non-uniform distribution of the molecule, particularly in the outer, cooler part of the CSE which dominates NH_3(1,1) emission and $aR(0, 0)$ absorption.

The input parameters, together with the resultant radial intensity profiles at $V_{\mathrm{LSR}} = 65\ \mathrm{km\ s^{-1}}$ and at the systemic velocity ($V_{\mathrm{LSR}} = 75\ \mathrm{km\ s^{-1}}$), are plotted in Fig. 2.24. At $V_{\mathrm{LSR}} = 65\ \mathrm{km\ s^{-1}}$, while this model is able to fit the radial intensity profiles within uncertainties, it tends to underestimate the line intensity ratio of NH_3(2,2)/NH_3(1,1). The model cannot produce a satisfactory fit to the radial intensity profiles at the systemic velocity.

The NH_3 abundance of $\sim 10^{-6}$ is significantly higher, by a factor ranging from 5 to 12.5, than that derived for the inversion lines by Menten et al. (2010). In their model, they used a

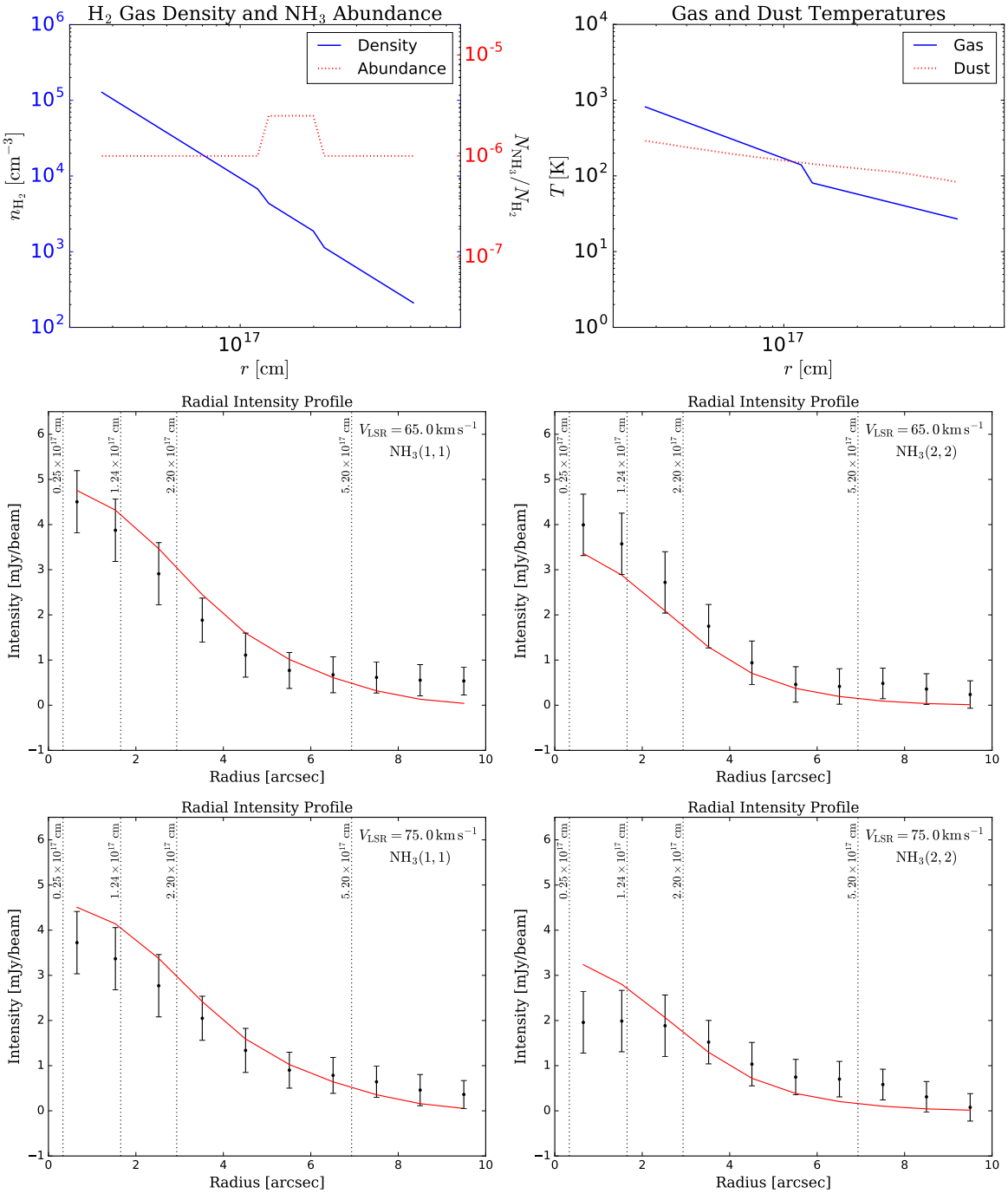

Figure 2.24.: The first model for IRC +10420 with low gas density and high NH_3 abundance. *Top left*: Input gas density and NH_3 abundance profiles. Only the radii with abundance $>10^{-10}$ are plotted. *Top right*: Input gas and dust temperature profiles. *Middle*: The radial intensity profiles of NH_3(1,1) (*left*) and NH_3(2,2) (*right*) at the velocity channel $V_{LSR} = 65\,km\,s^{-1}$, which show the strongest emission in both rotational and inversion transitions. *Bottom*: The radial intensity profiles of NH_3(1,1) (*left*) and NH_3(2,2) (*right*) at the velocity channel $V_{LSR} = 75\,km\,s^{-1}$, which is the systemic velocity of IRC +10420. In the radial intensity profiles, black points indicate the binned data points from the VLA images and red curves show the modelled profiles.

much higher density which corresponds to a constant mass-loss rate of $2 \times 10^{-3}\,M_{\odot}\,\mathrm{yr}^{-1}$ and is approximately seven times higher than our assumed density. Similar models requiring high gas density to explain molecular line emission have also been reported by Wong (2013) and Quintana-Lacaci et al. (2016) for the SiO molecule. The modelling exercises of Wong (2013) found that it was impossible to explain the SiO emission, in particular the radial intensity profiles, with the model of two disconnected gas shells from Castro-Carrizo et al. (2007). Indeed, a higher gas density throughout the entire SiO-emitting region is required (Wong, 2013; Quintana-Lacaci et al., 2016). Therefore, it is speculated that the SiO emission originates from localised clumpy structures, possibly created by shocks, that are not represented by the global mass-loss history as traced by CO emission (Wong, 2013, Dinh-V.-Trung et al., in prep.).

Assuming that the dense gas associated with SiO emission is distinct from the diffuse gas producing the bulk of the CO emission, Wong (2013) introduced two models of density and abundance stratification both different from those based on CO. The 'three-zone model' retains the shell boundaries in the model of Castro-Carrizo et al. (2007), but adopts an at least four times higher gas density throughout the modelled region (Sect. 5.4 of Wong, 2013); whereas the 'two-zone model' consists of two bordering zones with a higher SiO abundance in the inner one and has the gas density following a single power-law at a shallower gradient than a uniformly expanding envelope (Sect. 6.4 of Wong, 2013). The gas density of the two-zone model is generally higher than the CO-based density from Castro-Carrizo et al. (2007) except at the innermost radii ($\lesssim 5 \times 10^{16}$ cm).

We consider the gas density from the two-zone model as the high-end estimate for the CSE of IRC +10420 and derive the minimum NH_3 abundance from the optically thin inversion lines. Our adopted gas density profile is slightly modified from that of Wong (2013) and is described as

$$n_{\mathrm{H_2}}(r) = 2.30 \times 10^4\,\mathrm{cm}^{-3} \cdot {r_{17}}^{-0.7} \quad \text{if} \quad 0.25 \leq r_{17} \leq 6.00. \tag{2.19}$$

By fitting the radial intensity profiles at the systemic velocity, we obtain the following NH_3 abundance distribution:

$$n_{\mathrm{NH_3}}/n_{\mathrm{H_2}} = \begin{cases} 2.5 \times 10^{-7} & \text{if } 0.25 \leq r_{17} \leq 2.35 \\ 4.0 \times 10^{-8} & \text{if } 2.35 < r_{17} \leq 6.00 \end{cases}. \tag{2.20}$$

Figure 2.25 shows our model fitting with two different d/g ratios to all available spectra and Fig. 2.26 shows the plots of the input parameters and the resultant radial intensity profiles. The quality of the fitting and the effects of the d/g ratio are similar to our first model, but the NH_3 abundance has been reduced by at least one order of magnitude. Because of the ambiguity of the gas density and abundance, we are unable to conclusively determine the NH_3 abundance in the CSE of IRC +10420, which is likely in the range $\sim 10^{-7}$–10^{-6}. In any case, the density of NH_3-emitting gas cannot be the same as that of the ambient medium as traced by CO for a considerable range of radii; we therefore speculate that NH_3 emission probably also comes from the dense, localised clumps throughout IRC +10420's CSE.

2.4.5. Ammonia chemistry

Table 2.6 summarises the adopted parameters and results of our NH_3 models. In general, the NH_3 abundance required to explain the spectral line data is of the order of 10^{-7}, except for IRC +10420 where this value is a lower limit due to the ambiguous gas density of the CSE. The abundances in IK Tau and VY CMa are a few times lower than those obtained by Menten et al. (2010), in which MIR radiative pumping of the molecule to the $v_2 = 1$ state was not considered. The decrease in the inferred abundance upon the inclusion of infrared pumping

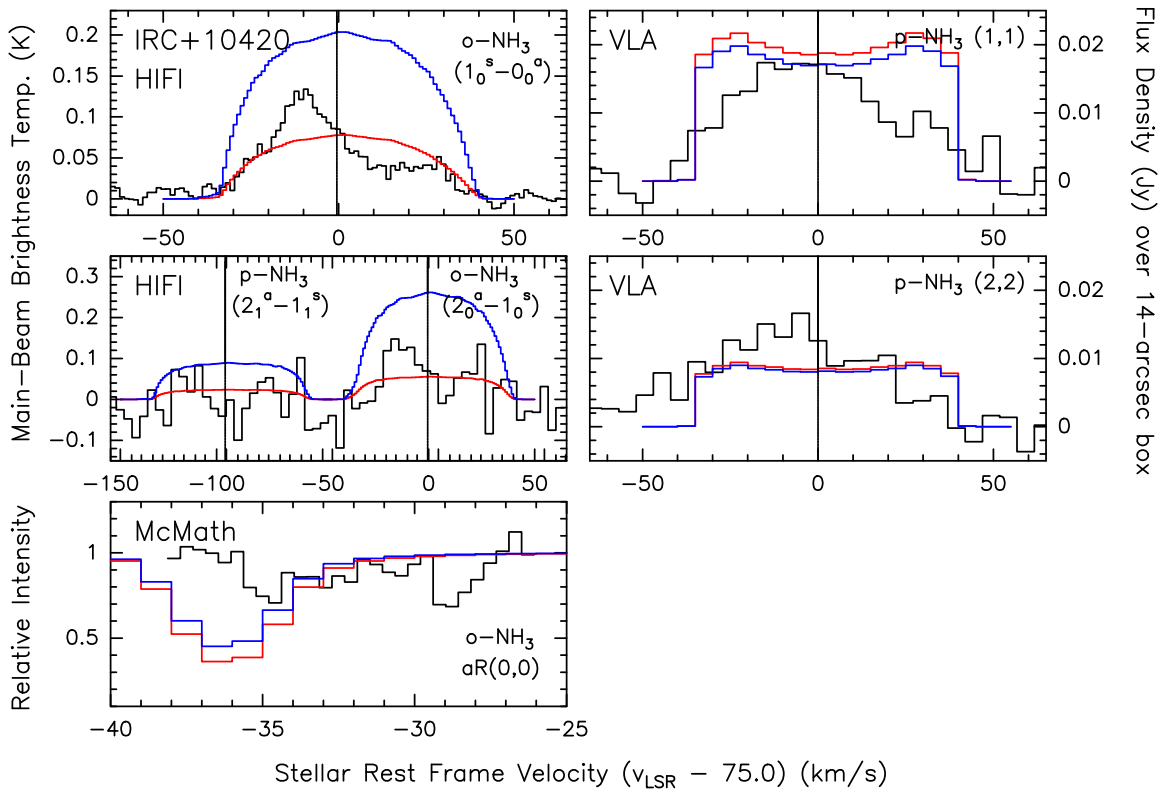

Figure 2.25.: NH_3 spectra of IRC +10420. Black lines show the observed spectra; red and blue lines show the modelled spectra from the second model (high density, low abundance) assuming a dust-to-gas mass ratio of 0.001 and 0.005, respectively. The *top-left* and *middle-left* spectra are *Herschel*/HIFI spectra of IRC +10420. The two spectra on the *right* are VLA spectra showing the flux density integrated over a 14″ × 14″ box centred at IRC +10420, i.e. the same region as shown in Fig. 2.22. The black spectrum in the *bottom* panel shows the old $aR(0,0)$ spectrum from the McMath Solar Telescope, as reproduced from Fig. 3 of McLaren & Betz (1980, © AAS. Reproduced with permission.).

has also been reported by Schmidt et al. (2016) for the carbon star IRC +10216, which exhibits a peak abundance of about 3×10^{-8}.

2.4.5.1. Inner radius of NH_3 distribution

The inner boundaries of the NH_3 abundance distribution are $<100\,R_\star$ for IK Tau, VY CMa, and OH 231.8+4.2. The values of $R_{\rm in}$ are chosen to reproduce the observed line ratios and depend heavily on our assumptions of the gas density and temperature profiles. The MIR profiles of IK Tau, VY CMa, and IRC +10420 appear near the terminal expansion velocities, suggesting that the MIR-absorbing NH_3 is in the outer, accelerated part of the CSEs.

None of the four targets in this study shows a significant amount of NH_3 at radii close to the stellar photosphere, where pulsation-driven shocks dominate the chemistry. Spatially-resolved images of IK Tau and IRC +10420 show NH_3-emitting clumps that are offset from the star; unresolved images of VY CMa and OH 231.8+4.2 also show slight departure of the peak emission from the stellar continuum. Furthermore, had NH_3 been produced at smaller radii where both density and temperature are very high, emission from higher-J transitions would have been much stronger than the lower ones and the inversion line profiles would have shown narrow features at the outflow or infall velocities during the time of observations. Hence, we

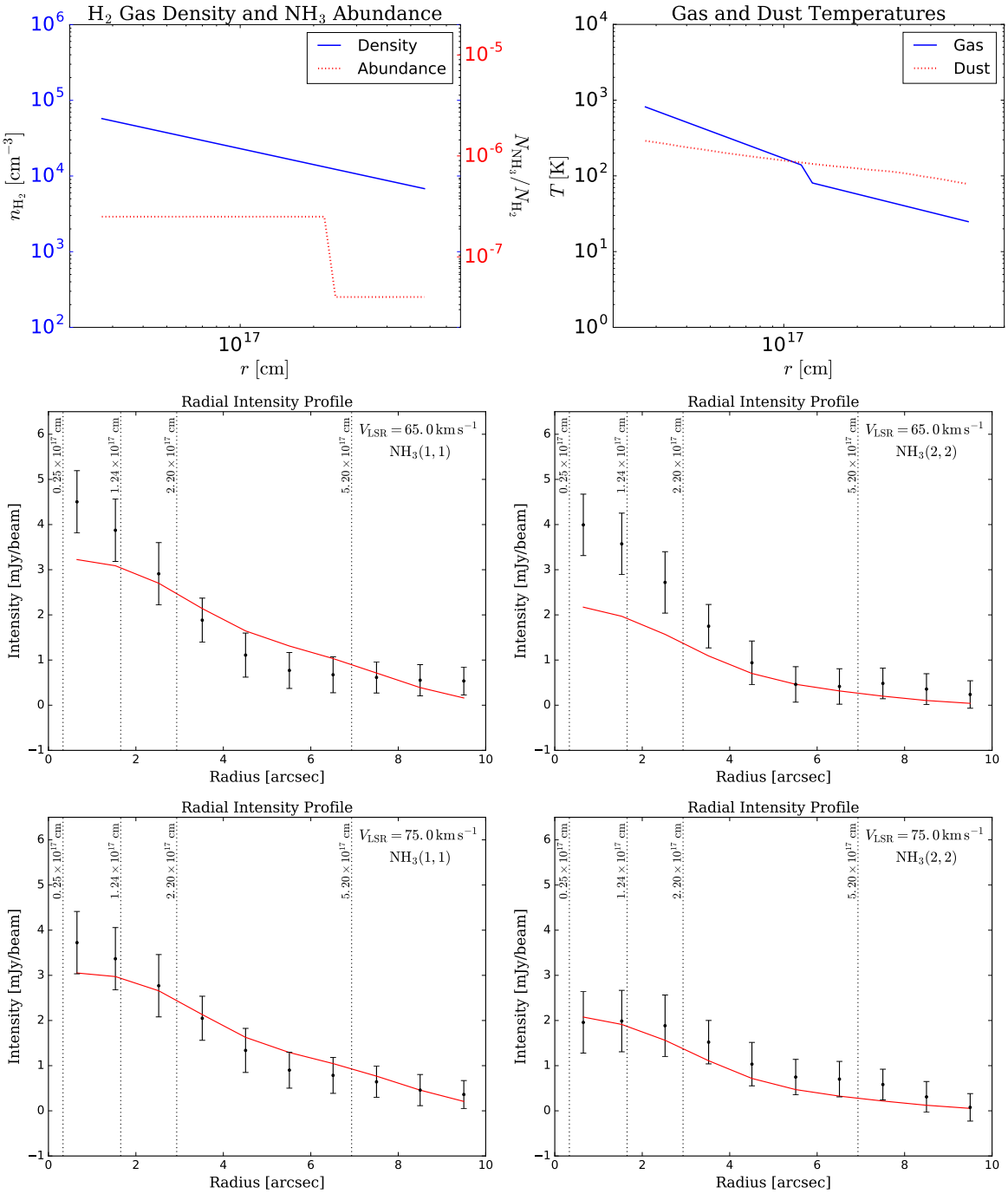

Figure 2.26.: The second model for IRC +10420 with high gas density and low NH_3 abundance. *Top left*: Input gas density and NH_3 abundance profiles. Only the radii with abundance $>10^{-10}$ are plotted. *Top right*: Input gas and dust temperature profiles. *Middle*: The radial intensity profiles of NH_3(1,1) (*left*) and NH_3(2,2) (*right*) at the velocity channel $V_{LSR} = 65\,km\,s^{-1}$, which show the strongest emission in both rotational and inversion transitions. *Bottom*: The radial intensity profiles of NH_3(1,1) (*left*) and NH_3(2,2) (*right*) at the velocity channel $V_{LSR} = 75\,km\,s^{-1}$, which is the systemic velocity of IRC +10420. In the radial intensity profiles, black points indicate the binned data points from the VLA images and red curves show the modelled profiles.

conclude that NH_3 do not form near the stellar photosphere or in the pulsation-driven shocks in our targets even thought tight constraints of R_{in} could not be determined from available data[32].

2.4.5.2. *o* Cet (Mira)

Earlier detection of NH_3 MIR absorption from O-rich AGB stars includes the Mira variables *o* Cet and, less likely, R Leo (see Table 2.2). Betz & Goldhaber (1985) reported large velocity variation in the absorption profiles observed towards *o* Cet in 1981–1982. At some epochs, NH_3 even exhibited redshifted absorption, which is indicative of infall and has never been seen in the NH_3 spectra of any other evolved stars. The NH_3 absorption up to 20% of the continuum intensity was very strong. In their unpublished spectra, the velocity of the absorption relative to the systemic could reach $\sim$30 km s^{-1} at its utmost (Betz & Goldhaber, 1985). Modern dynamic atmosphere models of Mira variables predict that such strongly-varying and high-velocity motions occur in the vicinity of the infrared photosphere ($\sim 1\,R_\star$; e.g. Ireland et al., 2008, 2011; Freytag et al., 2017). Chemical model suggests that a strong shock of velocity $\gtrsim$30 km s^{-1} at $1.0\,R_\star$ could produce a considerable amount of NH_3 (Gobrecht et al., 2016). Hence, the MIR lines detected towards *o* Cet in 1981–1982 likely came from the pulsating wind. However, NH_3 detection in *o* Cet is only sporadic. Our IRTF/TEXES observations in 2016 did not detect NH_3 absorption above $\sim$5% of the continuum intensity; the *Herschel*/HIFI observation[33] in 2010 also did not find any emission in the rotational transition $J = 1$–0. In any case, *o* Cet does not show evidence of high NH_3 abundance in the outer CSE and, therefore, it has a very different ammonia chemistry from the targets of this study. The main difference between *o* Cet and IK Tau is the mass-loss rate (and hence the gas density), which is much lower in *o* Cet than in IK Tau by a factor of $\sim$30 (Ryde & Schöier, 2001; Decin et al., 2010b). High gas density may be one of the criteria of efficient NH_3 production.

2.4.5.3. IRC +10420

IRC +10420 is a peculiar target with a known history of episodic mass loss. The NH_3 emission from this star is very far away from the centre of the CSE compared to other targets of this study. Because of the resemblance of NH_3's kinematics and radial intensity distribution to other molecules that are associated with photochemistry (e.g. SO; Willacy & Millar, 1997) or shock chemistry (e.g. SiO; Wong, 2013, Dinh-V.-Trung et al., in prep.), the formation of NH_3 in IRC +10420 is probably linked to photodissociation or shocks, or both. It is unclear whether the internal UV radiation field from the star is strong enough to dissociate N-bearing parent species in the inner envelope. The CSE of IRC +10420 is highly obscured by dust and no X-rays or UV emission was detected (De Becker et al., 2014). We note that the lack of central NH_3 emission has also been observed in CRL 2688. Dinh-V.-Trung et al. (2009a) found that NH_3 in CRL 2688 mainly traces warm molecular gas in four distinct spatial-kinematic components/lobes, which are associated with shocked gas as traced by CO and near-infrared H_2 emission; therefore, the authors suggested that the NH_3 abundance in the nebula could be enhanced by shocks.

[32] (Sub)millimetre rotational transitions within the $v_2 = 1$ state near 140 GHz and 466 GHz from would be detected in emission towards VY CMa with on-source time of $\sim$10 hours with the IRAM 30m Telescope or the APEX 12-metre telescope (Atacama Pathfinder EXperiment) if NH_3 reached a high abundance near the stellar photosphere. Given a velocity law, the predicted line profiles of these transitions are sensitive to the inner radius. However, no such observations exist to our knowledge.

[33] *Herschel* OBSID: 1342200904.

Table 2.6.: Parameters of our NH_3 models.

Target	d (pc)	$R_\star$ (AU, mas)	$T_\star$ (K)	V_{sys} ($km\,s^{-1}$)	V_{exp} ($km\,s^{-1}$)	b_{Dopp} ($km\,s^{-1}$)	R_{in} ($R_\star$)	R_e ($R_\star$, arcsec)	f_0 (n_{NH_3}/n_{H_2})
IK Tau	265[a]	1.00, 3.8[a]	2200[a]	34[b]	17.7[a]	4.0	75	600, 2.″3	6×10^{-7}
VY CMa	1140[c]	6.60, 5.8[d]	3490[d]	22[e]	35[f]	7.5	60	350, 2.″0	7×10^{-7}
OH 231.8+4.2	1540[g]	2.93, 1.9[h]	2300[i]	34[j]	—[k]	1.0	20	2100, 4″	5×10^{-7}
IRC +10420	5000[l]	1.75, 0.35[m]	8250[n]	75[p]	37[p]	1.8	955	∼20 000, 7″–8″	$\gtrsim 2.5 \times 10^{-7}$

Notes. The columns are (from *left* to *right*): target, distance (d; pc), stellar radius ($R_\star$; AU or mas), stellar temperature ($T_\star$; K), systemic velocity in LSR (V_{sys}; $km\,s^{-1}$), terminal expansion velocity (V_{exp}; $km\,s^{-1}$), Doppler-b parameter (b_{Dopp}; $km\,s^{-1}$), inner radius of NH_3 distribution (R_{in}; $R_\star$), e-folding radius of NH_3 (R_e; $R_\star$ or arcsec), and the peak NH_3 abundance (f_0; relative to H_2).
[a] Decin et al. (2010b). [b] Velilla Prieto et al. (2017). [c] Choi et al. (2008). [d] Wittkowski et al. (2012). [e] Alcolea et al. (2013). [f] Decin et al. (2006). [g] Choi et al. (2012). [h] From Stefan–Boltzmann law (Sect. 2.4.3). [i] Sánchez Contreras et al. (2002). [j] Sánchez Contreras et al. (2015); Velilla Prieto et al. (2015). [k] Equation (2.13). [l] Jones et al. (1993). [m] Oudmaijer & de Wit (2013). [n] Shenoy et al. (2016). [p] Castro-Carrizo et al. (2007).

2.5. Speculated origins of circumstellar ammonia

Several explanations have been proposed in the literature to account for the extraordinarily high abundance of circumstellar ammonia. In the following parts, we will discuss these suggestions in the context of our modelling results.

2.5.1. Pulsation-driven shocks

Our modelling shows that NH_3 emission probably arises from denser and more turbulent gas than the ambient medium. We find that the turbulence parameters of the NH_3-emitting gas in IK Tau and VY CMa have to be significantly higher than the typical values in the bulk of the circumstellar gas so as to fit the broad emission wings in the rotational transitions; our model of OH 231.8+4.2 suggests that a density enhancement of about three to four times is required to fit the spectral lines (Sect. 2.4.3.3); the strongest NH_3 emission of VY CMa and OH 231.8+4.2 comes from localised spatial-kinematic features that could be associated with molecules such as SO and SO_2 (Sects. 2.4.2.1, 2.4.2.2, and 2.4.3.1). We note that the abundance of sulphur oxides is yet another mystery in circumstellar chemistry of O-rich stars (e.g. Yamamura et al., 1999b; Fu et al., 2012; Adande et al., 2013; Danilovich et al., 2016; Velilla Prieto et al., 2017). Our results may be indicative of some violent processes, such as shocks, in the formation of NH_3. A similar interpretation has also been suggested to explain the high abundance and clump distributions of NH_3 observed towards the carbon-rich PPNe CRL 2688 (Egg Nebula) and CRL 618 (Martin-Pintado & Bachiller, 1992a; Martin-Pintado et al., 1993, 1995; Truong-Bach et al., 1996; Dinh-V.-Trung et al., 2009a).

Shocks in the inner wind may be strong enough to dissociate molecular N_2, thereby releasing free N atoms to form NH_3. However, theoretical models including shock-induced chemistry within the dust condensation zone have failed to produce a significantly higher NH_3 abundance than yielding from equilibrium chemistry. The chemical model for carbon-rich AGB stars by Willacy & Cherchneff (1998) showed that even strong shocks of the velocity as high as $20\,\mathrm{km\,s^{-1}}$ would not be able to enhance the NH_3 abundance by even an order of magnitude. Similar models for oxygen-rich stars found that NH_3 can only be produced at an abundance of $\sim 10^{-10}$–10^{-9} under shock-induced chemistry (Duari et al., 1999; Gobrecht et al., 2016).

In particular, Gobrecht et al. (2016) found that NH_3 may form at an abundance $\sim 10^{-9}$ *only if* the shock radius is very close to the star and the shock velocity is very high ($r_{\mathrm{shock}} = 1\,R_\star$ and $V_{\mathrm{shock}} = 32\,\mathrm{km\,s^{-1}}$ in their adopted model). Shocks occurring at an outer radius or at a lower velocity would result in lower post-shock gas densities, under which the formation of other N-bearing molecules, such as HCN and PN, are favoured over NH_3 (Gobrecht 2017, priv. comm.).

Even if NH_3 is produced at a moderate abundance in the shocked regions, its abundance drops rapidly at radii outside of the shock because this molecule is then converted to other N-bearing species, such as HCN and NO (Duari et al., 1999; Gobrecht et al., 2016, Gobrecht 2017, priv. comm.). These inner-wind NH_3 molecules do not contribute to the strong NH_3 emission or absorption as reported in the observations summarised in Sect. 2.1.2.

While circumstellar shocks may play a role in producing the excess amount of NH_3, the formation mechanism of the molecule in such a scenario is still unknown. In particular, shocks cannot explain the source of free nitrogen atoms. The bond dissociation energy of N_2 exceeds 110 000 K and is much higher than that of NH_3 (by about 60 000 K; Darwent, 1970) because of the N≡N triple bond. Strong shocks are likely to be present near the stellar photosphere, but our observations and chemical models do not find much NH_3 in those radii. In addition, the non-detection of emission in the non-metastable ($J > K$) inversion transitions or rotational

transitions within the vibrationally excited state from IK Tau argues against the presence of very dense and hot NH_3-emitting gas in the CSE, which would be expected if NH_3 forms in shocked gas right after collisional dissociation of the parent species N_2.

2.5.2. Deep ultraviolet photodissociation

Ultraviolet (UV) photons from the interstellar radiation field usually only affects the outer CSE. The inner part of the CSE (radii just beyond the dust formation zone) is shielded from dissociative photons by dust and molecules at outer radii if the CSE is uniform. The main shielding species include molecules/atoms that are the most abundant in the CSEs, such as H_2, H, CO, and N_2 (Li et al., 2013). Recent calculations by Li et al. (2016) have shown that self-shielding of N_2 may shift its photodissociation region by about seven times further, to $r{\sim}10^{17}$ cm in O-rich CSEs, corresponding to a few thousand stellar radii.

It has been suggested that a clumpy CSE may allow deep penetration of UV radiation into the inner radii ($<10^{14}$ cm) (Decin et al., 2010a), which would then trigger photochemistry that would have only occurred in the outer envelopes. Clumpiness has been observed in AGB stellar winds (e.g. Castro-Carrizo et al., 2010). Assuming that one-fourth of the solid angle of the incoming UV flux was unattenuated, Agúndez et al. (2010) predicted a high peak NH_3 abundance of nearly 10^{-7} in an O-rich star with the mass-loss rate of IK Tau ($\sim10^{-5}\ M_\odot\ \mathrm{yr}^{-1}$). This abundance is only a few times lower than our derived value. Their photochemical model for C-rich star is also consistent with the recently refined value of the observed NH_3 abundance in IRC +10216 (Schmidt et al., 2016).

On the other hand, deep UV photodissociation also leads to the rapid formation of carbon-bearing molecules like methane (CH_4) by dissociating CO molecules and producing free carbon atoms, which in turn leads to the formation of excess methanol (CH_3OH) and ethynyl radical (C_2H) (Charnley et al., 1995). However, C_2H and CH_3OH have never been detected towards 'typical' O-rich AGB stars[34] like IK Tau (e.g. Latter & Charnley, 1996a,b; Charnley & Latter, 1997; Marvel, 2005; Gómez et al., 2014).

2.5.3. Enhanced nitrogen production

Besides NH_3, other N-bearing molecules have also been detected in O-rich objects, where HCN has the brightest emission among these molecules (Deguchi & Goldsmith, 1985; Deguchi et al., 1986; Nercessian et al., 1989). Other rarer N-bearing molecules include NO, CN, NS, PN and are detected from three of the targets in this study: OH 231.8+4.2 (Velilla Prieto et al., 2015; Sánchez Contreras et al., 2015), IRC +10420 (Quintana-Lacaci et al., 2013, 2016), and IK Tau (Velilla Prieto et al., 2017). These results suggest nitrogen-rich circumstellar chemistry in these targets and Sánchez Contreras et al. (2015); Quintana-Lacaci et al. (2016) speculated that enhanced ^{14}N production by stellar nucleosynthesis may occur in some evolved stars.

For intermediate-mass AGB stars between 4 and 8 solar masses, nitrogen enrichment could happen due to hot bottom burning (HBB), a process which converts carbon into nitrogen at the base of the convective envelope (e.g. Karakas & Lattanzio, 2014). HBB enhances the surface nitrogen abundance at the end of the AGB evolution by up to an order of magnitude (Karakas & Lattanzio, 2014; Ventura et al., 2017).

[34] Recently, CH_3OH has been detected towards two evolved stars and one evolved star candidate. These objects include the post-AGB object HD 101584 (Olofsson et al., 2017), the YHG IRC +10420 (only at marginal S/N ratios; Quintana-Lacaci et al., 2016), and the peculiar object IRAS 19312+1950 (Nakashima et al., 2015), which is located in a complex region that contains dense interstellar gas (see also Nakashima et al., 2016; Cordiner et al., 2016).

In massive stars ($M \gtrsim 8\,M_{\odot}$), nitrogen is primarily produced in the CN branch of the CNO cycles (Henry et al., 2000). Mixing of the CN-cycled gas may increase the surface ^{14}N abundance of supergiants, but only by a factor of a few (<10) (Venn, 1995; Lyubimkov et al., 2011). Optical spectroscopy of one of our targets, IRC +10420, also found a similar enrichment factor of nitrogen (Klochkova et al., 1997).

The factor of nitrogen enrichment due to nucleosynthesis is too small to account for the abundances of N-bearing molecules in our targets. Circumstellar chemical models that assume a high ^{14}N-enrichment factor of 40 in OH 231.8+4.2 do not seem to reproduce the observed abundances of N-bearing molecules (Velilla Prieto et al., 2015; Sánchez Contreras et al., 2015). Also, nitrogen in IRC +10420 has to be enriched by at least 20 times compared to the solar abundance in order to explain the observed NO emission (Quintana-Lacaci et al., 2013). On the other hand, there is no indication of nitrogen-rich chemistry in the CSE of VY CMa from the line surveys of Tenenbaum et al. (2010a) and Kamiński et al. (2013), yet this supergiant shows the brightest NH_3 rotational emission among our targets. Furthermore, the low-mass AGB star IK Tau is not expected to be enriched in elemental nitrogen abundance through HBB process or CNO cycles, but it shows signs of N-rich chemistry by exhibiting NS, NO, and PN emission (Velilla Prieto et al., 2017).

Our observations do not find significant production of NH_3 near the stellar photosphere, which suggests that most nitrogen nuclei are locked in other N-bearing species (predominately N_2). Even if the elemental nitrogen abundance is enriched, some other processes (which are yet to be unidentified) still have to take place to convert N_2 into NH_3. Thus, we conclude that the contributions of nitrogen enrichment (if any) to the observed high NH_3 abundance are insignificant.

CHAPTER 3

The ALMA view of the extended atmosphere and inner wind of Mira

This chapter is adapted from the published paper of Wong, K. T., Kamiński, T., Menten, K.M., and Wyrowski, F. 2016, A&A 590, A127.
DOI: 10.1051/0004-6361/201527867 [arXiv:1603.03371]

Brief summary

Before the era of the Atacama Large Millimeter/submillimeter Array (ALMA), the extended atmosphere of AGB stars has only been studied by spatially unresolved absorption spectroscopy, imaging of maser emission, and mid-infrared interferometry. High-angular resolution, high-spectral resolution, and sensitive observations with ALMA offer a new tool to study the extended atmosphere and inner wind of nearby AGB stars in unprecedented detail.

The archetypal Mira variable, *o* Cet, was observed as one of the five Science Verification targets in the 2014 ALMA Long Baseline Campaign. The array with the longest projected baseline of 15 km produces images that clearly resolved the stellar continuum and molecular line absorption/emission of SiO and H_2O. At the frequency of 220 GHz (wavelength of 1.36 mm), the angular resolution of the images is about 30 mas. For the first time, molecular line absorption against the background stellar continuum at the millimetre-wavelength has been clearly imaged.

In order to derive the physical conditions, molecular abundances, and gas kinematics of the extended atmosphere of *o* Cet, radiative transfer models are constructed to reproduce the absorption and emission profiles of the SiO and H_2O lines near 215–230 GHz. The derived gas density, temperature, and velocity profiles are also compared to the predictions from hydrodynamical models.

3.1. Introduction

3.1.1. Mira Ceti

Mira A (*o* Ceti; Mira) is an oxygen-rich, long-period variable star on the asymptotic giant branch (AGB). Mira A is the archetype of Mira variables. Its period of visual brightness variation is about 332 days and the visual V-band magnitude of the star varies by up to about 8.1 mag (a factor of > 1700) in each cycle (based on the data in the AAVSO[1] International Database). The large variation in the visual magnitude is caused by a combined effect of stellar pulsation and variable opacity of metal oxides whose abundance changes with the effective

[1] American Association of Variable Star Observers.

temperature of the star (Reid & Goldston, 2002). Mira A has a companion, Mira B (also VZ Ceti), which is possibly a white dwarf (Sokoloski & Bildsten, 2010). The two stars form a symbiotic binary system Mira AB. The distance of the Mira AB system was estimated to be 110±9 pc (Haniff et al., 1995), which is based on the period-luminosity relation derived by Feast et al. (1989), the infrared K-band magnitude from Robertson & Feast (1981), and the period of the visual V variation from the GCVS (Kholopov, 1987). Throughout the chapter we adopt this value, which is roughly consistent with the revised Hipparcos value of 92 ± 10 pc (van Leeuwen, 2007).

3.1.2. Previous observations of the extended atmosphere

Traditionally, AGB star atmospheres have been probed by molecular absorption spectroscopy, which delivers spatially unresolved line-of-sight information. Examples include the detection of the near-infrared H_2O absorption band from the warm molecular forming layer (known as the MOLsphere) around M giant stars and Mira variables with the Infrared Space Observatory (ISO) (e.g. Tsuji et al., 1997; Woitke et al., 1999; Tsuji, 2000). In addition, near- and mid-infrared interferometry with the Very Large Telescope Interferometer (VLTI) can also probe the molecular layers and dust shells around these stars (e.g. Ohnaka et al., 2005; Karovicova et al., 2011). High-fidelity aperture-synthesis image reconstruction with infrared interferometry has been a challenging task due to the sparseness of the baseline coverage (e.g. Monnier et al., 2014; Sanchez-Bermudez et al., 2016; Baron, 2016, and references therein) and only becomes possible recently (e.g. Hofmann et al., 2014; Weigelt et al., 2016; Ohnaka et al., 2017). Maser emission from SiO and/or H_2O in the extended atmospheres of Mira variables has also been imaged. Examples of maser imaging studies can be found in Cotton et al. (2004) and Perrin et al. (2015) with the Very Long Baseline Array (VLBA), and Reid & Menten (2007) with the Very Large Array (VLA).

3.1.3. Motivation of ALMA observations

In order to test the predictions of existing hydrodynamical models for the extended atmospheres of Mira variables, which typically has a radius of only a few $R_\star$ (a few tens of milliarcseconds for Mira A), high-angular resolution and high-spectral resolution observations of the molecular emission and absorption from these regions are mandatory. The Atacama Large Millimeter/submillimeter Array (ALMA) with long baselines thus allows us to reach the required angular resolution at high sensitivity and to study the detailed kinematics of the innermost envelope of Mira A. Observations of radio and (sub)millimetre wavelength molecular line emission/absorption, particularly in the rotational transitions not exhibiting strong masers, can be used to compare and test the predicted structures of the extended atmospheres by hydrodynamical models. Through modelling the radiative transfer of the transition lines with the predicted atmospheric structures used as the inputs, synthesised spectra can be produced and compared to the observed ones.

In this chapter, we present the new ALMA observations of the Mira AB system, which was selected as one of the Science Verification (SV) targets in the 2014 ALMA Long Baseline Campaign to demonstrate the high angular resolution capability of ALMA (ALMA Partnership et al., 2015b). Based on the visual magnitude data in the AAVSO International Database, the stellar phase of Mira A was about 0.45 at the time of this campaign, and we adopt this phase throughout the chapter. In Sect. 3.2, we describe the SV observation of Mira AB and the data processing. In Sect. 3.3, we present the results including the radio continuum data of Mira A and B in the SV dataset, and the images and spectra of the SiO and H_2O lines from Mira A as covered in the observations. In Sect. 3.4, we present our radiative transfer modelling results of

the SiO and H_2O spectra of Mira A. In Sect. 3.5, we discuss the implications of our modelling results for our understanding of Mira A's extended atmosphere, including the structures, dust condensation process, shock dissipation, and the kinematics and compare these values with predictions from hydrodynamical models.

3.2. Observations and data processing

The Mira AB system was observed with ALMA[2] on 2014 October 17 and 25 (ALMA Band 3) and on 2014 October 29 and November 1 (ALMA Band 6) as part of the 2014 ALMA Long Baseline Campaign (LBC) Science Verification (SV) with the longest projected baseline of 15.24 km.

3.2.1. Atacama Large Millimeter/submillimeter Array (ALMA)

General References: Wootten & Thompson (2009); ALMA Partnership et al. (2015b, 2017).

ALMA is a (sub)millimetre interferometer on the Chajnantor plateau in the Atacama Desert of northern Chile. ALMA consists of 66 high-precision antennae: 50 antennae of 12-m diameter in the 12-m (main) Array, 12 antennae of 7-m diameter in the 7-m Array, and 4 12-m antenna in the Total-Power Array. Ultimately, ALMA will be able to cover the frequency range of 31–950 GHz in 10 frequency bands. The antennae can be arranged into 10 configurations, yielding projected baselines ranging from about 15 m to 16 km. One of the primary objectives of ALMA is to produce images with angular resolutions of ~0.″01 with its longest baselines; therefore the 2014 ALMA LBC was conducted in order to test ALMA's capability of long-baseline observations.

3.2.2. The 2014 ALMA Long Baseline Campaign

General References: Wootten & Thompson (2009); ALMA Partnership et al. (2015b).

The 2014 ALMA LBC took place between September and November in 2014. Five SV targets were selected for scientific observations to produce high-fidelity, high-resolution images of the continuum and spectral line emission. One of the SV targets is the famous protoplanetary disc HL Tau which produced revolutionary[3,4] images showing previously unseen substructures in the protoplanetary disc (see Fig. 3.1 and ALMA Partnership et al., 2015a).

3.2.3. Observations of Mira AB

The Mira AB system was the only evolved-star target in the 2014 LBC. By referring to the AAVSO visual data for Mira, we find that the ALMA observations took place between the visual phases 0.42 (2014 Oct 17) and 0.47 (2014 Nov 01)[5].

[2] The Atacama Large Millimeter/submillimeter Array.

[3] http://www.almaobservatory.org/en/press-release/revolutionary-alma-image-reveals-planetary-genesis/.

[4] http://www.eso.org/public/news/eso1436/.

[5] The period of Mira changes by a few days on a time span of decades (Templeton & Karovska, 2009) and the dates of maximum need to be determined observationally for each cycle to provide a reliable phase scaling. In recent cycles, however, the phases preceding and during the maxima cannot be observed in the optical because Mira is too close to the Sun. To obtain the phases of the ALMA observations in 2014, we first phased the AAVSO data for the cycles in 2000–2013 with a period of 333 days and the date of maximum on JD 2 452 161.0, which had a bright and very well-defined maximum (Kamiński et al., 2016). The data covering the cycle of the 2014 ALMA observations were then phased with the same period but their date of maximum (or phase 0) was determined by a phase shift of about +0.05 with respect to JD 2 452 161.0 (as adopted for the 2000–2013 cycles). In this way we are able to match the data in the 2014 cycle with the phased data from

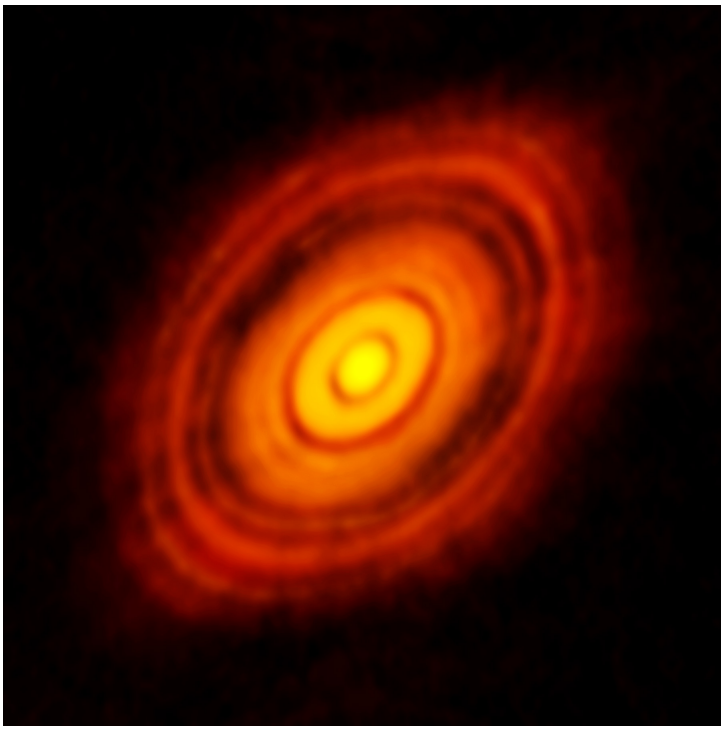

Figure 3.1.: The ALMA image of the protoplanetary disc surrounding the young star HL Tau – as observed during the 2014 ALMA Long Baseline Campaign – which shows substructures of the disc at an unprecedented detail. Credit: ALMA (ESO/NAOJ/NRAO).

The long-baseline observations of Mira were conducted in two frequency bands of ALMA near the wavelengths of 3 mm (Band 3) and 1.3 mm (Band 6). In ALMA Band 3, three continuum windows at 88.2, 98.2, and 100.2 GHz were observed, in addition to four spectral line windows of 58.6 MHz bandwidth around the transitions of ^{28}SiO $v = 0, 1, 2$ $J = 2$–1 and ^{29}SiO $v = 0$ $J = 2$–1. The channel width of the spectral windows is 61.0 kHz (~0.21 km s^{-1}). In Band 6, a continuum window at 229.6 GHz together with six spectral line windows of 117.2 MHz bandwidth around ^{28}SiO $v = 0, 1, 2$ $J = 5$–4, ^{29}SiO $v = 0$ $J = 5$–4, H_2O $v_2 = 1$ $J_{K_a,K_c} = 5_{5,0}$–$6_{4,3}$, and the H30α recombination line were observed. The channel width of the four SiO windows is 122.1 kHz (~0.17 km s^{-1}) and that of the H_2O and H recombination line windows is 61.0 kHz (~0.08 km s^{-1}). Table 3.1 summarises the observed spectral lines in Band 6 and their parameters.

Figure 3.2 shows the array configuration of ALMA during the LBC observations. The shortest baselines (and the maximum number of antennae) in the observations of Band 3 ($\lambda \sim 3$ mm) and Band 6 (~1 mm) are 29.07 m (38) and 15.23 m (39), respectively. The maximum recoverable scales[6] of the SiO lines in Bands 3 and 6 are therefore ~14.″8 and ~11.″3, respectively, and that of the H_2O $v_2 = 1$ line in Band 6 is 10.″5.

3.2.4. Data calibration

The data from SV observations were calibrated by staff members of the Joint ALMA Observatory (JAO) and the ALMA Regional Centres (ARCs), with the CASA software package version 4.2.2. Detailed calibration scripts, preliminarily calibrated data products prior to self-

2000–2013 and therefore we obtain slightly later phases for the ALMA observations than those calculated from a periodicity scale given by AAVSO and used in Matthews et al. (2015).

[6] Defined to be 0.6 × (wavelength/shortest baseline) (ALMA Partnership et al., 2017).

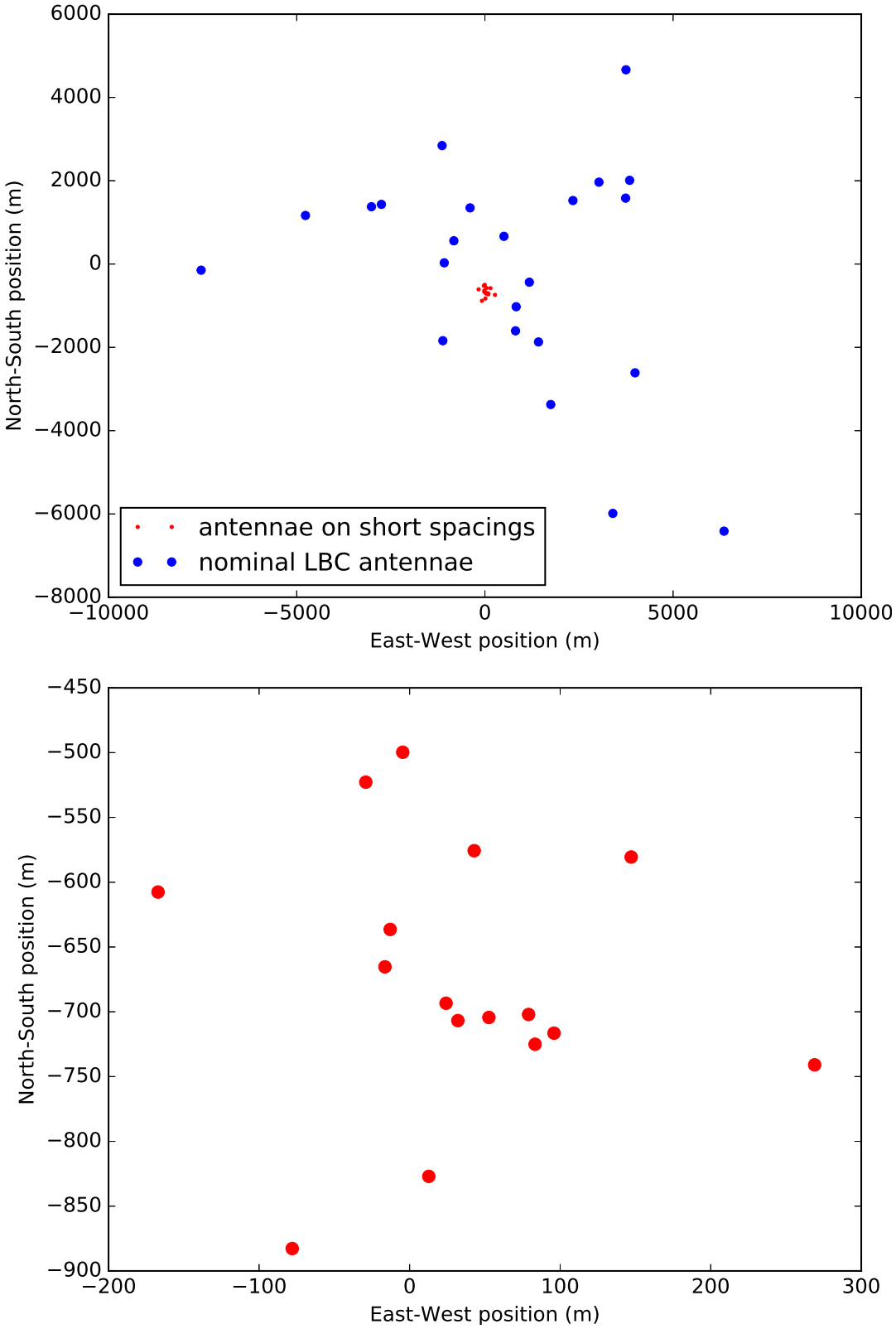

Figure 3.2.: Array configuration of ALMA during the observations of Mira in the 2014 LBC. *Upper*: Blue dots represents the positions (antenna stations) of the nominal LBC array relative to the array centre and red dots represents the additional antennae on short spacings. *Lower*: The zoomed plot showing only the antennae on short spacings. These additional antennae allow us to recover the emission from smooth structures on large spatial scales.

Table 3.1.: Observed spectral lines in ALMA Band 6.

Species	Spectral Line	Rest Frequency GHz	E_{up}/k K	ΔV km s^{-1}
SiO	$v = 0, J = 5$–4	217.104919	31.26	0.169
SiO	$v = 1, J = 5$–4	215.596018	1800.17	0.170
SiO	$v = 2, J = 5$–4	214.088575	3551.97	0.169
^{29}SiO	$v = 0, J = 5$–4	214.385752	30.87	0.171
H_2O	$v_2 = 1, J_{K_a,K_c} = 5_{5,0}$–$6_{4,3}$	232.68670	3461.88	0.079

Notes. Columns are, from left to right, molecule, quantum numbers of observed transition, rest frequency, energy level of the upper state, and channel width in velocity of the raw data. The SiO and ^{29}SiO transition frequencies were taken form the Cologne Database for Molecular Spectroscopy (CDMS). They are based on laboratory data presented by Müller et al. (2013) and have an accuracy of about 1 kHz, except for the SiO $v = 0, J = 5$–4 transition which has an accuracy of 2 kHz. The H_2O transition frequency is taken from Belov et al. (1987) and has an accuracy of 50 kHz.

calibration, and the self-calibration solutions for both continuum and spectral line data are available at the ALMA Science Portal[7].

The solutions for self-calibration were derived from the continuum data for the continuum data itself and from the strongest spectral channels of the ^{28}SiO $v = 1$ data – which exhibits strong maser emission – for all the spectral line data. We downloaded the self-calibration solutions from the ALMA Science Portal and applied them to the preliminarily calibrated data, and then imaged the continuum and spectral line data. We used CASA version 4.2.2 for the self-calibration and imaging (except for the image binning task as mentioned below), and the Miriad package (Sault et al., 1995) for our continuum analysis in Sects. 3.3.1.

3.2.5. Continuum positions of Mira A

By fitting the image produced from the visibility data before self-calibration, we are able to determine the absolute position of the continuum emission from Mira A. The fitted centre of Mira A's continuum is determined to be at (RA, Dec) = ($02^h19^m20\overset{s}{.}795, -02°58'43\overset{''}{.}05$) = ($34\overset{s}{.}836\,646, -2\overset{''}{.}978\,625$) near 229.6 GHz. The position and proper motion of Mira A in the Hipparcos Catalogue are ($34\overset{s}{.}836\,611, -2\overset{''}{.}977\,061$) at the Julian epoch 1991.25 and ($9.33 \pm 1.99, -237.36 \pm 1.58$) mas yr^{-1}, respectively (van Leeuwen, 2007). At the epoch of the ALMA SV observations, ~2014.83 (JD 2 456 959.6 and JD 2 456 962.7), the expected coordinates of Mira A due to proper motion should be ($34\overset{s}{.}836\,667, -2\overset{''}{.}978\,615$) ± ($0\overset{s}{.}000\,013, 0\overset{''}{.}000\,010$). Hence, the observed absolute position of Mira A is within 2σ of the predicted position of the Hipparcos Catalogue.

3.2.6. Continuum subtraction

We then produced two sets of spectral line images, with and without subtraction of the continuum. The continuum was subtracted with the `uvcontsub` task in CASA by fitting a linear polynomial to the real and imaginary parts of the visibility data of the line-free (i.e. continuum-only) channels in each spectral window. Our selection of the line-free channels was slightly different from that in the example imaging script provided along with the SV data[8].

[7] http://www.almascience.org/almadata/sciver/MiraBand6/

[8] available from the CASA Guides: https://casaguides.nrao.edu/index.php?title=ALMA2014_LBC_SVDATA&oldid=18077

3.2.7. Image reconstruction

The spectral line image data cubes of the SiO and H_2O lines in ALMA Band 6 were created by the image deconvolution task `clean` in CASA. The task performs an inverse Fourier transform to the visibility data (*uv*-data) and creates a raw image data cube (the DIRTY image), then deconvolves the ALMA point-spread function from each frequency plane of the image with the Clark image deconvolution algorithm (Högbom, 1974; Clark, 1980) (the CLEAN process). The product of image deconvolution for each frequency is a set of point sources (the CLEAN component models) which, in aggregate, reproduce the same input DIRTY image when convolving with the array's point-spread function. The task finally restores the CLEAN component models with a restoring beam (the CLEAN beam) of parameters either determined from fitting the point-spread function (taking its FWHM) or specified by the user. The local standard of rest (LSR) velocities covered by the image cubes range from 26.7 km s^{-1} to 66.7 km s^{-1}, centred at the systemic (centre of mass) LSR velocity of $V_{\rm LSR}$ = 46.7 km s^{-1}, which corresponds to 57.0 km s^{-1} in the heliocentric rest frame. We determined the systemic velocity from the mid-point of the total velocity ranges of the entire line-emitting/absorbing region, assuming that the global infall or expansion motions at the extreme velocities are symmetric about the stellar systemic velocity. We weighted the visibilities with a robust (Briggs) parameter of $\mathcal{R}_{\rm Briggs}$ = 0.5 and CLEANed the images down to a threshold of ~2–3 mJy beam^{-1}, which is about 1.5 times the rms noise level. We restored the images with a circular beam of FWHM 0.″032 for the ^{28}SiO and ^{29}SiO lines, and of FWHM 0.″030 for the H_2O v_2 = 1 line. The FWHM of the beams are the geometric means of the major- and minor-axes of the elliptical point-spread functions fitted by the `clean` task.

3.2.8. Primary beam

At 220 GHz, the primary beam FWHM of the 12m array is about 28″, which is much larger than the size of the line emission/absorption, and therefore no primary beam correction is needed. Figure 3.3 is the only primary beam-corrected image in this chapter, which shows remote emission in the vibrational ground state ^{28}SiO up to a distance of ~3″. There is no significant difference in the flux of detectable emission from the image without primary beam correction.

3.2.9. Channel maps

The spectral line channel maps presented in Sect. 3.3.2 and Appendix E are further binned with the image binning task `imrebin` (new from version 4.3.0) in CASA version 4.4.0. We use Python to generate plots with the aid of the `matplotlib` plotting library (version 1.4.3) (Hunter, 2007), the PyFITS module (version 3.3), and the Kapteyn Package[9] (version 2.3) (Terlouw & Vogelaar, 2015).

The cell size and total size of the images are 0.″005 × 0.″005 and 15″ × 15″, respectively. Figure 3.3 shows the map of the SiO v = 0 J = 5–4 line at the systemic velocity channel over a 7.″5 × 7.″5 region centred at Mira A. As shown in this figure, there is remote, arc-like emission extending up to about 3 arcsec from the star between the LSR velocities of 43.7 km s^{-1} and 49.7 km s^{-1}.

Moreover, we use the images without continuum subtraction for our spectral line modelling (Sect. 3.3.3 and later), instead of the continuum-subtracted images as in the reference images in the ALMA Science Portal. As a result, our images only contain emission from spectral line and/or the radio continuum from Mira A and B throughout without any real negative signals.

[9] http://www.astro.rug.nl/software/kapteyn/

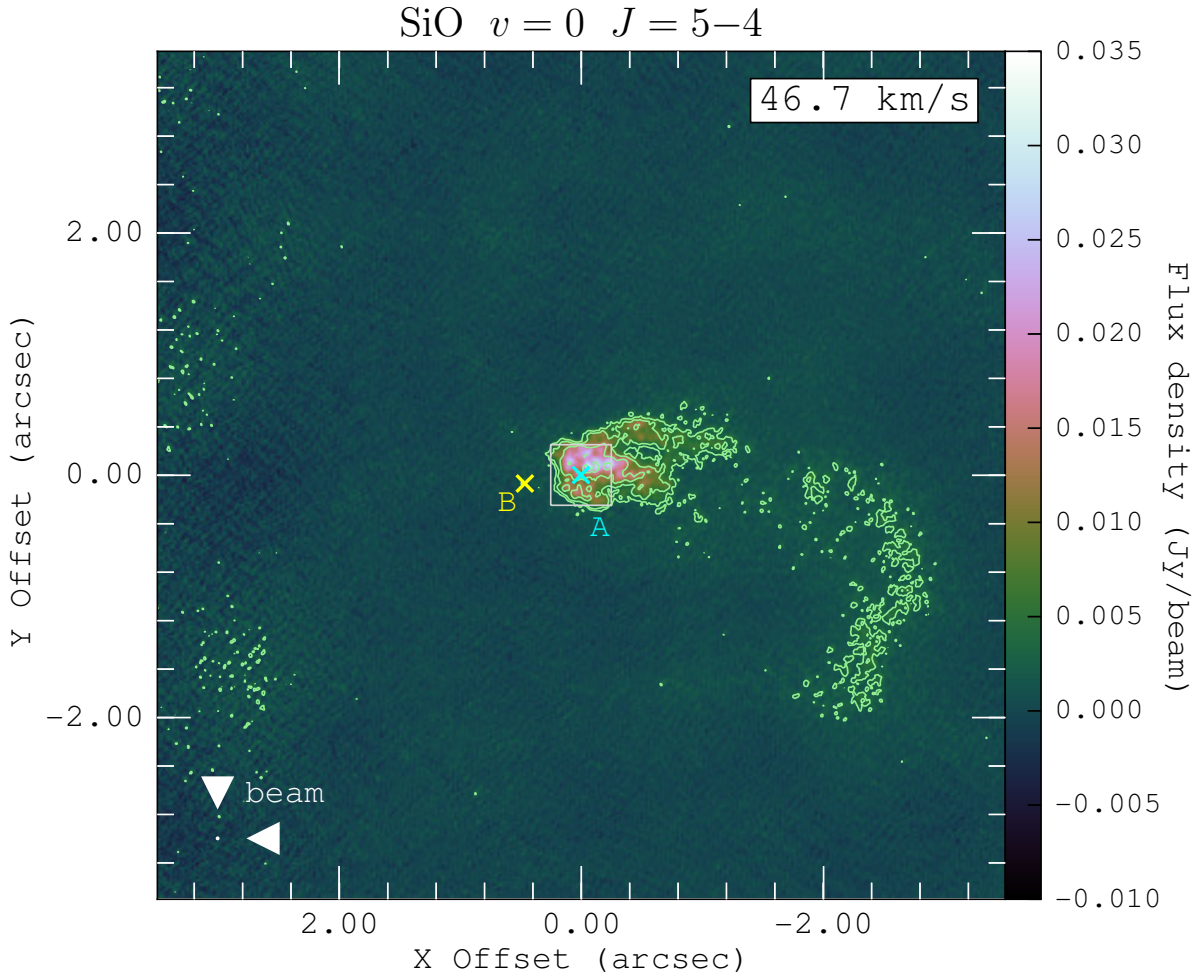

Figure 3.3.: Map of SiO $v = 0$ $J = 5$–4 (with the continuum) at the channel of the systemic velocity (46.7 km s^{-1}) with a channel width of 1.0 km s^{-1}. The positions of Mira A (o Ceti; cyan cross) and Mira B (VZ Ceti; yellow cross) are indicated in the image. The horizontal and vertical axes are the relative offsets (arcsec) in the directions of right ascension (X) and declination (Y), respectively, with respect to the continuum centre of Mira A. The white box centred at the fitted position of Mira A indicates the 0.″50 × 0.″50 region as shown in Fig. 3.14, within which we extract the SiO and H_2O line spectra from an array of positions. The horizontal and vertical axes are the relative offsets (arcsec) with respect to the Mira A in right ascension and declination, respectively. The light green contours represent 4, 8, 16, and 32σ of the SiO emission from the gas near Mira A, where the map rms noise is σ = 0.80 mJy beam^{-1}. The circular restoring beam of 0.″032 FWHM for the SiO image is indicated in white in the bottom left corner.

As we will explain in further detail in Appendix D, we find spurious 'bumps' in the absorption profiles of continuum-subtracted spectra. We believe that the image deconvolution of the strong line emission surrounding Mira's radio photosphere may have impaired the deconvolution of the region showing line absorption against the background continuum. The images (and hence the spectra) deconvolved without continuum subtracted should better represent the real emission and absorption of the SiO and H_2O lines.

3.3. Results

3.3.1. Continuum analysis

3.3.1.1. Previous results

Prior to our study, Matthews et al. (2015) and Vlemmings et al. (2015) have independently analysed the continuum data of the Mira AB system in both ALMA Bands 3 (96 GHz) and 6 (229 GHz) of this SV dataset. In addition to the long-baseline ALMA data, Matthews et al. (2015) also included the continuum data from their radio Q-band (46 GHz) observations with the Karl G. Jansky Very Large Array (VLA) in 2014; Vlemmings et al. (2015) also include the continuum data from the ALMA Band 7 (338 GHz) observations of Ramstedt et al. (2014).

By fitting the visibility data in this SV dataset, both Matthews et al. (2015) and Vlemmings et al. (2015) found that the continuum of Mira A in Band 6 can be better fitted with a two-component model consisting of (1) an elliptical uniform disc plus (2) an additional Gaussian component than with a single-component model. However, the quantitative results from both groups of authors differ significantly.

The size and flux density of the elliptical disc component fitted by Matthews et al. (2015) are 52.2 mas×40.7 mas ($d \equiv \sqrt{\theta_{\rm maj}\theta_{\rm min}} = 7.6\times10^{13}$ cm) and $S_{229.6\,\rm GHz} = 92\pm30$ mJy, respectively, and those of the additional Gaussian component are 26.0 mas × 23.9 mas ($d = 4.1\times10^{13}$ cm) and $S_{229.6\,\rm GHz} = 59$ mJy, respectively.

In the continuum analysis of Vlemmings et al. (2015), the fitted elliptical disc component has a size of ~43.4 mas × 38.5 mas ($d = 6.7\times10^{13}$ cm) and a flux density of $S_{229.6\,\rm GHz} = 139\pm0.2$ mJy. However, they found a much more compact size for the additional Gaussian component. The additional component – assumed to be circular – has $d = 4.7$ mas (0.8×10^{13} cm) in FWHM and $S_{229.6\,\rm GHz} = 9.6\pm0.1$ mJy. At 229.6 GHz, the brightness temperature of the 4.7-mas Gaussian component is approximately 10 000 K (Vlemmings et al., 2015), which is much higher than that of the uniform elliptical disc component of Mira A. Vlemmings et al. (2015) therefore argue the existence of a hotspot, or a cluster of unresolved spots, and speculate that its origin may be connected to the stellar magnetic activity of Mira A.

3.3.1.2. Single-component models

We conducted a similar analysis of the Band 6 continuum SV data of Mira A and B as the above authors. In our first models, we only fit the visibility data with a single model component for Mira A, i.e. an elliptical uniform disc or an elliptical Gaussian, but not both. Table 3.2 shows the results of our single-component fitting in the continuum window centred at 229.6 GHz. The brightness temperature of the uniform disc model of Mira A is found to be 2611 ± 51 K.

3.3.1.3. Detailed continuum analysis of Mira A and B

Besides the single-component fitting of Mira A and B, we repeated the continuum analyses of Matthews et al. and Vlemmings et al. in order to verify the presence of the compact hotspot on the surface of Mira A by introducing an additional Gaussian component to Mira A.

In addition to the data in the 229.6-GHz continuum spectral windows (`spw` = 0, 7) of this

Table 3.2.: Photospheric parameters from fitting the continuum visibility data, using the `uvfit` task in the Miriad software, of Mira A and B in the continuum window at 229.6 GHz of ALMA Band 6.

Object	$S_{229.6\,\mathrm{GHz}}$ (mJy)	θ_{maj} (mas)	θ_{min} (mas)	P.A. (°)	T_b (K)
Mira A Uniform Disc Model + Mira B Gaussian Model					
Mira A (Disc)	148.0 ± 0.5	45.96 ± 0.03	41.25 ± 0.03	−36.4 ± 0.3	2611 ± 51
Mira B (Gaussian)	11.4 ± 0.5	25.70 ± 0.26	21.38 ± 0.30	65.7 ± 2.7	—
Mira A Gaussian Model + Mira B Gaussian Model					
Mira A (Gaussian)	151.7 ± 0.5	30.50 ± 0.02	26.93 ± 0.02	−45.6 ± 0.3	—
Mira B (Gaussian)	11.1 ± 0.5	25.73 ± 0.28	22.14 ± 0.34	78.2 ± 2.9	—

Notes. The columns are (from left to right): the object being fitted and the type of model (uniform disc or Gaussian), total flux at 229.6 GHz ($S_{229.6\,\mathrm{GHz}}$, mJy), major axis (θ_{maj}, mas), minor axis (θ_{min}, mas), the position angle (P.A., degrees) of each elliptical component, and the brightness temperature (T_b, K) of the uniform disc model for Mira A. The quoted uncertainties are all the formal quantities resulting from model fitting. The real uncertainty of the flux is dominated by the absolute flux calibration, which is estimated to be of order 20%. The uncertainty of the brightness temperature including the contribution from the absolute flux calibration is about 565 K. The total integrated fluxes of Mira A and B in the 229.6-GHz continuum map are 149.70 ± 0.04 mJy and 11.19 ± 0.04 mJy, respectively.

SV dataset as already analysed by Matthews et al. and Vlemmings et al., we also include the continuum data from the six spectral line windows (`spw` = 1–6 and 8–13). The continuum data in these spectral line windows were prepared by averaging and splitting out the line-free channels in the windows corresponding to each distinct frequency range (see the first two columns of Table 3.3), and then exporting the visibility data to Miriad. The visibilities of Mira A and B were fitted simultaneously using the similar model adopted by Matthews et al. (2015) and Vlemmings et al. (2015), i.e. a uniform disc plus an additional Gaussian component for Mira A, and a single Gaussian model for Mira B. We fit the visibilities with the task `uvfit` (Revision 1.10, 2013 August) in Miriad. Miriad/`uvfit` is preferred to the `uvmodelfit` task in CASA because it allows multiple model components to be fitted simultaneously. We cross-checked the *uv*-fitting results from the respective tasks in Miriad and CASA with single-component models, and both tasks return similar results. To compare the results of Matthews et al. (2015) and Vlemmings et al. (2015), the visibilities of the 229 GHz continuum windows (`spw` = 0, 7) were fitted in a similar manner.

Table 3.3 shows the *uv*-fitting results to the continuum data in all spectral windows. For Mira A, whilst the major and minor axes of the elliptical components appear to be consistent among all windows, the fluxes shared by the uniform disc and the Gaussian components show great variation. The formal errors of the fluxes reported by `uvfit` are ∼9 mJy for the continuum window at 229.6 GHz and 35–40 mJy for the six spectral line windows. Hence, the fitted fluxes of the individual components of Mira A in the line windows are not as reliable as those in the continuum window. Figures 3.4 and 3.5 show the visibility plots and the maps, respectively, of the fitted continuum models and residuals for all seven continuum and spectral line windows in the Band 6 data. In the maps, there are some $\sim 6\sigma$ residuals in the continuum window. However, our experiment shows that adding one or two more Gaussian components to the *uv*-fitting does not significantly improve the results. The residuals in the spectral line windows appear to be less significant than those in the continuum window, probably because the map rms noises are much higher by a factor of about four.

Table 3.3.: Photospheric parameters from fitting the continuum visibility data, with the `uvfit` task in the Miriad software, of Mira A and B in different continuum and spectral line windows of ALMA Band 6.

SPWs	Freq. Range	Mira A Uniform Disc Model		Mira A Gaussian Model		Mira B Gaussian Model	
		$S_\nu(\Delta S_\nu)$	$\theta_{\rm maj} \times \theta_{\rm min}$, P.A.	$S_\nu(\Delta S_\nu)$	$\theta_{\rm maj} \times \theta_{\rm min}$, P.A.	$S_\nu(\Delta S_\nu)$	$\theta_{\rm maj} \times \theta_{\rm min}$, P.A.
	(GHz)	(mJy)	(mas × mas, °)	(mJy)	(mas × mas, °)	(mJy)	(mas × mas, °)
2, 9	213.982–214.100	84(36)	51.2×39.1, −48.3	45(37)	27.4×23.5, 38.2	9.4(1.8)	25.7×19.0, −81.4
1, 8	214.279–214.397	76(37)	53.1×39.1, −55.1	56(37)	29.2×24.5, 17.6	9.4(1.9)	25.6×19.0, −60.1
3, 10	215.489–215.607	97(40)	50.8×40.6, −50.0	35(41)	26.8×20.4, 31.9	9.2(1.7)	23.4×19.1, 82.3
4, 11	216.995–217.113	90(35)	52.2×38.8, −41.8	43(36)	29.1×22.6, 48.0	9.8(1.9)	24.7×19.7, −89.6
0, 7	228.681–230.417	102(9)	51.2×41.0, −45.0	47(9)	26.4×22.4, 34.0	11.3(0.5)	25.5×22.5, 72.7
6, 13	231.788–231.906	91(40)	52.1×40.6, −57.1	61(41)	29.5×23.7, 17.9	11.3(2.2)	28.1×22.4, 12.3
5, 12	232.574–232.692	95(36)	51.1×39.5, −60.4	59(36)	31.8×23.5, 21.3	11.1(2.1)	25.8×24.7, 43.1

Notes. The columns are (from left to right): ALMA Band 6 spectral windows (SPWs), rest frequency range of the continuum data (GHz), and the total flux (S_ν, mJy) and the formal error of the fitting in the brackets (ΔS_ν, mJy), major and minor axes ($\theta_{\rm maj}$, $\theta_{\rm min}$, mas) and the position angle (P.A., degrees) of each component adopted in the visibility fitting. Mira A was fitted with an elliptical uniform disc together with an elliptical Gaussian component, and Mira B with an elliptical Gaussian model. The formal errors for the major and minor axes are typically $\lesssim$1 mas for the models of Mira A, and $\lesssim$2 mas for Mira B, except for the continuum windows (`spw` = 0, 7) in which the errors are $\lesssim$0.2 mas for Mira A and $\sim$0.3 mas for Mira B. The choices of model components are the similar to those adopted by Matthews et al. (2015) and Vlemmings et al. (2015).

At the frequency of 229.6 GHz, the total flux in the continuum image (Fig. 3.5) of Mira A is 149.70 ± 0.04 mJy and that of Mira B is 11.19 ± 0.04 mJy. In our visibility fitting, the elliptical uniform disc component for Mira A has a size (in FWHM) of about (51.2 ± 0.1) mas × (41.0 ± 0.1) mas, PA = −45.0° ± 0.5° and a flux of $S_{229.6\,\mathrm{GHz}}$ = 102 ± 9 mJy. This corresponds to a brightness temperature of 1630 ± 175 K. The uncertainly takes into account the formal errors of the flux (which is the dominant formal error), major and minor axes of the disc model (∼0.1 mas), and the bandwidth of the continuum spectral window (∼1.7 GHz). The additional Gaussian component of Mira A has a fitted flux of about 47 ± 9 mJy and and a size of about (26.4 ± 0.2) mas × (22.4 ± 0.2) mas, PA = 34.0° ± 1.7°, which is much larger than the size of the purported 4.7 mas hotspot from Vlemmings et al. (2015). The brightness temperature of our Gaussian component corresponds to 1856 ± 419 K, which is much smaller than 10 000 K, the value for the compact hotspot. Our elliptical Gaussian model for Mira B has a size of about (25.5 ± 0.3) mas × (22.5 ± 0.3) mas, PA = 72.7° ± 3.6° and a flux of about (11.3 ± 0.5) mJy. In general, our results are consistent with those reported by Matthews et al. (2015) within uncertainties, but significantly differ from those of Vlemmings et al. (2015). We did not find any evidence of the compact hotspot as reported by Vlemmings et al. (2015).

In addition to the spectral window of 229.6 GHz, we also computed the total continuum flux, S_ν, from Mira A at the frequencies of the four SiO and one H_2O spectral line windows in Band 6. The total flux in each window is computed by integrating the signals within a 0.″25-radius circle in the images (Fig. 3.5). This region safely includes all possible continuum emission from Mira A, but does not contain any emission from Mira B. The resultant spectral index in Band 6 is 1.82 ± 0.33, which is consistent with the value (1.86) derived by Reid & Menten (1997a).

3.3.1.4. The compact hotspot model of Mira A

We have tested the *uv*-fitting model of Vlemmings et al. (2015) in Miriad/`uvfit` by setting their model parameters for Mira A and B as the initial inputs. Without fixing any parameters, all the fitting trials with Miriad/`uvfit` eventually converge to our values as presented in Table 3.3. The derived major and minor axes of the additional Gaussian component of Mira A are always in the range of ∼20–30 mas, which are much larger than 4.7 mas as reported by Vlemmings et al. (2015). On the other hand, even when we fixed the sizes of the uniform disc and Gaussian components to be the same as their values, we were still not able to obtain the same results as in Vlemmings et al. (2015). Figures 3.6 (top two panels) and 3.7 show the visibility plots and the maps, respectively, in the 229 GHz continuum window of the continuum model and residuals of both Mira A and B using the parameters fitted by Vlemmings et al. (2015). In the model where Mira A was fitted with two components, a uniform disc (UD) and a 4.7 mas Gaussian, we obtain huge residuals that appear to be completely different to the residual image presented in Fig. 1 (right) of Vlemmings et al. (2015). Moreover, in the UD-only model for Mira A (using the best-fit disc model by Vlemmings et al.), we do not obtain the single, compact and bright hotspot near the phase centre as shown in Fig. 1 (middle) of Vlemmings et al. (2015). Instead, we find a pair of strong positive residual features along the SE-NW axis and strong negative features along the SW-NE axis, which may be indicative of an inappropriate shape of the subtracted uniform disc component. We also note that the UD-only residual image of Vlemmings et al. (2015) may show a negative spot in the north-east of the central compact hotspot (their Fig. 1 middle). However, Vlemmings et al. (2015) did not show any negative contour lines or negative colour scale in their figures.

Vlemmings et al. (2015) fitted the continuum visibilities differently from those in Matthews et al. (2015) and from ours in two ways. First, they fitted the continuum dataset of each

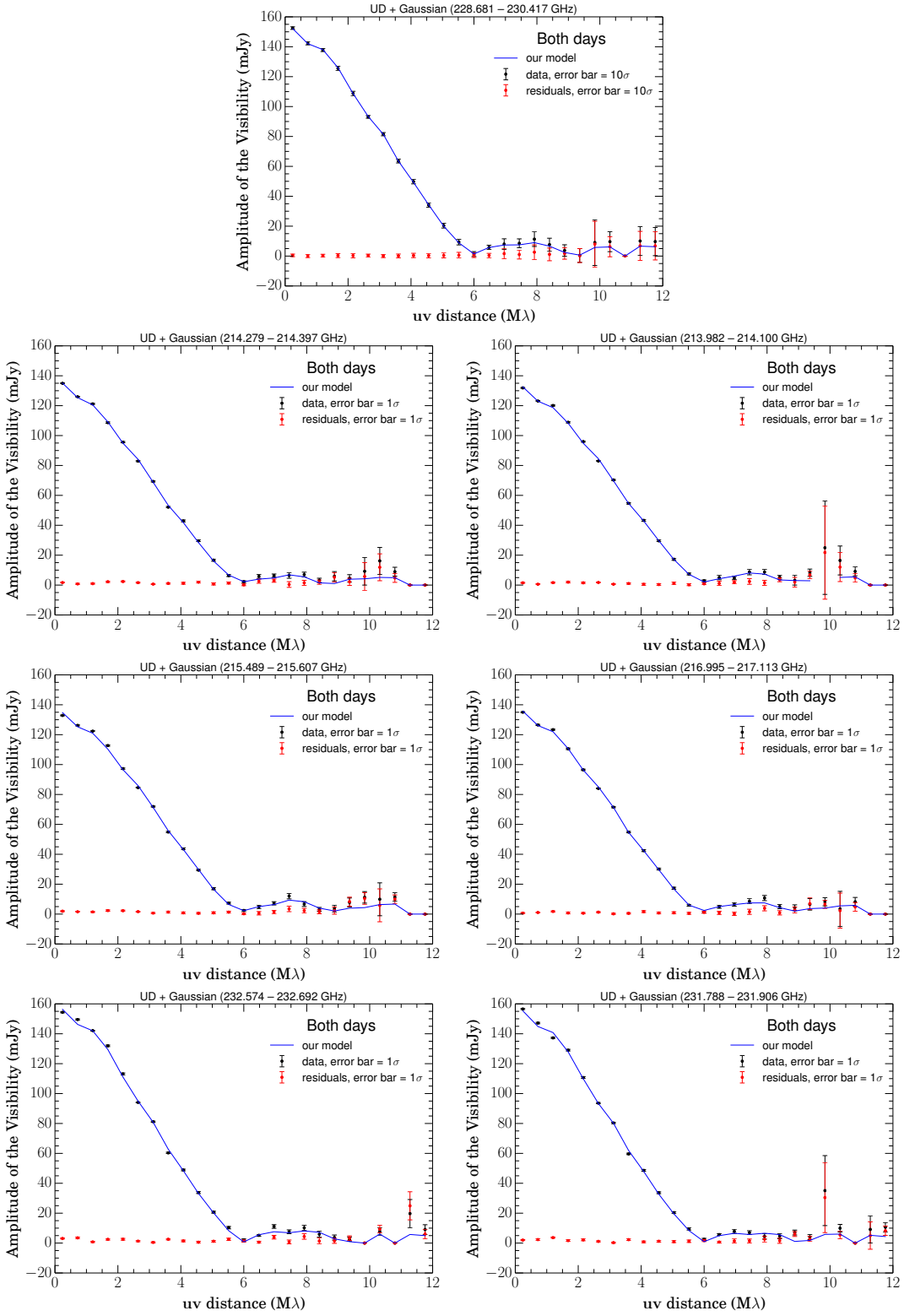

Figure 3.4.: Visibility plots of the continuum fitting with the task `uvfit` in Miriad. The plot on the top is the continuum window at 229.6 GHz, and the six below are (from top to bottom, and from left to right) the spectral line windows in ascending order of frequency: 214.0 GHz, 214.3 GHz, 215.5 GHz, 271.1 GHz, 231.8 GHz, 231.6 GHz as listed in Table 3.3. The error bars in the continuum window and spectral line windows are 10 times and 1 time, respectively, the standard deviation in the mean of the amplitude of visibilities in the respective bin of *uv*-distance. The large error bar near 10 Mλ is due to the small number of data points.

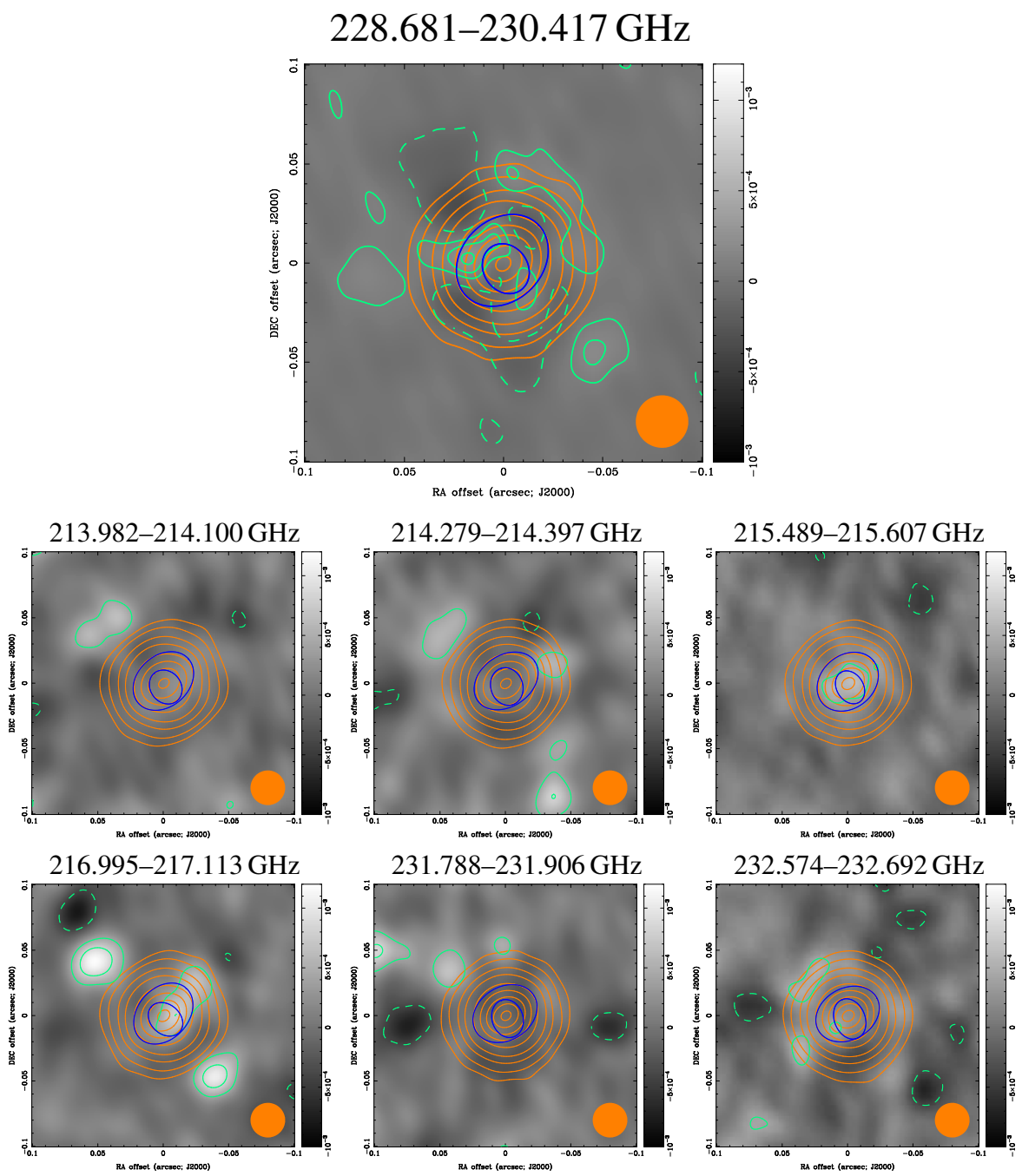

Figure 3.5.: Continuum fitting results with the task `uvfit` in Miriad. The large map on the top is the continuum window at 229.6 GHz, the six smaller maps below are (from top to bottom, and from left to right) the spectral line windows in ascending order of frequency: 214.0 GHz, 214.3 GHz, 215.5 GHz, 271.1 GHz, 231.8 GHz, and 231.6 GHz as listed in Table 3.3. In all the panels, the orange contours are the continuum models for Mira A, with parameters listed in Table 3.3. The sizes of the uniform disc and Gaussian models for the respective spectral windows are shown by blue open ellipses (larger and smaller, respectively). The continuum contour levels are $-3, 3, 10, 30, 60, 120, 180, 240, 300, 340 \times 0.20$ mJy. The green contours and the greyscale maps are the residual images (difference between the data and modelled continuum) of the respective spectral windows. The residual contour levels are $-2, 2, 4, 6 \times \sigma$, where $\sigma = 0.04$ mJy for the continuum window (top) and $\sigma = 0.20$ mJy for the six line windows (bottom two rows). The restoring beam of 0.″027 FWHM is indicated in orange in the bottom right corner in each panel.

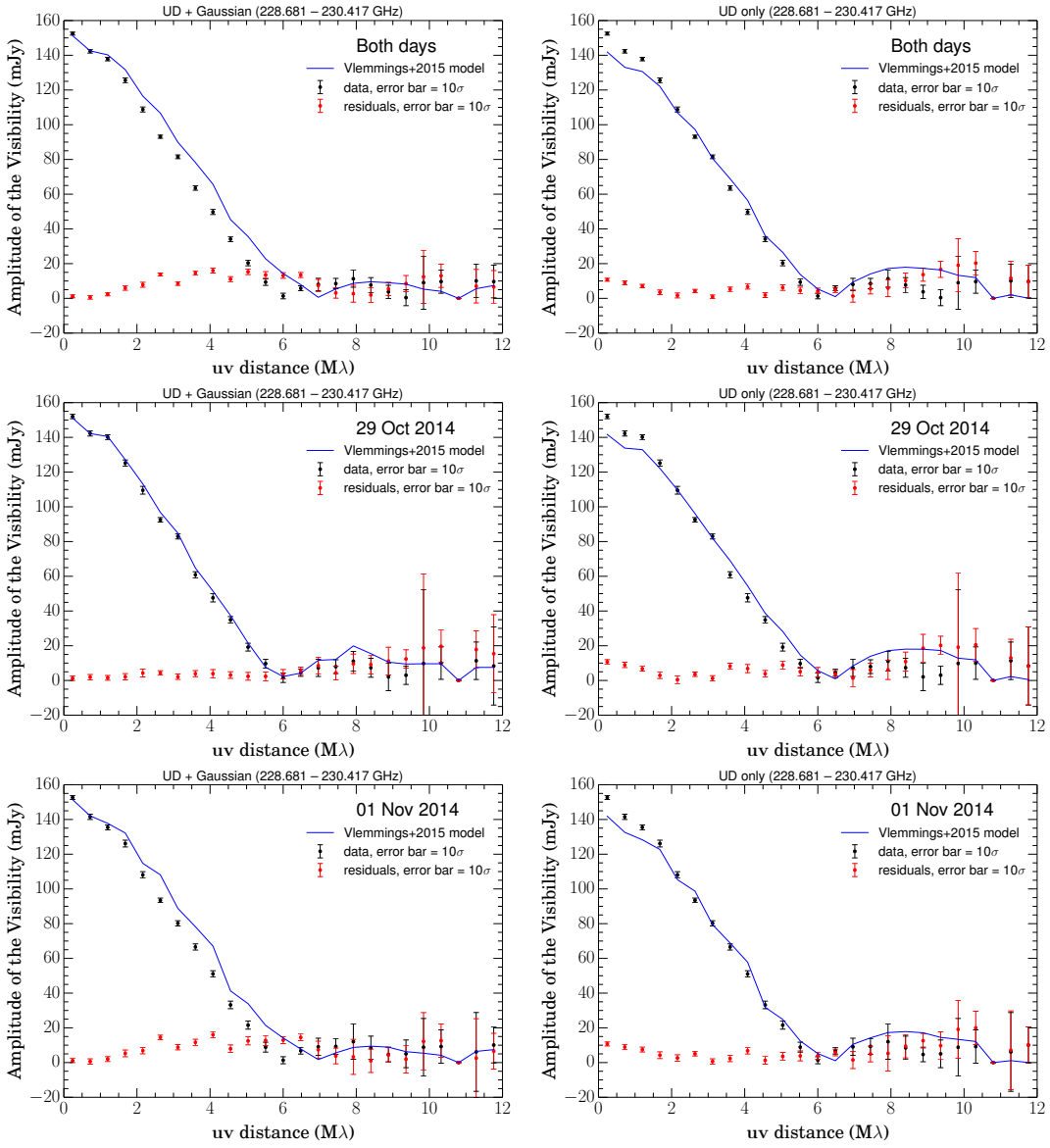

Figure 3.6.: Visibility plots of the continuum fitting with the task `uvfit` in Miriad using the parameters obtained by Vlemmings et al. (2015). All the plots are the results of the continuum window at 229.6 GHz. The top panels are the results without splitting the datasets into individual days. The middle and bottom panels are the results of split data for 2014 October 29 and 2014 November 01, respectively. The three panels on the left are the results using uniform disc and a Gaussian to fit Mira A, and the three on the right are the results using only a uniform disc for Mira A. The error bars in the continuum window and spectral line windows are 10 times and 1 time, respectively, the standard deviation in the mean of the amplitude of visibilities in the respective bin of *uv*-distance. The large error bar near 10 Mλ is due to the small number of data points.

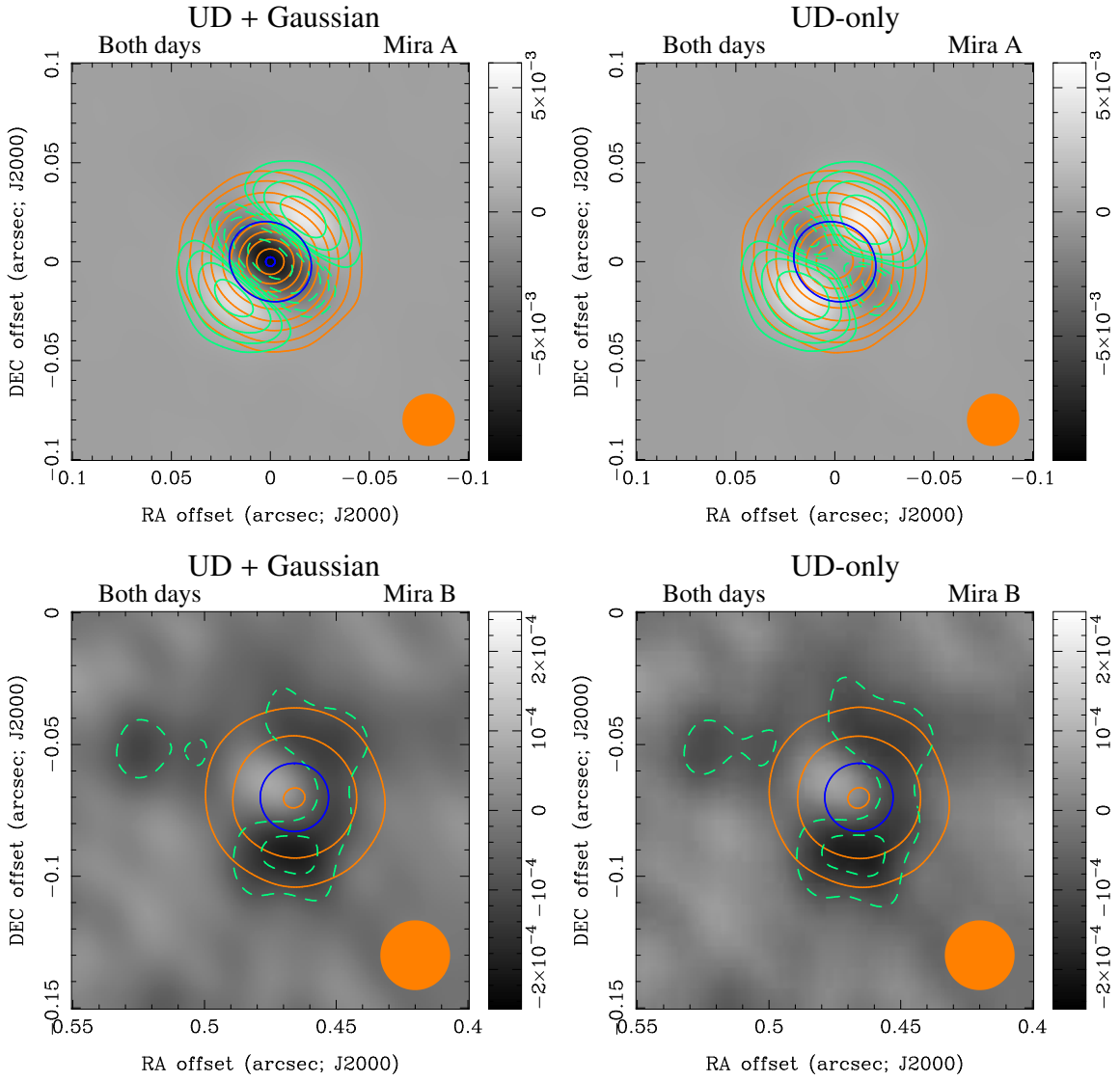

Figure 3.7.: Results of continuum fitting with the task `uvfit` in Miriad without splitting the data into two observing days. The top and bottom rows show the results for Mira A and Mira B, respectively. The left column shows the results when Mira A was fitted with a uniform disc and a Gaussian (UD + Gaussian), while the right shows the results when Mira was fitted with the same uniform disc only (UD-only). The parameters for Mira A and B are fixed to those from Vlemmings et al. (2015), except the position of the additional Gaussian component for the UD + Gaussian model of Mira A. The sizes of the uniform disc and Gaussian models for the respective spectral windows are shown by blue open ellipses/circles (larger and smaller, respectively). In all the panels, the orange contour levels for the continuum model are 3, 10, 30, 60, 120, 180, 240, 300, 360, 420, and 540×0.20 mJy. The green contours and the greyscale maps are the residual images produced after the modelled continuum visibilities have been subtracted from the respective windows. The residual contour levels for the images of Mira A (top row) are $-160, -80, -40, -20, -10, 10, 20, 40$, and $80 \times \sigma$, and for Mira B (bottom row) are $-4, -2, 2$, and $4 \times \sigma$, where $\sigma = 0.04$ mJy. The restoring beam of 0.″027 FWHM is indicated in orange in the bottom right corner in each panel.

observing day independently, instead of combing both days together. Second, Vlemmings et al. (2015) used a different *uv*-fitting tool, `UVMULTIFIT`, which has been developed by the Nordic ALMA Regional Center Node[10] and can be implemented in CASA (Martí-Vidal et al., 2014).

We conducted additional tests to see if we were able to reproduce the fitting results of Vlemmings et al. (2015) by following any one, or both aspects of their approach. Figures 3.6 (middle two and bottom two panels) and 3.8 show the visibility plots and maps, respectively, of the fitting results using Miriad/`uvfit`, by splitting the continuum data into individual days of observation. In the fitting, we fixed the sizes and flux densities of the model components of Mira A and B to be the same as used by Vlemmings et al. (2015). The positions of the uniform disc (UD) component of Mira A and the Gaussian component of Mira B were also fixed at the respective stellar positions. The only free parameter in the UD + Gaussian model is therefore the position of the additional Gaussian component of Mira A. Although there are some significant differences between the residual maps on the two observing days, we did not obtain any satisfactory fitting with the parameters obtained by Vlemmings et al. (2015), nor did we find any evidence for the bright spot in the UD-only model. In the UD + Gaussian model for the first day of observation (2014 Oct 29), we even found the best-fit position of the purported hotspot to be outside the uniform disc component of Mira A, which is far away from the best-fit position as reported by Vlemmings et al. (2015).

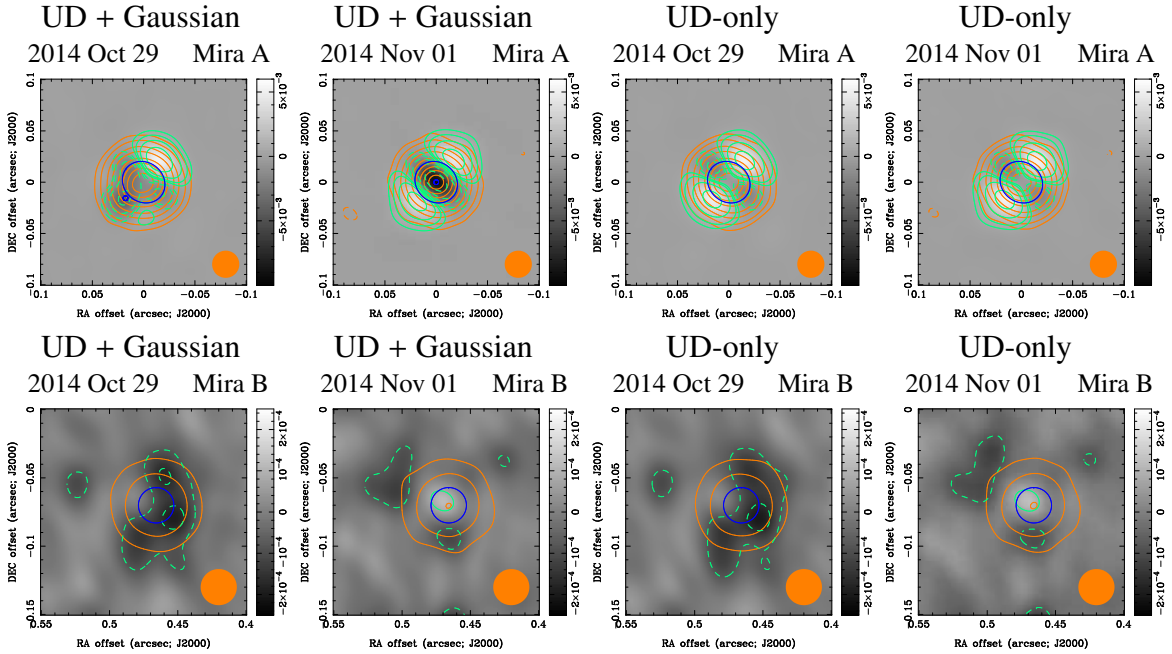

Figure 3.8.: Same as Fig. 3.7 for the fitting results on each day of observation.

Using CASA/`UVMULTIFIT` (version 2.1.4-r3), we also obtained similar results to those reported above. Assuming that the additional Gaussian component is circular, which is exactly the same model as used by Vlemmings et al. (2015), the size and flux density of the elliptical disc component for Mira A are found to be 50.3 mas×41.0 mas and $S_{229.6\,\mathrm{GHz}} = 92.9 \pm 0.1$ mJy, respectively, and those of the additional Gaussian component are 25.4 mas × 25.4 mas and $S_{229.6\,\mathrm{GHz}} = 56.6 \pm 0.1$ mJy, respectively.

[10] https://www.oso.nordic-alma.se/software-tools.php

We therefore failed to reproduce any evidence of the compact (<5 mas) Gaussian component in Mira A as suggested by Vlemmings et al. (2015), even if we carried out the fitting using the exact same approach with the same set of model components (elliptical uniform disc + circular Gaussian). Self-calibration may be a possible cause for the discrepancy. However, from their Sect. 2, it is unclear whether Vlemmings et al. (2015) have derived the self-calibration solutions on their own or obtained the solutions from the ALMA Science Portal (as we did). Although Vlemmings et al. (2015) discovered a compact hotspot from their fitting in Band 6, they could not find a similar structure in the continuum data of Band 3 (94.2 GHz) in this ALMA SV dataset with a rms sensitivity of $\sim$40 μJy beam^{-1}. Assuming the size of 4.7 mas and Gaussian brightness distribution, Vlemmings et al. (2015) estimated in their Sect. 4.1.3 the upper limit of the hotspot brightness temperature in Band 3 to be $T_b \lesssim 17\,500$ K. However, by repeating the same calculation, we obtained an upper limit of $T_b \lesssim 250$ K, which is a factor of 70 lower than their estimate. Hence we cast doubt on the existence of any detectable compact hotspot near the centre of Mira A's radio continuum disc near 229 GHz in this ALMA SV dataset.

3.3.2. Images

Figure 3.3 shows the map of the SiO $v = 0$ $J = 5$–4 transition in the LSR velocity of 46.7 km s^{-1}, which is the systemic (centre-of-mass) velocity of Mira A, over a $7\farcs5 \times 7\farcs5$ box centred at Mira A. The position of Mira B, $02^{\rm h}19^{\rm m}20\fs826$, $-02\degr58\arcmin43\farcs12$, determined by fitting its image produced from the *uv*-data before self-calibration, is also indicated on the map. To the west of Mira A, the SiO vibrational ground state emission extends to a larger projected radial distance than other directions. This emission feature emerges from the west and north-west of Mira A and appears as an arc-like feature, which turns south at $\sim$2″ west of the star and reaches a maximum projected distance of $\sim$3″.

As we explain in Appendix D, there are spurious bumps in the spectra extracted from the line of sight towards the continuum of Mira in the maps produced from the data continuum-subtracted before imaging. Since we are more confident in the quality of the image deconvolution without the subtraction of the continuum, we extract the spectra from the maps retaining the continuum (full data maps) for our radiative transfer modelling in Sects. 3.3.3 and later. These full data maps are presented in Appendix E. In this section, we only show the maps that are first imaged with the continuum, and *then* continuum-subtracted with the CASA task `imcontsub`. Such post-imaging continuum subtraction can avoid the spurious features seen in pre-imaging continuum-subtracted images (and also the spectra).

Figure 3.9 shows the continuum-subtracted channel maps of the SiO $v = 0$ $J = 5$–4 transition in the LSR velocity range of 35.7–58.7 km s^{-1} over a $1\farcs1 \times 1\farcs1$ box centred at Mira A (Mira hereafter). Contour lines at the -36, -6, 6, 12, 24, 48, and 72σ levels, where $\sigma = 0.80$ mJy beam^{-1}, are drawn to indicate the region with significant line absorption (yellow contours for negative signals) or emission (white contours for positive signals).

Figure 3.10 shows the same channel maps as Fig. 3.9, but zoomed in to show the inner $0\farcs22 \times 0\farcs22$ region around Mira. Overall, the emission of the vibrational ground state SiO line in the inner winds of Mira ($\lesssim$0$\farcs$2) appears to be spherically symmetric, although we find significant inhomogeneities with stronger emission from clumps that are localised in relatively small regions and which stretch over limited velocity ranges.

As shown in Fig. 3.11, the absorption and emission in the $J = 5$–4 transition of the vibrational ground state of the ^{29}SiO isotopologue appears to have a very similar extent to that observed in the analogous line to the main isotope of SiO. On larger scales, the ^{29}SiO emission

also appears to extend to the west of Mira, while its intensity falls off much more rapidly with increasing radius and no significant emission is seen beyond ∼0.5″. This is expected because the isotopic ratio of ^{28}Si/^{29}Si in oxygen-rich giants is ≳13 (e.g. Tsuji et al., 1994; Decin et al., 2010b; Ohnaka, 2014). The ^{29}SiO emission within ∼0.″2 also exhibits (1) general spherical symmetry and (2) localised, clumpy structures with more intense emission. While the maps in both isotopologues have a similar overall morphology, the peaks in the ^{29}SiO emission do not all coincide with the ^{28}SiO peaks.

Figures 3.12 and 3.13 show the continuum-subtracted maps of the SiO $v = 2$ $J = 5$–4 and H_2O $v_2 = 1$ $J_{K_a,K_c} = 5_{5,0}$–$6_{4,3}$ lines, respectively. Since the emission of these two lines is more smoothly distributed than that in the vibrational ground state SiO and ^{29}SiO lines, we can clearly see ring-like emission structures around the line absorption against Mira's continuum in the velocity channels around the systemic velocity (46.7 km s^{-1}). In most velocity channels, the emission from both lines are confined well within 0.″1 of the centre of the continuum, and there is no remote emission beyond ∼0.″1 as in the ground state SiO lines.

Close to the systemic velocity, there is a clump at about 0.″05 to the east of Mira which strongly emits in both the SiO $v = 2$ and H_2O $v_2 = 1$ lines. The brightness temperatures of the SiO $v = 2$ and H_2O $v_2 = 1$ emission are ∼600 K and ∼1000 K, respectively. However, this eastern clump is not prominent in the vibrational ground state SiO and ^{29}SiO lines, which have very low excitation energies (i.e. the upper-state energy, E_{up}). This clump therefore probably contains shock-heated gas at a high kinetic temperature ($T_{kin} \gtrsim 1000$ K). On the other hand, the intensely emitting clumps in the ground state of SiO or ^{29}SiO lines do not appear in the highly excited SiO $v = 2$ and H_2O $v_2 = 1$ lines, which have excitation energies of $E_{up}/k \gtrsim 3500$ K.

3.3.3. Spectra

We have extracted the SiO and H_2O spectra from the centre of Mira's continuum, and from an array of positions at radii 0.″032, 0.″064, 0.″096, 0.″128, and 0.″160 from the centre, along the legs at PA = 0°, 90°, 180°, and 270°. The positions are shown in Fig. 3.14, which is the map of SiO $v = 0$ $J = 5$–4, without subtraction of the continuum, in the channel of the stellar systemic velocity (V_{LSR} = 46.7 km s^{-1}). The full set of the spectra are presented along with the modelling results in Sect. 3.4. Because the inner envelope around Mira is partially filled with intense clumpy emission, we did not compute the azimuthally averaged spectra in order to avoid the averaged spectra from being contaminated by isolated intense emission and to obtain a more representative view of the general physical conditions of the envelope.

Figure 3.15 shows the spectra of various lines in ALMA Band 6 extracted from the centre of the continuum. As we did not subtract the continuum from the data, the flat emission towards the low- and high-velocity ends of the spectra represents the flux from the radio continuum of Mira near the frequencies of the respective spectral lines. In Appendix D, we show the spectra with the continuum subtracted (in the visibility data) before imaging.

The SiO $v = 1$ $J = 5$–4 transition shows strong maser emission across a wide range of LSR velocities, which introduces sharp spikes in its spectrum. For other lines which do not show strong maser emission (i.e. all except SiO $v = 1$), absorption against the continuum ranges between the offset velocity (relative to the stellar LSR velocity) of approximately −4 km s^{-1} and +14 km s^{-1}. The absorption is in general redshifted relative to the systemic velocity. This indicates that the bulk of the material in the inner envelope is infalling towards Mira during the ALMA SV observation (near stellar phase 0.45). Infall motion at phase 0.45 is expected for another oxygen-rich Mira variable, W Hya, based on the detailed modelling of the CO $\Delta v = 3$ line profiles, as observed by Lebzelter et al. (2005), presented in the paper

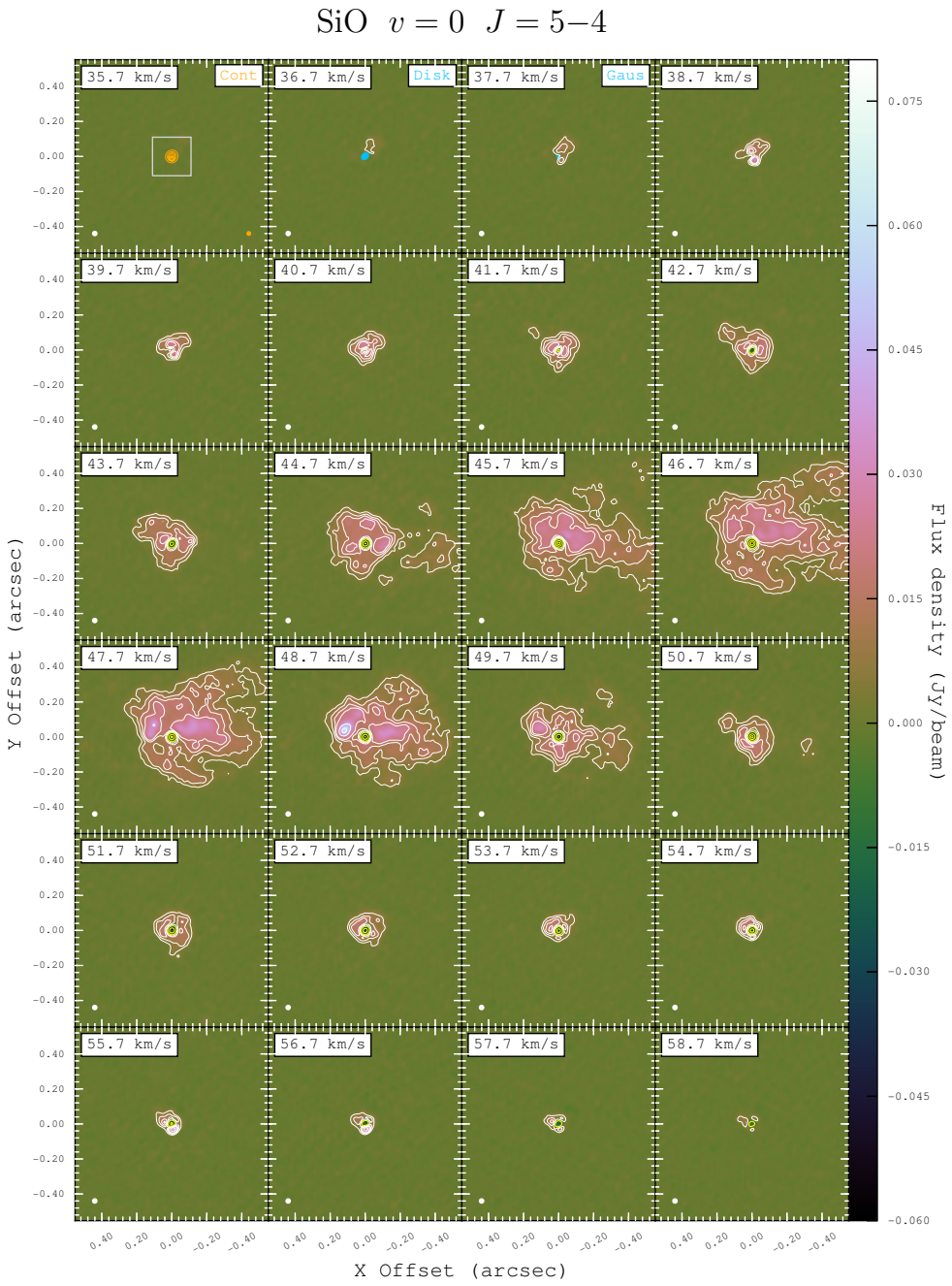

Figure 3.9.: Channel maps of post-imaging continuum-subtracted SiO $v = 0$ $J = 5$–4 from LSR velocity 35.7 km s^{-1} to 58.7 km s^{-1}, with a channel width of 1.0 km s^{-1}. The systemic velocity is 46.7 km s^{-1}. The horizontal and vertical axes indicate the relative offsets (arcsec) in the directions of right ascension (X) and declination (Y), respectively, with respect to the fitted absolute position of Mira A. The white contours represent 6, 12, 18, 24, 48, and 72σ and yellow contours represent -60, -36, and -6σ, where $\sigma = 0.80$ mJy beam^{-1} is the map rms noise. The circular restoring beam of 0.″032 FWHM for the SiO image is indicated in white in the bottom left corner of each panel. In the first panel of the top row, orange contours at 0.1, 0.3, 0.5, 0.7, and 0.9 times the peak flux density (73.4 mJy beam^{-1}) of the 229 GHz continuum emission are also drawn and the corresponding restoring beam of 0.″028 FWHM is indicated in orange in the bottom right corner. The white box centred at Mira A indicates the 0.″22 × 0.″22 region of the zoomed maps of SiO $v = 0$ (Fig. 3.10), $v = 2$ (Fig. 3.12), and H_2O $v_2 = 1$ (Fig. 3.13). In the second and third panels of the top row, the sizes of the uniform disc and Gaussian models, respectively, in our continuum analysis are drawn in blue.

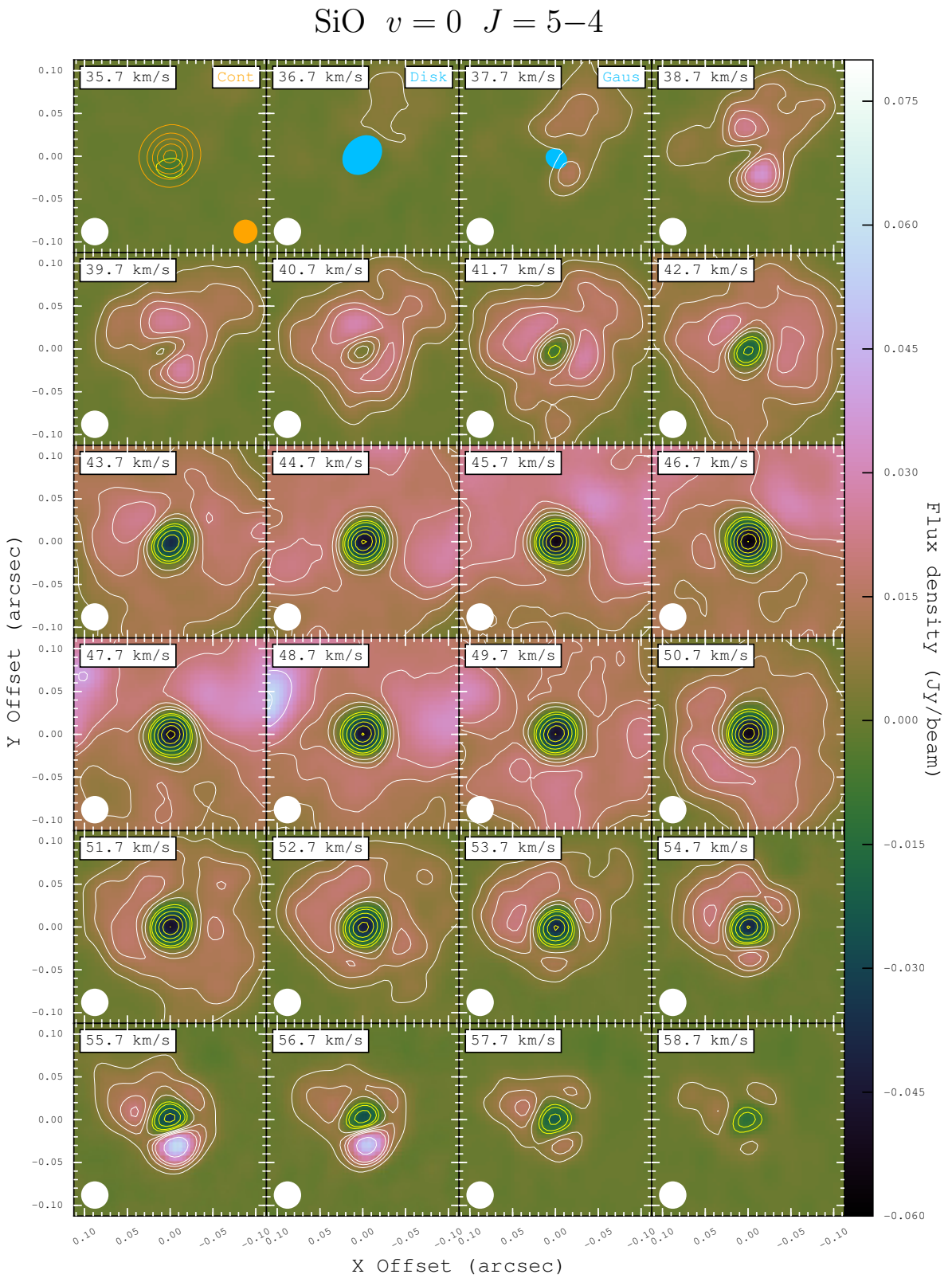

Figure 3.10.: Same as Fig. 3.9 for the zoomed (0.″22 × 0.″22) channel maps of post-imaging continuum-subtracted SiO $v = 0$ $J = 5$–4. The white contours represent 6, 12, 18, 24, 48, and 72σ and yellow contours represent −72, −60, −48, −36, −24, −12, and −6σ, where $\sigma = 0.80$ mJy beam^{-1} is the map rms noise.

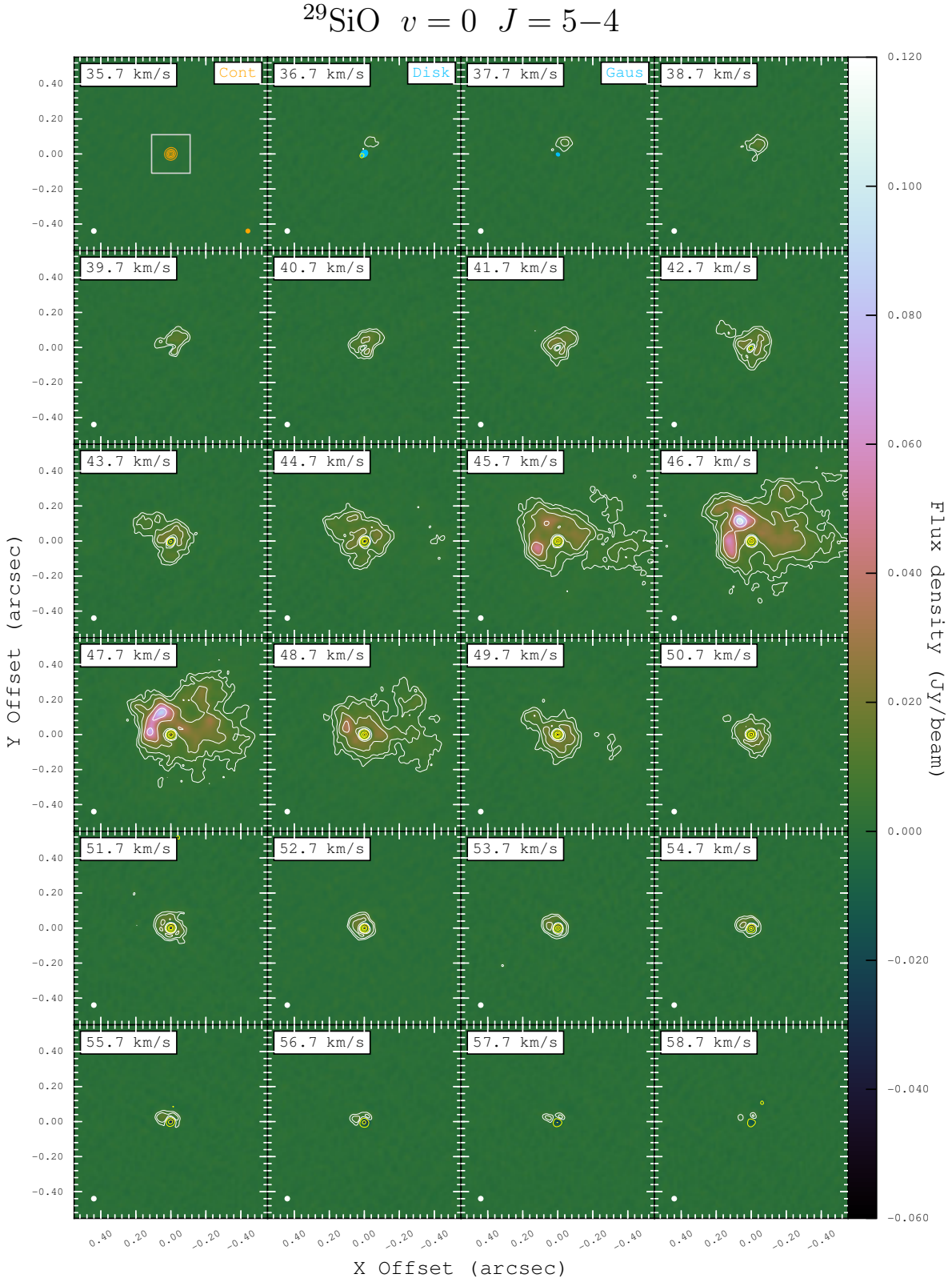

Figure 3.11.: Same as Fig. 3.9 for the channel maps of post-imaging continuum-subtracted ^{29}SiO $v = 0$ $J = 5$–4. The white contours represent 6, 12, 24, 48, 96, and 144σ and yellow contours represent −72, −54, −36, and −6σ, where $\sigma = 0.65$ mJy beam^{-1} is the map rms noise.

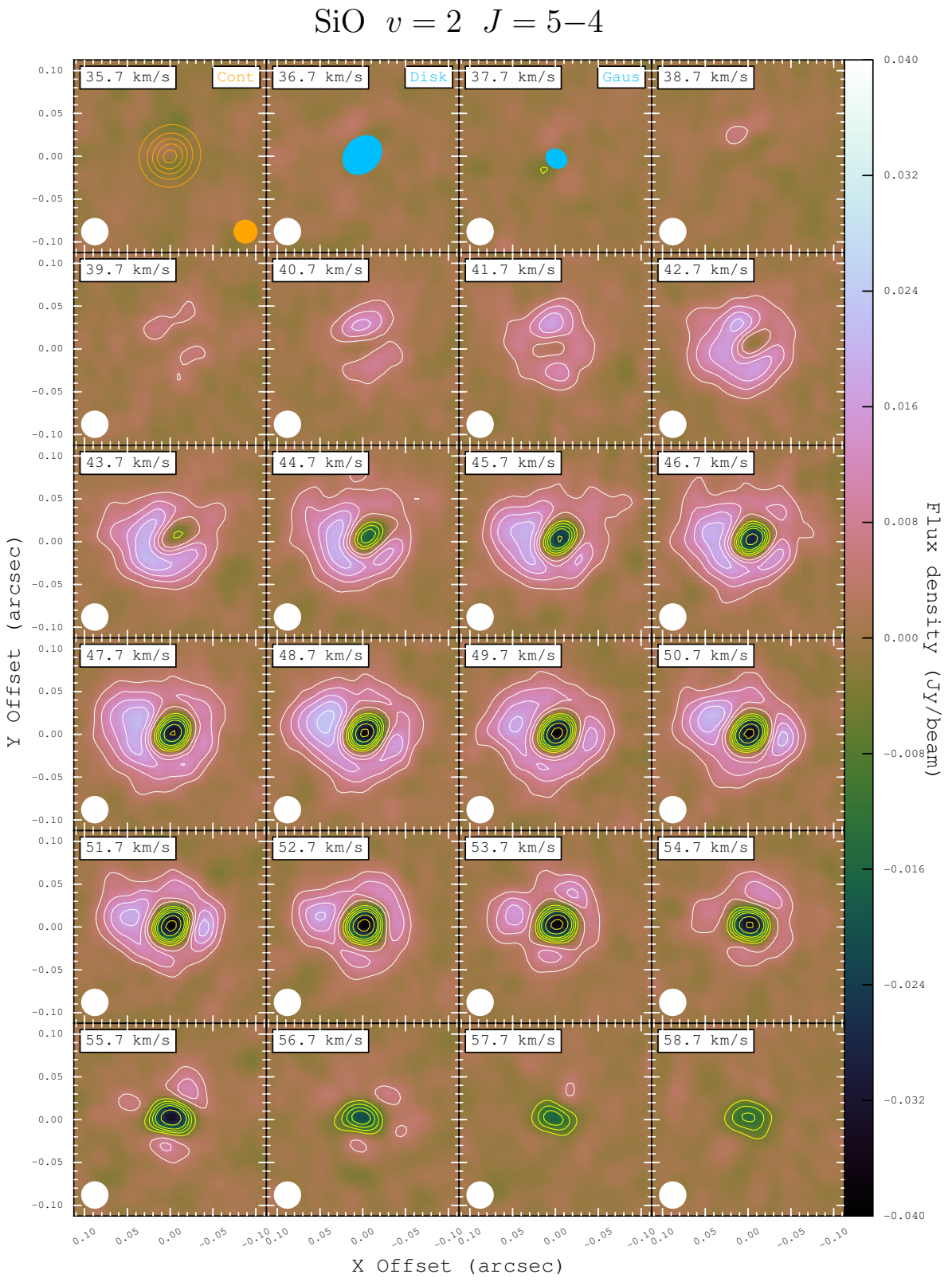

Figure 3.12.: Same as Fig. 3.9 for the zoomed (0.″22 × 0.″22) channel maps of post-imaging continuum-subtracted SiO $v = 2$ $J = 5$–4. The white contours represent 6, 12, 18, 24, and 30σ and yellow contours represent −48, −36, −24, −18, −12, and −6σ, where $\sigma = 0.72$ mJy beam^{-1} is the map rms noise.

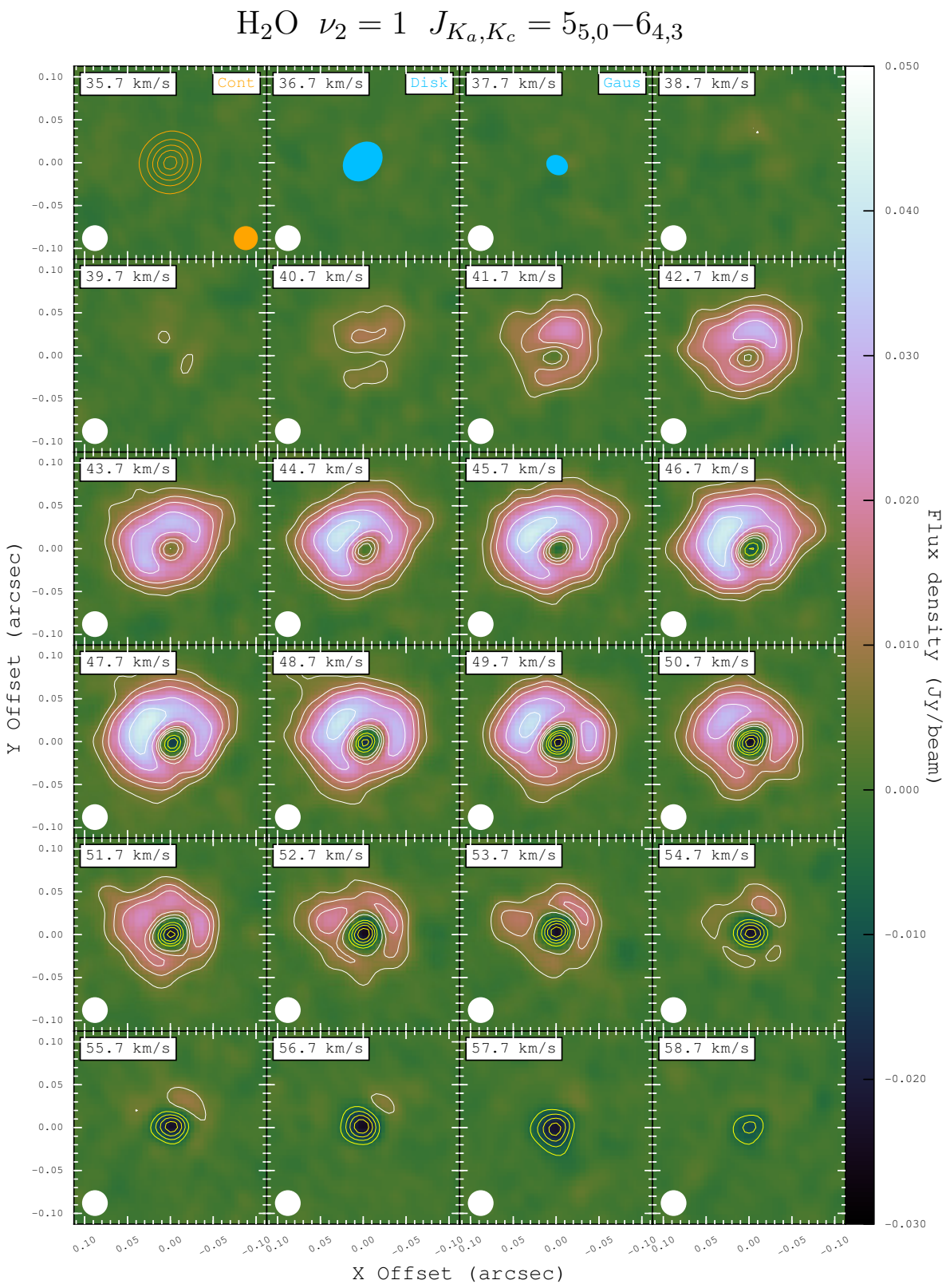

Figure 3.13.: Same as Fig. 3.9 for the zoomed (0.″22 × 0.″22) channel maps of post-imaging continuum-subtracted H_2O $v_2 = 1$ $J_{K_a,K_c} = 5_{5,0}$–$6_{4,3}$. The white contours represent 6, 12, 18, 30, and 42σ and yellow contours represent −24, −18, −12, and −6σ, where $\sigma = 0.85$ mJy beam^{-1} is the map rms noise. The circular restoring beam of 0.″030 FWHM for the H_2O images is indicated in white in the bottom left corner of each panel.

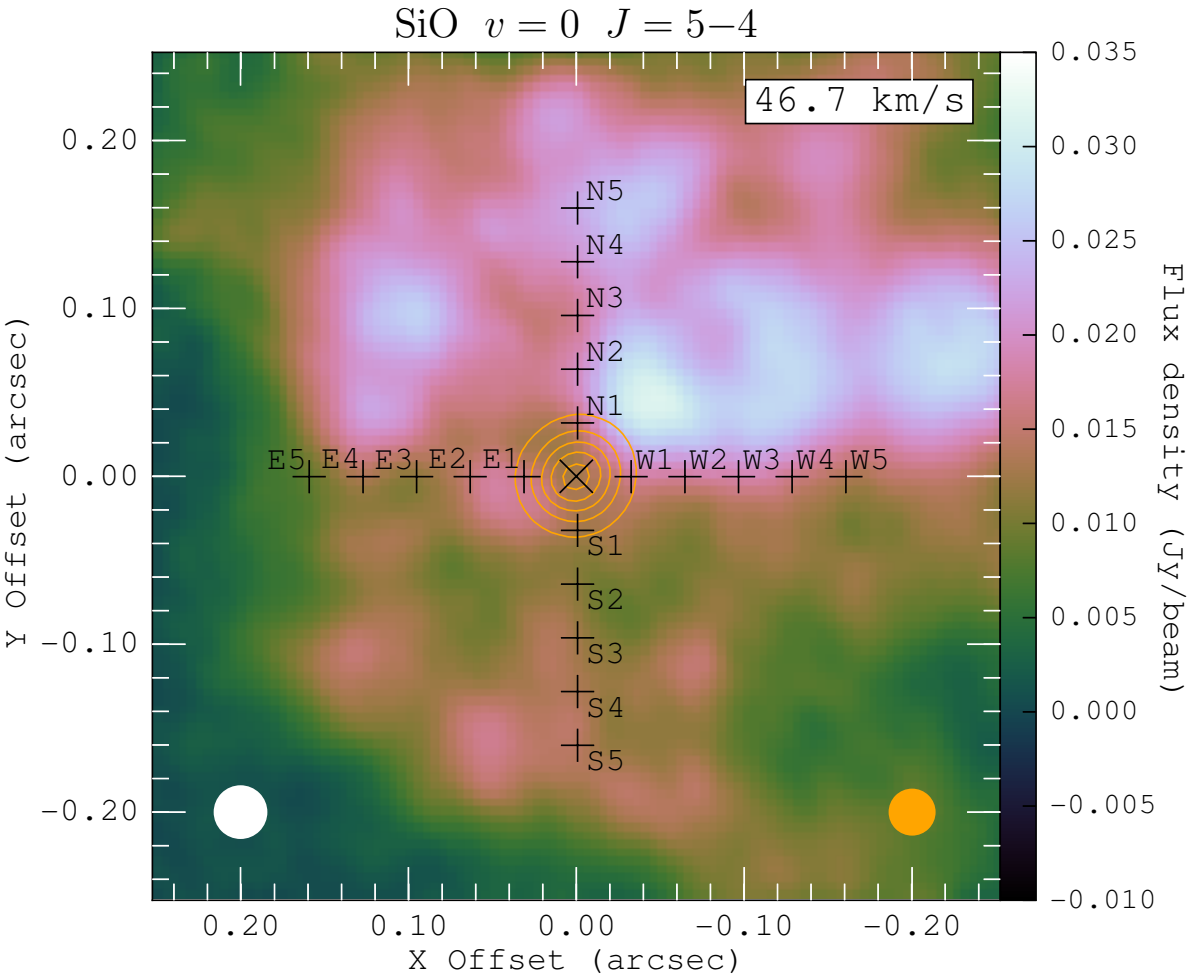

Figure 3.14.: Map of SiO $v = 0$ $J = 5$–4 (with the continuum) at the channel of the systemic velocity (46.7 km s^{-1}) with a channel width of 1 km s^{-1}. The centre of Mira's continuum is indicated by a black cross. Orange contours represent 10%, 30%, 50%, 70%, and 90% of the peak continuum flux (73.4 mJy beam^{-1}). The black plus signs (+) indicate the positions at which SiO and H_2O spectra are sampled and modelled in Sect. 3.4. The sampling positions are separated by 32 mas along each arm of this array of points. The circular restoring beam of 0.″032 FWHM for the SiO image is indicated in white at the bottom left and that of 0.″028 FWHM for the 229 GHz continuum contours is indicated in orange at the bottom right.

of Nowotny et al. (2010). The CO $\Delta v = 3$ lines probe the pulsation-dominated layers of the atmospheres of Mira variables, and therefore the radial velocity variation of these lines indicate the infall or expansion velocities of the global motion of the extended atmospheres below the dust formation (and circumstellar wind acceleration) regions (e.g. Hinkle et al., 1982; Nowotny et al., 2005a).

The spectra of ^{28}SiO $v = 0$ $J = 5$–4 and ^{29}SiO $v = 0$ $J = 5$–4 appear to be virtually identical. From the similarity of the line profiles and considering the high expected isotopic ratio of ^{28}Si/^{29}Si ($\gtrsim$ 13), the vibrational ground state ^{28}SiO and ^{29}SiO lines we see in Fig. 3.15 are likely to be both very optically thick (saturated) and thermalised.

In Fig. 3.15, we can also see trends in the width and depth of the absorption profiles with excitation. The vibrationally excited SiO $v = 2$ and H_2O $v_2 = 1$ lines show narrower and shallower absorption than the two ground state SiO lines. This suggests that the vibrationally

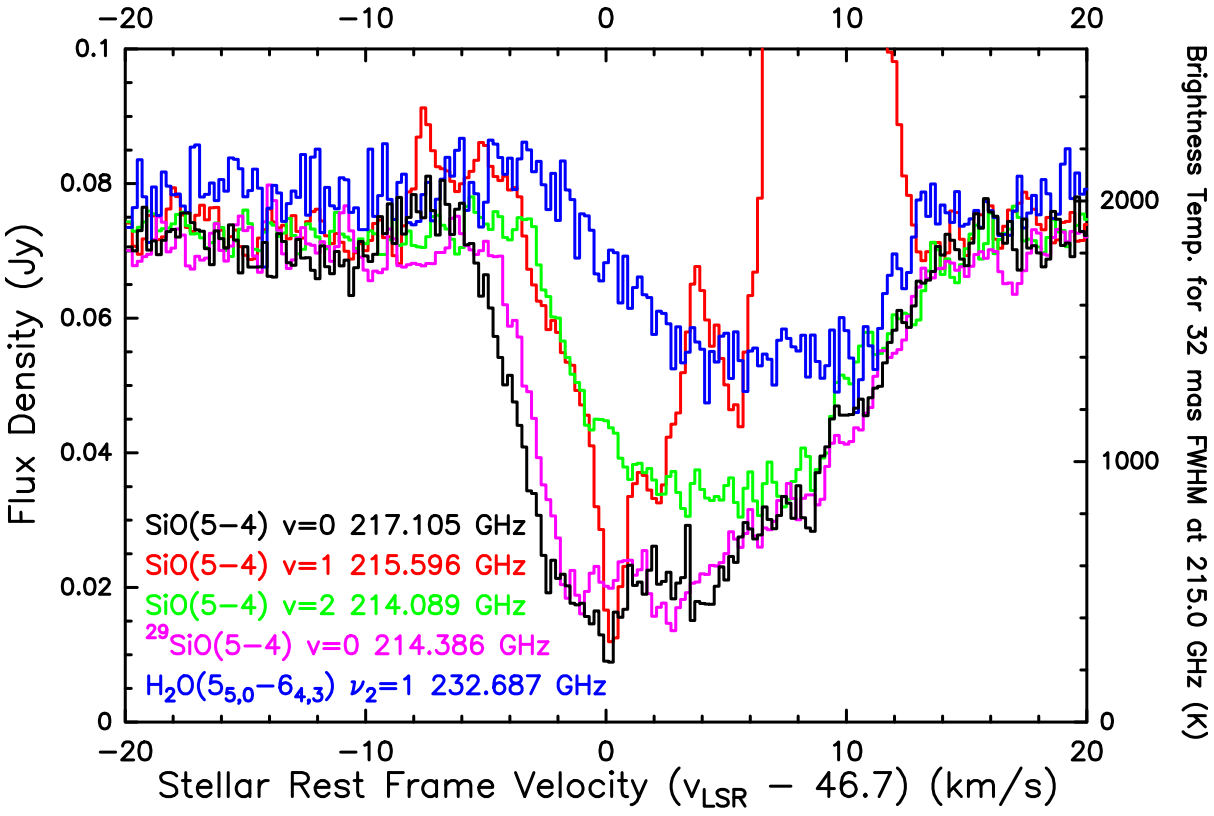

Figure 3.15.: Spectral lines in ALMA Band 6 extracted from the line of sight towards the centre of Mira's continuum. The SiO $v = 1$ $J = 5$–4 transition (in red) shows intense maser emission around +10 km s^{-1}, with the peak flux density of 1.73 Jy at +8.8 km s^{-1}. The maser spectrum above 0.10 Jy is not shown in this figure.

excited energy levels are less readily populated than the ground state levels, and hence the kinetic temperature of the bulk of the infalling material should be much lower than 3500 K, which corresponds to the excitation energies of SiO $v = 2$ and H_2O $v_2 = 1$ lines. This also explains the small radial extent of these two lines as shown in the channel maps because the kinetic temperature (and hence the excitation) in general falls off with the radial distance from the star. Because the SiO $v = 2$ and H_2O $v_2 = 1$ lines have very similar excitation energy ($E_{up}/k \sim 3500$ K), the difference in their line profiles is probably due to differences in the molecular abundance and molecular parameters such as the (de-)excitation rate coefficients.

There are two features in the spectra that strongly constrain our modelling in Sect. 3.4. The first is the small blueshifted emission feature at the offset velocities between −10 and −3 km s^{-1}. The size of the synthesised beam under robust weighting ($\mathcal{R}_{Briggs} = 0.5$) is about 0.″03, which is comparable to that of the disc of the continuum emission (with minor axis about 0.″04). Hence, some emission from the hottest inner layers of the envelope just outside the edge of the continuum disc is expected to 'leak' into the beam. Since the innermost envelope shows global infall kinematics, the flux leakage should appear as excess blueshifted emission, i.e. an inverse P Cygni profile. We have also checked the spectra at different offset positions (some of which are modelled in Sect. 3.4) and found that over the same blueshifted velocity range, the excess emission becomes more prominent as the continuum level decreases towards outer radial distances. For the H_2O transition, we also find a much weaker emission component near the offset velocity of −3 km s^{-1}, and a similar check at different offset positions also indicates that the component is likely to be real.

The other feature is presented by the redshifted wings in the offset velocity range between +10 and +14 km s^{-1} of the ^{28}SiO $v = 0$ and 2 and the ^{29}SiO $v = 0$ lines, which do not show strong maser emission. As shown in Fig. 3.15, the redshifted part of the absorption profiles of all these lines appears to be nearly identical. The lines could be in the optically thin regime only if the isotopic ratio of ^{28}SiO/^{29}SiO is close to unity, which is not expected. So we believe that all the lines are in the optically thick regime in this velocity range. The brightness temperatures of the redshifted wings thus give an indication of the kinetic temperature of the coolest gas around the corresponding infall velocities.

3.4. Radiative transfer modelling

We modelled the H_2O and SiO spectra with the radiative transfer code RATRAN (Hogerheijde & van der Tak, 2000). The public version of the code accepts 1-D input models only. Despite the clumpy structures of the inner envelope, we find that the line spectra exhibit general spherical symmetry within ~0.″16 and therefore 1-D modelling is applicable. Since the ALMA SV observations only provide a snapshot of Mira's extended atmosphere in its highly variable pulsation cycles, and the hydrodynamical models that we compare and discuss in Sect. 3.5.3 are also one dimensional, using a multi-dimensional radiative transfer code probably does not lead to better understanding of the general physical conditions of Mira's extended atmosphere. RATRAN solves the coupled level population and radiative transfer equations with the Monte Carlo method and generates an output image cube for each of the modelled lines. We then convolved the image cubes with the same restoring beam as in our image processing and extracted the modelled spectra from the same set of positions as the observed spectra (Figure 3.14). Section A explains the theoretical background of radiative transfer modelling. In the following subsections, we describe the details of our modelling, including the molecular data of H_2O and SiO, and the input physical models for the inner envelope with the continuum.

3.4.1. H_2O molecular data

The molecular data include information about all the energy levels considered in our radiative transfer model, and all possible transitions among these levels. The energies and statistical weights of the energy levels, and the Einstein A coefficients (the rates of spontaneous emission), frequencies, upper level energies, and collisional rate coefficients at various kinetic temperatures of the transitions are stored in a molecular datafile. The molecular datafile of H_2O is from the Leiden Atomic and Molecular DAtabase[11] (LAMDA; Schöier et al., 2005). The LAMDA H_2O datafile includes rovibrational levels up to about $E_{up}/k = 7190$ K (Tennyson et al., 2001). In our modelling, we only include 189 energy levels up to 5130 K in order to speed up the calculation. The selection includes 1804 radiative transitions and 17 766 downward collisional transitions. The numbers of energy levels and transitions were reduced by more than half and three quarters, respectively, compared to the original LAMDA file. Experiments have shown that such truncation of the datafile only has minute effects on the modelled spectra. The Einstein A coefficients were provided by the BT2 water line list[12] (Barber et al., 2006) and the collisional rate coefficients of H_2O with ortho-H_2 and para-H_2 were calculated by Faure & Josselin (2008a). The rates for ortho-H_2 and para-H_2 were weighted using the method described in Schöier et al. (2005).

[11] http://home.strw.leidenuniv.nl/~moldata/
[12] http://www.exomol.com/data/molecules/H2O/1H2-160

3.4.2. SiO molecular data

Our radiative transfer modelling of SiO lines considers the molecule's vibrational ground and the first two excited states ($v = 0, 1$, and 2) up to an upper-state energy, $E_{\rm up}/k$, of about 5120 K, similar to that for our H_2O modelling. There are a total of 167 rotational energy levels in these vibrational states, where $J(v = 0) \leq 69$, $J(v = 1) \leq 56$, and $J(v = 2) \leq 39$. Among these energy levels are 435 radiative transitions (subject to the dipole selection rule $\Delta J = \pm 1$) and 13 861 downward collisional transitions. The energies and statistical weights of the energy levels, and the line frequencies and Einstein A coefficients of the radiative transitions are obtained from the EBJT SiO line list[13] (Barton et al., 2013). These values are similar to those in the CDMS[14] (version Jan 2014) (Müller et al., 2001, 2005, 2013). The collisional rate coefficients of SiO–H_2 are described in Appendix B.2.

In our modelling, line overlapping between SiO and H_2O transitions, which may significantly affect the pumping of SiO masers (e.g. Desmurs et al., 2014, and references therein), is neglected.

3.4.3. Continuum emission

We include the continuum emission in the modelling. In RATRAN, however, the ray-tracing code (SKY) assumes that the size of the continuum is much smaller than the pixel size, which is not true in this ALMA dataset. Hence, we cannot include the continuum by setting the default RATRAN *central* parameter, which describes the radius and blackbody temperature of the central source, in the straightforward manner. Instead, in our input physical model, we have created a pseudo-continuum in the innermost three grid cells of the 1-D input model by setting (1) the outer radius of the third grid cell to be the physical radius of the radio continuum, (2) the 'kinetic temperature' to be the brightness temperature of the continuum, (3) the outflow velocity to zero, (4) the turbulence velocity to 100 km s^{-1} to get an effectively flat continuum spectrum within the velocity range of interest, and (5) the molecular abundance to be exceedingly high to get an optically thick core which blocks all the line emission from behind it. The exact number of grid cells representing the pseudo-continuum does not affect the results. The velocity range of the RATRAN image cubes was selected to be ± 25 km s^{-1} from the systemic velocity, which is the same as for our ALMA image products.

In our modelling, the continuum level and spectral line absorption/emission were fitted from independent sets of parameters. The radius and effective temperature of the radio continuum were determined by fitting the modelled continuum levels to the ones in the observed spectra extracted from the centre, from 32 mas and from 64 mas. Beyond these distances the continuum level is effectively zero. The derived radius and effective temperature of the pseudo-continuum is $R_{\rm continuum} = 3.60 \times 10^{13}$ cm (21.8 mas) and 2600 K, respectively. These values are comparable to the mean radii and brightness temperatures of the elliptical discs fitted by us (Sect. 3.3.1), by Matthews et al. (2015), and by Vlemmings et al. (2015).

3.4.4. Modelling results

In the models of Mira's extended atmosphere and its inner wind, power-laws are adopted for the H_2 gas density and kinetic temperature profiles such that the density and temperature attain their maximum values at the outer surface of the radio photosphere, $R_{\rm continuum}$. The profiles of the physical parameters are expressed as functions of the radial distance from the continuum centre, which is defined as 'radius' in the following discussion and in the plots of the input

[13] http://www.exomol.com/data/molecules/SiO/28Si-160
[14] Cologne Database for Molecular Spectroscopy; http://www.astro.uni-koeln.de/cdms/

physical models.

In order to reproduce the intensity of the spectra extracted from the centre and different projected distances, the SiO abundance (relative to molecular hydrogen abundance) has to decrease with radius. We assume a simple two-step function for the SiO abundance, where the outer abundance is ∼1% of the inner abundance. The radius at which SiO abundance drops significantly is assumed to be $r_{\rm cond} = 1.0 \times 10^{14}$ cm $\approx 5\,R_\star$ in our preferred model (Model 3). As we will discuss in Sect. 3.5.2.3, the observed spectra can still be fitted if $r_{\rm cond} \gtrsim 4\,R_\star$ or if the outer SiO abundance is ∼10% of the inner value (i.e. a degree of condensation of 90%). The depletion of SiO molecule represents the dust condensation process in the transition zone between the inner dynamical atmosphere and the outer, fully accelerated circumstellar envelopes.

For the H_2O molecule, however, condensation onto dust grains or solid ice is not expected in the modelled region where the gas temperature is at least a few hundred Kelvin. Furthermore, in the non-equilibrium chemical modelling of Gobrecht et al. (2016), the H_2O abundance in the inner winds of the oxygen-rich Mira variable IK Tau remains roughly constant with radius at a given stellar pulsation phase. Hence, we assume the H_2O abundance (relative to H_2) near Mira to be constant at 5.0×10^{-6} throughout the modelled region (out to 5.0×10^{14} cm $\approx 25\,R_\star \approx 0\farcs3$). For the reason discussed in Sect. 3.4.4.3, we also considered an alternative H_2O abundance profile with a sharp increase in H_2O abundance near the radio photosphere.

In our radiative transfer modelling, the expansion/infall velocity, gas density, and gas kinetic temperature are the crucial parameters in the input physical model. We empirically explored different types of profiles that are plausible in the inner winds and circumstellar envelopes of evolved stars. In Sects. 3.4.4.1 and 3.4.4.2, we present two models, Models 1 and 2, that fail to reproduce the observed SiO and H_2O spectra around Mira in ALMA Band 6; in Sect. 3.4.4.3, we show our preferred model (Model 3) in which both infall and outflow layers coexist in the extended atmosphere of Mira.

In Sect. 3.5.3, we will compare the velocity, density, and temperature profiles in our preferred model with those predicted by current hydrodynamical models of pulsating stellar atmospheres. We will also produce synthetic spectra of the observed lines using the atmospheric structures derived from those hydrodynamical models.

3.4.4.1. Model 1: infall-only model

We first test the infall velocity profiles with monotonically increasing infall velocity (Model 1). Figure 3.16 shows the profiles of the gas density (top left), infall velocity (top right), SiO and H_2O abundances (middle) and the kinetic temperature (bottom). The bottom row of Fig. 3.16 also shows the excitation temperatures of the SiO and H_2O transitions (in colour).

Figures 3.17, 3.18, and 3.19 show our modelled and observed spectra for SiO $v = 0$ $J = 5$–4, SiO $v = 2$ $J = 5$–4, and H_2O $v_2 = 1$ $J_{K_a,K_c} = 5_{5,0}$–$6_{4,3}$, respectively. The top left panel of these figures show the spectra extracted from the line of sight towards the continuum centre. Although Model 1 may fit well to the redshifted wings (about +10 to +15 km s^{-1}) of the SiO spectra, there is significant excess emission from the blueshifted velocities between about −10 and −4 km s^{-1}. The excess blueshifted emission is also seen in the spectra extracted from 32 mas. Additionally, in this spectra extracted from 32 mas, there is an absorption feature against the continuum near the redshifted velocity of about +10 km s^{-1}, which is not present in the observed spectra.

As we mention in Sect. 3.3, the observed weak blueshifted emission feature around the velocities from −10 to −3 km s^{-1} originates from the emission from the far side of Mira's

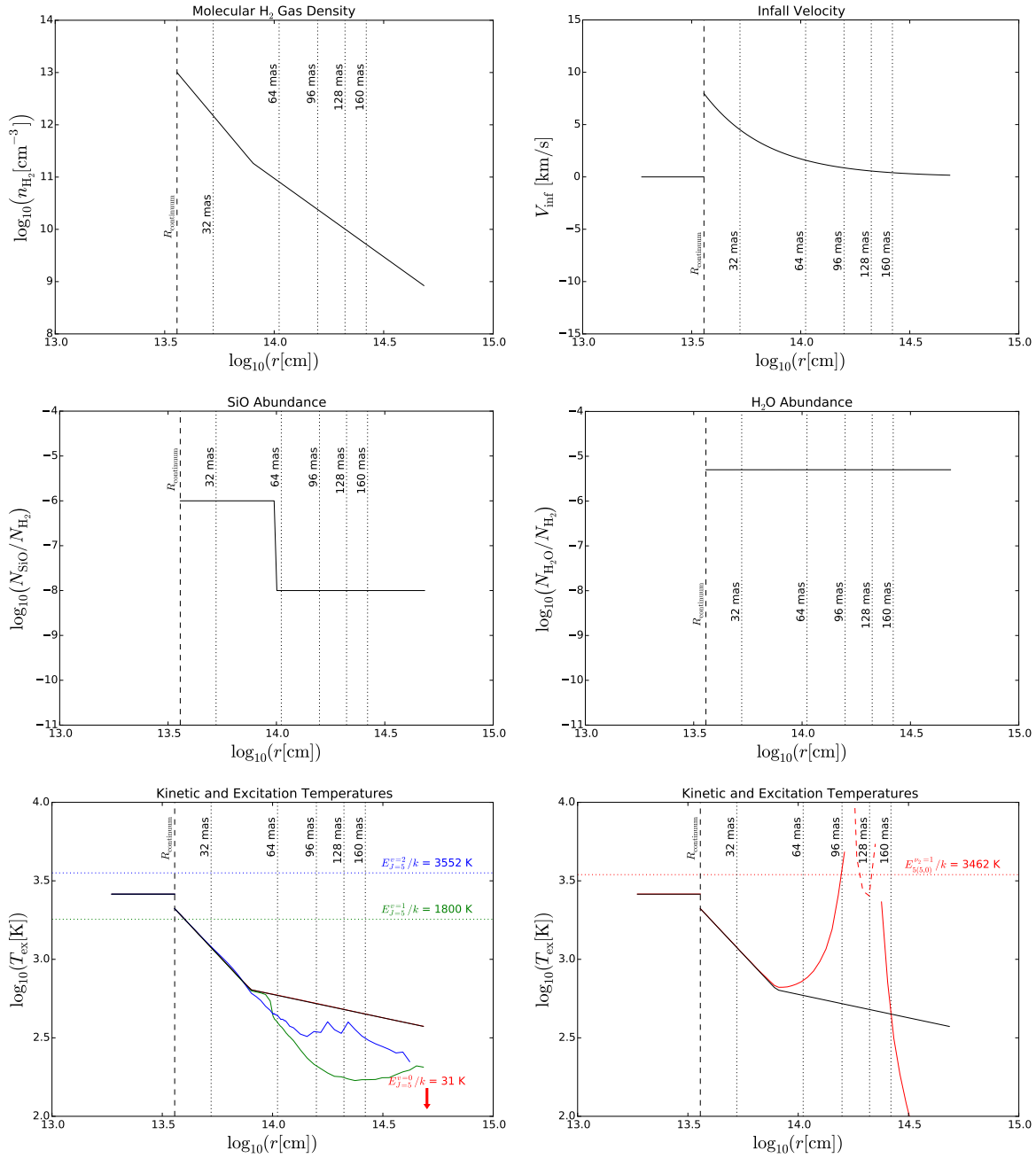

Figure 3.16.: Inputs for Model 1. Shown in the panels are the H_2 gas density (*top left*) , infall velocity (negative represents expansion) (*top right*), ^{28}SiO abundance (*middle left*), H_2O abundance (*middle right*), and the kinetic temperature (in black) and excitation temperatures (in colours) of the three ^{28}SiO transitions (*bottom left*) and the H_2O transition (*bottom right*). In the bottom right panel, the solid red line indicates positive excitation temperature (i.e. non-maser emission) of the H_2O transition, and the dashed red line indicates the absolute values of the negative excitation temperature (i.e. population inversion) between 1.7×10^{14} and 2.2×10^{14} cm. Small negative values for the excitation temperature would give strong maser emission. Vertical dotted lines indicate the radii at which the spectra were extracted; coloured horizontal dotted lines in the bottom panels indicates the upper-state energy (E_{up}/k) of the respective transitions. The innermost layer within $R_{continuum}$ represents the grid cells for the pseudo-continuum, where the input values for H_2 gas density and molecular abundances are above the range of the plots.

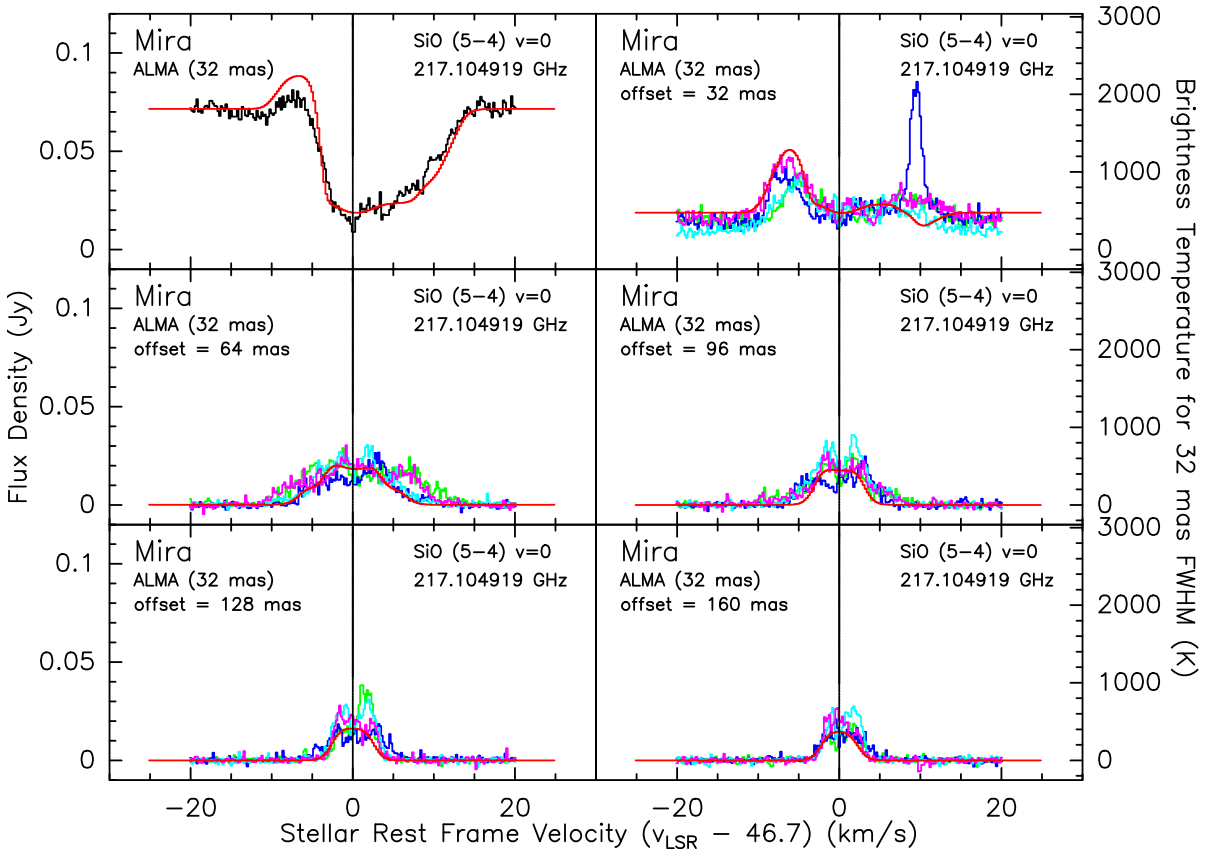

Figure 3.17.: Model 1: Spectra of SiO $v = 0$ $J = 5$–4 at various positions. The black histogram is the observed spectrum at the centre of continuum; the green, blue, cyan, and magenta histograms are the observed spectra along the eastern, southern, western, and northern legs, respectively, at various offset radial distances as indicated in each panel. The red curves are the modelled spectra predicted by RATRAN.

extended atmosphere. As the line of sight moves away from the continuum disc, the emission flux of the radio continuum, which is represented by a circular uniform disc in our input model and appears as a flat line in the spectra, falls off rapidly with radius; the flux of the far side molecular emission, on the other hand, decreases more gradually. Hence, the inverse P Cygni profile of the molecular transition emerges from the decreasing continuum level. The blueshifted emission feature in the resultant spectra after beam convolution represents the combined effect of the inner continuum-dominated emission and the outer line-dominated emission. The excess blueshifted emission in Model 1 therefore suggests two possibilities: (1) the gas temperature at the innermost radii in this model is significantly overestimated, and/or (2) this model does not reproduce sufficient absorption in the blueshifted velocities.

3.4.4.2. Model 2: infall-only model with reduced temperature at the innermost radii

For the first postulation, we constructed Model 2, which is identical to Model 1, the only exception being that the gas temperature near the radio photosphere is significantly reduced from 2100 K in the original model to about 1400 K. Figure 3.20 shows the input gas temperature and the modelled excitation temperature profiles for the SiO and H_2O transitions. Figures 3.21, 3.22, and 3.23 show the modelled spectra with reduced input gas temperature.

Our modelling results in Figs. 3.21, 3.22, and 3.23 show that even if we reduce the kinetic temperature to $\lesssim$ 1400 K in the entire inner wind of Mira, there is still an excess in

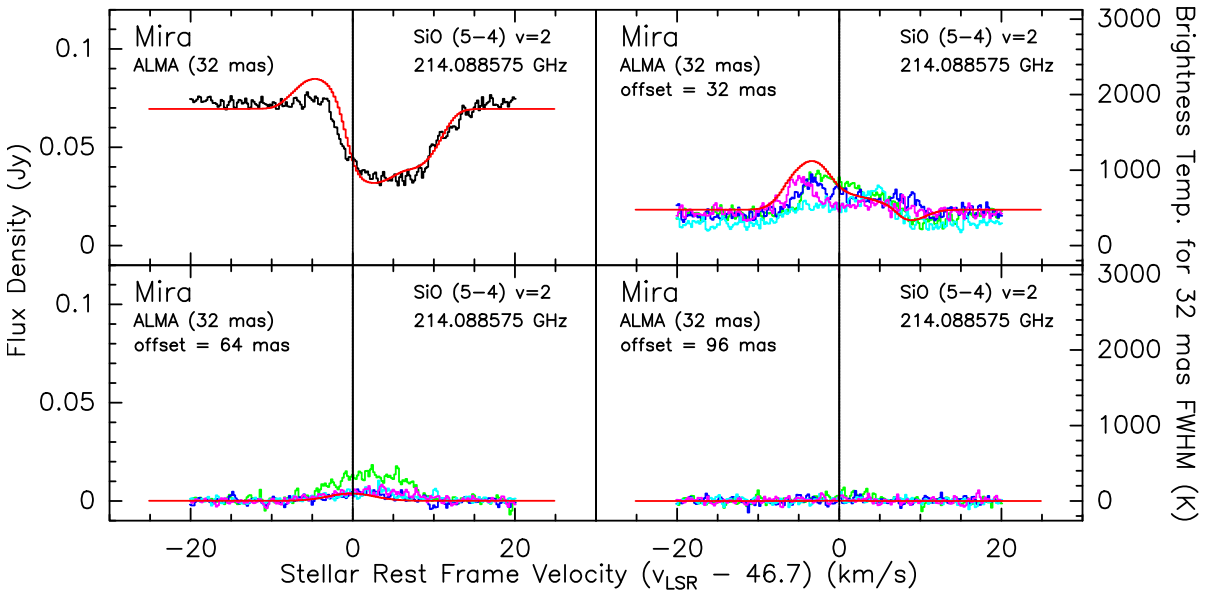

Figure 3.18.: Model 1: Spectra of SiO $v = 2$ $J = 5$–4 at various positions. The black histogram is the observed spectrum at the centre of continuum; the green, blue, cyan, and magenta histograms are the observed spectra along the eastern, southern, western, and northern legs, respectively, at various offset radial distances as indicated in each panel. The red curves are the modelled spectra predicted by RATRAN.

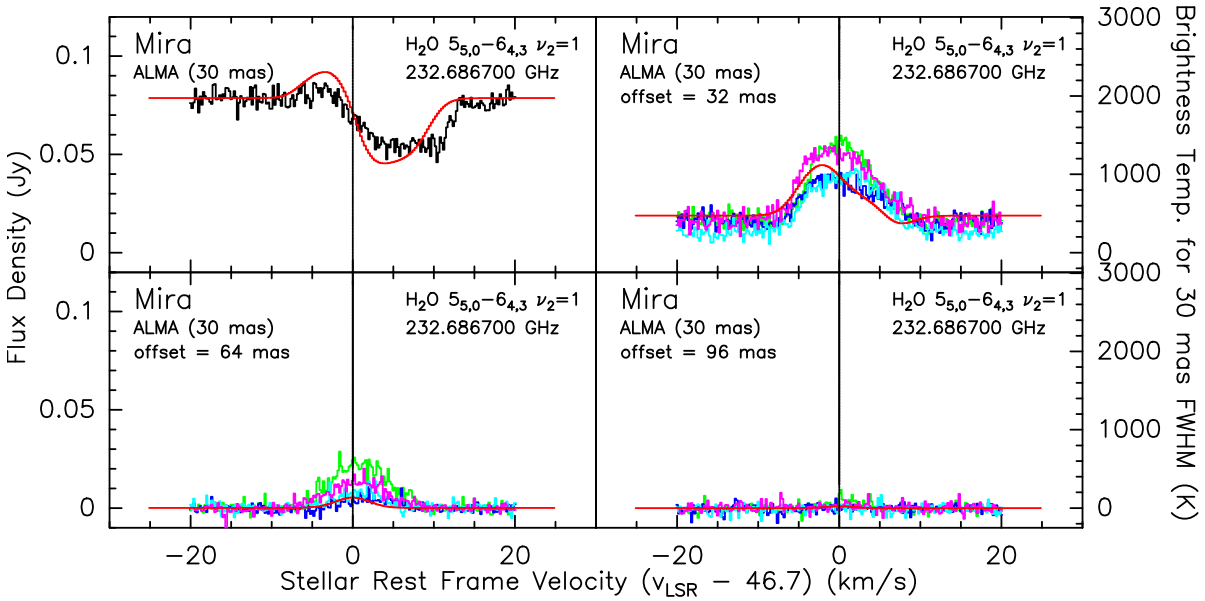

Figure 3.19.: Model 1: Spectra of H_2O $v_2 = 1$ $J_{K_a,K_c} = 5_{5,0}$–$6_{4,3}$ at various positions. The black histogram is the observed spectrum at the centre of continuum; the green, blue, cyan, and magenta histograms are the observed spectra along the eastern, southern, western, and northern legs, respectively, at various offset radial distances as indicated in each panel. The red curves are the modelled spectra predicted by RATRAN.

the blueshifted emission. In fact, we have found that the gas temperature near the radio photosphere has to be much lower than 1000 K in order to get rid of this excess emission. In addition, when the kinetic temperature in the proximity of the continuum is reduced, excess

absorption relative to the observed spectra would appear in both the SiO and H_2O spectra. Although the excess absorption may be compensated by adopting different gas density and molecular abundance profiles, we do not consider the low-temperature atmosphere to be a likely solution.

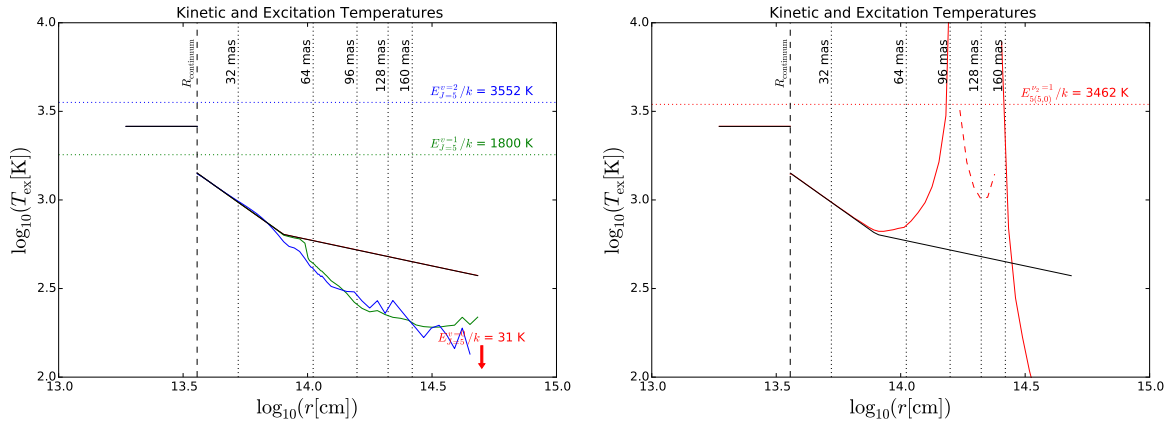

Figure 3.20.: Input temperature for Model 2. The panels show the kinetic temperature (in black) and excitation temperatures (in colours) of the three ^{28}SiO transitions (*left*) and the H_2O transition (*right*). In the right panel, the solid red line indicates positive excitation temperature (i.e. non-maser emission) of the H_2O transition, and the dashed red line indicates the absolute values of the negative excitation temperature (i.e. population inversion) between 1.7×10^{14} and 2.4×10^{14} cm. Small negative values for the excitation temperature would give strong maser emission. Vertical dotted lines mark the radii at which the spectra were extracted; coloured horizontal dotted lines in the bottom panels indicates the upper-state energy ($E_{\rm up}/k$) of the respective transitions. The innermost layer within $R_{\rm continuum}$ represents the grid cells for the pseudo-continuum.

We therefore speculate that in the hot and dense part of the extended atmosphere of Mira (presumably at the innermost radius), there should be a relatively low infall velocity, or even an expanding component contributing to the absorption in the blueshifted part of the spectra. In other words, the infall velocity in the modelled region should not increase monotonically towards the star, but has to decelerate at some radii. In our preferred model (Model 3), we modify the velocity profile such that the motion of the bulk material switches from infall to expansion rapidly at 3.75×10^{13} cm, which is just above our adopted radio photosphere ($R_{\rm continuum} = 3.60\times10^{13}$cm). This expansion zone lies beneath the infall region and hence a large-scale shock of velocity $\Delta V \lesssim 12$ km s^{-1} (constrained by the width of the line profile) could be created near this radius.

3.4.4.3. Model 3: mixed infall and outflow

Our modelling shows that pure infall would produce too much emission in the blueshifted velocities of the spectra than is observed (Sects. 3.4.4.1 and 3.4.4.2). The excess emission component, as we have discussed in Sect. 3.3.3, originates from the far-side of the innermost layer (beyond the radio photosphere) of Mira's extended atmosphere that is not blocked by the radio continuum disc. In our preferred model, we introduce a thin expanding layer ($\sim5\times10^{11}$ cm $\approx 0.03\,R_\star$) in the innermost radii between the radio photosphere and the globally infalling layer. Alternating outflow and infall velocity profiles have been calculated numerically by Bowen (1988a,b) for Mira-like variables, and subsequently adopted by Humphreys et al. (1996, 2001) to simulate the SiO and H_2O masers from a Mira-like M-type variable

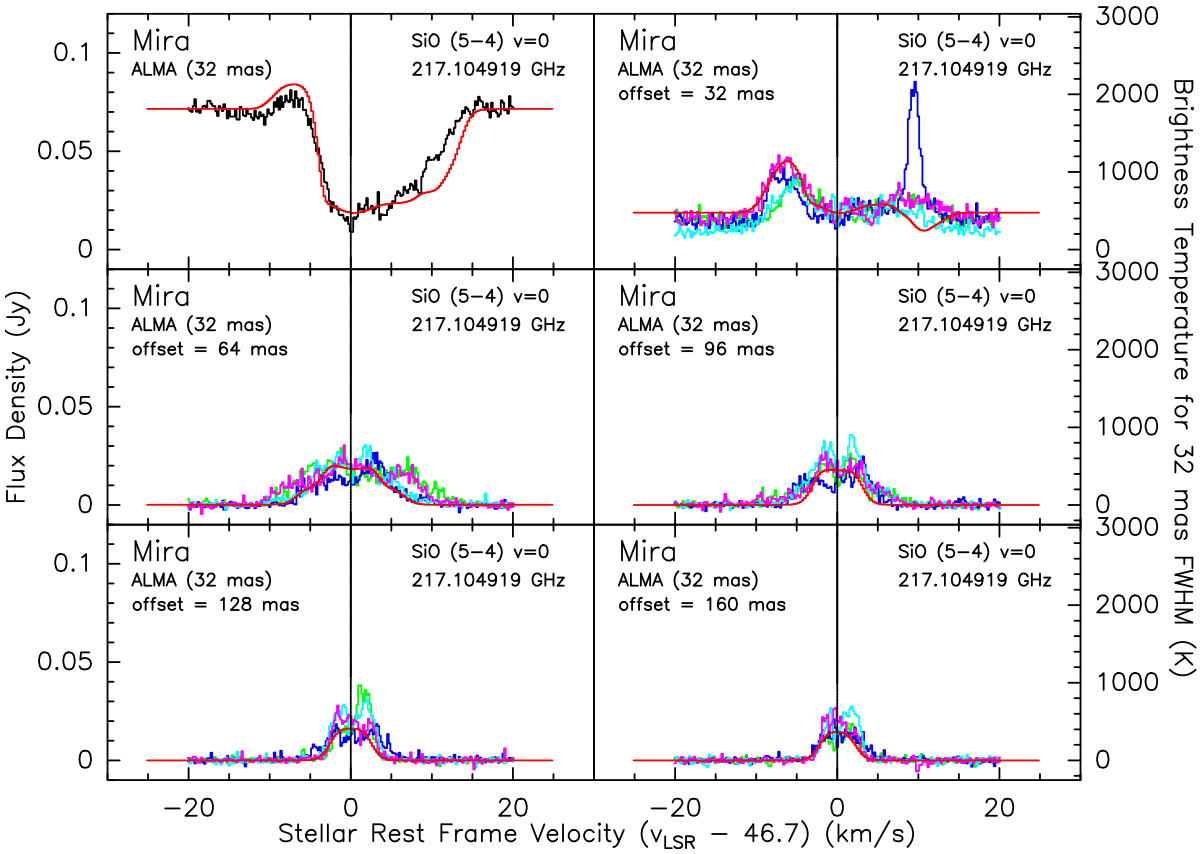

Figure 3.21.: Model 2: Spectra of SiO $v = 0$ $J = 5$–4 at various positions. The black histogram is the observed spectrum at the centre of continuum; the green, blue, cyan, and magenta histograms are the observed spectra along the eastern, southern, western, and northern legs, respectively, at various offset radial distances as indicated in each panel. The red curves are the modelled spectra predicted by RATRAN.

star at a single stellar phase. The infall velocity immediately above this expanding layer is about 7.3 km s^{-1}, and the expansion velocity below this layer is about 4.0 km s^{-1}. The outer infalling gas and the inner expanding layer produce a shocked region with the shock velocity of $\Delta V \lesssim 12$ km s^{-1} near the radio photosphere of Mira. The maximum gas infall speed of $\sim$7 km s^{-1} is consistent with the proper motions of SiO maser spots around another oxygen-rich Mira variable TX Cam, which lie in the velocity range of 5–10 km s^{-1} (Diamond & Kemball, 2003). The emission from the far-side of the expanding layer would appear at redshifted velocities and the absorption from the near-side would be in the blueshifted part (i.e. the usual P Cygni profile). The excess emission from the pure infall models is therefore reduced to a level that fits the observed spectra.

To properly fit the line profiles, the radius of peak infall velocity adopted is 3.75×10^{13} cm, where the gas density is almost 10^{13} cm^{-3}. Figure 3.24 shows the important input parameters in our model, including the molecular H_2 gas density (top left), infall velocity (top right), molecular SiO and H_2O abundances (middle), and the gas kinetic temperature (bottom). The bottom row of Fig. 3.24 also shows the excitation temperatures of the SiO and H_2O transitions (in colour).

Figures 3.25, 3.26, and 3.27 show the comparison of our modelled and observed spectra of SiO $v = 0$ $J = 5$–4, SiO $v = 2$ $J = 5$–4, and H_2O $v_2 = 1$ $J_{K_a,K_c} = 5_{5,0}$–$6_{4,3}$, respectively. The

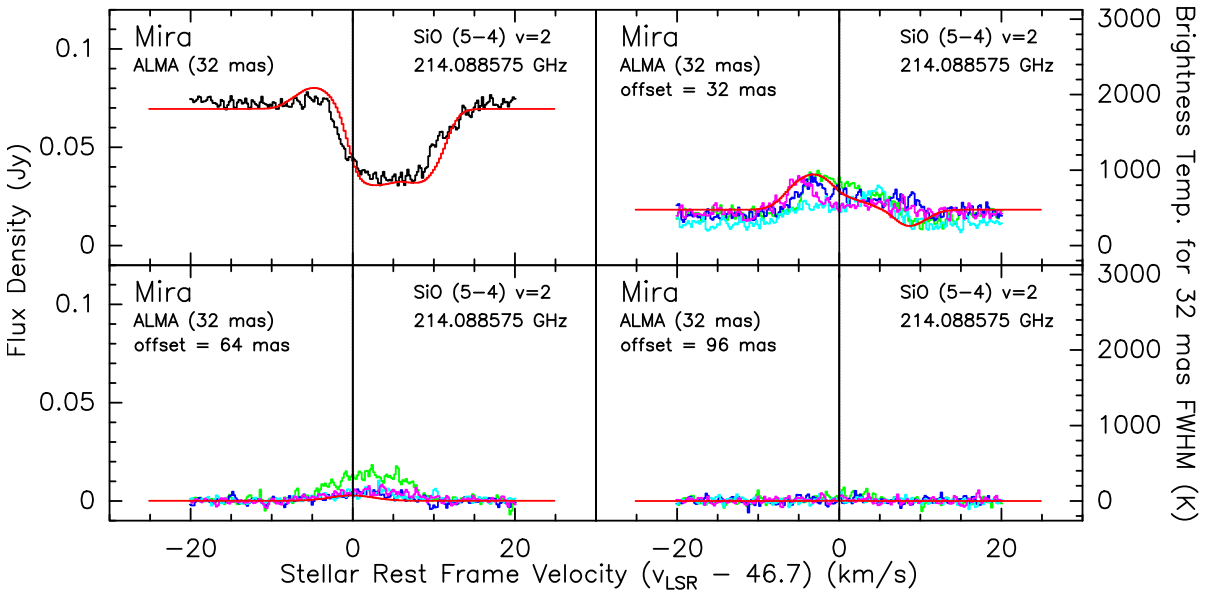

Figure 3.22.: Model 2: Spectra of SiO $v = 2$ $J = 5$–4 at various positions. The black histogram is the observed spectrum at the centre of continuum; the green, blue, cyan, and magenta histograms are the observed spectra along the eastern, southern, western, and northern legs, respectively, at various offset radial distances as indicated in each panel. The red curves are the modelled spectra predicted by RATRAN.

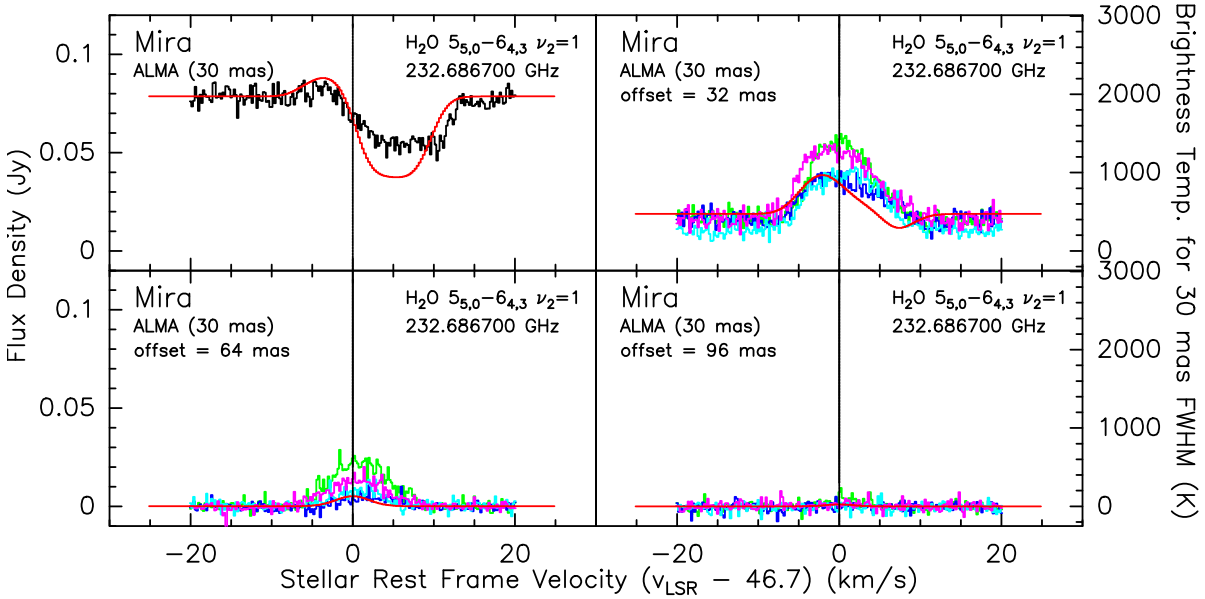

Figure 3.23.: Model 2: Spectra of H_2O $v_2 = 1$ $J_{K_a,K_c} = 5_{5,0}$–$6_{4,3}$ at various positions. The black histogram is the observed spectrum at the centre of continuum; the green, blue, cyan, and magenta histograms are the observed spectra along the eastern, southern, western, and northern legs, respectively, at various offset radial distances as indicated in each panel. The red curves are the modelled spectra predicted by RATRAN.

top left panel of these figures show the spectra extracted from the line of sight towards the continuum centre.

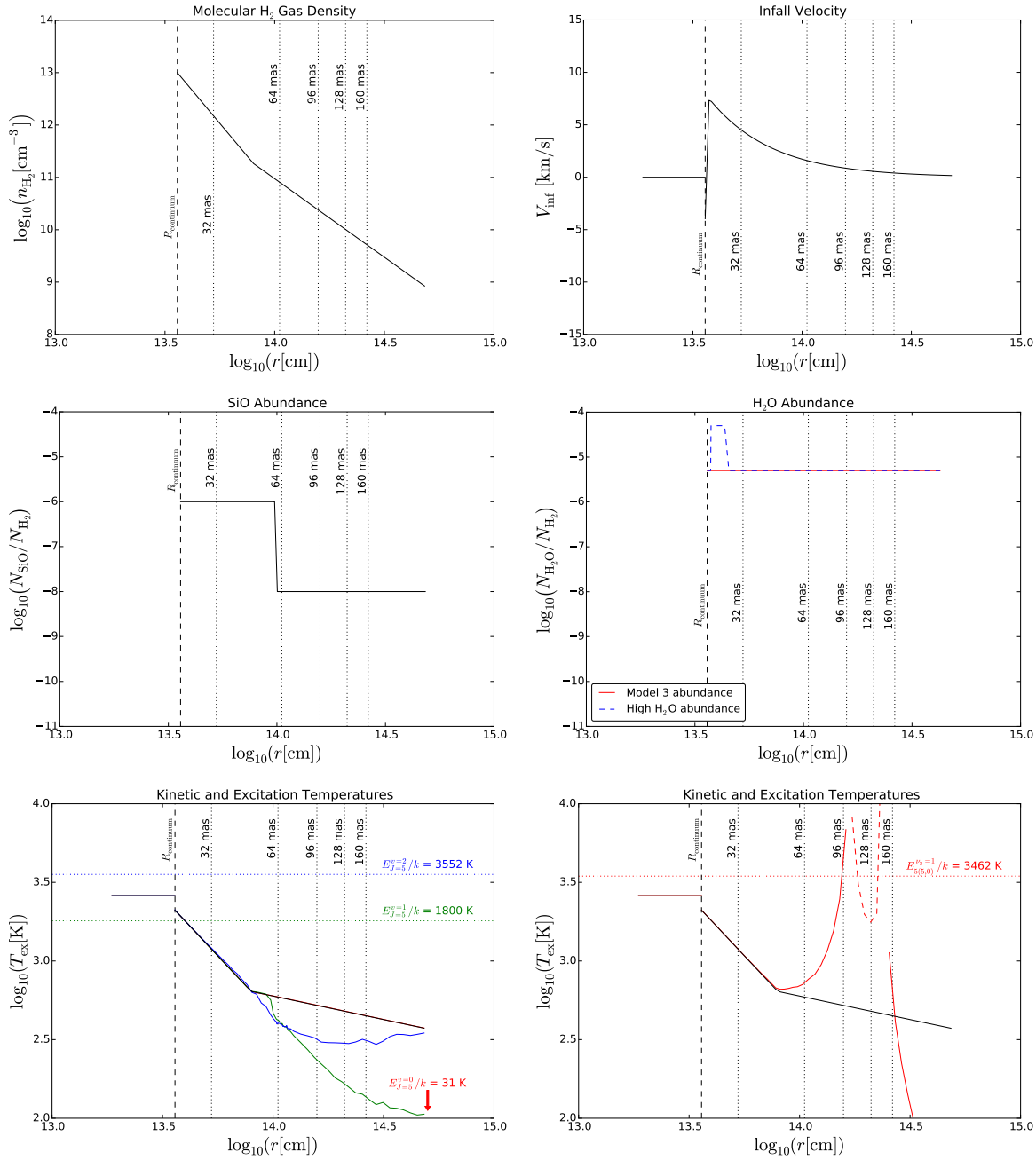

Figure 3.24.: Inputs of our preferred model. Shown in the panels are the H_2 gas density (*top left*) , infall velocity (negative represents expansion) (*top right*), ^{28}SiO abundance (*middle left*), H_2O abundance (*middle right*), and the kinetic temperature (in black) and excitation temperatures (in colours) of the three ^{28}SiO transitions (*bottom left*) and the H_2O transition (*bottom right*). In the bottom right panel, the solid red line indicates positive excitation temperature (i.e. non-maser emission) of the H_2O transition, and the dashed red line indicates the absolute values of the negative excitation temperature (i.e. population inversion) between 1.7×10^{14} and 2.4×10^{14} cm. Small negative values for the excitation temperature would give strong maser emission. Vertical dotted lines indicate the radii where the spectra were extracted; coloured horizontal dotted lines in the bottom panels indicates the upper-state energy ($E_{\rm up}/k$) of the respective transitions. The innermost layer within $R_{\rm continuum}$ represents the grid cells for the pseudo-continuum, whose input values for H_2 gas density and molecular abundances are above the range of the plots.

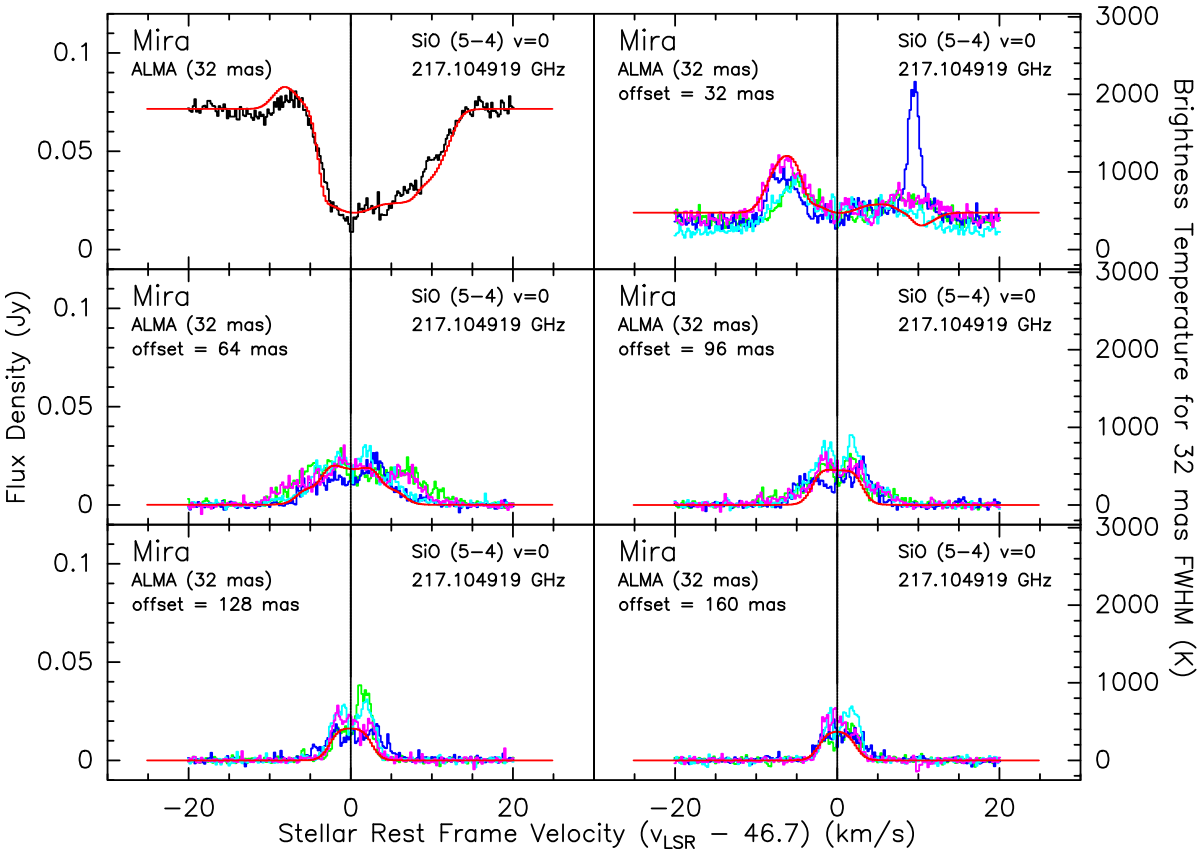

Figure 3.25.: Preferred model: spectra of SiO $v = 0$ $J = 5$–4 at various positions. The black histogram is the observed spectrum at the centre of continuum, green, blue, cyan, and magenta histograms are the observed spectra along the eastern, southern, western, and northern legs, respectively, at various offset radial distances as indicated in each panel. The red curves are the modelled spectra predicted by RATRAN. Our model does not produce the population inversion (i.e. negative excitation temperature) required for maser emission in this SiO transition, so we do not expect our modelled spectra to show any maser emission, as seen in the spike in the upper right panel (see text for the discussion of the spike).

The top right panel of Fig. 3.25 shows the modelled and observed SiO spectra at 32 mas. In our modelled spectrum, there is a small absorption feature near the redshifted velocity of +10 km s^{-1}, which is not seen in the data. This spectral feature is indeed part of the broad absorption as seen along the line of sight towards the radio continuum, which appears in the spectra at 32 mas owing to beam convolution. Hence, we may have introduced too much absorption into the model, in particular near the peak infall velocities. Inhomogeneities in the images may have introduced additional emission features to the spectra, but this is not the case here. For example, there is a sharp spike in the observed spectra extracted from the southern position (in blue). This feature is due to an intensely emitting SiO clump at ~26 mas to the south of the continuum centre. The maximum brightness temperature of this clump in the map is ~2300 K. The intense emission from this clump is probably due to maser action; if it were thermal in nature, then one would also expect the corresponding ^{29}SiO line to be detected with intense emission from this clump. However, this clump is too far away from the other positions from which the spectra were extracted to contribute significant emission. Another possible explanation is that the infall velocity in our model may decrease too quickly with radius. For

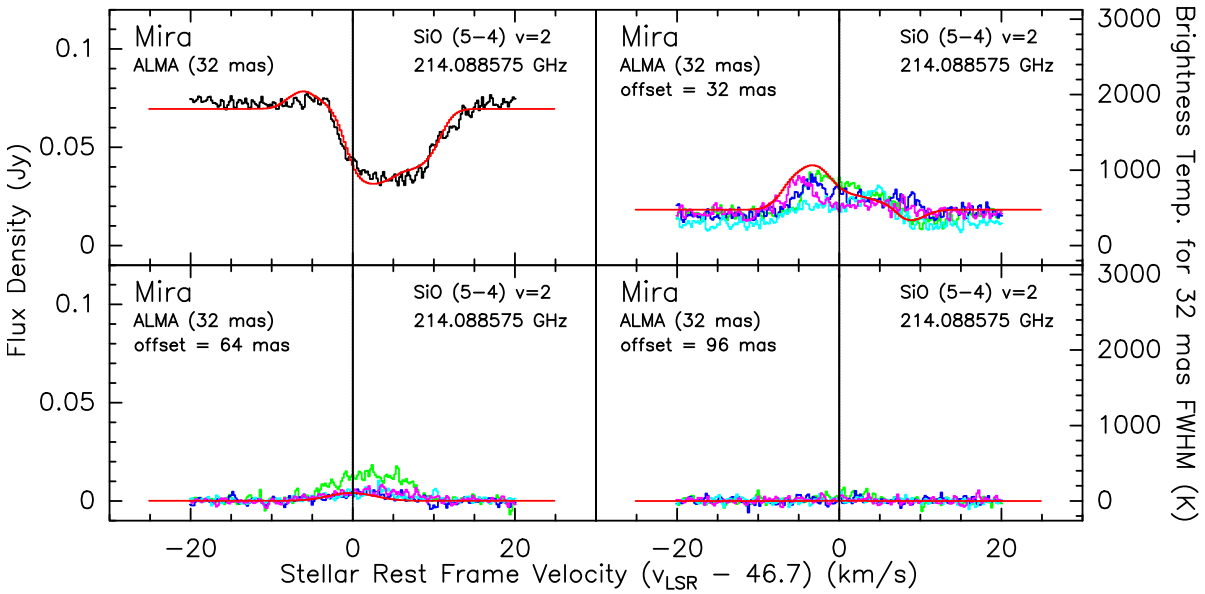

Figure 3.26.: Preferred model: spectra of SiO $v = 2$ $J = 5$–4 at various positions. The black histogram is the observed spectrum at the centre of continuum, green, blue, cyan, and magenta histograms are the observed spectra along the eastern, southern, western, and northern legs, respectively, at various offset radial distances as indicated in each panel. The red curves are the modelled spectra predicted by RATRAN.

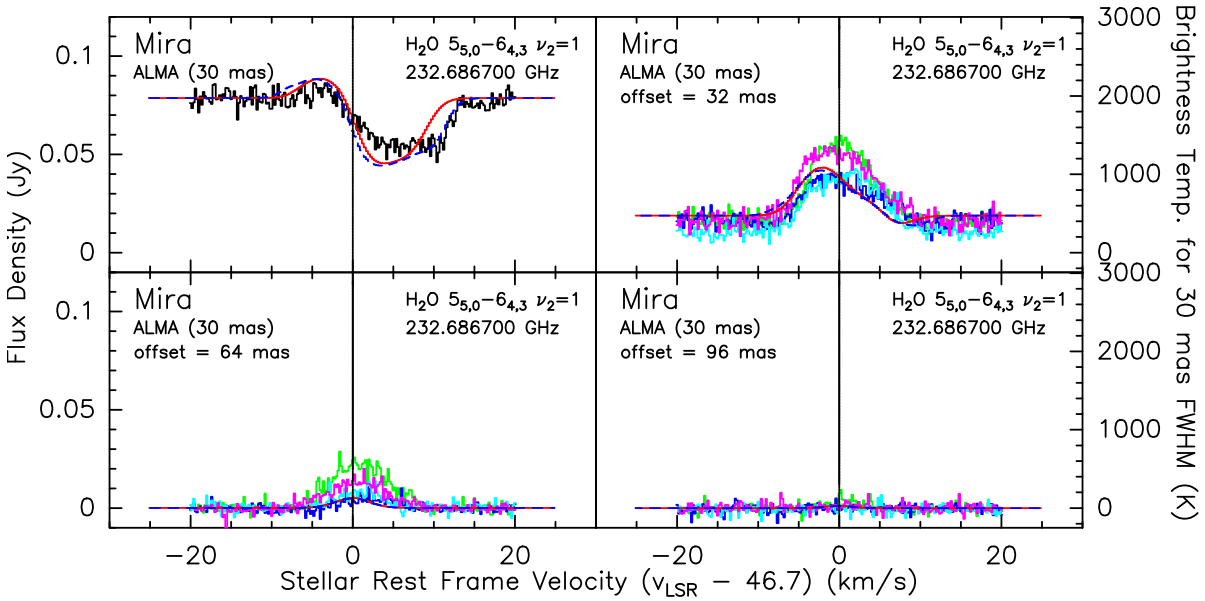

Figure 3.27.: Preferred model: spectra of H_2O $v_2 = 1$ $J_{K_a,K_c} = 5_{5,0}$–$6_{4,3}$ at various positions. The black histogram is the observed spectrum at the centre of continuum, green, blue, cyan, and magenta histograms are the observed spectra along the eastern, southern, western, and northern legs, respectively, at various offset radial distances as indicated in each panel. The red curves are the modelled spectra predicted by RATRAN, and the blue dashed curves are the same model adopting a high H_2O abundance (see the middle right panel of Fig. 3.24).

example, at the offset of 64 mas, our modelled SiO $v = 0$ spectrum appears to be narrower than the observed spectra (middle left panel of Fig. 3.25). We tried including a constant velocity

layer of 10^{13} cm at the peak infall velocity, but we were not able to eliminate the absorption feature near +10 km s^{-1}. If we adopt a much higher temperature, up to about 2600 K, in the immediate proximity of the radio photosphere, then we would introduce too much blueshifted emission to the resultant spectra. Also, our spherically symmetric and homogeneous model obviously fails to reproduce the features arising in individual clumps.

In Fig. 3.27, we present two different models of the H_2O spectral fitting using different input abundance profiles, which are plotted in the middle right panel of Fig. 3.24. As shown in the top left panel of Fig. 3.27, the modelled spectra using constant abundance profile ('Model 3 abundance'; in red) do not fit well to the observed H_2O absorption spectra (in black) along the line of sight towards the continuum centre. In particular, the modelled spectrum does not show the strong observed absorption in the extreme redshifted velocities > 10 km s^{-1}. Hence, we have to introduce a sharp rise in the input H_2O abundance by about 10 times, to 5.0×10^{-5}, within the innermost region where the infall velocity peaks ('High H_2O abundance'; in blue) in order to reproduce the strong redshifted absorption feature in the spectrum.

Overall, considering the complexity of Mira's extended atmosphere and inner wind, we believe that Model 3 can satisfactorily reproduce most of the features in the observed SiO and H_2O spectra in ALMA Band 6. We therefore adopt it as our preferred model and use it as the base model of our further tests in Sect. 3.5.

3.5. Discussion

3.5.1. Caveat in the interpretation of the gas density

In our modelling, we assume that the gas in Mira's extended atmosphere is composed of purely neutral, molecular hydrogen (H_2) in its rotationally ground state, $J = 0$. At radii close to the radio photosphere of evolved stars, atomic hydrogen could be the dominant species in terms of number density (Glassgold & Huggins, 1983; Doel, 1990; Reid & Menten, 1997a). Glassgold & Huggins (1983) have demonstrated that the atmosphere of an evolved star with the effective temperature of about 3000 K would be essentially atomic, and that the atmosphere of a star of about 2000 K would be essentially molecular. Since the effective temperature of the star is expected to be higher than the brightness temperature of the radio photosphere (e.g. Reid & Menten, 1997a), there should be a significant amount of atomic hydrogen present in the regions being modelled. Intense hydrogen Balmer series emission lines have long been detected in the atmosphere of Mira (e.g. Joy, 1926, 1947, 1954; Gillet et al., 1983; Fabas et al., 2011). The hydrogen emission is thought to be the result of dissociation and recombination of the atom due to shock waves propagating through the partially ionized hydrogen gas in the atmospheres of Mira variables (e.g. Fox et al., 1984; Fadeyev & Gillet, 2004). In addition, molecular hydrogen could well be excited to higher rotational levels (see our discussion in Appendix B.2.3).

We note that the collisional rate coefficients between SiO molecule and atomic hydrogen (H) and electrons (e^-) have already been computed by Palov et al. (2006) and Varambhia et al. (2009), respectively. However, in this study we did not attempt to calculate the fractional distribution of atomic/molecular hydrogen or to consider the collisions between SiO molecules and atomic hydrogen, helium, or electrons. Hence, the derived H_2 gas density from our RATRAN modelling is just a proxy of the densities of all possible collisional partners of SiO, including rotationally excited molecular hydrogen, atomic hydrogen, helium, and even electrons, in the extended atmosphere of Mira.

In order to examine how well the H_2 gas density in our preferred model is constrained, we modelled the SiO and H_2O spectra by scaling the gas density by various factors. Figure

3.28 shows the results of these sensitivity tests on the input gas density. We find that the SiO spectra, extracted from the line of sight towards the centre of the continuum, does not vary too much, even if the gas density is varied by about an order of magnitude. On the other hand, the H_2O spectra extracted from the centre shows significant change in the absorption depth even if the gas density is changed by a factor of ~2. Hence, assuming other input parameters (particularly the molecular abundances and gas temperature) of Model 3 are fixed, our derived gas density is tightly constrained. The gas density reaches 10^{12}–10^{13} cm^{-3}, just beyond the radio photosphere. This is consistent with other models that explain the radio continuum fluxes from Mira's radio photosphere (Reid & Menten, 1997a) and the near-infrared H_2O spectrum (Yamamura et al., 1999a). On the other hand, the derived gas density is much higher (by 2–4 orders of magnitude) than those predicted from hydrodynamical models (see Sect. 3.5.3.3).

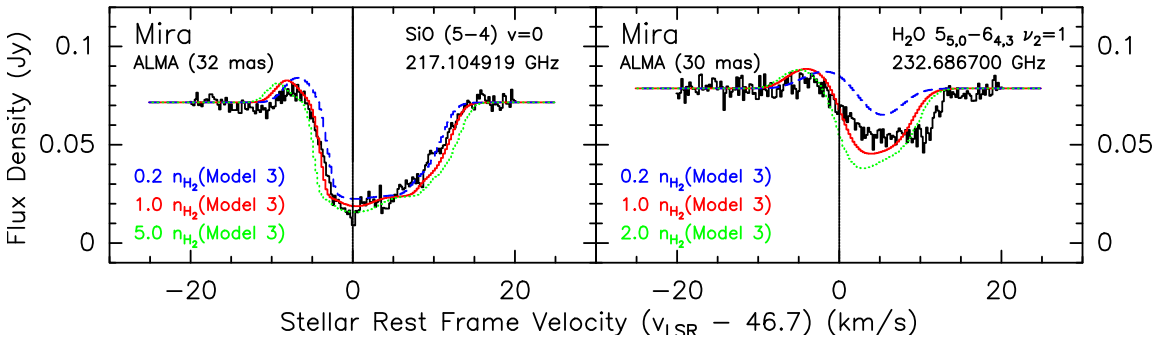

Figure 3.28.: Spectra of SiO $v = 0$ $J = 5$–4 (left) and H_2O $v_2 = 1$ $J_{K_a,K_c} = 5_{5,0}$–$6_{4,3}$ (right) extracted from the centre of the continuum. The black histogram is the observed spectrum and the red curves are the modelled spectra from our preferred model, Model 3. The blue dashed curves are the spectra obtained by reducing the input H_2 gas density by a factor of 5; and the green dotted curves are the spectra obtained by increasing the input gas density by a factor of 5 for the modelling of SiO, and a factor of 2 for H_2O.

3.5.2. Structure of the extended atmospheres

Our modelling results of the molecular emission and absorption of SiO and H_2O gas allow us to compare the structure of the extended atmosphere of Mira as inferred from previous observations in various frequencies. We first briefly summarise the relevant observations of Mira in Sect. 3.5.2.1, then discuss our interpretation on Mira's molecular layer in Sect. 3.5.2.2, and the dust condensation zone in Sect. 3.5.2.3.

3.5.2.1. Previous observations

Combining their centimetre-wavelength observations and millimetre/infrared fluxes in the literature, Reid & Menten (1997a) have demonstrated that long-period variables have a 'radio photosphere' with a radius about twice that of the optical/infrared photosphere. In the following discussion, we adopt the value of $R_\star$ to be 12.3 mas (or 292 $R_\odot$) as determined by Perrin et al. (2004). The spectral index at the radio wavelengths is found to be 1.86(≈2), close to the Rayleigh-Jeans law at low frequencies of an optically thick blackbody (Reid & Menten, 1997a). Matthews et al. (2015) and Planesas et al. (2016) found that this spectral index can also fit well the submillimetre flux densities of o Cet at 338 GHz in ALMA Band 7 and at 679 GHz in ALMA Band 9, respectively.

The radio photosphere encloses a hot, optically thick molecular layer (~2×10^3 K) predominantly emitting in the infrared. Observations have revealed that this molecular layer lies

between radii of ~1 and 2 $R_\star$. Haniff et al. (1995) found that, for *o* Cet, the derived radius of the strong TiO absorption near 710 nm with a uniform disc model is about $1.2 \pm 0.2\,R_\star$. Perrin et al. (2004) have fitted a model consisting of an infrared photosphere and a thin, detached molecular (H_2O+CO) layer to the infrared interferometric data, and have found that the radius of the molecular layer around *o* Cet is about $2.07 \pm 0.02\,R_\star$. Alternatively, Yamamura et al. (1999a) have modelled the H_2O spectral features in the near-infrared (~2–5 μm) spectrum of *o* Cet with a stack of superposing plane-parallel layers: the star, an assumed hot SiO (2000 K) layer, a hot H_2O (2000 K), and a cool H_2O (1200 K) layers. Assuming the hot SiO layer has a radius of $2.0\,R_\star$, they have derived the radii of the hot and cool H_2O layers to be $2.0\,R_\star$ and $2.3\,R_\star$, respectively. Ohnaka (2004) have employed a more realistic model for the extended molecular layer with two contiguous spherical shells, a hotter and a cooler H_2O shell, above the mid-infrared photosphere. By fitting to the 11 μm spectrum, Ohnaka (2004) have derived the radii of $1.5\,R_\star$ and $2.2\,R_\star$ for the hot (1800 K) and cool (1400 K) H_2O shells, respectively.

Beyond the molecular layer and the radio photosphere, there is a ring-like region of SiO maser emission at the radius between $2\,R_\star$ and $3\,R_\star$. Maser emission naturally arises from a ring-like structure because the maser requires a sufficiently long path length of similar radial velocity in order to be tangentially amplified to a detectable brightness (Diamond et al., 1994). Such a SiO maser ring has been imaged in detail at various stellar phases towards the oxygen-rich Mira variable TX Cam (e.g. Diamond & Kemball, 2003; Yi et al., 2005). For *o* Cet, Reid & Menten (2007) have directly imaged the radio photosphere and the SiO $J = 1$–0 maser emission at 43 GHz and found that the radii of the radio photosphere and the SiO maser ring are about $2.1\,R_\star$ and $3.3\,R_\star$, respectively, with $R_\star = 12.29 \pm 0.02$ mas being the radius of the infrared photosphere as model-fitted by Perrin et al. (2004).

Further out, beyond the SiO maser emission region, dust grains start to form. The major types of dust around oxygen-rich AGB stars are corundum (Al_2O_3) and silicate dust. Using the hydrodynamical model from Ireland et al. (2004a) and Ireland et al. (2004b), Gray et al. (2009) have modelled SiO maser emission in Mira variables and found that the presence of Al_2O_3 dust may either enhance or suppress SiO maser emission. From interferometric observations of various Mira variables at near-infrared (2.2 μm), mid-infrared (8–13 μm), and radio (43 GHz, 7 mm) wavelengths, Perrin et al. (2015) have fitted the visibility data with models similar to those of Perrin et al. (2004) (stellar photosphere + detached shell of finite width) and found that Al_2O_3 dust predominantly forms between $3\,R_\star$ and $4.5\,R_\star$, while silicate dust forms in $12\,R_\star$–$16\,R_\star$, which is significantly beyond the radius of SiO maser emission and the silicate dust formation radius derived from previous observations (e.g. Danchi et al., 1994).

3.5.2.2. Molecular layer

From our visibility analysis (see Sect. 3.3.1), we determine the mean radius of the 1.3 mm photosphere to be $R_{229\,\mathrm{GHz}} = 22.90 \pm 0.05$ mas ($543\,R_\odot$). This is about 1.9 times the size of the near-infrared photosphere ($R_\star = 12.3$ mas; $292\,R_\odot$) determined by Perrin et al. (2004). As we have summarised, previous visibility modelling of near- (2–5 μm) and mid-infrared (11 μm) interferometric data has suggested the existence of an optically thick, hot molecular H_2O+SiO layer with a maximum radius of $2.3\,R_\star$ (~30 mas) (Yamamura et al., 1999a; Ohnaka, 2004). Thus, this ALMA SV observation has a sufficient angular resolution to resolve the hot molecular layer in the millimetre-wavelength regime and, in addition, allows its velocity structure to be probed.

Modelling the spectral lines of H_2O and SiO molecules at various projected radial distances from the star, we have determined that the kinetic gas temperature within the mid-infrared molecular layer (30 mas $\sim 5 \times 10^{13}$ cm) has to be about 1400–2100 K. The temperature range

is consistent with those previously modelled by Reid & Menten (1997a) from their centimetre-wavelength observations of Mira's radio photosphere, and by Yamamura et al. (1999a) and Ohnaka (2004) from infrared observations using simple models of contiguous, uniform molecular H_2O+SiO layers.

In our maps, the emission from the vibrationally excited ($E_{up}/k > 3500$ K) SiO $v = 2$ and H_2O $v_2 = 1$ lines has an extent of $\lesssim$100 mas ($\lesssim 8\,R_\star$). The core emission region of the SiO 5–4 $v = 0$ vibrational ground state line (i.e. excluding the extended filamentary or arc-like emission feature to the west/south-west) that is detected at $\geq 3\sigma$ has radii between 200 mas (3.3×10^{14} cm; to the south-east) and 600 mas (9.9×10^{14} cm; to the west), and the size of the half-maximum emission is roughly 100–150 mas (see Fig. 3.9). Hence, SiO emits rotational emission up to a radius of $\sim 50\,R_\star$, far beyond the radius of the molecular layer probed by infrared interferometers. Perrin et al. (2015), assuming that the mid-infrared N-band visibilities between 7.80 μm and 9.70 μm are the only signature of gas-phase SiO emission, concluded that the SiO can only be found in gas phase within $3\,R_\star$. We suggest that this discrepancy is due to the excitation effect of SiO molecules. The ground state SiO line in the ALMA SV observation has an energy above the ground of only ~30 K, and therefore is excited throughout the region within the silicate dust condensation zone. While the ALMA images indicate a significant amount of gas-phase SiO molecules, the gas temperature beyond the molecular layer ($\lesssim$1000 K) is insufficient to collisionally excite the SiO molecules to higher vibrational states. Thus, the SiO molecule does not produce detectable infrared emission beyond $\sim 3\,R_\star$ even if it is abundant there.

3.5.2.3. Dust shells and the sequence of dust condensation

The radii of dust shells around Mira were measured with infrared interferometry at 11 μm by Danchi et al. (1994) and Lopez et al. (1997). A single silicate dust shell from 60–2500 mas with a dust temperature of 1063 K at the inner radius was adopted in the model of Danchi et al. (1994). Lopez et al. (1997) used a two-shell model composed purely of silicate grains at radii of 50 mas and 200 mas. The dust temperature of the inner radius of the inner dust shell is about 1160–1380 K. These results suggest that dust grains start to form around Mira at a temperature above 1000 K and a radius of ~ 2–$3\,R_\star$, where $R_\star$ was determined to be 19.3–23.6 mas. If we use our adopted value of 12.3 mas for $R_\star$, then the inner dust formation radius would be ~4–$5\,R_\star$. Compared to the recent model of Perrin et al. (2015), this range is significantly smaller than the silicate formation radii, which is at least $12\,R_\star$, but is consistent with the radii of corundum formation.

Studies of silicate dust formation suggest that efficient condensation occurs only when the gas temperature drops to below 600 K (e.g. Gail & Sedlmayr, 1998). This allows the SiO gas to emit to a much larger radius in the extended atmosphere of Mira than the radii of its dust shells derived previously and described above. The discussion of higher silicate dust condensation temperatures has been recently revived by Gail et al. (2013). Their new measurements of the vapour pressure of solid SiO suggest that gas-phase SiO molecules may first nucleate into SiO clusters and then condense onto dust grains (Gail et al., 2013). The gas temperature at which SiO gas start to deplete (also assumed to be the dust temperature at the inner boundary of the dust shell) is estimated to be about 600 K, for a mass-loss rate, $\dot{M}$, of $\sim 10^{-6}\,M_\odot\,\mathrm{yr}^{-1}$, increasing to 800 K for $\dot{M} = 10^{-4}\,M_\odot\,\mathrm{yr}^{-1}$. The SiO nucleation process thus allows the depletion of SiO gas to begin at a higher gas temperature, i.e. at a smaller inner radius, than previously thought. However, the result of Gail et al. (2013) still cannot explain the high dust temperature (> 1000 K) as derived from visibility fitting by Danchi et al. (1994) and Lopez et al. (1997).

In our Model 3, the radius at which the ^{28}SiO abundance decreases significantly is ~60 mas,

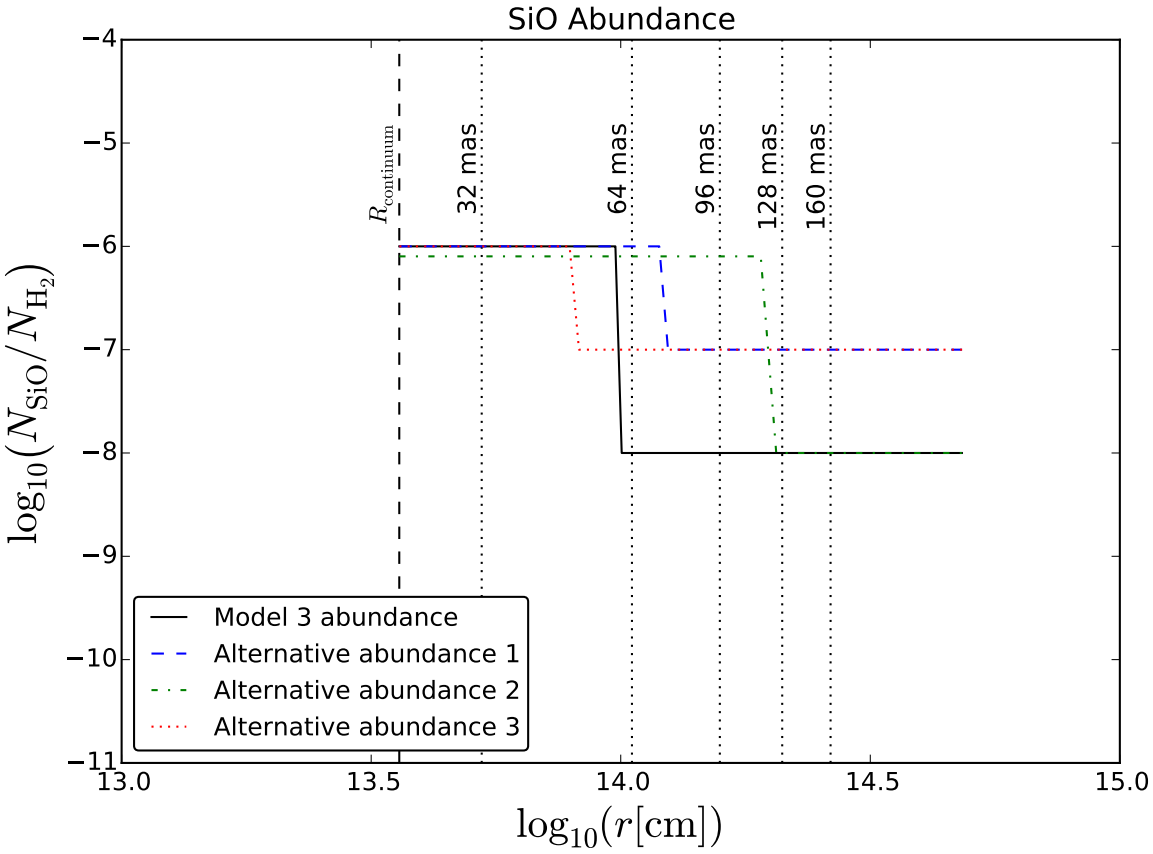

Figure 3.29.: Alternative input ^{28}SiO abundance profiles for Model 3 which produce similar modelled spectra. The solid black curve is the same two-step abundance profile as in Model 3, which is close to the minimum possible abundance to fit the ALMA spectra. The three other coloured curves are alternative abundance profiles also using two-step functions. Abundance profile 1 (blue, dashed) has an inner abundance of 1×10^{-6} up to the radius of $\sim 6\,R_\star$ and an outer abundance of 1×10^{-7}; profile 2 (green, dash-dotted) has an inner abundance of 8×10^{-7} up to $\sim 10\,R_\star$ and an outer abundance of 1×10^{-8}; and profile 3 (red, dotted) has an inner abundance of 1×10^{-6} up to $\sim 4\,R_\star$ and an outer abundance of 1×10^{-7}.

which corresponds to 1.0×10^{14} cm or $\sim 5\,R_\star$. The modelled gas temperature at this radius is $\sim$600 K. In addition to this SiO abundance profile, we have also tested with other two-step functions in order to determine the maximum and minimum amount of SiO and the possible range of SiO depletion radii required to reproduce the observed ALMA spectra. Figure 3.29 shows three examples of alternative SiO abundance models. All these models are as good as our Model 3 in reproducing the spectra. Our experiments show that, at the very least, the SiO abundance should be $\sim 1 \times 10^{-6}$ within $\sim 4\,R_\star$ and $\sim 10^{-8}$–10^{-7} beyond that. In other words, SiO molecules cannot deplete onto dust grains in a significant amount within $\sim 4\,R_\star$. This radius is consistent with the inner radius of the silicate dust shells derived in the literature. Our tests, however, have shown that the synthesised SiO spectra in the outer radii are not sensitive to a higher value of the SiO abundance, or the exact shape of the abundance profile. The actual radius where gas-phase SiO molecule condenses onto dust grains may therefore be much further from the star than $4\,R_\star$. Moreover, the actual degree of SiO gas depletion, through silicate dust condensation, nucleation of molecular clusters, or other gas-phase chemical reactions (e.g. Gail et al., 2013; Gobrecht et al., 2016), may not be as high as assumed in our

preferred model.

The gas temperature at which SiO gas starts to deplete in our models is about 490–600 K, far below the dust temperature at the inner dust shells as derived observationally by Danchi et al. (1994) and Lopez et al. (1997). This temperature is also somewhat lower, by about 100 K, than the gas temperature at which SiO gas starts to nucleate into clusters (Gail et al., 2013). However, we note that the visibility models derived by Danchi et al. (1994) and Lopez et al. (1997) have assumed that the dust around Mira is composed of pure silicate grains. The derived parameters are therefore based on the adopted optical properties of silicate dust grains. Other possible compositions of dust grains around oxygen-rich stars such as corundum or the mixture of corundum and silicate cannot be excluded, but have not been explored in those models.

Corundum, the crystalline form of aluminium oxide (Al_2O_3), has a high condensation temperature of ~1700 K (e.g. Grossman & Larimer, 1974; Lorenz-Martins & Pompeia, 2000) and is the most stable aluminium-containing species at a temperature below 1400 K (Gail & Sedlmayr, 1998). Little-Marenin & Little (1990) classified the circumstellar dust shells of oxygen-rich AGB stars into several groups according to the spectral features found in their mid-infrared spectral energy distributions (SEDs). These SED groups show (a) broad emission features from 9 to 15 μm; (b) multiple components with peaks near 10, 11.3, and 13 μm; and (c) strong, well-defined characteristic silicate peaks at 9.8 and 18 μm. Little-Marenin & Little (1990) have also suggested that the circumstellar dust shells follow an evolutionary sequence starting from the class showing the broad feature, then multiple components, and finally silicate features in the SED. From a survey of O-rich AGB stars, most of which are Mira variables, Lorenz-Martins & Pompeia (2000) have successfully fitted the SEDs showing (a) broad features, (b) multiple components (or the intermediate class), and (c) silicate features and with corundum grains, a mixture of corundum and silicate grains, and pure silicate grains, respectively. Their results show that the inner radius of the modelled dust shells increases from the broad class, the intermediate class, and the silicate class. The fitted dust temperature of the hottest grains also follows the same sequence. In addition, they also found that the optical depths of the corundum-dominated emission are much smaller than those of the silicate-dominated emission. Lorenz-Martins & Pompeia (2000) thus concluded that their results were consistent with the evolutionary sequence suggested by Little-Marenin & Little (1990). Corundum grains are the first species to form in the circumstellar dust shells, at a small radius of ~2–3 $R_\star$ and a temperature of ~1400–1600 K. At a later stage, silicate grains start to form and dominate the emission features in the SED. The inner radius of the silicate dust shells and temperature of the hottest silicate grains are ~5–20 $R_\star$ and ~500–1000 K, respectively.

Our modelling results have shown that gas-phase SiO starts to deplete at a radius of *at least* 4 $R_\star$ and a gas temperature of $\lesssim$600 K. In addition, the observed spectra show that SiO molecules survive in the gas-phase well below 1000 K. This is apparently inconsistent with the fitting by Danchi et al. (1994) and Lopez et al. (1997) who found that the silicate dust shells form at a temperature above 1000 K. We therefore suggest that the inner hot dust shells around Mira may indeed be composed of other grain types, possibly corundum, instead of silicate grains as previously assumed. Although no prominent spectral features of corundum have been reported (e.g. Lopez et al., 1997; Lobel et al., 2000), we note that the corundum grains may be coated with silicates when the temperature becomes low further out in the dust shell (e.g. Karovicova et al., 2013, Sect. 6.1 and references therein). The optical depth of pure corundum grains, which only exist close to the star, may also be much lower than that of silicate grains (e.g. Lorenz-Martins & Pompeia, 2000) and therefore the corundum features

may not be easily distinguished in the SED from the silicate features.

3.5.2.4. Maser emission

Among all the spectral lines covered in this ALMA SV observation, only SiO $v = 1$ $J = 5$–4 and $v = 1$ $J = 2$–1 (in ALMA Band 3; not included in this chapter) exhibit strong maser emission (Fig. 3.15). In the images, isolated SiO $v = 1$ $J = 5$–4 maser spots are seen outside Mira's radio photosphere, primarily at the radial distances between ~30 and 120 mas from the fitted position of the radio continuum. The relative spatial distribution of the SiO $v = 1$ maser is consistent with those previously reported by Boboltz & Claussen (2004) and Cotton et al. (2008) (and references therein) in other lower-J maser transitions. The presence of maser emission indicates that the SiO gas in those maser-emitting spots *must not* be in local thermodynamic equilibrium (LTE). In our preferred model (1-D and smooth), the gas density is uniformly high throughout the maser-emitting region and hence all possible maser action is quenched. The predicted excitation temperature does not show any negative values throughout the modelled region (Fig. 3.24) and therefore population inversion, a prerequisite for maser emission to take place, of the SiO $v = 1$ transition cannot be predicted by our simple model. We note that our model does not include any external infrared radiation field, in particular the infrared pumping band of SiO molecule near 8.1 μm ($\Delta v = 1$, fundamental) and 4.0 μm ($\Delta v = 2$, first overtone). The only input radiation field in our model is a blackbody of 2600 K representing the radio photosphere of Mira. This temperature is lower than the typical infrared effective temperature of Mira, which is about 3200 K (Woodruff et al., 2004). So the radiation field does not realistically approximate the radiative excitation of SiO molecule to higher vibrational states. Because our modelling aims to explain the *general* physical conditions of Mira's extended atmosphere, we did not attempt to construct a sophisticated model to explain both maser and non-maser emission.

The water line covered in this SV observation, H_2O $v_2 = 1$ $J_{K_a,K_c} = 5_{5,0}$–$6_{4,3}$, near 232.7 GHz does not show any maser emission. Gray et al. (2016) have conducted extensive radiative transfer modelling to explore the physical conditions under which the modelled H_2O lines (including all possible lines covered by ALMA) would exhibit maser emission in the envelopes of evolved stars. Slab geometry and silicate dust, which is optically thin at the millimetre wavelengths and optically thick in the radiative pumping bands of H_2O's vibrational states (e.g. the ν_2 band at 6.27 μm), have been assumed in their modelling (Gray et al., 2016). The 232.7 GHz H_2O emission is seen from the radio photosphere up to about 80 mas (Fig. 3.13). Hence, the H_2O-emitting region corresponds to the kinetic temperature of ~550–2100 K, the gas density of n_{H_2}~4×10^{10}–1×10^{13} cm^{-3}, and hence the H_2O molecular density of n_{H_2O}~2×10^5–5×10^7 cm^{-3} in our preferred model. Our derived H_2O molecular density lies well within the range in the model of Gray et al. (2016) that is predicted to exhibit strong maser emission in the 232.7 GHz transition *if* the dust temperature is high enough. The absence of the 232.7 GHz H_2O maser is consistent with a silicate-type dust temperature lower than approximately 900, 1000, and 1600 K for the respective gas kinetic temperature of about 500, 1000, and 1500 K (see Fig. 10 of Gray et al., 2016). These comparisons, although not a conclusive proof, suggest that hot dust grains that are optically thick at the ν_2 band (6.27 μm) did not exist in Mira's extended atmosphere during the ALMA SV observation.

3.5.3. Comparison with current hydrodynamic models

3.5.3.1. Early hydrodynamic models for stellar pulsation

There are many numerical hydrodynamical calculations on Mira variables to simulate the variation of pulsation velocity, number density, and kinetic temperature as functions of the stellar

phase and/or radial distance from the star. Pioneering work includes the studies of Willson & Hill (1979), Hill & Willson (1979), Wood (1979), Willson (1987), as well as Beach et al. (1988) and Bowen (1988a,b, 1989) (hereafter Bowen's models). Wood (1979), Willson (1987), and Bowen (1988a,b, 1989) have compared the effect of radiation pressure on dust on the mass-loss rate and the velocities of the stellar outflows. The outflow/infall velocity profiles as a function of radius as derived from these models are qualitatively similar. These authors all predict alternating outflow and infall layers in close proximity to the star, within about 4–6×10^{13} cm. Beyond that radius, the dust-driven winds exhibit accelerating outflow. In the region where material expands and falls back, large-scale shocks are produced at the interface between the outer infall layer and the inner outflow.

Infall motions in the extended atmosphere of the star can be observed as inverse P Cygni profiles in the spectra. The material at the near side of the star will show redshifted absorption and the material at the far side that is not blocked by the continuum will show blueshifted emission. These emission features are present even if there is no hot material (perhaps shock-heated) with a temperature higher than the continuum brightness temperature, and are also known as the 'nebular' effect (e.g. Bessell et al., 1996; Scholz & Wood, 2000), in which the large volume of the highly extended atmosphere, albeit only weakly emitting per unit volume, adds up to produce significant emission. For example, the redshifted absorption in the CO second overtone lines ($\Delta v = 3$) from *o* Cet indicates infall motions in the deep photospheric layers of the star (Hinkle et al., 1984). Results from the early spectroscopy by Joy (1926, 1954) also suggest infall motion in the extended atmosphere of *o* Cet based on modern information on the systemic (i.e. centre of mass) velocity of the star (see also the interpretation by Gabovitš, 1936).

Bowen's models were adopted by Humphreys et al. (1996) and Humphreys et al. (2001) to simulate the SiO ($v = 1$ and 2) and H_2O (ground state and $v_2 = 1$) masers from a template M-type Mira (parameters were based on *o* Cet) at a single stellar phase, and by Gray & Humphreys (2000) and Humphreys et al. (2002) to simulate the variability of SiO ($v = 1$) masers at various epochs of a stellar cycle of the model Mira. Gray et al. (2009) have comprehensively reviewed the success and limitations of these precursor models for SiO maser simulations. One major drawback of Bowen's hydrodynamical solutions is that the pulsation phase in the model (with phase 0 defined as the moment when the inner boundary of the model atmosphere, or the 'piston', is moving outwards at the maximum speed) is disconnected from the stellar phase as determined from the optical or infrared brightness variations (Humphreys et al., 1996). In addition, the assumption of a constant infrared radiation field by dust and the stellar photosphere was also too simplistic for Mira variables (Gray et al., 2009).

Solving the hydrodynamical equations as presented in Richtmyer & Morton (1967, Chap. 12), who adopted the von Neumann-Richtmyer pseudo-viscosity method as the artificial shock dissipation mechanism (von Neumann & Richtmyer, 1950), the authors of early hydrodynamic models derived the dynamical structures around Mira-like variables. Bowen's models also considered the thermal relaxation of shocks via radiative cooling from neutral hydrogen atoms at high temperatures ($\gtrsim$6000 K) and from other species (which is represented by an assumed cooling coefficient) at low temperatures (see Sects. II(b) and II(c)(iii) of Bowen, 1988a). Bowen's models predicted the existence of an extended ($\sim 10^{14}$ cm) post-shock region of elevated gas temperatures ($\sim$10 000 K) near the optical/infrared photosphere.

On the other hand, using the hydrogen Balmer series emission lines as the signatures of shock-heated region, Fox et al. (1984) and Fox & Wood (1985) developed a theoretical model of shock waves in the atmospheres of Mira variables and predicted that these pulsation-driven

shocks dissipate within a very thin region in the extended atmospheres, that is several orders of magnitude smaller than the stellar radius (i.e. $\ll 10^{12}$ cm). The circumstellar shock models by Willacy & Cherchneff (1998) and Gobrecht et al. (2016) predict that the cooling length of H_2 dissociation, depending on the shock velocities, is typically $<10^8$ cm. The very narrow post-shock region suggests that the relaxation of the shocked material towards radiative equilibrium and local thermodynamic equilibrium is essentially instantaneous and therefore the post-shock heating might be neglected. Woitke et al. (1996) argued that Bowen's cooling rate was underestimated by a few orders of magnitude, thus resulting in an atmosphere with highly elevated gas temperature. Furthermore, based on the observational constraints from Mira's radio continuum emission at 8 GHz, Reid & Menten (1997a,b) have shown that the amplitude of gas temperature disturbance, probably due to shocks or pulsations, can only be about 300 K (assuming a shock propagation speed of 7.3 km s^{-1}). These are in contrast with Bowen's non-equilibrium models which expect a rather extended shock-heated region with highly elevated gas temperature. Bessell et al. (1989) compared the synthesised spectra from Bowen's non-equilibrium model with the observed spectrum between 600 nm and 4 μm, and found that they did not match at all. Moreover, the hydrogen spectra (e.g. Hα) predicted by Luttermoser & Bowen (1990, 1992) using Bowen's model were much broader and had line profiles that were different to what was actually observed (Woodsworth, 1995). Hence, the non-equilibrium models with extended high-temperature regions are not suitable for the extended atmospheres of Mira variables (see also the discussions in Woitke, 1998; Willson, 2000).

For the purpose of verification, we have also conducted similar tests to those of Bessell et al. (1989) by introducing into our preferred model (Model 3) an arbitrary extended layer ($\gtrsim 10^{12}$ cm) of elevated gas temperature (~4000 K) at various radial distances from Mira. The elevated temperature is significantly higher than the brightness temperature of the stellar radio continuum (~2600 K). Figure 3.30 shows an example of our tests. Even though the gas temperature is elevated for just a relatively thin layer (2×10^{13} cm $\sim R_\star$) compared to Bowen's non-equilibrium model ($\sim 10^{14}$ cm), the synthesised spectra exhibit very strong emission features that are absent in the data. In fact, if we extend the zone of elevated gas temperature further, the emission spikes only become more prominent. Therefore our tests suggest that during this particular ALMA SV observation, the extended atmosphere of Mira did not contain an extended ($\gtrsim 10^{12}$ cm) shock-heated (above the brightness temperature of the radio continuum) region as was predicted from the non-equilibrium model. This is consistent with those shock wave models that suggest that the shock relaxation in the Mira atmosphere takes place within a very thin zone compared to the stellar radius (e.g. Fox et al., 1984; Fox & Wood, 1985). In addition, we do not expect the existence of stellar chromosphere beyond the radio photosphere of Mira during this ALMA SV observation. Stellar chromosphere was suggested to explain the Hα absorption lines from some semi-regular variables (Luttermoser et al., 1994; Wood et al., 2004), but it may not exist around Mira at all because the Hα line from the star has only been seen in emission, not absorption (e.g. Joy, 1947; Gillet et al., 1983, 1985).

3.5.3.2. More recent hydrodynamic models

Based on the assumption of negligible post-shock heating, Bessell et al. (1996) and Hofmann et al. (1998) made series of pulsation models to theoretically calculate the photospheric structure (e.g. density, temperature, outflow/infall velocities) of Mira variables. Applying the predictions from these model series, Bessell et al. (1996) and Scholz & Wood (2000) predicted the near-infrared spectra of selected atomic and molecular lines, which exhibit both the normal and inverse P Cygni profiles, and show significant variations with the stellar phase.

New hydrodynamical solutions have also been derived by Ireland et al. (2004a,b) and adopted

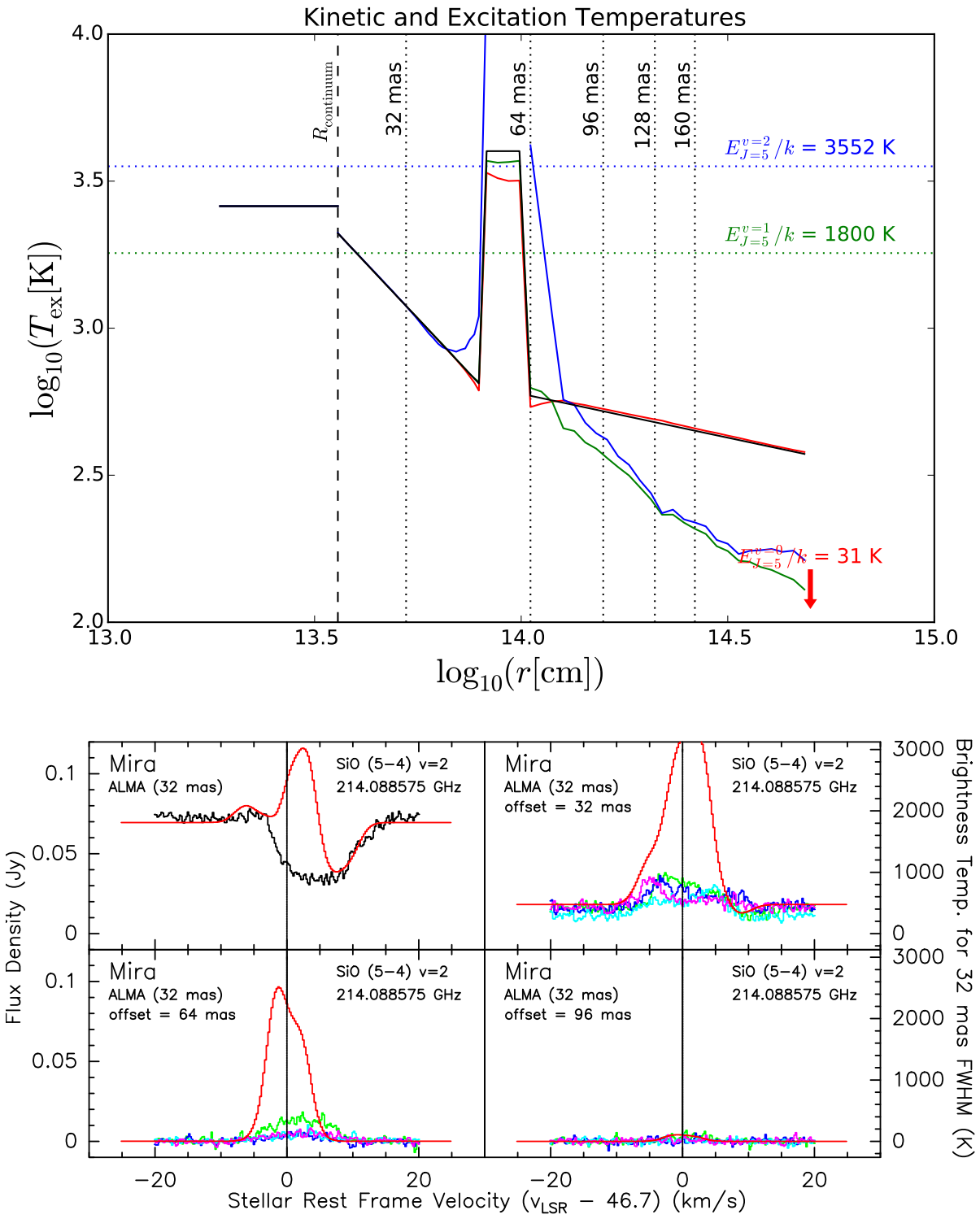

Figure 3.30.: Preferred model with a layer of an elevated gas temperature. The layer has a width of 2.0×10^{13} cm and an arbitrarily chosen temperature of 4000 K. The left panel shows the elevated gas temperature profiles and the right panel shows the observed and modelled SiO $v = 2$ $J = 5$–4 spectra as examples. All other parameters are the same as our preferred model (Model 3).

by Gray et al. (2009) to simulate SiO maser emission in Mira variables. The model series are based on self-excited pulsation as in Hofmann et al. (1998), instead of piston-generated pulsation in other hydrodynamical models. Simulations have shown that SiO masers form a ring of typically ~2.2 $R_\star$ around the star (Gray et al., 2009), which is close to but beyond the radius of the radio photosphere. The results are consistent with the previous observations of SiO maser shells around Mira by Reid & Menten (1997a, 2007). Hence, strong SiO masers within the radio photosphere are prohibited (Reid & Menten, 1997a; Gray et al., 2009). Comparing the hydrodynamical solutions of Ireland et al. (2004a,b) with observations, the strongest inner shocks (with $\Delta V > 20\,\mathrm{km\,s^{-1}}$) are enclosed within the radio photosphere, and the shocks beyond that only cause a velocity change of $\sim 7\,\mathrm{km\,s^{-1}}$. The low shock velocity beyond the radio continuum is also consistent with the proper motion velocities of SiO masers observed in TX Cam (Diamond & Kemball, 2003) and the nearly constant radio light curves observed in several Mira variables (Reid & Menten, 1997a,b). In addition, Gray et al. (2009) have found that the presence of corundum (Al_2O_3) dust grains can both enhance or suppress SiO maser emission.

More recently, Ireland et al. (2008, 2011) and Scholz et al. (2014) have developed the Cool Opacity-sampling Dynamic EXtended (CODEX) atmosphere models, based on an improved self-excited pulsation code by Keller & Wood (2006) to determine the pressure and luminosity, and an opacity-sampling method to derive the gas and dust temperatures (see also the review by Ireland, 2011). The mass density and velocity profiles in the extended atmosphere can also be computed. Thus far, the CODEX models have only been compared to the spectro-interferometric and spectro-photometric observations of Mira variables at the infrared wavelengths (e.g. Woodruff et al., 2009; Wittkowski et al., 2011; Hillen et al., 2012). Our radiative transfer modelling of the submillimetre molecular transitions from Mira as observed by the ALMA long baselines, including the vibrational ground state lines that are less affected by excitation effects, can provide an alternative probe to the detailed physical conditions in Mira's extended atmosphere at a spatial scale of a few $R_\star$. In Sects. 3.5.3.3 and 3.5.3.4 we present our modelling results using the predicted atmospheric structures from CODEX and alternative velocity profiles in Mira's extended atmosphere.

3.5.3.3. Kinematics

As described above, our high angular-resolution ALMA long baseline data clearly resolve the line emission/absorption from the extended atmosphere of Mira. Employing radiative transfer modelling we can test the atmospheric structures predicted by the latest hydrodynamical models. In particular, we consider the hydrodynamical model series, CODEX, developed by Ireland et al. (2008, 2011) and Scholz et al. (2014). We use the o54 5400 $L_\odot$ model series, which is based on the stellar parameters of our target source, Mira (*o* Cet). From the CODEX developers we have obtained the atmospheric structure information of the o54 model series, including the total mass density, kinetic temperature (which is not the computed non-grey equilibrium temperature in the final model atmospheres; see Ireland et al., 2008), and the radial expansion or infall velocity of the gas at different radii. Among the six complete stellar pulsation cycles computed by the developers, the models at the stellar phases closest to this 2014 ALMA SV dataset (near phase 0.45) are models 250420[15] (phase 0.38), 261740 (0.40), 286060 (0.41),

[15] These model numbers correspond to various phases of the models in the o54 series in chronological order. Models 248480–251160 are the models in the compact atmospheric cycles where most of the mass in the model atmosphere is contained within a relatively small radial extent, models 260820–263740 are those in the extended atmospheric cycles, and models 285180–291860 cover almost four consecutive pulsation cycles of the model atmosphere with intermediate extents of the mass-zones (see Fig. 1 and Tables 2, 3, and 4 in Ireland

287880 (0.40), 289440 (0.40), and 291820 (0.41) (Ireland et al., 2008, 2011).

Because of the assumption of instantaneous shock dissipation, there is no extended zone of elevated gas kinetic temperature above the stellar brightness temperature in the extended atmosphere. The gas temperature profiles of the CODEX models are lower (by <500 K) and higher (by <700 K) than the values we empirically derive in Sect. 3.4.4 for the inner radii ($\lesssim 5 \times 10^{13}$ cm $\approx 2.5\,R_\star$) and outer radii, respectively. The temperature in Mira's extended atmosphere is always <2000 K, except at radii very close to the radio continuum.

The CODEX code computes the mass density of all particles in the atmosphere. In our RATRAN input models, we convert the mass density to number density by division with the average mass of the particles in the wind, $m_{\rm part} = 0.7 m_{\rm H_2} + 0.3 m_{\rm He} = 4.3372 \times 10^{-24}$ g, assuming the typical helium mass fraction of $Y \approx 0.3$ (e.g. Wood & Cahn, 1977; Lattanzio & Wood, 2003; Ireland et al., 2008; Ventura et al., 2013). In our modelling, however, we only consider the collision of H_2O and SiO with rotational ground-state H_2 molecules.

However, if we apply this conversion to the input models, the number density in Mira's extended atmosphere will be about 10^8–10^{10} cm^{-3}, which is too low to excite the molecules and to produce significant emission or absorption in the synthesised spectra. The deep absorption features observed towards the continuum disc and the emission profiles towards various radial distances from the star can only be reproduced by arbitrarily increasing the converted number density by a large factor. In our modelling, therefore, we scale the number density of all CODEX models by a factor of 10^4 such that the density outside the radio photosphere reaches at least 10^{12} cm^{-3}. This density is similar to the value adopted in our empirical modelling (Sect. 3.4), and is also consistent with that derived by Reid & Menten (1997a), who modelled the centimetre-wavelength radio fluxes from the radio photospheres of Mira variables (including Mira). Furthermore, the density is also compatible with the lower limit of 10^{11} cm^{-3}, which is estimated by modelling the near-infrared H_2O spectrum and assuming a relatively high H_2O abundance of $\sim 3 \times 10^{-4}$ (Yamamura et al., 1999a). If the adopted H_2O abundance is similar to our assumed value of $\sim 10^{-5}$, then the lower limit of the gas density derived by Yamamura et al. (1999a) would also be close to the values in our modelling. We note, however, that the gas density should be interpreted with caution – see our discussion in Sect. 3.5.1.

In our initial test, we replaced our preferred model (Model 3) with the CODEX-predicted gas number density (scaled by 10^4), kinetic temperature, and radial velocity profiles. All other parameters, namely the SiO abundance profile, the local velocity dispersion, and the radio continuum, are the same as in Model 3. The outer radius of our model is greater than the outer boundaries of the CODEX models. The outer boundaries depend on individual CODEX models. For each model, we extrapolate the number density and kinetic temperature in power laws near the outer boundary, i.e. linear extrapolation in log-log relation. We also assume the infall or expansion velocity at and beyond the CODEX model boundary to be constant because we have no information of the kinematics beyond that. Since the gas density and molecular SiO abundance are usually too low to cause significant excitation in the outer regions, the precise extrapolation method has little effect on the synthesised spectra.

Figure 3.31 shows the results of our initial test of the velocity profiles from these six CODEX models. Remarkably, near the observed stellar phase all six models are able to qualitatively reproduce the general spectral features, including (1) the strong absorption profile in the line of sight towards the radio continuum of Mira and (2) gradually decreasing emission flux and line width in the lines of sight towards increasing radial offsets from the star. Closer inspection

et al., 2011).

reveals that all six models produce an extra high-velocity absorption wing in either the redshifted or blueshifted part of the spectra towards the centre of the continuum. The velocities of the absorption wings correspond to the high-velocity gas at 10–20 km s^{-1} near the radio continuum of Mira, i.e. 3.6×10^{13} cm ($1.8\,R_\star$). Because there is no sign of any absorption wings broader than ±10 km s^{-1} in the observed spectra, the strong velocity variation as seen in these models, in particular models 261740, 286060, 287880, and 289440, cannot explain the specific atmosphere structure of Mira during the time of the 2014 ALMA SV observation.

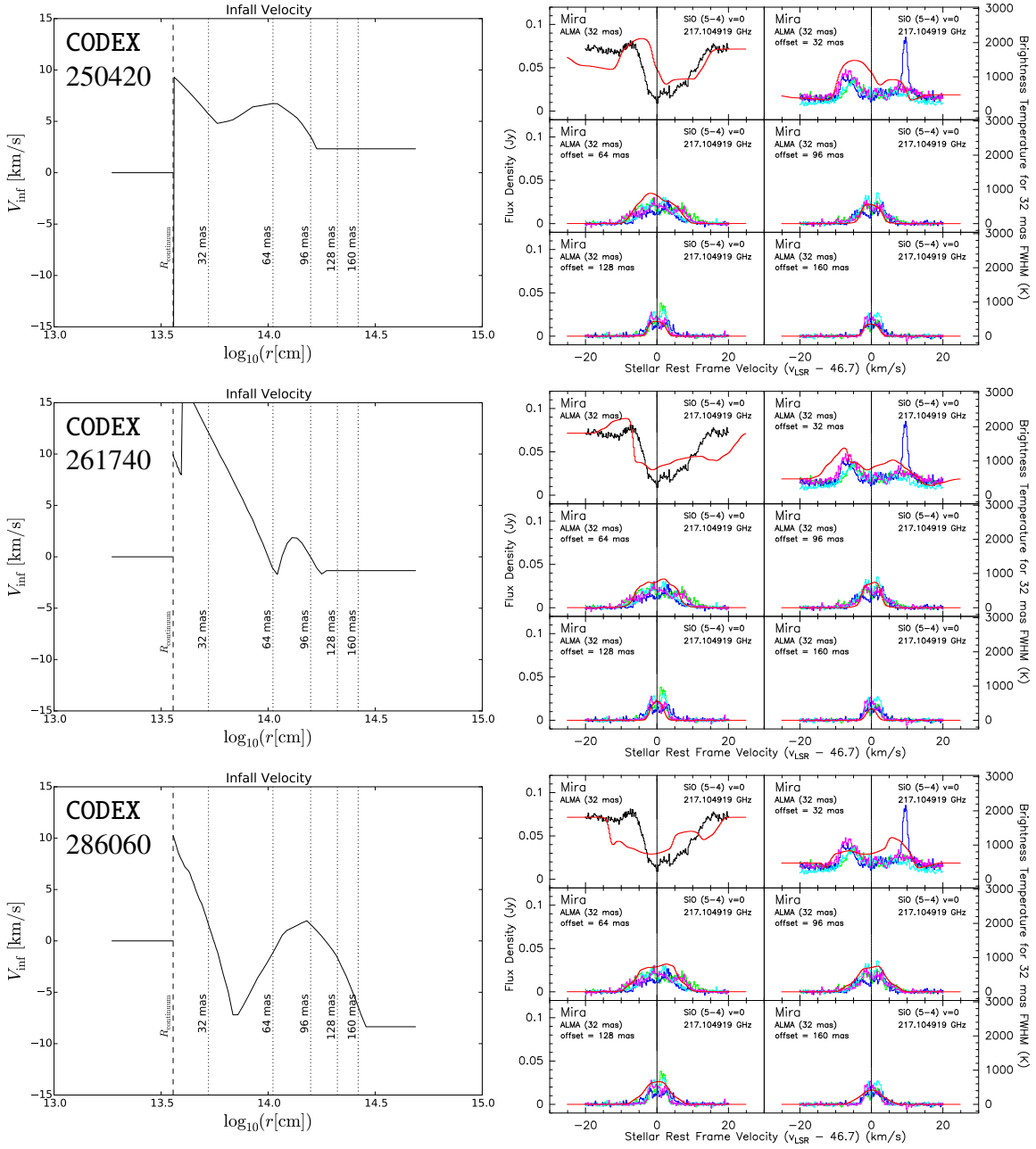

Figure 3.31.: Modified Model 3 with input gas density, kinetic temperature, and velocity profiles from CODEX models 250420 (top), 261740 (middle), and 286060 (bottom). Special scaling has been applied to the input gas density (see text). The infall velocity profiles are plotted on the left and the selected resultant spectra are shown on the right. We applied constant extrapolation of the infall velocity beyond the outer boundary of CODEX models.

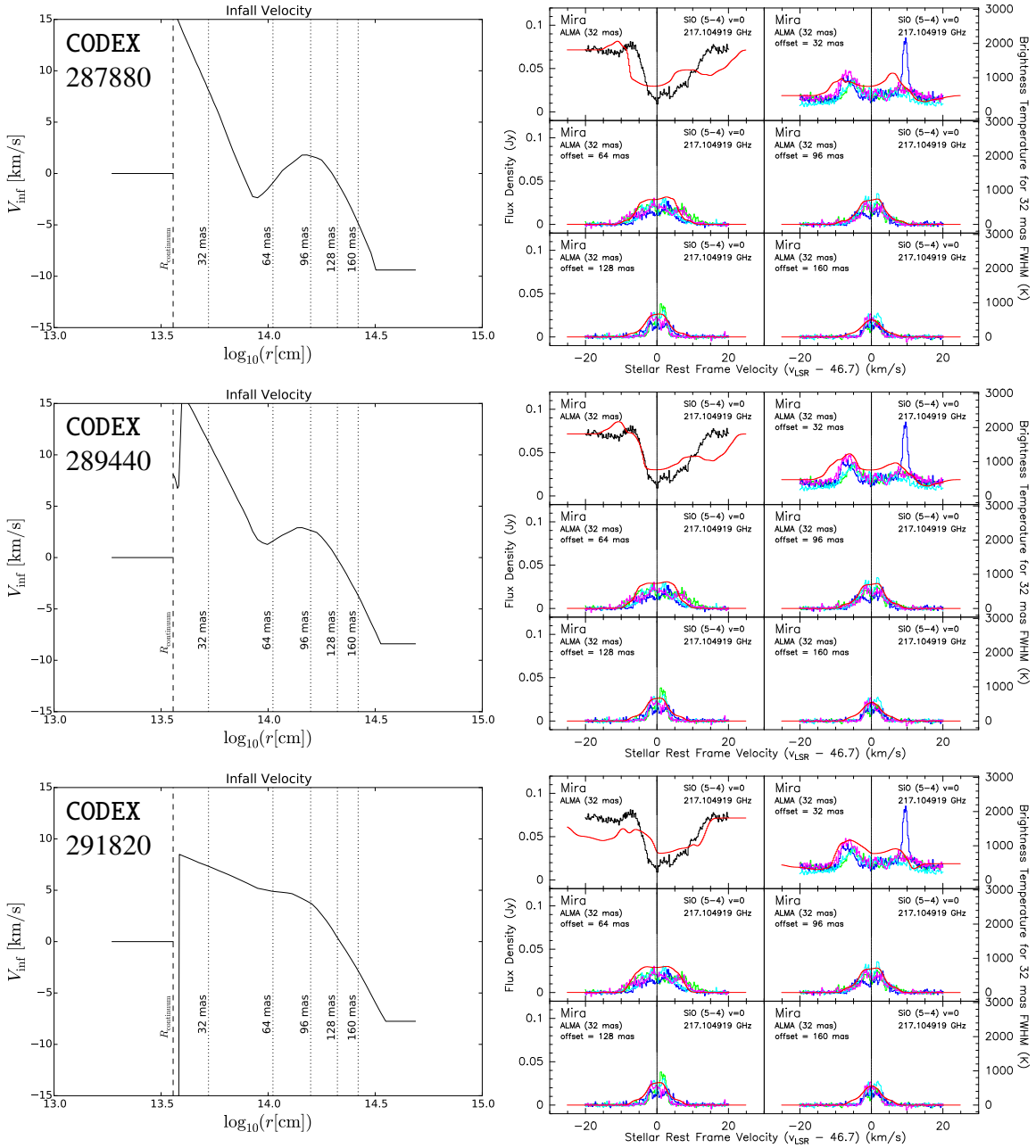

Figure 3.31.: Continued for CODEX models 287880 (top), 289440 (middle), and 291820 (bottom).

The velocity profiles of CODEX models 250420 and 291820 are qualitatively similar to our Model 3 (see Fig. 3.24, top right panel). First, the extended atmosphere exhibits slowly varying, infall motion over a wide range of radii. Second, there is a sharp change in velocity, representing a strong shock front with $\Delta V \gtrsim 10$ km s^{-1} just outside the radio continuum (3.60×10^{13}cm). The strong shock front in model 250420 is located at 3.64×10^{13}cm, and in model 291820 it is at 3.83×10^{13}cm (Ireland et al., 2011). In our second test, we increase the radius of our radio pseudo-continuum to engulf the strong shock fronts in models 250420 and 291820. Figure 3.32 shows the modelled spectra as a result of hiding the strong shock fronts. The high-velocity absorption wings in the blueshifted part of the SiO spectra extracted from the continuum centre has disappeared, and hence the synthesised spectra can now better fit the

observed ALMA spectra. We therefore conclude that, at the time of the 2014 ALMA SV observation (stellar phase ∼0.45), there is no strong shock with a high velocity of $\Delta V \gtrsim 20$ km s^{-1} in the extended atmosphere of Mira *beyond* the radius of its 229-GHz radio photosphere. Furthermore, the infall and outflow velocities of the gas beyond the radio photosphere of Mira are bounded by ∼7 km s^{-1} and ∼4 km s^{-1}, respectively.

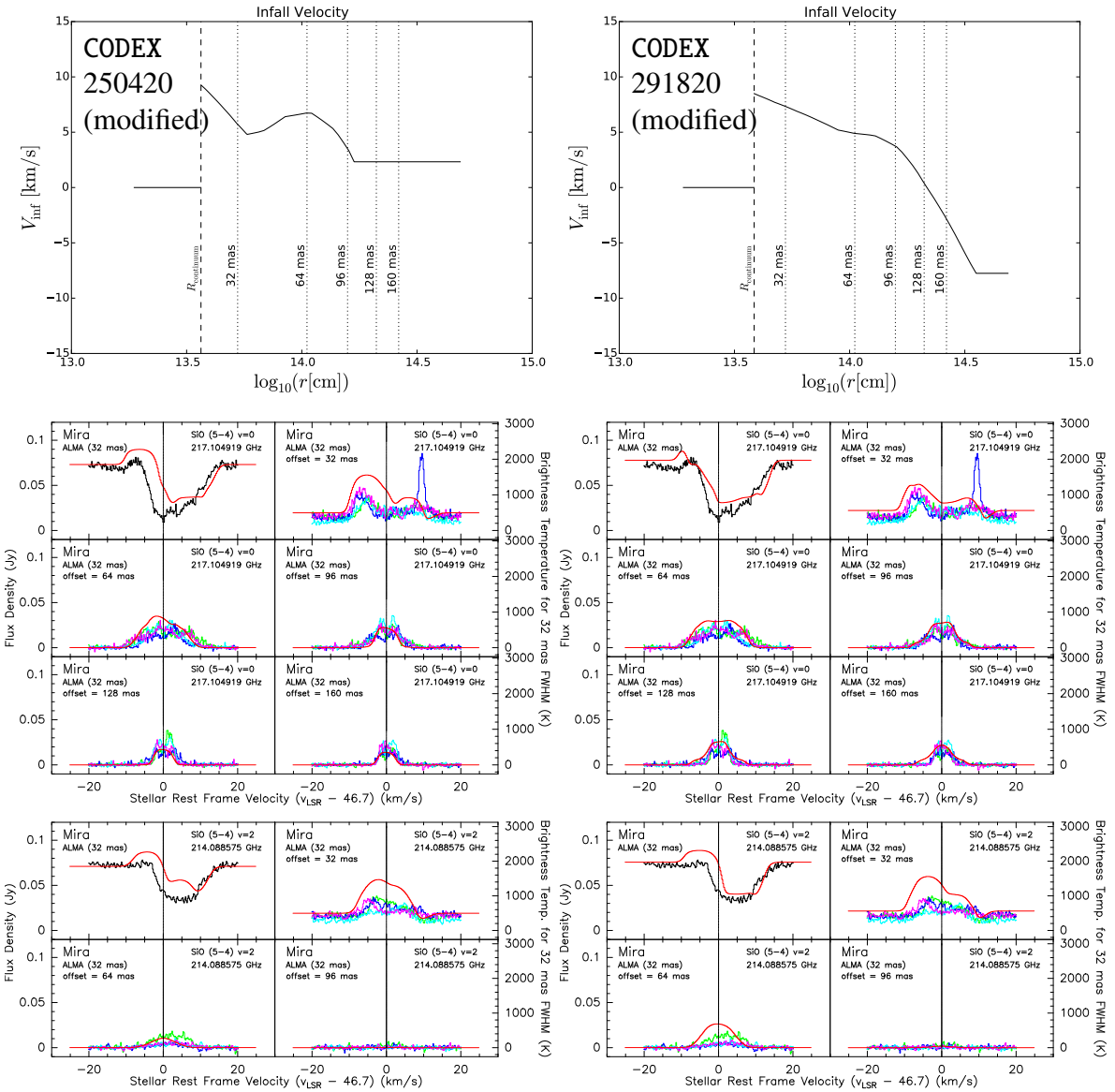

Figure 3.32.: Similar to Fig. 3.31, except that the radius of the pseudo-continuum in the model, $R_{\rm continuum}$, is changed to 3.65×10^{13}cm for model 250420 (left column) and 3.85×10^{13}cm for model 291820 (right column). The modelled continuum levels are therefore slightly higher than those adopting $R_{\rm continuum} = 3.60 \times 10^{13}$cm. The strong shock fronts predicted in these two models are hidden inside the radio continuum. The middle and bottom rows show the selected resultant SiO spectra from the corresponding models.

Our finding is consistent with previous observations of SiO maser emission from other oxygen-rich Mira variables. For example, Wittkowski et al. (2007) found that the expansion velocity of the SiO maser-emitting shell around S Ori is about 10 km s^{-1} by fitting the projected radii of the maser spots and their line-of-sight velocities; Diamond & Kemball (2003) also found that the infall velocities of the SiO maser emission around TX Cam range from

5–10 $\mathrm{km\,s^{-1}}$ by tracing the proper motions of the maser spots. Based on their shock damping model, Reid & Menten (1997b) have excluded the shock propagation velocities significantly (by a few $\mathrm{km\,s^{-1}}$) higher than 7 $\mathrm{km\,s^{-1}}$ in order to explain the multi-epoch radio flux variation of Mira at 8 GHz, assuming that the amplitude of temperature disturbance due to shocks is $\gtrsim$300 K or the factor of density compression is $\gtrsim$2. Hence, any gas infall or outflow motion with speed above 10 $\mathrm{km\,s^{-1}}$ is unlikely beyond the radio photosphere of Mira, and therefore the very high-velocity shocks of $\Delta V \gtrsim 20$ $\mathrm{km\,s^{-1}}$ as predicted by the CODEX models, in particular models 285180 (phase 0.80) and 287980 (phase 0.61) in the same `o54` model series (Ireland et al., 2011), are not expected.

The above exercises have demonstrated that the atmospheric structures predicted by the CODEX models can qualitatively reproduce the general spectral features of the molecular transitions originating from the extended atmospheres and the inner wind of Mira. As already suggested by the authors of CODEX, the derived structures of the model atmosphere, such as the stellar radius, mass density, gas temperature, and velocity, exhibit significant cycle-to-cycle variations and appear to be chaotic (Ireland et al., 2011; Ireland, 2011). The combination of the expansion/infall velocity profile and the locations of shock fronts are different in each cycle. It may take tens of stellar cycles (over a decade) for similar atmospheric structures to reappear (e.g. Fig. 1 of Ireland et al., 2011). We therefore expect that the radio and (sub)millimetre spectra of the molecular transitions would also exhibit significant cycle-to-cycle variation in addition to rapid variation within a single cycle. Long-term monitoring (multi-cycle and multi-epoch) of Mira variables with the ALMA long baseline is therefore necessary to fully test the predictions from hydrodynamical models, especially the amplitudes of pulsation-driven shocks above the radio photospheres of these stars.

3.5.3.4. Wind acceleration

Höfner et al. (2003) also developed models of the dynamical atmospheres by solving time-dependent dynamic equations and frequency-dependent radiative transfer equations (i.e. non-grey dynamical model), including a time-dependent description of dust formation for carbon-rich atmospheres (see also the review by Höfner, 2015). Based on the hydrodynamical model of Höfner et al., Gautschy-Loidl et al. (2004) were able to reproduce the infrared spectra of carbon-rich stars in the wavelength range of 0.5–25 μm, observed at various stellar phases, with a single consistent model atmosphere for each star. Nowotny et al. (2005a,b, 2010) have also compared the synthesised spectra of CO and CN at the infrared wavelengths with the observed spectra of carbon-rich stars and found that the general line profiles and radial velocities of the observed photospheric lines can be explained by the model atmospheres derived from the hydrodynamical code of Höfner et al. (2003). On the other hand, in the case of oxygen-rich model atmospheres, Höfner et al. (2003) have adopted a simple parametrised description for the dust opacity as in Eq. (5) of Bowen (1988a). If non-grey radiative transfer were considered in the dynamical models, however, there would be too little radiation pressure to drive the winds in oxygen-rich stars (e.g. Woitke, 2006; Höfner & Andersen, 2007). Both Woitke (2006) and Höfner (2007) have concluded that the iron content of the wind-driving dust grains must be low, otherwise the dust condensation radius would be too far away from the star ($> 10\,R_\star$) and hence dust-driven winds could not form. Höfner & Andersen (2007) have considered the possibility that the winds being driven by a small amount of carbon-bearing grains in the oxygen-rich atmospheres. By varying the grain properties in their dynamical models, Höfner (2008) has predicted that the size of the wind-driving (iron-free) grains must be in the narrow range between 0.1 and 10 μm. Scicluna et al. (2015) have reported the detection of large grains with an average size of $\sim$0.5 μm in the oxygen-rich circumstellar envelope of the

red supergiant (RSG) VY Canis Majoris based on optical polarimetric imaging. However, the implication of their results on AGB stars, which are the low-mass counterparts of RSGs, is unclear. In contrast, Ireland et al. (2011) and Ireland (2011) have found that both large iron-poor grains and small (<70 nm) iron-rich grains may drive the winds in oxygen-rich atmospheres, although the material still has to be lifted to a radius of at least 3–5 $R_\star$ where dust grains start to condensate efficiently.

One notable difference between the results of the CODEX code and that developed by Höfner et al. is that CODEX models exhibit large-scale velocity variations at radii up to ~10 $R_\star$, while the latter models only show large-scale velocity variation of $\Delta V > 10$ km s^{-1} within ~2–3 $R_\star$. In the model atmospheres of Höfner et al., the winds are efficiently accelerated by Fe-free dust grains that condense at ~3 $R_\star$ (e.g. Höfner, 2009, 2015) and therefore the velocity profile becomes a generally continuous outflow with small-amplitude pulsation ($\Delta V \lesssim 2$ km s^{-1}) due to previous shock episodes (e.g. Höfner et al., 2003; Nowotny et al., 2005a, 2010).

We have conducted another test to examine whether the large-scale velocity variations of $\Delta V \sim 5$ km s^{-1} at a large radial distance ~10 $R_\star$ from the star are possible. Instead of employing the model atmospheres of Höfner et al. directly, we constructed a model nearly identical to our preferred Model 3 with a modified input velocity profile. Figure 3.33 shows the results of this test. The model in the left column presents the input velocity profile (top panel), the modelled and observed SiO $v = 0$ (middle) and SiO $v = 2$ (bottom) spectra of Model 3 for comparison. The model in the right column shows the input and results of the alternative velocity variation. This alternative model exhibits significant increase in the infall velocity, $\Delta V \approx 6$ km s^{-1} at ~9 $R_\star$, which can only be seen in CODEX atmospheres but not in those of Höfner et al.. As long as the infall velocity does not exceed ~5 km s^{-1}, the modelled spectra does not show a significant difference regardless of the radial distance where the gas from the extra shock episode is located. Based on the molecular spectra of Mira at this particular stellar phase alone, we cannot distinguish whether such an extra episode of shocked gas exists at all nor can we determine its possible distance from the star. On the other hand, our test concerning the SiO molecular abundance in Sect. 3.5.2.3 shows that the radius at which SiO starts to condense onto dust grains is at least 4 $R_\star$. This suggests that the actual wind acceleration may occur beyond ~4 $R_\star$ and hence some velocity variations could still be possible beyond ~2–3 $R_\star$.

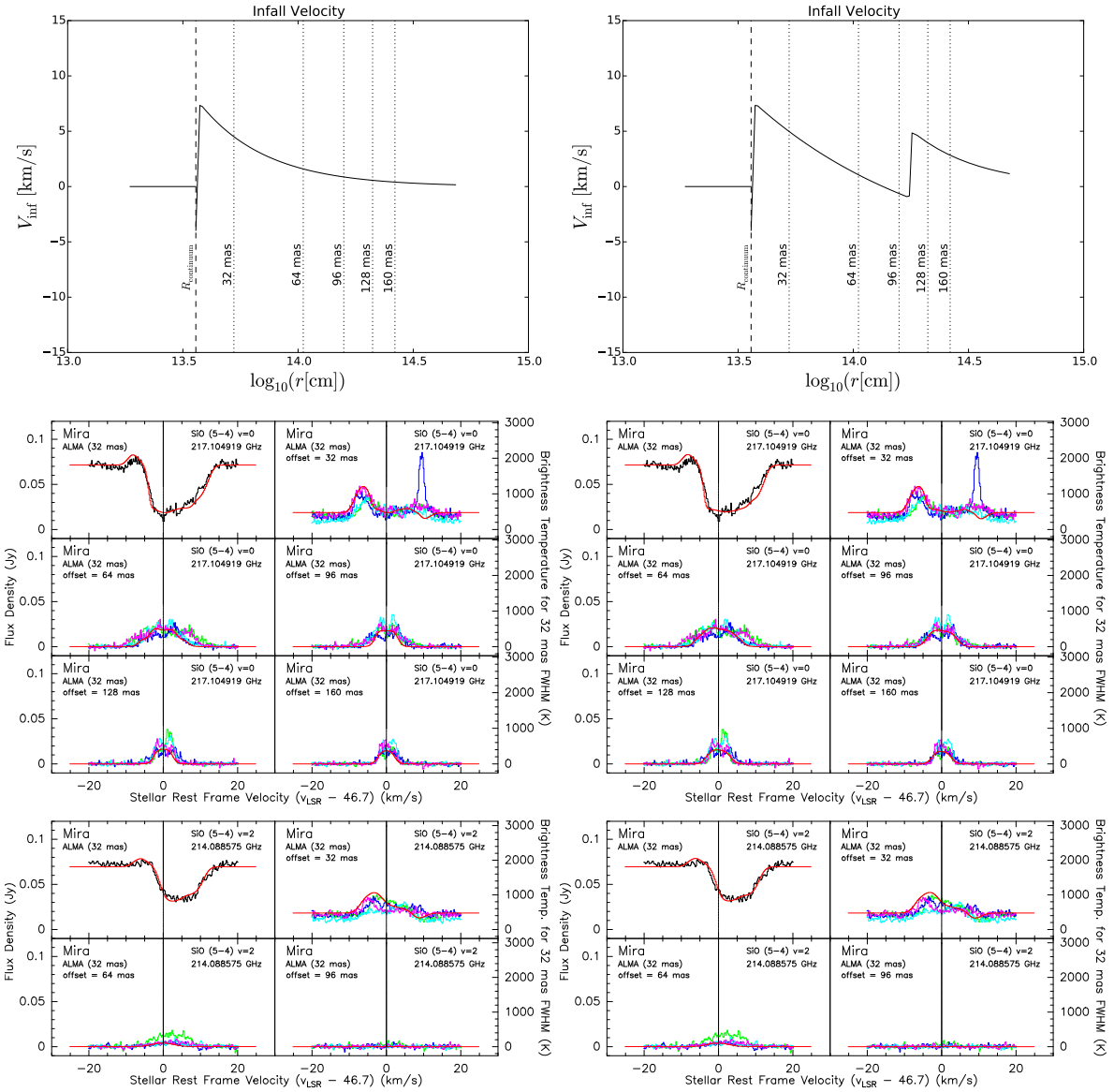

Figure 3.33.: The input radial velocity profile (top row) and the modelled SiO (middle and bottom rows) spectra of two nearly identical models, except that for the model on the left there is only one large-scale velocity variation close to the radio continuum, while for the model on the right there is an additional strong velocity variation near 1.8×10^{14} cm = 109 mas $\sim 5\,R_\star$.

CHAPTER 4

Summary and outlook

4.1. The ammonia enigma

4.1.1. Conclusions

In Chap. 2, multi-wavelength observations of NH_3 line emission or absorption in the circumstellar environments of four carefully selected oxygen-rich post-main sequence stars were presented. The targets include the AGB star IK Tau, the red supergiant VY CMa, the pre-planetary nebula OH 231.8+4.2, and the yellow hypergiant IRC +10420. These targets were selected because of their diversity in evolutionary stages, previous detection of NH_3, and the availability of radiative transfer and chemical models. Emission was detected in multiple inversion transitions in the radio K band (∼1.3 cm) with the VLA and ground-state rotational transitions at the submillimetre wavelengths with *Herschel*/HIFI from all four targets. The rotational transition in the first vibrationally excited state ($v_2 = 1$) near 140 GHz (2.14 mm) from IK Tau was not detected. In addition, multiple NH_3 rovibrational absorption lines were detected from IK Tau and VY CMa in the MIR N band (∼10 μm) with the TEXES instrument at IRTF. Specific results with different instruments include:

1. The VLA images show that NH_3 in IK Tau forms quite close to the star at radii within 100 $R_\star$. In VY CMa, the angular resolution is not enough to clearly resolve the distribution of the gas; however, there are some indications that the strongest NH_3 emission is slightly displaced from the stellar continuum by $\lesssim 1''$ to the south-west and is apparently associated with the SW Clump. The NH_3 emission from OH 231.8+4.2 predominantly arises from the central clump, I3. Some fraction of NH_3 in OH 231.8+4.2 resides in the bipolar outflow and a distinct kinematic feature (possibly a disc-like structure).
2. *Herschel*/HIFI spectra show broad emission lines in all four targets. In IK Tau, VY CMa, and IRC +10420, the line widths are close to or slightly exceed the terminal expansion velocities of the respective targets; therefore, the bulk of the line-emitting gas locate in the fully accelerated CSEs.
3. IRTF spectra show blueshifted absorption close to (IK Tau) or smaller than (VY CMa) the expansion velocity. Hence, the MIR-absorbing gas in VY CMa is probably near the end of the wind acceleration zone.

Radiative transfer modelling was carried out on all available spectra. MIR excitation of the molecule to the first vibrationally excited state ($v_2 = 1$) is included. The NH_3 abundance is generally of the order of 10^{-7}, which is a few times lower than previous results without MIR pumping (e.g. Menten et al., 2010). Comparing our results with those of IRC +10216 (Schmidt et al., 2016), the NH_3 abundance in O-rich CSEs is more than 10 times higher than in C-rich

CSEs. Both studies find that the inclusion of radiative pumping of NH_3 by the MIR continuum from the star and dust shells is important to correctly estimate the molecular abundance: the revised abundances in both environments are significantly lower than previously thought.

It is speculated that the high NH_3 abundance in circumstellar environments is possibly associated with shock-induced chemistry and photodissociation. However, detailed theoretical models including both shock- and photo-chemistry are not available. Furthermore, the origins of free nitrogen atoms or ions cannot be identified. Free nitrogen is required to trigger successive hydrogenation which leads to the formation of NH_3 (e.g. Willacy & Millar, 1997; Decin et al., 2010a).

4.1.2. Prospects

Future imaging of the NH_3 inversion line emission with the VLA at sub-arcsecond resolutions would be useful to constrain the inner radius and the spatial-kinematic distribution of the NH_3 emission, especially for the strong emission detected in OH 231.8+4.2 and IRC +10420. In addition, simultaneous coverage of SO_2 transitions in the radio K band would allow us to verify the association of NH_3 with SO_2 as seen in some targets. The envisioned next generation Very Large Array (ngVLA; Isella et al., 2015; ngVLA Science Advisory Council, 2017) will be useful in searching for non-metastable ($J > K$) inversion lines, which exclusively trace the densest part ($\gtrsim 10^8$ cm^{-3}) of the NH_3-carrying gas (Sweitzer et al., 1979; Ho & Townes, 1983). At the (sub)millimetre wavelengths, it is also important to compare the spatial distribution and kinematics of NH_3 with other species associated with shocks and photodissociation (such as CS, SO, SO_2) and species in the nitrogen network (such as NO, N_2H^+) under high angular resolutions. Shocked-excited H_2 emission can be observed in the near-infrared to verify the speculation of circumstellar shocks.

The rovibrational absorption profiles provide important constraints on the radii of NH_3 molecules by comparing the line absorption velocity and the CSE expansion velocity. There are indications that NH_3 forms close to the end of the wind acceleration zone (VY CMa) or exhibits temporal variations in abundance and absorption velocity (o Cet). Additional MIR N-band observations of other massive stars and Mira variables (such as IRC +10420, VX Sgr, R Leo) at high spectral resolution ($R \sim 10^5$) are necessary to fully understand the formation of the molecule in evolved stars.

Above $v_2 = 1$, the next lowest vibrationally excited levels are $v_2 = 2$ (s-state only) at 1597.47 cm^{-1} and $v_4 = 1$ (both states) at 1626.28 and 1627.38 cm^{-1} (e.g. Yu et al., 2010). These vibrational states are connected to the ground state (0 and 0.79 cm^{-1}) by MIR photons of wavelengths between 6.1–6.3 μm. In Chap. 2, it was assumed that these energy levels are not significantly populated by the MIR radiation of the star and dust. Verification of the assumption by modelling is extremely computationally expensive because the number of transitions increases exponentially. Observations with MIR instruments near 6 μm, such as TEXES at ground-based telescopes or EXES[1] aboard the airborne telescope of SOFIA[2], would be useful to examine the extent of vibrational excitation of NH_3.

[1] Echelon-Cross-Echelle Spectrograph (Richter et al., 2006, 2010).
[2] Stratospheric Observatory For Infrared Astronomy (Young et al., 2012; Temi et al., 2014).

4.2. Extended atmospheres of evolved stars

4.2.1. Conclusions

In Chap. 3, the ALMA long-baseline observations of Mira (*o* Cet) were presented. With the long ALMA baselines of ~15 km, it is now possible to probe the physical conditions in the extended atmospheres and the inner winds (within the dust condensation zone) of AGB stars in unprecedented detail. The angular resolution of Mira's observations during the 2014 ALMA Long Baseline Campaign was ~30 mas at 220 GHz, which is high enough to resolve the radio continuum of Mira. For the first time, spectral line absorption against the stellar radio continuum has been clearly imaged at the millimetre wavelengths (1.3 mm) in the transitions of SiO $v = 0, 1, 2$ $J = 5$–4, ^{29}SiO $v = 0$ $J = 5$–4, and H_2O $v_2 = 1$ $J_{K_a,K_c} = 5_{5,0}$–$6_{4,3}$.

Mira's radio continuum emission at 229.6 GHz was fitted and the results were compared to two other independent results published in mid-2015. The continuum models for Mira A and B presented in this thesis are consistent with those fitted by Matthews et al. (2015). The single uniform disc model for Mira A is consistent with a radio photosphere with a brightness temperature of 2611 ± 51 K. On the other hand, there was no sign of a compact (~4.7 mas) hotspot ($T_b \sim 10\,000$ K) in Mira A's continuum as suggested by Vlemmings et al. (2015) even though the identical fitting procedure has been adopted and cross-checking has been done with another visibility fitting software.

Through radiative transfer modelling, detailed physical conditions of Mira's extended atmosphere were constructed. These include the gas density, kinetic temperature, molecular abundances of SiO and H_2O, and the expansion/infall velocity as functions of radial distance from the star. The SiO and H_2O spectra along the lines of sight towards the stellar continuum and towards positions at various sky-projected radii and position angles from the star were fitted. In the preferred model (Model 3), which successfully reproduces the spectra of SiO $v = 0, 2$ and H_2O $v_2 = 1$, the extended atmosphere shows infall motion in general. A shock of velocity $\Delta V \sim 12$ km s^{-1} is found above Mira's 229 GHz radio photosphere. The SiO abundance drops significantly from 1×10^{-6} to 1×10^{-8}–1×10^{-7} at the radius of about 1.0×10^{14} cm $= 5\,R_\star$, where $R_\star = 12.3$ mas $= 292\,R_\odot$ is the adopted radius of Mira's infrared photosphere. However, it has been shown that the SiO depletion radius may indeed be anywhere from $4\,R_\star$ outwards. In addition, the H_2O spectra may be better fitted by adopting an abundance distribution that shows a sharp rise in abundance (of about 10 times) near the radio photosphere.

The predictions from current hydrodynamical models, in particular the CODEX model series that are tailored for Mira, were also tested. The predicted atmospheric structures were used as the inputs of the line radiative transfer modelling. The models are able to qualitatively reproduce the absorption features against the continuum. After fine-tuning the radial distances and the magnitudes of the major shock front(s), which are chaotic in nature, the synthesised spectra from the CODEX models can then fit the observed spectra in this SV observation reasonably well. Considering the chaotic nature of Mira's extended atmosphere, the modelled spectra from the CODEX atmospheres fit the observed ALMA spectra remarkably well. In addition, some other models of Mira's circumstellar environment (e.g. the presence of a chromosphere) do not have support in this ALMA data.

4.2.2. Prospects

The long ALMA baselines have demonstrated their capability to produce high-angular resolution and high-sensitivity spectral line images in the extended atmospheres of evolved stars. In order to test the validity of current hydrodynamical models, long-term monitoring (multi-cycle

and multi-epoch) of Mira variables and AGB stars is necessary. In 2017, an ALMA Cycle 5 proposal of follow-up long-baseline observations on *o* Cet and new observations on IK Tau has been accepted. The new data will certainly give new insight into the long-standing puzzle of dust condensation and wind-driving mechanism in oxygen-rich evolved stars.

References

Adande, G. R., Edwards, J. L., & Ziurys, L. M. 2013, ApJ, 778, 22

Agúndez, M., Cernicharo, J., & Guélin, M. 2010, ApJ, 724, L133

Albrecht, M. A. 1983, A&A, 127, 409

Alcolea, J., Bujarrabal, V., Planesas, P., et al. 2013, A&A, 559, A93

Alcolea, J., Bujarrabal, V., & Sanchez Contreras, C. 1996, A&A, 312, 560

Alcolea, J., Bujarrabal, V., Sánchez Contreras, C., Neri, R., & Zweigle, J. 2001, A&A, 373, 932

ALMA Partnership, Asayama, S., Biggs, A., et al. 2017, ALMA Cycle 5 Technical Handbook ALMA, ALMA Doc. 5.3, ver. 1.0, available at https://almascience.eso.org/documents-and-tools/cycle5/alma-technical-handbook

ALMA Partnership, Brogan, C. L., Pérez, L. M., et al. 2015a, ApJ, 808, L3

ALMA Partnership, Fomalont, E. B., Vlahakis, C., et al. 2015b, ApJ, 808, L1

Arai, H., Nagai, M., Fujita, S., et al. 2016, PASJ, 68, 76

Astropy Collaboration, Robitaille, T. P., Tollerud, E. J., et al. 2013, A&A, 558, A33

Bajaja, E. & van Albada, G. D. 1979, A&A, 75, 251

Balança, C. & Dayou, F. 2017, MNRAS, 469, 1673

Barber, R. J., Tennyson, J., Harris, G. J., & Tolchenov, R. N. 2006, MNRAS, 368, 1087

Baron, F. 2016, in Astronomy at High Angular Resolution, eds. H. M. J. Boffin, G. Hussain, J.-P. Berger, & L. Schmidtobreick (Cham: Springer International Publishing Switzerland), 75

Barton, E. J., Yurchenko, S. N., & Tennyson, J. 2013, MNRAS, 434, 1469

Beach, T. E., Willson, L. A., & Bowen, G. H. 1988, ApJ, 329, 241

Bell, M. B., Kwok, S., & Feldman, P. A. 1980, in Interstellar Molecules, ed. B. H. Andrew, IAU Symp., 87, 495

Belov, S. P., Kozin, I. N., Polyansky, O. L., Tret'yakov, M. Y., & Zobov, N. F. 1987, J. Mol. Spectr., 126, 113

Benson, J. M., Mutel, R. L., Fix, J. D., & Claussen, M. J. 1979, ApJ, 229, L87

Bessell, M. S., Brett, J. M., Wood, P. R., & Scholz, M. 1989, A&A, 213, 209

Bessell, M. S., Scholz, M., & Wood, P. R. 1996, A&A, 307, 481

Bethe, H. A. 1939, Phys. Rev., 55, 103

Betz, A. L. 1996, in Amazing Light, ed. R. Y. Chiao, 73

Betz, A. L. & Goldhaber, D. M. 1985, in Mass Loss from Red Giants, eds. M. Morris & B. Zuckerman, ASSL, 117, 83

Betz, A. L. & McLaren, R. A. 1980, in Interstellar Molecules, ed. B. H. Andrew, IAU Symp., 87, 503

Betz, A. L., McLaren, R. A., & Spears, D. L. 1979, ApJ, 229, L97

Bieging, J. H., Knee, L. B. G., Latter, W. B., & Olofsson, H. 1998, A&A, 339, 811

Bieniek, R. J. & Green, S. 1981, Chem. Phys. Lett., 84, 380

Bieniek, R. J. & Green, S. 1983a, ApJ, 265, L29

Bieniek, R. J. & Green, S. 1983b, ApJ, 270, L101
Boboltz, D. A. & Claussen, M. J. 2004, ApJ, 608, 480
Bouhafs, N., Rist, C., Daniel, F., et al. 2017, MNRAS, 470, 2204
Bowen, G. H. 1988a, ApJ, 329, 299
Bowen, G. H. 1988b, in Pulsation and Mass Loss in Stars, eds. R. Stalio & L. A. Willson (Dordrecht: Kluwer Academic Publishers), ASSL, 148, 3
Bowen, G. H. 1989, in Evolution of Peculiar Red Giant Stars, eds. H. R. Johnson & B. Zuckerman (Cambridge: Cambridge University Press), IAU Colloq., 106, 269
Braun, R. & Walterbos, R. A. M. 1985, A&A, 143, 307
Bunker, P. R. 1979, Microwave Symmetry and Spectroscopy (New York: Academic Press, Inc.)
Burbidge, E. M., Burbidge, G. R., Fowler, W. A., & Hoyle, F. 1957, Rev. Mod. Phys., 29, 547
Cannon, R. D. 1967, The Observatory, 87, 231
Carrillo, R. E., McEwen, J. D., & Wiaux, Y. 2014, MNRAS, 439, 3591
Carter, M., Lazareff, B., Maier, D., et al. 2012, A&A, 538, A89
Castro-Carrizo, A., Quintana-Lacaci, G., Bujarrabal, V., Neri, R., & Alcolea, J. 2007, A&A, 465, 457
Castro-Carrizo, A., Quintana-Lacaci, G., Neri, R., et al. 2010, A&A, 523, A59
Cazzoli, G., Dore, L., & Puzzarini, C. 2009, A&A, 507, 1707
Charnley, S. B. & Latter, W. B. 1997, MNRAS, 287, 538
Charnley, S. B., Tielens, A. G. G. M., & Kress, M. E. 1995, MNRAS, 274, L53
Chen, P., Pearson, J. C., Pickett, H. M., Matsuura, S., & Blake, G. A. 2006, J. Mol. Spectr., 236, 116
Cherchneff, I. 2006, A&A, 456, 1001
Cherchneff, I. 2013, in Betelgeuse Workshop 2012. The Physics of Red Supergiants: Recent Advances and Open Questions, eds. P. Kervella, T. Le Bertre, & G. Perrin, EAS Publ. Ser., 60, 175
Cheung, A. C., Chui, M. F., Matsakis, D., Townes, C. H., & Yngvesson, K. S. 1973, ApJ, 186, L73
Cheung, A. C., Rank, D. M., Townes, C. H., Knowles, S. H., & Sullivan, III, W. T. 1969, ApJ, 157, L13
Cheung, A. C., Rank, D. M., Townes, C. H., Thornton, D. D., & Welch, W. J. 1968, Phys. Rev. Lett., 21, 1701
Choi, Y. K., Brunthaler, A., Menten, K. M., & Reid, M. J. 2012, in Cosmic Masers - from OH to H0, eds. R. S. Booth, W. H. T. Vlemmings, & E. M. L. Humphreys, IAU Symp., 287, 407
Choi, Y. K., Hirota, T., Honma, M., et al. 2008, PASJ, 60, 1007
Clark, B. G. 1980, A&A, 89, 377
Clegg, P. E., Ade, P. A. R., Armand, C., et al. 1996, A&A, 315, L38
Cohen, M. 1981, PASP, 93, 288
Cohen, M., Witteborn, F. C., Carbon, D. F., et al. 1992, AJ, 104, 2045
Cordiner, M. A., Boogert, A. C. A., Charnley, S. B., et al. 2016, ApJ, 828, 51
Cordiner, M. A. & Millar, T. J. 2009, ApJ, 697, 68
Cornwell, T. J., Uson, J. M., & Haddad, N. 1992, A&A, 258, 583
Cotton, W. D., Mennesson, B., Diamond, P. J., et al. 2004, A&A, 414, 275
Cotton, W. D., Perrin, G., & Lopez, B. 2008, A&A, 477, 853
Dabrowski, I. 1984, Canadian J. Phys., 62, 1639
Danby, G., Flower, D. R., Valiron, P., Schilke, P., & Walmsley, C. M. 1988, MNRAS, 235, 229

Danchi, W. C., Bester, M., Degiacomi, C. G., Greenhill, L. J., & Townes, C. H. 1994, AJ, 107, 1469
Daniel, F., Dubernet, M.-L., & Grosjean, A. 2011, A&A, 536, A76
Danilovich, T., Bergman, P., Justtanont, K., et al. 2014, A&A, 569, A76
Danilovich, T., De Beck, E., Black, J. H., Olofsson, H., & Justtanont, K. 2016, A&A, 588, A119
Darwent, B. d. 1970, Natl. Standard Ref. Data Ser., 31, DOI: 10.6028/NBS.NSRDS.31
Dayou, F. & Balança, C. 2006, A&A, 459, 297
De Beck, E., Kamiński, T., Patel, N. A., et al. 2013, A&A, 558, A132
De Beck, E., Vlemmings, W., Muller, S., et al. 2015, A&A, 580, A36
De Becker, M., Hutsemékers, D., & Gosset, E. 2014, New Astron., 29, 75
de Graauw, T., Haser, L. N., Beintema, D. A., et al. 1996, A&A, 315, L49
de Graauw, T., Helmich, F. P., Phillips, T. G., et al. 2010, A&A, 518, L6
de Jong, T., Dalgarno, A., & Chu, S.-I. 1975, ApJ, 199, 69
Decin, L., Agúndez, M., Barlow, M. J., et al. 2010a, Nature, 467, 64
Decin, L., Hony, S., de Koter, A., et al. 2006, A&A, 456, 549
Decin, L., Justtanont, K., De Beck, E., & et al. 2010b, A&A, 521, L4
Decin, L., Richards, A. M. S., Millar, T. J., et al. 2016, A&A, 592, A76
Deguchi, S., Claussen, M. J., & Goldsmith, P. F. 1986, ApJ, 303, 810
Deguchi, S. & Goldsmith, P. F. 1985, Nature, 317, 336
DePristo, A. E., Augustin, S. D., Ramaswamy, R., & Rabitz, H. 1979, J. Chem. Phys., 71, 850
Desmurs, J.-F., Bujarrabal, V., Lindqvist, M., et al. 2014, A&A, 565, A127
Diamond, P. J. & Kemball, A. J. 2003, ApJ, 599, 1372
Diamond, P. J., Kemball, A. J., Junor, W., et al. 1994, ApJ, 430, L61
Dinh-V.-Trung, Chiu, P. J., & Lim, J. 2009a, ApJ, 700, 86
Dinh-V.-Trung, Muller, S., Lim, J., Kwok, S., & Muthu, C. 2009b, ApJ, 697, 409
Doel, R. C. 1990, PhD Thesis, University of Bristol, available at http://ethos.bl.uk/OrderDetails.do?uin=uk.bl.ethos.667872
Doel, R. C., Gray, M. D., Humphreys, E. M. L., Braithwaite, M. F., & Field, D. 1995, A&A, 302, 797
Dolan, J. F. 1965, ApJ, 142, 1621
Dorschner, J., Begemann, B., Henning, T., Jaeger, C., & Mutschke, H. 1995, A&A, 300, 503
Draine, B. T. 2011, Physics of the Interstellar and Intergalactic Medium (Princeton: Princeton University Press)
Duari, D., Cherchneff, I., & Willacy, K. 1999, A&A, 341, L47
Edmonds, A. R. 1960, Angular Momentum in Quantum Mechanics, the second edn. (3rd printing) (Princeton: Princeton University Press)
Fabas, N., Lèbre, A., & Gillet, D. 2011, A&A, 535, A12
Fadeyev, Y. A. & Gillet, D. 2004, A&A, 420, 423
Faure, A., Hily-Blant, P., Le Gal, R., Rist, C., & Pineau des Forêts, G. 2013, ApJ, 770, L2
Faure, A. & Josselin, E. 2008a, A&A, 492, 257
Faure, A. & Josselin, E. 2008b, A&A, 492, 257
Feast, M. W., Glass, I. S., Whitelock, P. A., & Catchpole, R. M. 1989, MNRAS, 241, 375
Field, D. 1998, in The Molecular Astrophysics of Stars and Galaxies, eds. T. W. Hartquist & D. A. Williams (Oxford: Clarendon Press), Int. Ser. Astron. Astrophys., 4, 313
Flower, D. R. 1989, Phys. Rep., 174, 1
Flower, D. R. & Watt, G. D. 1984, MNRAS, 209, 25
Fonfría, J. P., Hinkle, K. H., Cernicharo, J., et al. 2017, ApJ, 835, 196

Fox, M. W. & Wood, P. R. 1985, ApJ, 297, 455
Fox, M. W., Wood, P. R., & Dopita, M. A. 1984, ApJ, 286, 337
Freytag, B., Liljegren, S., & Höfner, S. 2017, A&A, 600, A137
Fu, R. R., Moullet, A., Patel, N. A., et al. 2012, ApJ, 746, 42
Fujita, Y. 1966, Vistas Astr., 7, 71
Gabovitš, J. 1936, Publ. Tartu Astron. Obser., 29, 1
Gail, H.-P. & Sedlmayr, E. 1998, Faraday Discussions, 109, 303
Gail, H.-P., Wetzel, S., Pucci, A., & Tamanai, A. 2013, A&A, 555, A119
Gautschy-Loidl, R., Höfner, S., Jørgensen, U. G., & Hron, J. 2004, A&A, 422, 289
Gillet, D., Ferlet, R., Maurice, E., & Bouchet, P. 1985, A&A, 150, 89
Gillet, D., Maurice, E., & Baade, D. 1983, A&A, 128, 384
Glassgold, A. E. & Huggins, P. J. 1983, MNRAS, 203, 517
Gobrecht, D., Cherchneff, I., Sarangi, A., Plane, J. M. C., & Bromley, S. T. 2016, A&A, 585, A6
Goldflam, R., Kouri, D. J., & Green, S. 1977, J. Chem. Phys., 67, 4149
Goldhaber, D. M. 1988, PhD Dissertation, University of California at Berkeley, available via subscription at https://search.proquest.com/docview/303689762
Gómez, J. F., Uscanga, L., Suárez, O., Rizzo, J. R., & de Gregorio-Monsalvo, I. 2014, RMxAA, 50, 137
Gong, Y., Henkel, C., Spezzano, S., et al. 2015, A&A, 574, A56
Gordon, R. G. & Kim, Y. S. 1972, J. Chem. Phys., 56, 3122
Gray, M. D., Baudry, A., Richards, A. M. S., et al. 2016, MNRAS, 456, 374
Gray, M. D. & Humphreys, E. M. L. 2000, New Astron., 5, 155
Gray, M. D., Wittkowski, M., Scholz, M., et al. 2009, MNRAS, 394, 51
Green, S. 1976, J. Chem. Phys., 64, 3463
Grossman, L. & Larimer, J. W. 1974, Rev. Geophys. Space Phys., 12, 71
Hale, D. D. S., Bester, M., Danchi, W. C., et al. 1997, ApJ, 490, 407
Haniff, C. A., Scholz, M., & Tuthill, P. G. 1995, MNRAS, 276, 640
Harju, J., Walmsley, C. M., & Wouterloot, J. G. A. 1993, A&AS, 98, 51
Hasegawa, T. I., Kwok, S., Koning, N., et al. 2006, ApJ, 637, 791
Henry, R. B. C., Edmunds, M. G., & Köppen, J. 2000, ApJ, 541, 660
Hertzsprung, E. 1905, Z. Wiss. Photogr., 3, 442
Hertzsprung, E. 1907, Z. Wiss. Photogr., 5, 86
Hertzsprung, E. 1911, Publ. Astrophys. Obser. Potsdam, 63
Herzberg, G. 1945, Molecular Spectra and Molecular Structure. II: Infrared and Raman Spectra of Polyatomic Molecules (13th printing) (Princeton: D. Van Nostrand Company, Inc.)
Hevelius, J. 1662, in Historiola, Miræ Stellæ, 146, available at ETH-Bibliothek Zürich, Rar 10317, https://doi.org/10.3931/e-rara-22448
Hill, S. J. & Willson, L. A. 1979, ApJ, 229, 1029
Hillen, M., Verhoelst, T., Degroote, P., Acke, B., & van Winckel, H. 2012, A&A, 538, L6
Hinkle, K. H., Hall, D. N. B., & Ridgway, S. T. 1982, ApJ, 252, 697
Hinkle, K. H., Lebzelter, T., & Scharlach, W. W. G. 1997, AJ, 114, 2686
Hinkle, K. H., Scharlach, W. W. G., & Hall, D. N. B. 1984, ApJS, 56, 1
Ho, P. T. P., Barrett, A. H., Myers, P. C., et al. 1979, ApJ, 234, 912
Ho, P. T. P. & Townes, C. H. 1983, ARA&A, 21, 239
Hofmann, K.-H., Scholz, M., & Wood, P. R. 1998, A&A, 339, 846
Hofmann, K.-H., Weigelt, G., & Schertl, D. 2014, A&A, 565, A48
Höfner, S. 2007, in Why Galaxies Care About AGB Stars: Their Importance as Actors and

Probes, eds. F. Kerschbaum, C. Charbonnel, & R. F. Wing, ASP Conf. Ser., 378, 145
Höfner, S. 2008, A&A, 491, L1
Höfner, S. 2009, in Cosmic Dust - Near and Far, eds. T. Henning, E. Grün, & J. Steinacker, ASP Conf. Ser., 414, 3
Höfner, S. 2015, in Why Galaxies Care about AGB Stars III: A Closer Look in Space and Time, eds. F. Kerschbaum, R. F. Wing, & J. Hron, ASP Conf. Ser., 497, 333
Höfner, S. 2016, in 19th Cambridge Workshop on Cool Stars, Stellar Systems, and the Sun (CS19), 19, DOI: 10.5281/zenodo.154673
Höfner, S. & Andersen, A. C. 2007, A&A, 465, L39
Höfner, S., Bladh, S., Aringer, B., & Ahuja, R. 2016, A&A, 594, A108
Höfner, S., Gautschy-Loidl, R., Aringer, B., & Jørgensen, U. G. 2003, A&A, 399, 589
Högbom, J. A. 1974, A&AS, 15, 417
Hogerheijde, M. R. & van der Tak, F. F. S. 2000, A&A, 362, 697
Holler, C. 1999, *Diplomarbeit* [Master's Thesis], Ludwig-Maximilians-Universität München, quoted in Monnier et al. (2000b)
Howard, J. B. & Bright Wilson, Jr., E. 1934, J. Chem. Phys., 2, 630
Humphreys, E. M. L., Gray, M. D., Yates, J. A., et al. 1996, MNRAS, 282, 1359
Humphreys, E. M. L., Gray, M. D., Yates, J. A., et al. 2002, A&A, 386, 256
Humphreys, E. M. L., Yates, J. A., Gray, M. D., Field, D., & Bowen, G. H. 2001, A&A, 379, 501
Humphreys, R. M. 2016, in 11th Pacific Rim Conference on Stellar Astrophysics: Physics and Chemistry of the Late Stages of Stellar Evolution, J. Phys. Conf. Ser., 728, 022007
Humphreys, R. M., Helton, L. A., & Jones, T. J. 2007, AJ, 133, 2716
Hunter, J. D. 2007, Comput. Sci. Engg., 9, 90
Iben, Jr., I. & Renzini, A. 1983, ARA&A, 21, 271
Ireland, M. J. 2011, in Why Galaxies Care about AGB Stars II: Shining Examples and Common Inhabitants, eds. F. Kerschbaum, T. Lebzelter, & R. F. Wing, ASP Conf. Ser., 445, 83
Ireland, M. J., Scholz, M., Tuthill, P. G., & Wood, P. R. 2004a, MNRAS, 355, 444
Ireland, M. J., Scholz, M., & Wood, P. R. 2004b, MNRAS, 352, 318
Ireland, M. J., Scholz, M., & Wood, P. R. 2008, MNRAS, 391, 1994
Ireland, M. J., Scholz, M., & Wood, P. R. 2011, MNRAS, 418, 114
Isella, A., Hull, C. L. H., Moullet, A., et al. 2015, NGVLA Memo Ser.[arXiv:1510.06444], available at https://library.nrao.edu/public/memos/ngvla/NGVLA_06.pdf
Ivezić, Ž., Nenkova, M., & Elitzur, M. 1999, ArXiv e-prints [astro-ph/9910475], University of Kentucky Internal Report, available at http://www.pa.uky.edu/~moshe/dusty/
Jacquinet-Husson, N., Armante, R., Scott, N. A., et al. 2016, J. Mol. Spectr., 327, 31
Johnson, H. R. & Sauval, A. J. 1982, A&AS, 49, 77
Jones, E., Oliphant, T., P., P., & et al. 2001, SciPy: Open source scientific tools for Python, https://www.scipy.org/
Jones, T. J., Humphreys, R. M., Gehrz, R. D., et al. 1993, ApJ, 411, 323
Joy, A. H. 1926, ApJ, 63, 281
Joy, A. H. 1947, ApJ, 106, 288
Joy, A. H. 1954, ApJS, 1, 39
Junklewitz, H., Bell, M. R., Selig, M., & Enßlin, T. A. 2016, A&A, 586, A76
Jura, M., Chen, C., & Plavchan, P. 2002, ApJ, 574, 963
Kamiński, T., Gottlieb, C. A., Young, K. H., Menten, K. M., & Patel, N. A. 2013, ApJS, 209, 38

Kamiński, T., Menten, K. M., Tylenda, R., et al. 2015, Nature, 520, 322
Kamiński, T., Menten, K. M., Tylenda, R., et al. 2017a, A&A, in press [arXiv:1708.02261], DOI: 10.1051/0004-6361/201731287
Kamiński, T., Müller, H. S. P., Schmidt, M. R., et al. 2017b, A&A, 599, A59
Kamiński, T., Wong, K. T., Schmidt, M. R., et al. 2016, A&A, 592, A42
Karakas, A. I. & Lattanzio, J. C. 2014, PASA, 31, e030
Karovicova, I., Wittkowski, M., Boboltz, D. A., et al. 2011, A&A, 532, A134
Karovicova, I., Wittkowski, M., Ohnaka, K., et al. 2013, A&A, 560, A75
Kastner, J. H., Weintraub, D. A., Zuckerman, B., et al. 1992, ApJ, 398, 552
Keady, J. J. & Ridgway, S. T. 1993, ApJ, 406, 199
Keller, S. C. & Wood, P. R. 2006, ApJ, 642, 834
Kessler, M. F., Steinz, J. A., Anderegg, M. E., et al. 1996, A&A, 315, L27
Kholopov, P. N. 1987, General Catalogue of Variable Stars, the fourth edn. (Moscow: Publishing House of the Academy of Sciences of the U.S.S.R.)
Kippenhahn, R., Weigert, A., & Weiss, A. 2012, Stellar Structure and Evolution (Heidelberg: Springer-Verlag Berlin Heidelberg)
Klochkova, V. G., Chentsov, E. L., & Panchuk, V. E. 1997, MNRAS, 292, 19
Kłos, J. & Lique, F. 2008, MNRAS, 390, 239
Kramer, C., Peñalver, J., & Greve, A. 2013, Improvement of the IRAM 30m telescope beam pattern, v8.2, available at http://www.iram.es/IRAMES/mainWiki/CalibrationPapers
Kukolich, S. G. 1967, Phys. Rev., 156, 83
Kukolich, S. G. & Wofsy, S. C. 1970, J. Chem. Phys., 52, 5477
Kwok, S., Bell, M. B., & Feldman, P. A. 1981, ApJ, 247, 125
Lacy, J. H., Richter, M. J., Greathouse, T. K., Jaffe, D. T., & Zhu, Q. 2002, PASP, 114, 153
Lagadec, E., Verhoelst, T., Mékarnia, D., et al. 2011, MNRAS, 417, 32
Langer, S. H. & Watson, W. D. 1984, ApJ, 284, 751
Lattanzio, J. C. & Wood, P. R. 2003, in Asymptotic Giant Branch Stars, eds. H. J. Habing & H. Olofsson (New York: Springer Science+Business Media), 23
Latter, W. B. & Charnley, S. B. 1996a, ApJ, 463, L37
Latter, W. B. & Charnley, S. B. 1996b, ApJ, 465, L81
Le Bertre, T. 1993, A&AS, 97, 729
Lebzelter, T. & Hinkle, K. H. 2002, in Radial and Nonradial Pulsations as Probes of Stellar Physics, IAU Colloquium 185, eds. C. Aerts, T. R. Bedding, & J. Christensen-Dalsgaard, ASP Conf. Ser., 259, 556
Lebzelter, T., Hinkle, K. H., Wood, P. R., Joyce, R. R., & Fekel, F. C. 2005, A&A, 431, 623
Levesque, E. M. 2010, New Astron. Rev., 54, 1
Lewars, E. G. 2011, Computational Chemistry: Introduction to the Theory and Applications of Molecular and Quantum Mechanics, the second edn. (Dordrecht: Springer Science+Business Media B.V.)
Li, J. & Guo, H. 2014, Phys. Chem. Chem. Phys., 16, 6753
Li, X., Heays, A. N., Visser, R., et al. 2013, A&A, 555, A14
Li, X., Millar, T. J., Heays, A. N., et al. 2016, A&A, 588, A4
Li, X., Millar, T. J., Walsh, C., Heays, A. N., & van Dishoeck, E. F. 2014, A&A, 568, A111
Liljegren, S., Höfner, S., Eriksson, K., & Nowotny, W. 2017, A&A, 606, A6
Lique, F. & Kłos, J. 2008, J. Chem. Phys., 128, 034306
Little-Marenin, I. R. & Little, S. J. 1990, AJ, 99, 1173
Lloyd, C., Lerate, M. R., & Grundy, T. W. 2013, The LWS LO1 Pipeline, Version 1, available

at http://ida.esac.esa.int:8080/hpdp/technical_reports/technote34.html
Lobel, A., Bagnulo, S., Doyle, J. G., & Power, C. 2000, MNRAS, 317, 391
Lochner, M., Natarajan, I., Zwart, J. T. L., et al. 2015, MNRAS, 450, 1308
Lockett, P. & Elitzur, M. 1992, ApJ, 399, 704
Lomb, N. R. 1976, Ap&SS, 39, 447
Longuet-Higgins, H. C. 1963, Mol. Phys., 6, 445
Lopez, B., Danchi, W. C., Bester, M., et al. 1997, ApJ, 488, 807
Lorenz-Martins, S. & Pompeia, L. 2000, MNRAS, 315, 856
Luttermoser, D. G. & Bowen, G. H. 1990, in Cool Stars, Stellar Systems, and the Sun, ed. G. Wallerstein, ASP Conf. Ser., 9, 491
Luttermoser, D. G. & Bowen, G. H. 1992, in Cool Stars, Stellar Systems, and the Sun, eds. M. S. Giampapa & J. A. Bookbinder, ASP Conf. Ser., 26, 558
Luttermoser, D. G., Johnson, H. R., & Eaton, J. 1994, ApJ, 422, 351
Lyubimkov, L. S., Lambert, D. L., Korotin, S. A., et al. 2011, MNRAS, 410, 1774
Madhusudhan, N., Agúndez, M., Moses, J. I., & Hu, Y. 2016, Space Sci. Rev., 205, 285
Maercker, M., Danilovich, T., Olofsson, H., et al. 2016, A&A, 591, A44
Maercker, M., Schöier, F. L., Olofsson, H., Bergman, P., & Ramstedt, S. 2008, A&A, 479, 779
Maret, S., Faure, A., Scifoni, E., & Wiesenfeld, L. 2009, MNRAS, 399, 425
Martí-Vidal, I., Vlemmings, W. H. T., Muller, S., & Casey, S. 2014, A&A, 563, A136
Martin-Pintado, J. & Bachiller, R. 1992a, ApJ, 391, L93
Martin-Pintado, J. & Bachiller, R. 1992b, ApJ, 401, L47
Martin-Pintado, J., Gaume, R., Bachiller, R., & Johnson, K. 1993, ApJ, 419, 725
Martin-Pintado, J., Gaume, R. A., Johnston, K. J., & Bachiller, R. 1995, ApJ, 446, 687
Marvel, K. B. 2005, AJ, 130, 261
Matplotlib Developers. 2016, matplotlib: v1.5.3, DOI: 10.5281/zenodo.61948
Matsuura, M., Chesneau, O., Zijlstra, A. A., et al. 2006, ApJ, 646, L123
Matthews, L. D., Reid, M. J., & Menten, K. M. 2015, ApJ, 808, 36
Mauersberger, R., Henkel, C., & Wilson, T. L. 1988, A&A, 205, 235
McCabe, E. M., Smith, R. C., & Clegg, R. E. S. 1979, Nature, 281, 263
McCollom, T. M. 2013, AREPS, 41, 207
McElroy, D., Walsh, C., Markwick, A. J., et al. 2013, A&A, 550, A36
McLaren, R. A. & Betz, A. L. 1980, ApJ, 240, L159
Menten, K. M. & Alcolea, J. 1995, ApJ, 448, 416
Menten, K. M., Wyrowski, F., Alcolea, J., & et al. 2010, A&A, 521, L7
Messiah, A. 1962, Quantum mechanics, Volumne II, the first edn. (4th printing) (Amsterdam: North-Holland Publication)
Michelson, A. A. 1898, ApJ, 8, 37
Millar, T. J. 2016, in 11th Pacific Rim Conference on Stellar Astrophysics: Physics and Chemistry of the Late Stages of Stellar Evolution, J. Phys. Conf. Ser., 728, 052001
Millar, T. J., Herbst, E., & Bettens, R. P. A. 2000, MNRAS, 316, 195
Mills, E. A. C. & Morris, M. R. 2013, ApJ, 772, 105
Monnier, J. D., Berger, J.-P., Le Bouquin, J.-B., et al. 2014, in Optical and Infrared Interferometry IV, Proc. SPIE, 9146, 91461Q
Monnier, J. D., Danchi, W. C., Hale, D. S., et al. 2000a, ApJ, 543, 861
Monnier, J. D., Danchi, W. C., Hale, D. S., Tuthill, P. G., & Townes, C. H. 2000b, ApJ, 543, 868
Monnier, J. D., Fitelson, W., Danchi, W. C., & Townes, C. H. 2000c, ApJS, 129, 421
Morris, M., Guilloteau, S., Lucas, R., & Omont, A. 1987, ApJ, 321, 888

Mortier, A., Faria, J. P., Correia, C. M., Santerne, A., & Santos, N. C. 2015a, A&A, 573, A101
Mortier, A., Faria, J. P., Correia, C. M., Santerne, A., & Santos, N. C. 2015b, Astrophys. Source Code Libr. [ascl:1504.020]
Mueller, M., Jellema, W., Olberg, M., Moreno, R., & Teyssier, D. 2014, The HIFI Beam: Release 1, Release Note for Astronomers, Tech. Rep. HIFI-ICC-RP-2014-001, v1.1, HIFI-ICC, available at http://herschel.esac.esa.int/twiki/pub/Public/HifiCalibrationWeb/HifiBeamReleaseNote_Sep2014.pdf
Müller, H. S. P., Schlöder, F., Stutzki, J., & Winnewisser, G. 2005, J. Mol. Struct., 742, 215
Müller, H. S. P., Spezzano, S., Bizzocchi, L., et al. 2013, J. Phys. Chem. A, 117, 13843
Müller, H. S. P., Thorwirth, S., Roth, D. A., & Winnewisser, G. 2001, A&A, 370, L49
Muller, S., Dinh-V-Trung, Lim, J., et al. 2007, ApJ, 656, 1109
Nakashima, J.-i., Ladeyschikov, D. A., Sobolev, A. M., et al. 2016, ApJ, 825, 16
Nakashima, J.-i., Sobolev, A. M., Salii, S. V., et al. 2015, PASJ, 67, 95
Nedoluha, G. E. & Bowers, P. F. 1992, ApJ, 392, 249
Nercessian, E., Omont, A., Benayoun, J. J., & Guilloteau, S. 1989, A&A, 210, 225
Neugebauer, G., Habing, H. J., van Duinen, R., et al. 1984, ApJ, 278, L1
Nguyen-Q-Rieu, Graham, D., & Bujarrabal, V. 1984, A&A, 138, L5
ngVLA Science Advisory Council. 2017, NGVLA Memo Ser., available at https://library.nrao.edu/public/memos/ngvla/NGVLA_19.pdf
Nowotny, W., Aringer, B., Höfner, S., Gautschy-Loidl, R., & Windsteig, W. 2005a, A&A, 437, 273
Nowotny, W., Höfner, S., & Aringer, B. 2010, A&A, 514, A35
Nowotny, W., Lebzelter, T., Hron, J., & Höfner, S. 2005b, A&A, 437, 285
Ochsenbein, F., Bauer, P., & Marcout, J. 2000, A&AS, 143, 23
O'Gorman, E., Vlemmings, W., Richards, A. M. S., et al. 2015, A&A, 573, L1
Ohnaka, K. 2004, A&A, 424, 1011
Ohnaka, K. 2014, A&A, 561, A47
Ohnaka, K., Bergeat, J., Driebe, T., et al. 2005, A&A, 429, 1057
Ohnaka, K., Weigelt, G., & Hofmann, K.-H. 2017, Nature, 548, 310
Oka, T. 1976, in Molecular Spectroscopy: Modern Research, Volume II, ed. K. N. Rao (New York: Academic Press, Inc.), 229
Oka, T., Shimizu, F. O., Shimizu, T., & Watson, J. K. G. 1971, ApJ, 165, L15
Olofsson, H. 2003, in Asymptotic Giant Branch Stars, eds. H. J. Habing & H. Olofsson (New York: Springer Science+Business Media), 325
Olofsson, H., Vlemmings, W. H. T., Bergman, P., et al. 2017, A&A, 603, L2
Ossenkopf, V., Henning, T., & Mathis, J. S. 1992, A&A, 261, 567
Oudmaijer, R. D., Davies, B., de Wit, W.-J., & Patel, M. 2009, in The Biggest, Baddest, Coolest Stars, eds. D. G. Luttermoser, B. J. Smith, & R. E. Stencel, ASP Conf. Ser., 412, 17
Oudmaijer, R. D. & de Wit, W. J. 2013, A&A, 551, A69
Oudmaijer, R. D., Groenewegen, M. A. T., Matthews, H. E., Blommaert, J. A. D. L., & Sahu, K. C. 1996, MNRAS, 280, 1062
Palov, A. P., Gray, M. D., Field, D., & Balint-Kurti, G. G. 2006, ApJ, 639, 204
Pérez, F. & Granger, B. E. 2007, Comput. Sci. Engg., 9, 21, https://ipython.org/
Perley, R. A. & Butler, B. J. 2013, ApJS, 204, 19
Perrin, G., Cotton, W. D., Millan-Gabet, R., & Mennesson, B. 2015, A&A, 576, A70
Perrin, G., Ridgway, S. T., Mennesson, B., et al. 2004, A&A, 426, 279
Pety, J. 2005, in SF2A-2005: Semaine de l'Astrophysique Francaise, eds. F. Casoli, T. Contini, J. M. Hameury, & L. Pagani, 721

Pickett, H. M., Poynter, R. L., Cohen, E. A., et al. 1998, J. Quant. Spectr. Rad. Transf., 60, 883
Pilbratt, G. L., Riedinger, J. R., Passvogel, T., et al. 2010, A&A, 518, L1
Pillai, T., Wyrowski, F., Carey, S. J., & Menten, K. M. 2006, A&A, 450, 569
Planesas, P., Alcolea, J., & Bachiller, R. 2016, A&A, 586, A69
Poglitsch, A., Waelkens, C., Geis, N., et al. 2010, A&A, 518, L2
Poynter, R. L. & Kakar, R. K. 1975, ApJS, 29, 87
Quintana-Lacaci, G., Agúndez, M., Cernicharo, J., et al. 2013, A&A, 560, L2
Quintana-Lacaci, G., Agúndez, M., Cernicharo, J., et al. 2016, A&A, 592, A51
Ramaswamy, R., Depristo, A. E., & Rabitz, H. 1979, Chem. Phys. Lett., 61, 495
Ramstedt, S., Mohamed, S., Vlemmings, W. H. T., et al. 2014, A&A, 570, L14
Reid, M. J. & Goldston, J. E. 2002, ApJ, 568, 931
Reid, M. J. & Menten, K. M. 1997a, ApJ, 476, 327
Reid, M. J. & Menten, K. M. 1997b, Ap&SS, 251, 41
Reid, M. J. & Menten, K. M. 2007, ApJ, 671, 2068
Richter, M. J., Ennico, K. A., McKelvey, M. E., & Seifahrt, A. 2010, in Ground-based and Airborne Instrumentation for Astronomy III, Proc. SPIE, 7735, 77356Q
Richter, M. J., Lacy, J. H., Jaffe, D. T., et al. 2006, in Ground-based and Airborne Instrumentation for Astronomy, Proc. SPIE, 6269, 62691H
Richtmyer, R. D. & Morton, K. W. 1967, Difference Methods for Initial-Value Problems, the second edn. (New York: John Wiley & Sons)
Rizzo, J. R., Palau, A., Jiménez-Esteban, F., & Henkel, C. 2014, A&A, 564, A21
Robertson, B. S. C. & Feast, M. W. 1981, MNRAS, 196, 111
Roelfsema, P. R., Helmich, F. P., Teyssier, D., et al. 2012, A&A, 537, A17
Rohatgi, A. & Stanojevic, Z. 2016, WebPlotDigitizer: Version 3.10 of WebPlotDigitizer, DOI: 10.5281/zenodo.51157
Roueff, E. & Lique, F. 2013, Chem. Rev., 113, 8906
Royer, P., Decin, L., Wesson, R., et al. 2010, A&A, 518, L145
Rupen, M. P. 1999, in Synthesis Imaging in Radio Astronomy II, eds. G. B. Taylor, C. L. Carilli, & R. A. Perley, ASP Conf. Ser., 180, 229
Russell, H. N. 1914a, Pop. Astron., 22, 275
Russell, H. N. 1914b, Pop. Astron., 22, 331
Ryde, N. & Schöier, F. L. 2001, ApJ, 547, 384
Salinas, V. N., Hogerheijde, M. R., Bergin, E. A., et al. 2016, A&A, 591, A122
Sanchez-Bermudez, J., Thiébaut, E., Hofmann, K.-H., et al. 2016, in Optical and Infrared Interferometry and Imaging V, Proc. SPIE, 9907, 99071D
Sánchez Contreras, C., Bujarrabal, V., Neri, R., & Alcolea, J. 2000, A&A, 357, 651
Sánchez Contreras, C., Desmurs, J. F., Bujarrabal, V., Alcolea, J., & Colomer, F. 2002, A&A, 385, L1
Sánchez Contreras, C., Gil de Paz, A., & Sahai, R. 2004, ApJ, 616, 519
Sánchez Contreras, C., Velilla Prieto, L., Agúndez, M., et al. 2015, A&A, 577, A52
Sault, R. J. 1994, A&AS, 107
Sault, R. J., Teuben, P. J., & Wright, M. C. H. 1995, in Astronomical Data Analysis Software and Systems IV, eds. R. A. Shaw, H. E. Payne, & J. J. E. Hayes, ASP Conf. Ser., 77, 433
Savitzky, A. & Golay, M. J. E. 1964, Anal. Chem., 36, 1627
Scargle, J. D. 1982, ApJ, 263, 835
Schilke, P., Guesten, R., Schulz, A., Serabyn, E., & Walmsley, C. M. 1992, A&A, 261, L5
Schilke, P., Walmsley, C. M., Wilson, T. L., & Mauersberger, R. 1990, A&A, 227, 220
Schmidt, M. R., He, J. H., Szczerba, R., et al. 2016, A&A, 592, A131

Schöier, F. L., van der Tak, F. F. S., van Dishoeck, E. F., & Black, J. H. 2005, A&A, 432, 369
Scholz, M., Ireland, M. J., & Wood, P. R. 2014, A&A, 565, A119
Scholz, M. & Wood, P. R. 2000, A&A, 362, 1065
Schrey, U. 1986, *Dissertation* [PhD Dissertation], Technische Universität München, MPE Report 198, translated abstract is available at https://ntrl.ntis.gov/NTRL/dashboard/searchResults/titleDetail/N8715040.xhtml
Schwarzschild, M. 1975, ApJ, 195, 137
Scicluna, P., Siebenmorgen, R., Wesson, R., et al. 2015, A&A, 584, L10
Shenoy, D., Humphreys, R. M., Jones, T. J., et al. 2016, AJ, 151, 51
Sloan, G. C., Kraemer, K. E., Price, S. D., & Shipman, R. F. 2003, ApJS, 147, 379
Smith, N., Humphreys, R. M., Davidson, K., et al. 2001, AJ, 121, 1111
Sokoloski, J. L. & Bildsten, L. 2010, ApJ, 723, 1188
Sopka, R. J., Hildebrand, R., Jaffe, D. T., et al. 1985, ApJ, 294, 242
Suh, K.-W. 1999, MNRAS, 304, 389
Sutter, P. M., Wandelt, B. D., McEwen, J. D., et al. 2014, MNRAS, 438, 768
Sweitzer, J. S., Palmer, P., Morris, M., Turner, B. E., & Zuckerman, B. 1979, ApJ, 227, 415
Temi, P., Marcum, P. M., Young, E., et al. 2014, ApJS, 212, 24
Templeton, M. R. & Karovska, M. 2009, ApJ, 691, 1470
Tenenbaum, E. D., Dodd, J. L., Milam, S. N., Woolf, N. J., & Ziurys, L. M. 2010a, ApJS, 190, 348
Tenenbaum, E. D., Dodd, J. L., Milam, S. N., Woolf, N. J., & Ziurys, L. M. 2010b, VizieR Online Data Catalog, J/ApJS/190/348
Tennyson, J., Zobov, N. F., Williamson, R., Polyansky, O. L., & Bernath, P. F. 2001, J. Phys. Chem. Ref. Data, 30, 735
Terlouw, J. P. & Vogelaar, M. G. R. 2015, Kapteyn Package, version 2.3, Kapteyn Astronomical Institute, Groningen, available at http://www.astro.rug.nl/software/kapteyn/
Teyssier, D., Quintana-Lacaci, G., Marston, A. P., et al. 2012, A&A, 545, A99
Thomas, L. D., Kraemer, W. P., & Diercksen, G. H. F. 1980, Chem. Phys., 51, 131
Thompson, A. R., Moran, J. M., & Swenson, Jr., G. W. 2001, Interferometry and Synthesis in Radio Astronomy, the second edn. (Weinheim: WILEY-VCH Verlag GmbH & Co. KGaA)
Townes, C. H. & Schawlow, A. L. 1955, Microwave Spectroscopy (New York: Dover Publications, Inc.)
Truong-Bach, Graham, D., & Nguyen-Q-Rieu. 1996, A&A, 312, 565
Truong-Bach, Nguyen-Q-Rieu, & Graham, D. 1988, A&A, 199, 291
Tsuboi, M., Shimanouchi, T., & Mizushima, S. 1958, Spectrochim. Acta, 13, 80
Tsuji, T. 1964, Ann. Tokyo Astron. Obser., 9, 1
Tsuji, T. 1973, A&A, 23, 411
Tsuji, T. 2000, ApJ, 540, L99
Tsuji, T., Ohnaka, K., Aoki, W., & Yamamura, I. 1997, A&A, 320, L1
Tsuji, T., Ohnaka, K., Hinkle, K. H., & Ridgway, S. T. 1994, A&A, 289, 469
Turner, B. E., Chan, K.-W., Green, S., & Lubowich, D. A. 1992, ApJ, 399, 114
Urquhart, J. S., Morgan, L. K., Figura, C. C., et al. 2011, MNRAS, 418, 1689
van den Ancker, M. E., Asmus, D., Hummel, C., et al. 2016, in Observatory Operations: Strategies, Processes, and Systems VI, Proc. SPIE, 9910, 99102T
van der Tak, F. F. S., Black, J. H., Schöier, F. L., & et al. 2007, A&A, 468, 627
van der Walt, S., Colbert, S. C., & Varoquaux, G. 2011, Comput. Sci. Engg., 13, 22, http://www.numpy.org/
van Langevelde, H. J. & Cotton, W. D. 1990, A&A, 239, L5

van Leeuwen, F. 2007, A&A, 474, 653
VanderPlas, J., Connolly, A. J., Ivezic, Z., & Gray, A. 2012, in 2012 Conference on Intelligent Data Understanding, eds. K. Das, N. V. Chawla, & A. N. Srivastava, 47
VanderPlas, J. T. & Ivezić, Ž. 2015, ApJ, 812, 18
Varambhia, H. N., Gupta, M., Faure, A., Baluja, K. L., & Tennyson, J. 2009, J. Phys. B At. Mol. Phys., 42, 095204
Velilla Prieto, L., Sánchez Contreras, C., Cernicharo, J., et al. 2015, A&A, 575, A84
Velilla Prieto, L., Sánchez Contreras, C., Cernicharo, J., et al. 2016, VizieR Online Data Catalog, J/A+A/597/A25
Velilla Prieto, L., Sánchez Contreras, C., Cernicharo, J., et al. 2017, A&A, 597, A25
Venn, K. A. 1995, ApJ, 449, 839
Ventura, P., Di Criscienzo, M., Carini, R., & D'Antona, F. 2013, MNRAS, 431, 3642
Ventura, P., Stanghellini, L., Dell'Agli, F., & García-Hernández, D. A. 2017, MNRAS, 471, 4648
Vlemmings, W. H. T., Ramstedt, S., O'Gorman, E., et al. 2015, A&A, 577, L4
Volk, K. & Cohen, M. 1989, AJ, 98, 1918
von Neumann, J. & Richtmyer, R. D. 1950, J. Appl. Phys., 21, 232
Watson, J. K. G. 1971, J. Mol. Spectr., 40, 536
Weigelt, G., Hofmann, K.-H., Schertl, D., et al. 2016, A&A, 594, A106
Wieching, G. 2014, in Issue 1, ed. B. Hutawarakorn Kramer, Effelsberg Newslett., 5, available at https://issuu.com/effelsbergnewsletter/docs/effnews-jan14-final
Wienen, M., Wyrowski, F., Schuller, F., et al. 2012, A&A, 544, A146
Wild, W. 1999, The 30m Manual: A Handbook for the IRAM 30m Telescope, Pico Veleta, Spain, v2.0, available at http://www.iram.es/IRAMES/otherDocuments/manuals/
Willacy, K. & Cherchneff, I. 1998, A&A, 330, 676
Willacy, K. & Millar, T. J. 1997, A&A, 324, 237
Willson, L. A. 1987, in Late Stages of Stellar Evolution, eds. S. Kwok & S. R. Pottasch (Dordrecht: D. Reidel Publishing Company), ASSL, 132, 253
Willson, L. A. 2000, ARA&A, 38, 573
Willson, L. A. & Hill, S. J. 1979, ApJ, 228, 854
Wing, R. F. & Lockwood, G. W. 1973, ApJ, 184, 873
Winnewisser, G., Belov, S. P., Klaus, T., & Urban, S. 1996, Z. Nat. A, 51, 200
Wittkowski, M., Boboltz, D. A., Ireland, M., et al. 2011, A&A, 532, L7
Wittkowski, M., Boboltz, D. A., Ohnaka, K., Driebe, T., & Scholz, M. 2007, A&A, 470, 191
Wittkowski, M., Hauschildt, P. H., Arroyo-Torres, B., & Marcaide, J. M. 2012, A&A, 540, L12
Woitke, P. 1998, in Cyclical Variability in Stellar Winds, eds. L. Kaper & A. W. Fullerton (Berlin: Springer-Verlag), 278
Woitke, P. 2006, A&A, 460, L9
Woitke, P., Helling, C., Winters, J. M., & Jeong, K. S. 1999, A&A, 348, L17
Woitke, P., Krueger, D., & Sedlmayr, E. 1996, A&A, 311, 927
Wong, K. T. 2013, MPhil Thesis, University of Hong Kong, available at http://hub.hku.hk/handle/10722/195970
Wong, K. T., Kamiński, T., Menten, K. M., & Wyrowski, F. 2016, A&A, 590, A127
Wood, P. R. 1979, ApJ, 227, 220
Wood, P. R. & Cahn, J. H. 1977, ApJ, 211, 499
Wood, P. R., Olivier, E. A., & Kawaler, S. D. 2004, ApJ, 604, 800
Woodruff, H. C., Eberhardt, M., Driebe, T., et al. 2004, A&A, 421, 703

Woodruff, H. C., Ireland, M. J., Tuthill, P. G., et al. 2009, ApJ, 691, 1328
Woodsworth, A. W. 1995, ApJ, 444, 396
Wootten, A. & Thompson, A. R. 2009, IEEE Proc., 97, 1463
Yamamura, I., de Jong, T., & Cami, J. 1999a, A&A, 348, L55
Yamamura, I., de Jong, T., Onaka, T., Cami, J., & Waters, L. B. F. M. 1999b, A&A, 341, L9
Yang, Y., Shutler, A., & Grischkowsky, D. 2011, Opt. Express, 19, 8830
Yi, J., Booth, R. S., Conway, J. E., & Diamond, P. J. 2005, A&A, 432, 531
Young, E. T., Becklin, E. E., Marcum, P. M., et al. 2012, ApJ, 749, L17
Yu, S., Pearson, J. C., Drouin, B. J., et al. 2010, J. Chem. Phys., 133, 174317
Yurchenko, S. N., Barber, R. J., & Tennyson, J. 2011, MNRAS, 413, 1828
Zhang, B., Reid, M. J., Menten, K. M., & Zheng, X. W. 2012, ApJ, 744, 23
Ziurys, L. M., Milam, S. N., Apponi, A. J., & Woolf, N. J. 2007, Nature, 447, 1094

Radiative transfer modelling

General References: Hogerheijde & van der Tak (2000); van der Tak et al. (2007).

A.1. Radiative transfer equation

For a ray of radiation with intensity I_ν (at frequency ν) passing through a medium (for a path ds), the intensity changes due to absorption and emission by the medium,

$$\mathrm{d}I_\nu = -\alpha_\nu I_\nu \mathrm{d}s + j_\nu \mathrm{d}s, \tag{A.1}$$

where α_ν and j_ν are the absorption and emission coefficients, respectively. By defining the source function (S_ν) and the optical depth (τ_ν) as

$$S_\nu \equiv \frac{j_\nu}{\alpha_\nu}, \tag{A.2}$$

$$\mathrm{d}\tau_\nu \equiv \alpha_\nu \mathrm{d}s, \tag{A.3}$$

we have

$$\frac{\mathrm{d}I_\nu}{\mathrm{d}\tau_\nu} = -I_\nu + S_\nu. \tag{A.4}$$

In CSE, both dust and gas can contribute to emission and absorption of radiation. The dust emission and absorption are given by

$$j_\nu^{\mathrm{dust}} = \alpha_\nu^{\mathrm{dust}} B_\nu\left(T_{\mathrm{dust}}\right) \tag{A.5}$$

$$\alpha_\nu^{\mathrm{dust}} = \kappa_\nu \rho_{\mathrm{dust}}, \tag{A.6}$$

where $B_\nu\left(T_{\mathrm{dust}}\right)$ is the Planck function at the dust temperature T_{dust}, κ_ν is the dust opacity, and ρ_{dust} is the dust mass density. In addition, the emission and absorption of the molecular gas is due to the spectral line transition of the energy difference $h\nu$ between an upper level u and a lower lever l,

$$j_\nu^{\mathrm{gas}} = \frac{h\nu}{4\pi} n_{\mathrm{u}} A_{\mathrm{ul}} \phi(\nu) \tag{A.7}$$

$$\alpha_\nu^{\mathrm{gas}} = \frac{h\nu}{4\pi}\left(n_{\mathrm{l}} B_{\mathrm{lu}} - n_{\mathrm{u}} B_{\mathrm{ul}}\right)\phi(\nu), \tag{A.8}$$

where n_i is the level population of the level i for i in $\{\mathrm{u}, \mathrm{l}\}$, A_{ij} and B_{ij} are the Einstein A and B coefficients for the transition from level i to level j for i, j in $\{\mathrm{u}, \mathrm{l}\}$, and $\phi(\nu)$ is the normalised line profile of the transition.

The Einstein coefficients are related by (e.g. Draine, 2011)

$$B_{\rm ul} = \frac{c^3}{8\pi h\nu^3} A_{\rm ul} \tag{A.9}$$

$$B_{\rm lu} = \frac{g_{\rm u}}{g_{\rm l}} B_{\rm ul} = \frac{g_{\rm u}}{g_{\rm l}} \frac{c^3}{8\pi h\nu^3} A_{\rm ul}, \tag{A.10}$$

where g_i is the statistical weight of level i for i in $\{\rm u, l\}$.

A.2. Statistical equilibrium

To model the radiative transfer of a molecule, the populations of all energy levels are first computed from the input physical model assuming statistical equilibrium and the modelled spectral line profiles of interested transitions are then synthesised using the radiative transfer equation.

Figure A.1 shows a simple two-level system and all excitation and de-excitation processes. Under statistical equilibrium, the total rate of population gain equals to that of population loss for each energy level. For the upper level u in a two-level system, the statistical equilibrium is expressed as the following equation:

$$\text{Rate of de-excitation from level u} = \text{Rate of excitation to level u} \tag{A.11}$$

$$n_{\rm u}A_{\rm ul} + n_{\rm u}B_{\rm ul}\bar{J}_\nu + n_{\rm u}k_{\rm ul} = n_{\rm l}B_{\rm lu}\bar{J}_\nu + n_{\rm l}k_{\rm lu} \tag{A.12}$$

$$0 = -n_{\rm l}\left(B_{\rm lu}\bar{J}_\nu + k_{\rm lu}\right) + n_{\rm u}\left(A_{\rm ul} + B_{\rm ul}\bar{J}_\nu + k_{\rm ul}\right), \tag{A.13}$$

where n_i, A_{ij}, and B_{ij} follow the same definitions as in Eqs. A.7 and A.8; and k_{ij} is the collisional rate coefficient for the transition from level i to level j and for i, j in $\{\rm u, l\}$. $\bar{J}_\nu$ is the average intensity over all directions and integrated over the line profile $\phi(\nu)$ at the frequency of the transition ν. The energy difference is given by $h\nu$ and the average intensity $\bar{J}_\nu$ is given by

$$\bar{J}_\nu = \frac{1}{4\pi}\int I_\nu\left(n_{\rm l}, n_{\rm u}, \phi(\nu)\right) {\rm d}\Omega. \tag{A.14}$$

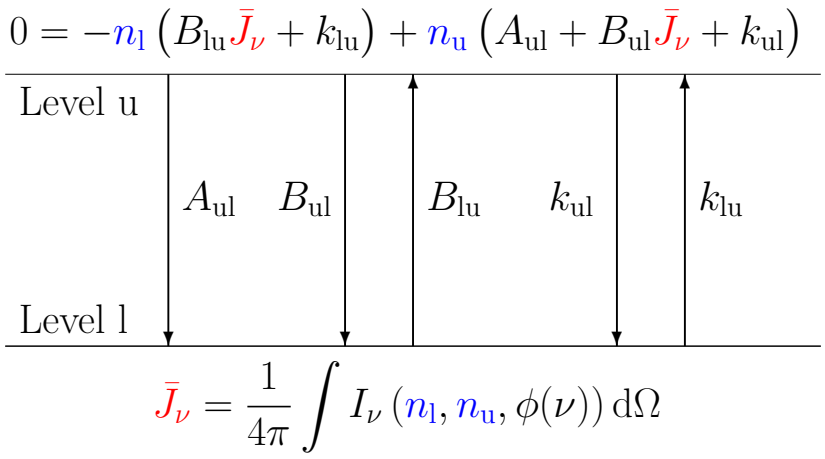

Figure A.1.: Statistical equilibrium of a two-level system.

From Eq. A.13, the intensity $\bar{J}_\nu$ has to be determined in order to solve the equation of statistical equilibrium and hence compute the level populations $n_{\rm u}$ and $n_{\rm l}$. On the other hand,

the radiation field depends on the level population (Eq. A.14). Hence, this is a coupled problem of molecular excitation and radiative transfer and the solution can only be obtained iteratively. In the two studies presented in this thesis, the radiative transfer code RATRAN was used to calculate the level populations of the modelled molecules.

Einstein A coefficients are available from molecular databases and the corresponding Einstein B coefficients can then be readily calculated by Eqs. A.9 and A.10. Collisional rate coefficients are derived from quantum chemical computations for a range of energy levels and a set of kinetic temperatures. Extrapolations are needed if the modelled parameter space is not covered by quantum calculations. In this thesis, the rate coefficients of NH_3 and SiO have been extrapolated from those delivered by quantum calculations. The extrapolation schemes are further explained in Appendix B.

Blank Page

APPENDIX B

Collisional rate coefficients

In this appendix, we describe the collisional rate coefficients of the NH_3–H_2 and SiO–H_2 collisional systems as adopted in our radiative transfer modelling. We used the Python libraries, NumPy[1] (version 1.9.2) (van der Walt et al., 2011) and SciPy[2] (version 0.15.1) (Jones et al., 2001) in our extrapolation of the collisional rate coefficients and compilation of the molecular datafiles.

B.1. Ammonia (NH_3)

In the model of Schmidt et al. (2016), the collisional rate coefficients used for the ground vibrational state of NH_3 were calculated by Danby et al. (1988) for the collisions with para-H_2 ($j = 0$) at temperatures $15\,\mathrm{K} \leq T_{\mathrm{kin}} \leq 300\,\mathrm{K}$ and were extrapolated to higher temperature assuming that they are proportional to $\sqrt{T_{\mathrm{kin}}}$, where T_{kin} is the kinetic temperature of para-H_2. These rate coefficients were computed in the transitions involving energy levels up to $J_{\mathrm{ortho}} = 6$ ($E_{\mathrm{up}}/k < 600\,\mathrm{K}$) for ortho-$NH_3$ and $J_{\mathrm{para}} = 5$ ($E_{\mathrm{up}}/k < 450\,\mathrm{K}$) for para-$NH_3$. Hence, higher energy levels are populated via radiative transitions only. By adopting some constant rate coefficients for other transitions, Schmidt et al. (2016) found that the collisional transitions involving higher ground-state levels or vibrationally excited levels were not important.

Bouhafs et al. (2017) reported new calculations on the rate coefficients of the collisions between NH_3 and atomic hydrogen (H), ortho-H_2, and para-H_2 at temperatures up to 200 K and in transitions involving energy levels up to $E_{\mathrm{up}}/k = 600\,\mathrm{K}$ ($J_{\mathrm{ortho}} \leq 6$ and $J_{\mathrm{para}} \leq 7$). Their calculations were based on the full-dimensional (9-D) NH_3–H potential energy surface (PES) of Li & Guo (2014) and the five-dimensional NH_3–H_2 PES of Maret et al. (2009) with an ad hoc approximation of the inversion wave functions using the method of Green (1976). The rate coefficients of NH_3–para-H_2 are thermalised over $j = 0$ and 2 and they are consistent with those of Danby et al. (1988) within a factor of 2. We do not consider the collisions with H in our models. The coefficients of NH_3 with ortho- and para-H_2 at 200 K are consistent within a factor of ~2 (up to 4). We weight the coefficients of the two H_2 species by assuming a thermal H_2 ortho-to-para ratio of 3 (Flower & Watt, 1984). Since the coefficients for most low-J and small-ΔJ transitions do not vary much with temperature (e.g. Fig. 2 of Bouhafs et al., 2017), we apply constant extrapolation of the coefficients from 200 K to higher temperatures. Vibrations were not included in the 5-D PES of NH_3–H_2. Quantum dynamics calculations have shown that vibrationally elastic ($\Delta v = 0$; purely rotational) excitation of linear molecules by collisions with noble gases (e.g. helium) is almost independent of the vibrational state v

[1] http://www.numpy.org
[2] https://www.scipy.org

(Roueff & Lique, 2013; Balança & Dayou, 2017, and references therein). This also appears to be valid in the elastic ($\Delta v_2 = 0$) transitions of the H_2O–H_2 collision system (Faure & Josselin, 2008b); therefore, we assume that the elastic (rotation-inversion) transitions within the $v_2 = 1$ state to have the same rate coefficients as the 'corresponding elastic transitions'[3] within the ground state. For vibrationally inelastic transitions ($v_2 = 1 \rightarrow 0$), we scale the coefficients of the 'corresponding elastic transitions' within the ground state by a constant factor of 0.05 (Faure 2017, priv. comm.; Faure & Josselin, 2008b), taking detailed balance into account. For all other transitions, i.e. vibrationally elastic (within $v_2 = 1$) or inelastic ($v_2 = 1 \rightarrow 0$) transitions that do not have a 'corresponding elastic transition' within the ground vibrational state, we adopt a constant rate coefficient of 2×10^{-11} cm^{3}s^{-1} for vibrationally elastic transitions and 1×10^{-12} cm^{3}s^{-1} for vibrationally inelastic transitions.

Our extrapolations in temperature and rovibrational transition are admittedly quite crude but they are necessary to make. Similar to the analysis of Schmidt et al. (2016, their Sect. 3), we compare the synthesised spectra of the transitions discussed in this chapter using the above-mentioned extended coefficients with those using only the coefficients of either Danby et al. (1988) or Bouhafs et al. (2017). Neglecting collisional transitions of high-J and v_2-excited levels, the coefficients of Danby et al. (1988) and Bouhafs et al. (2017) do not produce qualitatively different spectra. While the spectra of IK Tau are insensitive to the presence of the extended rate coefficients, those of the other targets are noticeably affected, especially in the rotational transitions (<50% in the peak intensity). Future quantum dynamics calculations, which require a full-dimensional (12-D) PES of NH_3–H_2, are necessary to determine the complete set of rate coefficients for circumstellar NH_3 modelling.

B.2. Silicon monoxide (SiO)

B.2.1. Pure rotational transitions in the vibrational ground state

Collisional rate coefficients between SiO and para-H_2 ($J = 0$) are often approximated by scaling the rate coefficients of the SiO–He system by the square root of the ratio of the reduced masses of the two collisional partners, i.e. $\sqrt{\frac{\mu_{\text{Si-He}}}{\mu_{\text{Si-H}_2}}} = 1.38$ (e.g. Schöier et al., 2005). Based on the Gordon-Kim electron gas model (Gordon & Kim, 1972), Bieniek & Green (1981) derived the potential energy surface (PES) of the SiO–He system, from which the potential energy of the system in terms of the orientation of the two molecules can be derived (e.g. Lewars, 2011, Chap. 2). Bieniek & Green (1983a,b) then computed the collisional cross sections and hence the corresponding rate coefficients for $v \leq 2$, $J \leq 39$ and $\Delta v = 0, 1$ for the H_2 gas temperature range between 1000 K and 3000 K. Turner et al. (1992) derived the rate coefficients, for $v = 0$ and $J \leq 20$ only, in a lower temperature range (20–300 K) by extrapolating the PES of Bieniek & Green (1981) to shorter collision distances between SiO and He. With the ab initio method as described in their Sect. 2, Dayou & Balança (2006) have derived a new PES for the SiO–He system which differs significantly from that derived by Bieniek & Green (1981). The resultant rate coefficients from Dayou & Balança (2006) are different from those from Turner et al. (1992) by up to an order of magnitude, with the odd/even-ΔJ propensity rule reversed. The differences are qualitatively similar to the finding by Thomas et al. (1980) that the rate coefficients derived by an electron gas model could be underestimated or overestimated by about 2 to 3 times in the odd- or even-ΔJ transitions, respectively, relative to ab initio calculation. Hence, in our SiO datafile, we adopt the rate coefficients from Dayou & Balança (2006) ($v = 0$, $J \leq 26$) for the collisional transitions of SiO molecule in the vibrational ground state. The rate

[3] The transition of the same ΔJ, ΔK, and change in symmetry.

coefficients for higher J and temperatures are extrapolated by empirically derived analytical approximations as described in the following. For all the function fitting in the following discussion, we use the Levenberg-Marquardt algorithm as the non-linear least squares fitting method. This algorithm is implemented in the Python/SciPy module `scipy.optimize`.

B.2.1.1. Extrapolation to high J ($J_\mathrm{u} > 26$)

At the gas temperature T, the collisional rate coefficients, $k_{J_\mathrm{u}J_\mathrm{l}}$, from the initial upper rotational level (J_u) to the final lower level (J_l) in the vibrational ground state ($v = 0$) can be computed with the infinite-order sudden approximation (IOS) (e.g. Goldflam et al., 1977),

$$k_{J_\mathrm{u}J_\mathrm{l}}(T) = (2J_\mathrm{l}+1)\sum_{j=|J_\mathrm{u}-J_\mathrm{l}|}^{J_\mathrm{u}+J_\mathrm{l}} \begin{pmatrix} J_\mathrm{u} & J_\mathrm{l} & j \\ 0 & 0 & 0 \end{pmatrix}^2 (2j+1)\, k_{j0}(T)\cdot A_j^{J_\mathrm{u}}(T), \tag{B.1}$$

where $\begin{pmatrix} j_\mathrm{i} & j_\mathrm{f} & j \\ 0 & 0 & 0 \end{pmatrix}$ is the Wigner 3-j symbol. For the special cases in which the bottom three entries of the 3-j symbol equal 0, it has been shown that (e.g. Edmonds, 1960; Messiah, 1962), if $S \equiv j_\mathrm{i} + j_\mathrm{f} + j$ is odd, then

$$\begin{pmatrix} j_\mathrm{i} & j_\mathrm{f} & j \\ 0 & 0 & 0 \end{pmatrix} = 0, \tag{B.2}$$

and if $S \equiv j_\mathrm{i} + j_\mathrm{f} + j$ is even, then

$$\begin{pmatrix} j_\mathrm{i} & j_\mathrm{f} & j \\ 0 & 0 & 0 \end{pmatrix} = (-1)^{S/2}\sqrt{\frac{(S-2j_\mathrm{i})!(S-2j_\mathrm{f})!(S-2j)!}{(S+1)!}} \times \frac{(S/2)!}{(S/2-j_\mathrm{i})!(S/2-j_\mathrm{f})!(S/2-j)!}. \tag{B.3}$$

The IOS approximation requires that the difference in the rotational energy levels be insignificant to the kinetic energy of the system, which may not be the case for high ΔJ transitions. An adiabaticity factor for purely rotational transitions (i.e. $\Delta v = 0$), $A_j^{J_\mathrm{u}}(T)$, is therefore required to account for this effect (Ramaswamy et al., 1979; DePristo et al., 1979). The adiabaticity factor at the gas temperature T is given by

$$A_j^{J_\mathrm{u}}(T) = \frac{6 + (0.129 j B_0 l_\mathrm{c})^2 \mu_{\mathrm{SiO\text{-}H_2}}/T}{6 + (0.129 J_\mathrm{u} B_0 l_\mathrm{c})^2 \mu_{\mathrm{SiO\text{-}H_2}}/T}, \tag{B.4}$$

where $B_0 = 0.724$ is the rotation constant of SiO ($v = 0$) in cm^{-1}, $l_\mathrm{c} \approx 3$ is the typical inelastic impact parameter in Å, and $\mu_{\mathrm{SiO\text{-}H_2}} = 1.93$ is the reduced mass of SiO–H_2 in atomic mass unit. To obtain the full set of rate coefficients up to $J_\mathrm{u} = 69$, we need to know the coefficients k_{j0} for j from 1 up to 137. The SiO–H_2 rate coefficients (scaled from SiO–He values) computed by Dayou & Balança (2006) are up to $j = 26$ only. We extrapolate the coefficients k_{j0} to higher rotational levels by fitting the Dayou & Balança coefficients to the function

$$\ln k_{j0} = a + bj. \tag{B.5}$$

The fitting function in Eq. (B.5) does not adopt a second-order term (cj^2) as in Schöier et al. (2005) in order to get consistent fitting for all values of temperatures. The values of k_{j0} become vanishingly small for $j \gg J_\mathrm{u}$, and hence their contributions to the summation of the

coefficient $k_{J_uJ_l}$ are insignificant. Odd and even j are fitted together, so the propensity rule is ignored for the extrapolated j-levels.

However, the rate coefficients computed with Eq. (B.1) and the extrapolated k_{j0} values are consistently smaller than those theoretically derived by Dayou & Balança (2006). In view of the discrepancy between the Dayou & Balança coefficients and the extrapolated coefficients, we make direct extrapolation of the rate coefficients $k_{J_uJ_l}$ instead of summing up the extrapolated k_{j0} in Eq. (B.1). For each $J_l \leq 23$, we extrapolated $k_{J_uJ_l}$ to higher J_u with

$$\ln k_{J_uJ_l} = a + bJ_u. \tag{B.6}$$

For a particular J_l, the variation of the collisional rate coefficients with J_u will then be smoother than in the LAMDA SiO datafile.

B.2.1.2. Extrapolation to high T

With the J-extrapolated collisional rate coefficients in the temperature range between 10 K and 300 K, we develop the following empirical relation to extrapolate the rate coefficients to higher temperatures:

$$\ln\left(\frac{k_{J_uJ_l}(T)}{10^{-10}\,\mathrm{cm^3\,s^{-1}}}\right) = \ln\left(\frac{m_{\Delta J}}{T}\right)^{\frac{1}{4}} - \left(\frac{n_{\Delta J}}{T}\right)^{\frac{1}{4}}. \tag{B.7}$$

The low-temperature (10–300 K) coefficients of all transitions with the same $\Delta J = J_u - J_l$ are globally fitted to Eq. B.7 with the same set of fitting parameters $m_{\Delta J}$ and $n_{\Delta J}$. The fitting parameters are dependent on ΔJ and their values in units of Kelvin are given in Table B.1. For individual transitions $J_u \rightarrow J_l$, we scale the extrapolated coefficient with a factor that ensures continuity with respect to temperature at $T = 300$ K,

$$\frac{k^{\mathrm{DB06}}_{J_uJ_l}(300\,\mathrm{K})}{\left(\frac{m_{\Delta J}}{300\,\mathrm{K}}\right)^{1/4}\exp\left[-\left(\frac{n_{\Delta J}}{300\,\mathrm{K}}\right)^{1/4}\right]\times 10^{-10}\,\mathrm{cm^3\,s^{-1}}}, \tag{B.8}$$

where $k^{\mathrm{DB06}}_{J_uJ_l}(300\,\mathrm{K})$ is the SiO–H_2 rate coefficients (scaled from the SiO–He values) derived by Dayou & Balança (2006) for the transition from J_u to J_l at $T = 300$ K. Our fitting function in Eq. (B.7) is modified from and has a similar form to the extrapolation functions empirically derived by de Jong et al. (1975), Albrecht (1983), and Bieging et al. (1998), respectively. The extrapolated rate coefficients up to 2000 K are generally consistent with the values in the LAMDA datafile, which are extrapolated by Eq. (13) in Schöier et al. (2005).

B.2.2. Transitions in the vibrational excited states of SiO

Rate coefficients of the rotational transitions involving vibrationally excited states (i.e. $v = 1, 2$, where $\Delta v = 0, 1$) can be computed with the infinite-order sudden (IOS) approximation (e.g. Goldflam et al., 1977), whose parameters are given by Bieniek & Green (1983a,b) for $J(v) \leq 39$ and $1000\,\mathrm{K} \leq T \leq 3000\,\mathrm{K}$. The collisional rate coefficients derived by Bieniek & Green (1983a,b) form the only set of available coefficients for vibrationally excited SiO in the literature. Thus, for all transitions involving the vibrationally excited states of SiO, we extrapolate from the coefficients of Bieniek & Green (1983a,b) (hereafter BG1983 coefficients).

B.2.2.1. Extrapolation to high-J and high-T

The extrapolation of BG1983 coefficients works on the parameters presented in Table 1 of Bieniek & Green (1983a,b). In their Table 1, the parameters $(2J_i + 1)k^{v_i,J_i}_{v_i,0}(T_0)$ and $q^{v_i,J_i}_{v_f,0}$ from

Table B.1.: Fitting parameters.

ΔJ	$m_{\Delta J}$(K)	$n_{\Delta J}$(K)	ΔJ	$m_{\Delta J}$(K)	$n_{\Delta J}$(K)
1	8.91E+04	1.19E+03	36	9.67E+06	1.76E+07
2	1.93E+04	3.98E+03	37	1.13E+07	1.95E+07
3	3.86E+05	8.03E+03	38	1.05E+07	2.12E+07
4	1.10E+03	1.06E+04	39	1.22E+07	2.34E+07
5	1.10E+06	2.77E+04	40	1.12E+07	2.54E+07
6	2.78E+03	2.95E+04	41	1.30E+07	2.79E+07
7	1.68E+06	7.13E+04	42	1.17E+07	3.01E+07
8	5.06E+04	8.16E+04	43	1.35E+07	3.29E+07
9	1.48E+06	1.55E+05	44	1.18E+07	3.53E+07
10	8.77E+05	1.97E+05	45	1.36E+07	3.85E+07
11	6.19E+05	2.82E+05	46	1.16E+07	4.11E+07
12	8.22E+06	4.11E+05	47	1.33E+07	4.47E+07
13	1.12E+05	4.31E+05	48	1.11E+07	4.75E+07
14	4.13E+07	7.65E+05	49	1.27E+07	5.15E+07
15	2.19E+04	6.09E+05	50	1.03E+07	5.45E+07
16	1.02E+08	1.28E+06	51	1.18E+07	5.89E+07
17	2.14E+04	9.24E+05	52	9.28E+06	6.21E+07
18	1.20E+08	1.94E+06	53	1.05E+07	6.69E+07
19	9.18E+04	1.50E+06	54	8.02E+06	7.02E+07
20	6.00E+07	2.69E+06	55	9.04E+06	7.55E+07
21	5.15E+05	2.37E+06	56	6.67E+06	7.90E+07
22	1.48E+07	3.47E+06	57	7.48E+06	8.46E+07
23	2.12E+06	3.56E+06	58	5.31E+06	8.83E+07
24	3.12E+06	4.32E+06	59	5.92E+06	9.44E+07
25	4.68E+06	4.99E+06	60	4.04E+06	9.81E+07
26	1.28E+06	5.42E+06	61	4.48E+06	1.05E+08
27	5.48E+06	6.40E+06	62	2.92E+06	1.08E+08
28	5.57E+06	7.22E+06	63	3.22E+06	1.15E+08
29	6.59E+06	8.24E+06	64	2.00E+06	1.19E+08
30	6.59E+06	9.22E+06	65	2.19E+06	1.27E+08
31	7.77E+06	1.04E+07	66	1.29E+06	1.30E+08
32	7.64E+06	1.16E+07	67	1.41E+06	1.38E+08
33	8.98E+06	1.30E+07	68	7.83E+05	1.41E+08
34	8.69E+06	1.44E+07	69	8.44E+05	1.50E+08
35	1.02E+07	1.60E+07			

$J_\mathrm{i} = 0$ to 39 are presented, where $k^{v_\mathrm{i},J_\mathrm{i}}_{v_\mathrm{f},0}(T_0)$ is the rate coefficient from the initial level $(v_\mathrm{i}, J_\mathrm{i})$ to the ground rotational level of the final vibrational state $(v_\mathrm{f}, 0)$ at $T_0 = 2000\,\mathrm{K}$, and $q^{v_\mathrm{i},J_\mathrm{i}}_{v_\mathrm{f},0}$ is the power-law index of the same transition, which describes the temperature dependence of the rate coefficients in the range 1000–3000 K such that

$$(2J_\mathrm{i}+1)k^{v_\mathrm{i},J_\mathrm{i}}_{v_\mathrm{f},0}(T) = (2J_\mathrm{i}+1)k^{v_\mathrm{i},J_\mathrm{i}}_{v_\mathrm{f},0}(T_0)\left(\frac{T}{T_0}\right)^{q^{v_\mathrm{i},J_\mathrm{i}}_{v_\mathrm{f},0}}. \tag{B.9}$$

We extrapolate the rate coefficient parameters and power-law indices to high-J with approximations similar to Eq. (B.6), i.e.

$$\ln\left[(2J_\mathrm{i}+1)k^{v_\mathrm{i},J_\mathrm{i}}_{v_\mathrm{f},0}(T_0)\right] = a + bJ_\mathrm{i}, \tag{B.10}$$

and

$$\ln\left(q^{v_\mathrm{i},J_\mathrm{i}}_{v_\mathrm{f},0}\right) = c + dJ_\mathrm{i}, \tag{B.11}$$

except for the rate coefficient parameters of $(v_\mathrm{i}, v_\mathrm{f}) = (1, 0)$, where we think the parameters are better fitted by a second-order polynomial,

$$\ln\left[(2J_\mathrm{i}+1)k^{v_\mathrm{i},J_\mathrm{i}}_{v_\mathrm{f},0}(T_0)\right] = a + bJ_\mathrm{i} + cJ_\mathrm{i}^2. \tag{B.12}$$

After the extrapolation, we then compute the full set of rate coefficients at 2000 K, $k^{v_\mathrm{i},J_\mathrm{i}}_{v_\mathrm{f},J_\mathrm{f}}(T_0)$, with the IOS approximation similar to Eq. (B.1), with the only differences being that J_u and J_l in Eq. (B.1) are replaced by J_i (initial level) and J_f (final level), respectively. We only apply the adiabaticity factor (Eq. B.4) to the terms within the summation for the pure rotational transition within the same vibrational state, i.e. $v_\mathrm{i} = v_\mathrm{f} = 1$ or 2. For transitions involving a change in the vibrational state, $\Delta v = v_\mathrm{i} - v_\mathrm{f} \neq 0$, DePristo et al. (1979) derived a factorisation for the summation terms to correct for the inaccuracy of IOS approximation when the kinetic energy is no longer much greater than the energy of the transition. However, because the rate coefficients are not accurate even with the correction (see our discussion in Appendix B.2.1) and the corrected coefficients would not change by many orders of magnitude, we do not think it worthwhile to carry out the factorisation which is quite complicated computationally. So, no adiabaticity correction has been applied to the rate coefficients of transitions with $\Delta v \neq 0$, i.e. $A^{J_\mathrm{i}}_j(T) \equiv 1$.

Although the power-law indices, $q^{v_\mathrm{i},J_\mathrm{i}}_{v_\mathrm{f},0}$, are supposed to be valid only for $T = 1000$–$3000\,\mathrm{K}$, we still adopt the same indices for rate coefficients at $T < 1000\,\mathrm{K}$ and $T > 3000\,\mathrm{K}$ because an alternative estimate is not available. For $v = 2 \rightarrow 0$ transitions, we simply assume the rate coefficients from $v = 2 \rightarrow 0$ to be 10% of those from $v = 2 \rightarrow 1$ transitions. We note that these coefficients in general do not affect the radiative transfer significantly (e.g. Langer & Watson, 1984; Lockett & Elitzur, 1992). New calculations of the collisional rate coefficients for a broad range of kinetic temperatures and for the vibrationally excited states with the updated PES model will be very useful (e.g. Balança & Dayou, 2017).

Our extrapolation scheme of the SiO–H_2 collisional rate coefficients is different from that described by Doel (1990), on which the rate coefficients adopted by Doel et al. (1995) and Humphreys et al. (1996) are based. In particular, their extrapolation of the rate coefficients (including those for $v = 0 \rightarrow 0$ transitions) was based entirely on the set of parameters given by Bieniek & Green (1983a,b), which was the most complete and accurate one available at that time; they also refrained from further extrapolating the parameters beyond $J(v) = 39$ for $v = 0, 1, \ldots, 4$ and beyond the temperature range considered by Bieniek & Green (1983a,b) (for detailed discussion, see Sect. 7.2 of Doel, 1990).

B.2.3. Collisions with rotationally excited H_2

Asymptotic giant branch stars typically have a surface temperature of ~3000 K. In the winds and circumstellar envelopes of these stars, the gas temperature ranges from a few hundred to $\lesssim$3000 K. Molecular hydrogen in these environments may be significantly populated in the upper rotational levels (e.g. Flower, 1989; Doel, 1990; Field, 1998). For example, the wavelengths of the lowest para-H_2 transition, $S(0)$ ($E_{\rm up}/k$ = 510 K) and the lowest ortho-H_2 transition, $S(1)$ ($E_{\rm up}/k$ = 1015 K) are 28.2 μm and 17.0 μm, respectively (Dabrowski, 1984). The approximation of the collisional rate coefficients by the scaled (by ~1.4) coefficients with atomic helium as the collision partner is only valid for the collisions with para-H_2 (J = 0), but not for other rotational states of H_2 (Field, 1998). Lique & Kłos (2008) and Kłos & Lique (2008) have found that the rate coefficients for the collisions between the diatomic molecule SiS with para-H_2 (J = 0) are significantly lower than those for the collisions with ortho-H_2 (J = 1) or para-H_2 (J = 2) by up to an order of magnitude. Similarly, Daniel et al. (2011, and references therein) have also found that the collisions between H_2O and rotationally excited H_2 in the J = 1 and 2 states are the dominant processes in the collisional (de-)excitation of H_2O molecule.

For the SiO molecule, because the currently available collisional rate coefficients do not consider rotationally excited H_2 (J = 1 or 2) as the collision partners, the collisional (de-)excitations of SiO in the radiative transfer modelling could well be inaccurate and it is not possible to estimate the errors. In our modelling, it appears that most of the absorption/emission is contributed by the regions which are close to local thermodynamic equilibrium, otherwise there would not be enough absorption along the line of sight towards the continuum or there would be strong maser emission in the SiO v = 0 and 2 transitions, which show very weak or no maser in the data. So the gas temperature and expansion/infall velocity profiles are probably not affected by the incomplete collisional rate coefficients, but the magnitudes of the H_2 gas density and SiO abundance may not be accurate.

Blank Page

APPENDIX C

Light curve and period of IK Tau

The most commonly quoted pulsation period of IK Tau is 470 ± 5 days, which was determined by curve-fitting the near-infrared (NIR) flux variation of the star at $1.04\,\mu$m (Wing & Lockwood, 1973). Wing & Lockwood (1973) suggested that the luminosity phase of IK Tau to be represented by

$$E = \frac{JD - 2\,439\,440}{470}, \tag{C.1}$$

where the integral and fractional parts of E are the number of complete cycles counting from the optical V-band maximum in 1966 Nov (Cannon, 1967) and the visual phase in the cycle, respectively. Hale et al. (1997) also derived the same period of 470 ± 5 days from the (sparsely sampled) MIR fluxes of IK Tau at $11.15\,\mu$m. On the other hand, Le Bertre (1993) determined a different period of 462^{+3}_{-1} days from Fourier analysis of the multi-band NIR (1.24–$4.64\,\mu$m) light curves of IK Tau.

Since the periods of long-period pulsating variable stars are known to be stochastically variable (Templeton & Karovska, 2009), the period of IK Tau derived $\gtrsim$20 years ago may no longer be valid. To reduce the accumulated errors in the stellar phases, the time of IK Tau's visual maximum in recent cycles is needed. Based on the photometric data from the American Association of Variable Star Observers (AAVSO) International Database, the relatively well-sampled optical V-band maxima of IK Tau occured in 2007–2009. The difference in periods of 8 days per cycle would lead to a phase difference of about 0.1 in our VLA observations of 2015–2016. In this appendix, we present new analysis the V-band light curve of IK Tau in order to improve the estimates of its pulsation period and phase zero date.

From the AAVSO Database, we only select the V-band observations by the end of 2016 and exclude those without reported uncertainties. These criteria allow observations between 2002 Aug 10 and 2016 Oct 07. Figure C.1 shows the V-band light curve of IK Tau and the corresponding time at which NH_3 observations were performed. We then carry out time-series analyses using the Lomb–Scargle (LS) periodogram (Lomb, 1976; Scargle, 1982) in different Python implementations, including the standard LS periodogram in `Astropy` (version 1.3; Astropy Collaboration et al., 2013), the generalised LS periodogram in `astroML` (VanderPlas et al., 2012; VanderPlas & Ivezić, 2015), and the Bayesian formalism of the generalised LS periodogram (BGLS; Mortier et al., 2015a,b).

The output of BGLS is a probability distribution of period, which allows us to compute the standard deviation straightforwardly. In the `Astropy` implementation of the standard LS periodogram, we compute the uncertainty from the standard deviation of all the LS peak periods derived from a set of 10 000 simulated light curves, assuming that the uncertainties of the nominal V-band magnitude obey Gaussian distribution. All the periodograms of the observed

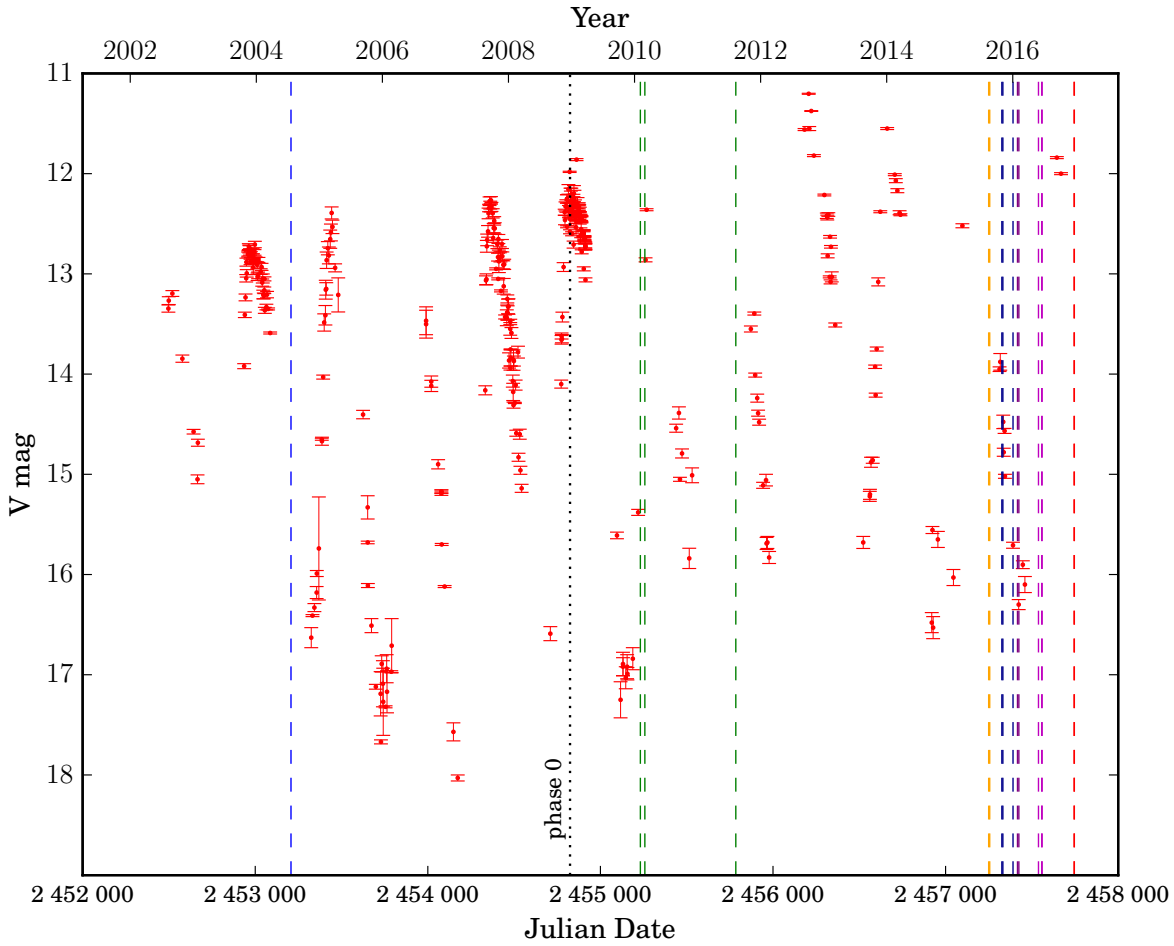

Figure C.1.: The V-band light curve of IK Tau in 2002–2016. The red points are the observations from the AAVSO International Database. We only include the observations with V magnitude uncertainties. The black vertical line indicates the date of V maximum on JD 2 454 824 (2008 Dec 23) as determined from the smoothed light curve as displayed in Fig. C.2. Other coloured vertical lines represent the dates of NH_3 observations with the VLA D-array (blue: 2004; dark blue: 2015–2016), C-array (purple), B-array (magenta), *Herschel*/HIFI (green), IRAM 30m (orange), and the IRTF/TEXES instrument (red).

V-band light curve show a prominent peak corresponding to the period of 460.05 days. The standard deviations of the period from the BGLS probability and from simulations are 0.02 and 0.06 days, respectively. Therefore, we report the V-band period of IK Tau as 460.05 ± 0.06 days.

We then phase the V-band light curve with the period of 460.05 days and smooth it with a Savitzky-Golay filter (Savitzky & Golay, 1964). We find that the phase zero date of JD 2 454 824 (2008 Dec 23) can produce an alignment of phase zero with the peak of the smoothed light curve. Figure C.2 shows the phased V-band data and the smoothed light curves. We search the phase zero date around the year 2009.0 because this peak is relatively well-sampled compared to more recent ones. The new phase of IK Tau is therefore given by

$$E = \frac{JD - 2\,454\,824}{460.05}, \tag{C.2}$$

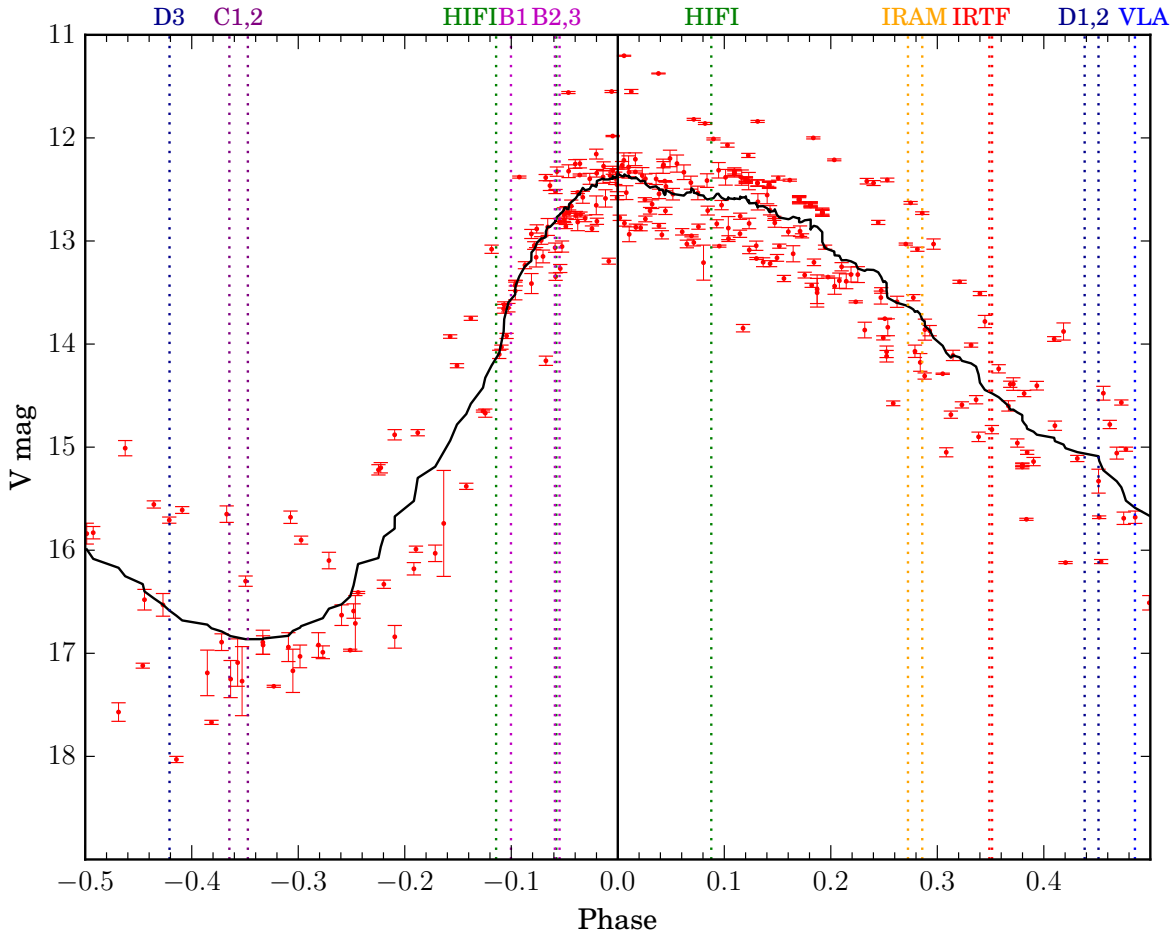

Figure C.2.: The phased V-band light curve of IK Tau in 2002–2016. Red points are the observations from the AAVSO International Database and the black curve is the smoothed light curve with a Savitzky-Golay filter. The phases of relevant NH_3 observations are labelled by vertical lines and on the top axis, with the same colour scheme as Fig. C.1. The label 'VLA' represents the 2004 VLA observation. The numerals after 'D', 'C', and 'B' are the ordinal numbers representing the dates of VLA observations in 2015–2016 with the corresponding arrays ('B4' is discarded, see Tables 2.4 and 2.5).

Blank Page

APPENDIX D

A discussion on continuum subtraction in spectral line imaging

It is a standard practice to subtract continuum emission from spectral line data (either from the visibility domain or from the image domain) before image deconvolution (e.g. van Langevelde & Cotton, 1990; Thompson et al., 2001, Sect. 11.9). Otherwise, the image deconvolution algorithm (e.g. CLEAN) has to reconstruct a continuum image for each individual, narrowband channel. Because of the non-linear nature of image deconvolution, small differences among channels (such as the frequency-dependent *uv*-coverage or the noise) may lead to very different convergence of the continuum image (e.g. Cornwell et al., 1992; Rupen, 1999, Sect. 6). Further discussions on the necessity of continuum subtraction in spectral line imaging can be found in Sect. 1 of Sault (1994), Sect. 16.9 of the Miriad User Guide[1] (version 14 Sep 2015), and Sect. 8.3 of the *AIPS*[2] *CookBook*[3] (version 31-DEC-2015).

D.1. Imaging problem

In our imaging exercises, we find that the images produced from the continuum-subtracted visibility data (hereafter, 'continuum-subtracted images/spectra') and those from the full line and continuum data (hereafter, 'full data images/spectra') are significantly different. Figure D.1 shows the continuum-subtracted spectra of all the observed SiO and H_2O lines in ALMA Band 6 extracted from the centre of Mira's radio continuum. Comparing these spectra to the full data spectra shown in Fig. 3.15, we expected the only differences to be the trivial constant offsets of about 70–80 mJy/beam, which are the peak radio continuum fluxes of Mira in the respective frequency ranges. In reality, however, the depths of absorption near the systemic velocity channels in the continuum-subtracted spectra are significantly shallower than expected, especially for the vibrational ground state transitions of ^{28}SiO and ^{29}SiO. The effects appear as perplexing bumps near the systemic velocity in the continuum-subtracted spectra. In these velocity channels, bright SiO-emitting clumps and large-scale ($\gtrsim 0\farcs1$) SiO emission are present around Mira's radio photosphere. The discrepancy also appears in the nearby pixels, which show SiO line absorption against the continuum of Mira's radio photosphere.

In the line-free channels (positive and negative velocity ends of the spectra), the continuum-subtracted spectra have much lower noise than the full data spectra. This is consistent with the fact that CLEAN would introduce additional noise to the image areas where real sources exist (in our case the radio continuum) (see e.g. Sect. 8.3 of the *AIPS CookBook*).

[1] http://www.atnf.csiro.au/computing/software/miriad/
[2] NRAO Astronomical Image Processing System.
[3] http://www.aips.nrao.edu/cook.html

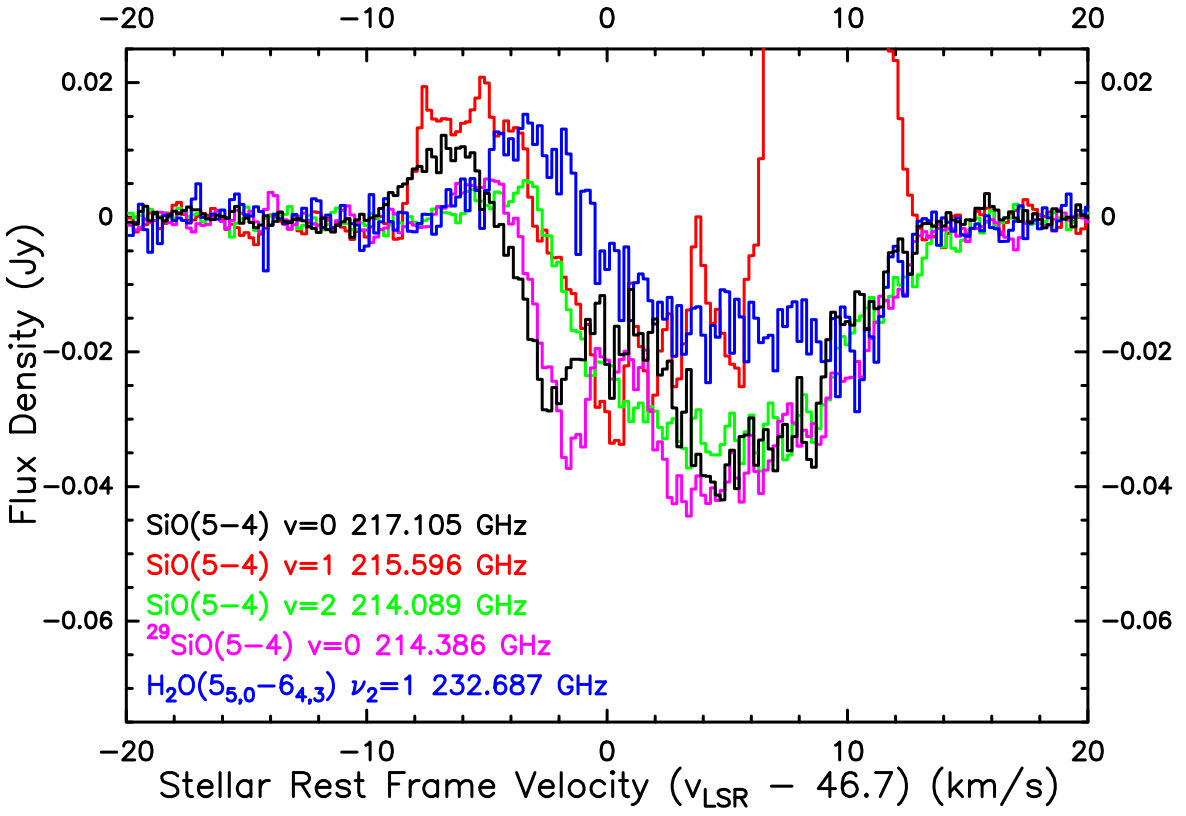

Figure D.1.: Spectral lines in ALMA Band 6 extracted from the line of sight towards the centre of Mira's continuum from the continuum-subtracted maps. The channel maps are presented in Figs. 3.9–3.13. The maser emission from SiO $v = 1$ $J = 5$–4 transition (in red) above 0.025 Jy is not shown in this figure.

D.2. Continuum subtraction in the visibility and the image domains

We first compared the imaging results of continuum subtraction in the visibility domain and in the (DIRTY) image domain, using the CASA tasks `uvcontsub` (then `clean`) and `imcontsub` (then `deconvolve`, which deconvolves the images purely in the image domain), respectively. Both approaches produce the same bumps in the absorption spectra. Hence, we conclude that the discrepancy between the continuum-subtracted and the full data images arises from the image deconvolution (CLEAN) process, but not continuum subtraction.

The following are the two most probable causes of the discrepancy:

1. the full data imaging has failed to recover all SiO line emission, possibly extended, around Mira's radio photosphere (i.e. missing emission) or, conversely,
2. the continuum-subtracted imaging has failed to recover the correct amount of SiO line absorption against Mira's radio continuum (i.e. missing absorption).

D.3. Natural weighting versus robust weighting

The first possibility depends on the scales of emission structures and the antenna configuration. In the full data images, all real astrophysical signals would have non-negative fluxes because the continuum emission is included in the data. The strongest line absorption can at most attenuate all the radio flux (i.e. down to zero, but not to a negative value) from the continuum behind the column of gas along the line of sight. In the continuum-subtracted im-

ages, on the other hand, strong negative signals would appear in the pixels of Mira's radio photosphere—representing the line absorption against the continuum—and, strong positive signals would appear around the continuum disc—representing the line-emitting gas outside the radio photosphere. Because of the negative 'hole' amidst the positive pixels, any real emission or absorption structures in the continuum-subtracted images would appear to be less extended than those in the full data images. Since the visibility plane sampling (*uv*-sampling) of ALMA in the long baseline configuration is rather sparse, full data imaging may not be able to recover all possible extended SiO emission from the inner wind of Mira.

Our imaging (Sect. 3.2) has adopted robust weighting with the parameter $\mathcal{R}_{\rm Briggs} = 0.5$. If the 'missing emission' scenario is true, then the discrepancy between the continuum-subtracted and the full data spectra should be alleviated under natural weighting, which gives relatively higher weightings to data of short baselines and hence is more sensitive to extended structures. Natural weighting can therefore recover more missing flux (if it exists at all) from the extended SiO emission around the radio photosphere of Mira. Since natural weighting gives a slightly larger synthesised beam than robust weighting, we only compare the maps of CLEAN component (hereafter, CC) models under the two different weighting schemes to eliminate the effect of the beam sizes. We integrate the total flux of the CC models within circles of various spatial scales, centred at Mira's radio continuum, and obtain the CC spectra of all the images. In contrast to what is expected from the missing emission scenario, we find that the full data CC spectra (not presented) are essentially identical under both weighting schemes. The fact that a higher weighting in short baselines does not recover more fluxes suggests that the ALMA antenna configurations in the SV observation were not missing a significant amount of extended SiO emission from Mira's inner wind. The absorption profiles of the continuum-subtracted CC spectra, on the other hand, show bumps that are even more prominent under natural weighting than under robust weighting.

In addition to the above test, we also do not expect any missing flux from extended emission structure for two reasons. First, the shortest baseline of this ALMA SV observation is 15 m, corresponding to a maximum recoverable scale[4] of over 11″ for the observed SiO transitions, which is at least one order of magnitude larger than the expected SiO depletion radius. Gas density and kinetic temperature also drop rapidly beyond the inner wind of Mira. So we expect the excitation of SiO molecules (both isotopologues) beyond the radius of the detected emission to be varying and very weak. It is unlikely that a smooth and large-scale SiO emission exists, and that the missing flux of which could significantly affect the absorption spectra. Second, negative 'bowls' around smaller-scale emission structures, which are characteristic features if smooth extended emission is missing (e.g. Bajaja & van Albada, 1979; Braun & Walterbos, 1985) are not seen in any of our images.

D.4. Number of CLEAN iterations

We therefore consider the second possibility in which the CLEAN process of the continuum-subtracted images may have underestimated the amount of foreground SiO line absorption against the background radio continuum. In order to trace the process of CLEAN iterations and the first batch of CC models selected by the algorithm, we make two additional sets of images, each using a small fixed number of CLEAN iterations instead of an rms noise-dependent threshold as the stopping criteria. Figure D.2 shows the spectra extracted from the images of SiO $v = 0$ $J = 5$–4 CLEANed with 200 and 1000 iterations, as well as the spectra from the DIRTY images (no CLEAN iteration) and the fully CLEANed images (down to the thresh-

[4] See footnote 6.

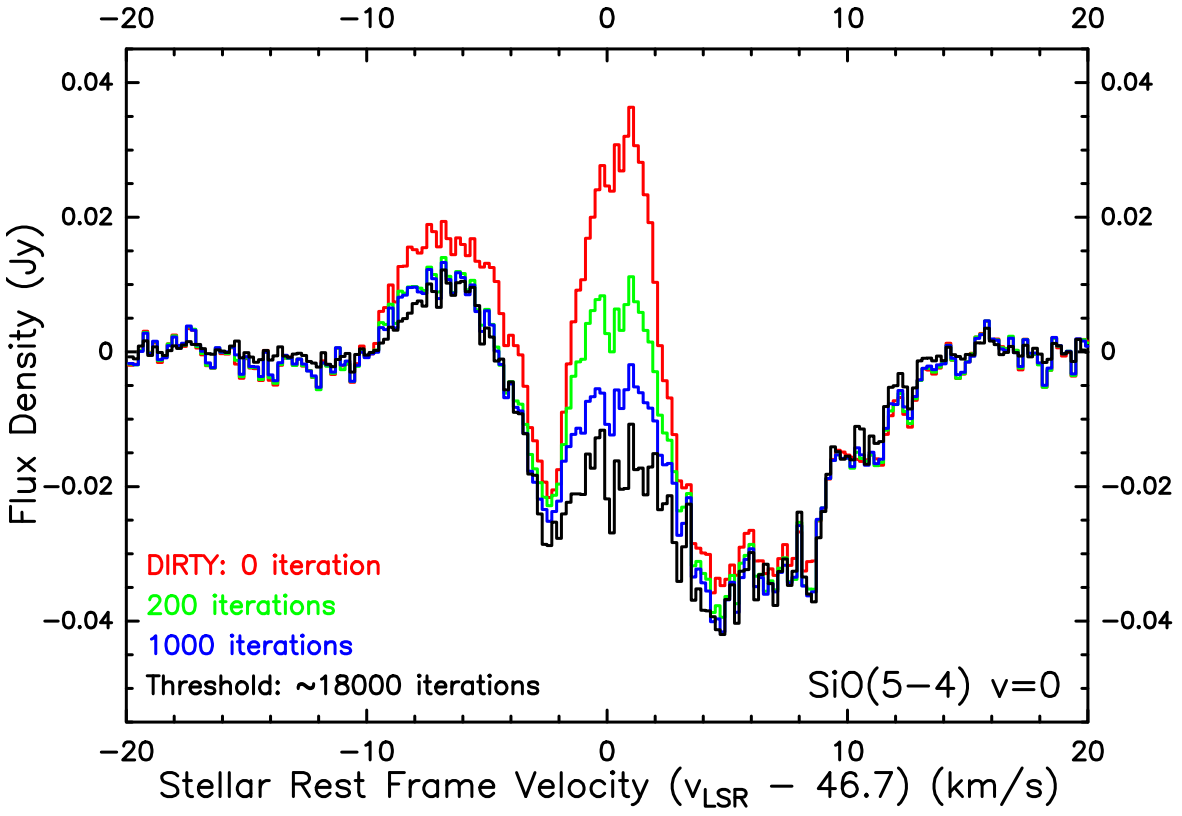

Figure D.2.: Continuum-subtracted absorption profiles of the SiO $v = 0$ $J = 5$–4 transition along the line of sight towards the centre of Mira's continuum extracted from images produced by different CLEAN stopping criteria. Images containing the spectra from top to bottom are CLEANed with: 0 iteration (i.e. DIRTY images), 200, 1000, and approximately 18 000 (fully CLEANed to the threshold, see Sect. 3.2) iterations.

old value as specified in Sect. 3.2). In Fig. D.2, the bump feature is seen in all spectra. Its amplitude reaches the maximum in the spectrum extracted from the DIRTY images, and gradually reduces as the number of iterations increases. In general, the DIRTY images are the most severely 'corrupted' by the sidelobes of ALMA's point-spread function (i.e. the DIRTY beam). As CLEAN proceeds to more iterations, the effect of the sidelobes should diminish and eventually vanish below the noise when a low-enough threshold is reached. The apparent resemblance of the bump in the fully CLEANed spectra to that in the DIRTY spectra and the decreasing trend of the bump's amplitude in the continuum-subtracted spectra with an increasing number of CLEAN iterations seem to suggest that the bump, or excess emission in individual channels, may indeed be the artefacts introduced by the sidelobes of the array's point-spread function that have not been completely removed by the CLEAN algorithm.

A closer inspection of the 200- and 1000-iteration CC model maps (not presented) shows that the first 1000 CC models selected by the CLEAN algorithm essentially all come from the strong SiO emission in the immediate proximity of Mira's radio photosphere. Only a handful of negative CC models were found within the radio continuum disc of Mira. We therefore speculate that the initial deconvolution of the strong, extended SiO emission (scales of the order of 0.″1) outside the radio continuum may have impaired the subsequent deconvolution of the line absorption within the continuum disc.

D.5. Long-baseline image deconvolution

To examine the performance of image deconvolution when we exclude the contribution from the extended (~0.″1) SiO emission outside Mira's radio photosphere, another set of continuum-subtracted images are produced for all the observed SiO and H_2O lines in Band 6 using only baselines longer than 500 m. The minimum baseline of 500 m corresponds to maximum recoverable scales of about 342–347 mas for the SiO lines, and about 319 mas for the H_2O line. In these long-baseline images, the detected flux of the SiO emission around the radio photosphere is significantly reduced or even eliminated. Figure D.3 shows the spectra extracted from the centre of the radio continuum in the long-baseline, continuum-subtracted images. The long-baseline spectra do not show any bumps in the original continuum-subtracted spectra (Fig. D.1), and resemble the similar inverse P Cygni absorption profiles in the full data spectra (Fig. 3.15). However, the maximum depths of absorption in the long-baseline spectra of the ^{28}SiO and ^{29}SiO $v = 0$ transitions appear to be even larger, by about 5 mJy, than the flux level of the radio continuum being absorbed (cf. Fig. 3.15). We do not have a definitive answer for this 'over-absorption' problem. In the long-baseline images, negative bowls are seen at radial distances larger than the SiO emission region. These are the expected characteristic features due to the lack of short baselines (<500 m). The region of the continuum disc amidst the SiO emission is exterior to the 'hollow' emission region, and therefore may indeed contain the artefactual negative signals due to the lack of short baselines in addition to the real absorption from the foreground SiO gas.

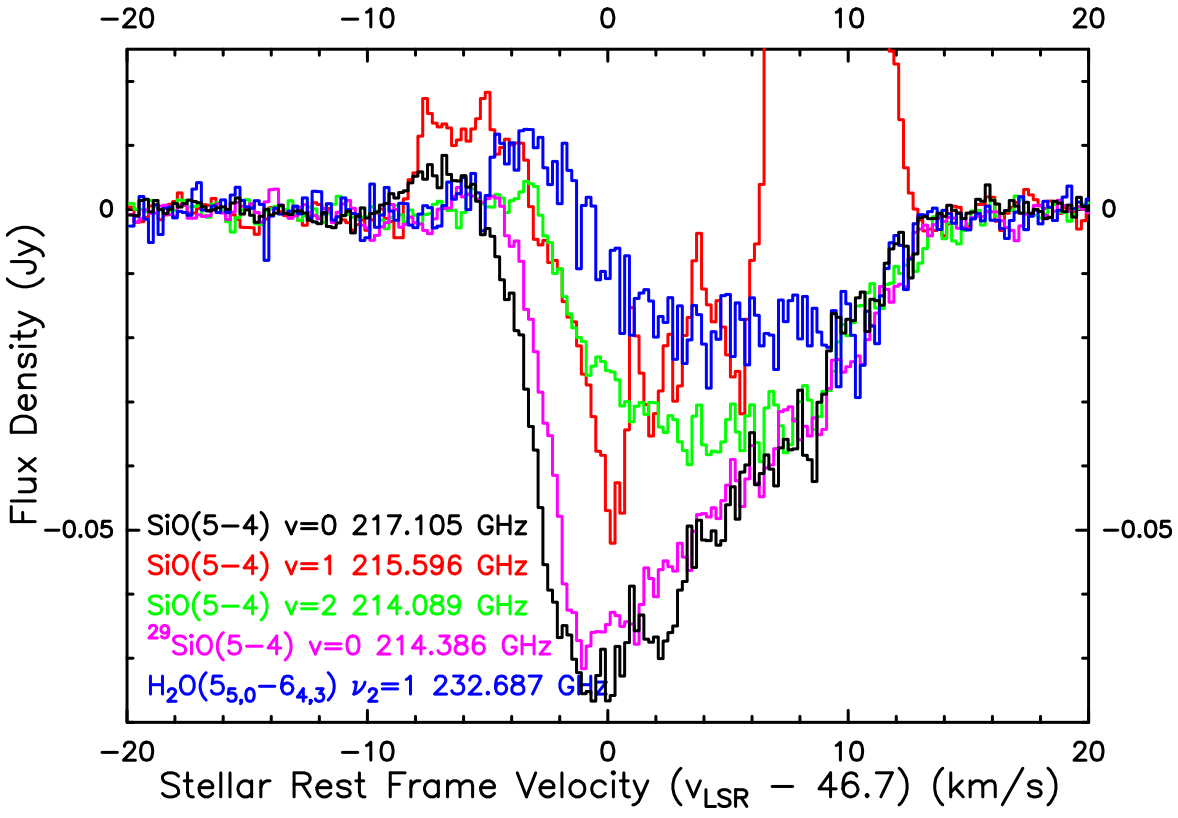

Figure D.3.: Spectral lines in ALMA Band 6 extracted from the line of sight towards the centre of Mira's continuum from the continuum-subtracted maps, only imaged with baselines longer than 500 m. The maser emission from SiO $v = 1$ $J = 5$–4 transition (in red) above 0.025 Jy is not shown in this figure.

D.6. CASA simulation of the ALMA SV observation

Finally, we also simulate the ALMA SV observation of Mira to test whether our preferred model (Sect. 3.4.4.3), which apparently produces satisfactory fits to the observed full data spectra, can also reproduce the observed bumps in the continuum-subtracted spectra. Positive results would imply that our preferred model can consistently reproduce both the full data and the continuum-subtracted spectra, regardless of the still uncertain causes of the discrepancy in the spectra; negative results, on the other hand, would suggest that our model is still far from approximately describing the structures and physical conditions of Mira's extended atmosphere and inner wind.

In the CASA simulation task `simobserve`, we use the SKY output model for the ^{28}SiO $v = 0$ $J = 5$–4 transition from RATRAN modelling (Sect. 3.4) as the input `skymodel`. For simplicity, we regard the two days of Mira's SV observation as one continuous observing block in the simulation, and adopt approximate values for the observation parameters. The hour angle at the mid-point of the simulated observation (`hourangle`) and the total on-source time (`totaltime`) are set to be −0.8 h and 4000 s, respectively. We also use the actual ALMA antenna configuration in Mira's SV observation as the input `antennalist`. Table D.1 lists all 39 ALMA antenna pads (stations) deployed in the SV observation. These antenna stations are also plotted in Fig. 3.2. We note, however, that only 35 or 36 antennae out of 39 were used in each day of observation (ALMA Partnership et al., 2015b). Moreover, we did not consider data flagging during the calibration process. These would slightly affect the array's point-spread function and the map rms noise, but we do not expect a significant deviation from the reality. The longest and shortest baselines also resemble those of the real visibility data. The task `simobserve` produces a simulated visibility data containing both the continuum and line data (as in our radiative transfer model). We then perform continuum subtraction (with the task `uvcontsub`) and imaging (with `clean`) in the exact same ways as for the real data, which are described in Sect. 3.2.

Table D.1.: ALMA antenna pads deployed in Mira's SV observations.

Nominal 2014 LBC array[a]				Additional antennae[b]		
A113	A131	W207	P401	A001	A029	A078
A118	A132	W210	P402	A004	A035	A082
A121	A133	S301	P404	A005	A058	T701
A122	W201	S303	P405	A006	A072	T703
A124	W204	S306	P410	A011	A075	
A127	W206	S309		A024	A076	

Notes. [(a)] 23 antennae in the nominal 2014 ALMA Long Baseline Campaign (LBC) configuration with a minimum baseline of about 400 m (i.e. blue dots in Fig. 3.2). [(b)] 16 additional antennae of short spacings that were available during either day, or both days, of the Science Verification observation of Mira in ALMA Band 6 (i.e. red dots in Fig. 3.2).

Figure D.4 shows the resultant spectra of the simulation, overlaid with the real spectra as already presented in Figs. 3.15 (full data) and D.1 (continuum-subtracted). Our simulation successfully reproduces the same bump with the same amplitude (within the noise) and in the same velocity range as in the absorption profile of the continuum-subtracted spectrum. Because this bump is not present in (1) the full data spectrum, (2) the spectrum extracted from modelled images convolved with a circular beam (i.e. the modelled spectrum in the top-left panel of Fig. 3.25), or (3) our input sky brightness model, we conclude that the bump in

the continuum-subtracted spectrum is indeed a spurious feature introduced during the imaging (CLEAN) process. We also suggest that the bump is caused by the missing absorption scenario described in Appendix D.2.

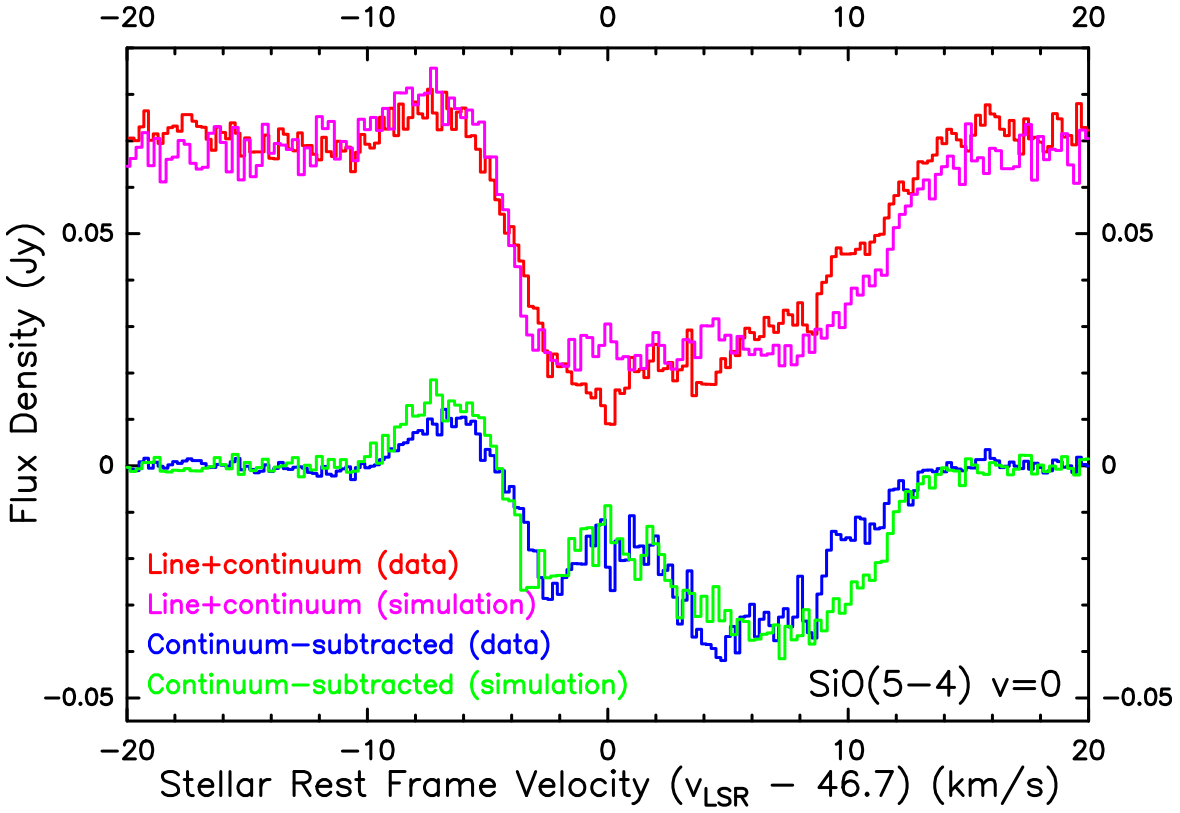

Figure D.4.: ^{28}SiO $v = 0$ $J = 5$–4 spectra extracted from the line of sight towards the centre of Mira's continuum from the full data images (line+continuum; red and magenta at the top) and from the continuum-subtracted images (blue and green at the bottom). The red and blue spectra correspond to the images from the actual data of Mira's ALMA SV observation, and the magenta and green spectra correspond to the simulated data using CASA task `simobserve`. The imaging procedures for the observed and simulated data are identical.

D.7. Concluding remarks

Based on the analyses in the previous sections (Appendices D.3–D.5), we speculate that the image deconvolution of the strong SiO emission surrounding the continuum disc, which corresponds to the first batch of the CLEAN component models, has probably impaired the deconvolution of the line absorption region in the images. However, it is still unclear how this has happened, even though CLEAN should be able to handle positive and negative signals equally well. In view of the possible limitations of the CLEAN algorithm, it may be worthwhile to perform imaging tests for this SV data with novel aperture synthesis techniques in radio astronomy (e.g. Sutter et al., 2014; Carrillo et al., 2014; Lochner et al., 2015; Junklewitz et al., 2016).

There are a few other important features in the simulated images and spectra. The noise in the line-free channels of the simulated full data spectrum is comparable to the observed value, and both are significantly higher than the observed/simulated continuum-subtracted spectra. This further supports our earlier claim in Appendix D.1 that CLEANing the radio continuum in individual channels could introduce additional noise to the image products.

We also note that the simulated spectra do not fit well to the observed ones near the velocity of +10 km s^{-1}. We attribute this to the imperfection of our physical model rather than issues in the data processing (see Sect. 3.4.4.3).

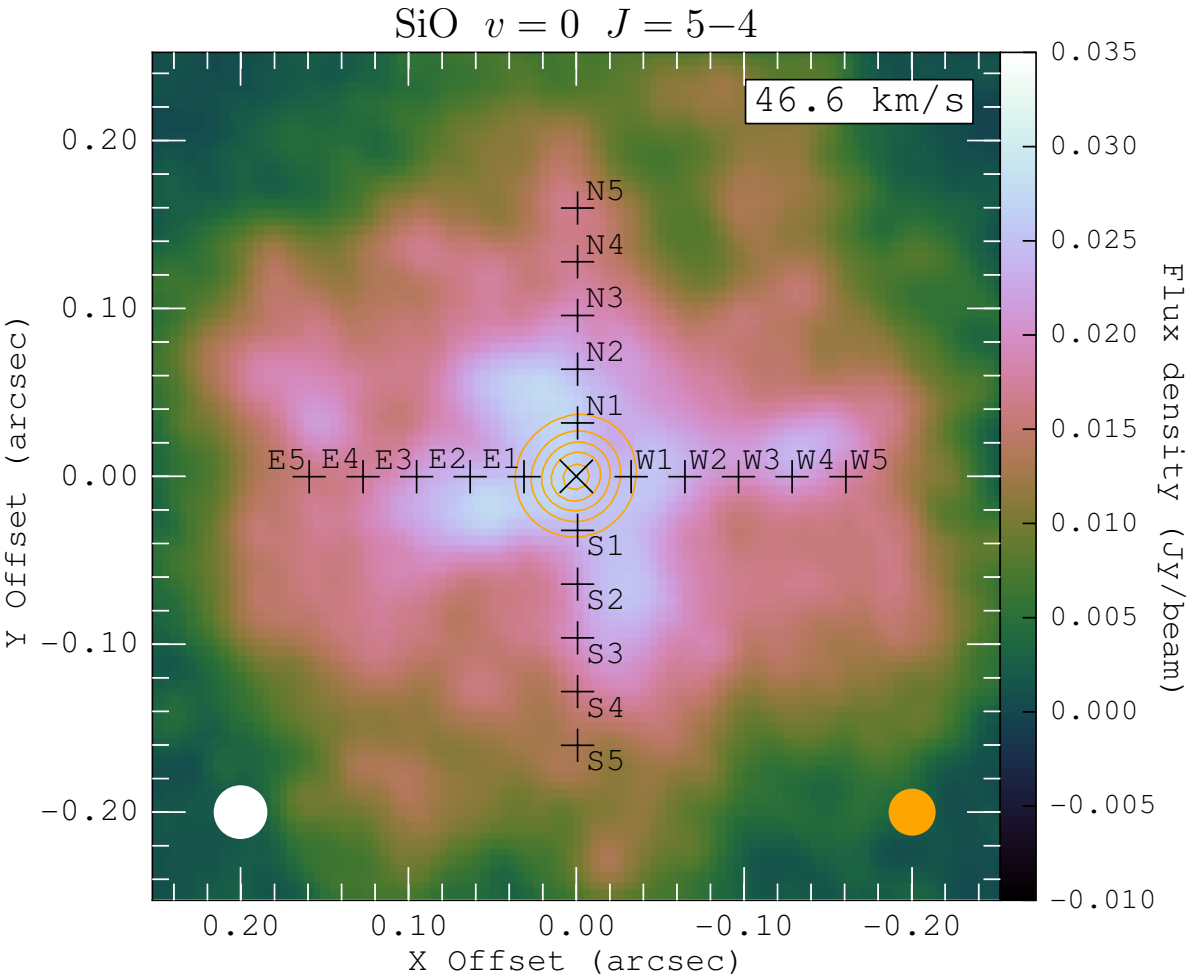

Figure D.5.: Same as Fig. 3.14 for the *simulated* map of SiO $v = 0$ $J = 5$–4 (with the continuum) at the channel of velocity 46.6 km s^{-1} with a channel width of 1 km s^{-1}. The velocity is slightly different from the systemic velocity of 46.7 km s^{-1} because of the different velocity grid in our model. The orange contours represent the real data of Mira's radio continuum at 229 GHz.

Our input sky brightness model, which only models the region around Mira up to 0.″3 and ignores the remote, arc-like emission feature, is spherically symmetric. The modelled intensity varies smoothly with radius, so it is expected that the simulated images behave in a similar manner. The simulated images, however, contain a lot of clumpy structures that are very similar to what we see in Figs. 3.9, 3.10, and 3.14. Figure D.5 shows the simulated full data image of the SiO $v = 0$ line near the systemic velocity, i.e. the channel in which the scale of the SiO emission is the largest. Similar to the same map from the actual observation (Fig. 3.14), the simulated map also shows structures of enhanced brightness all over the region being modelled. Figure D.6 shows the simulated channel maps of the images, with the continuum subtracted *after* imaging. These maps also resemble the real data counterpart as shown in Fig. 3.9: the core SiO line-emitting region appears to be globally spherically symmetric, but it also contains some irregular structures of the similar spatial scales. Qualitatively speaking, the

simulated maps are more symmetric and smoother than the real observed maps. The presence of clumpy structures in the simulated images may be due to the sparse *uv*-sampling of the ALMA long baseline configuration, which makes image deconvolution difficult. In addition, the signal-to-noise ratio may not be sufficient to clearly detect the SiO emission in Mira's extended atmosphere. Hence, the simulated ALMA observation suggests that the clumpy structures in the extended atmosphere and inner wind of Mira may not be all real.

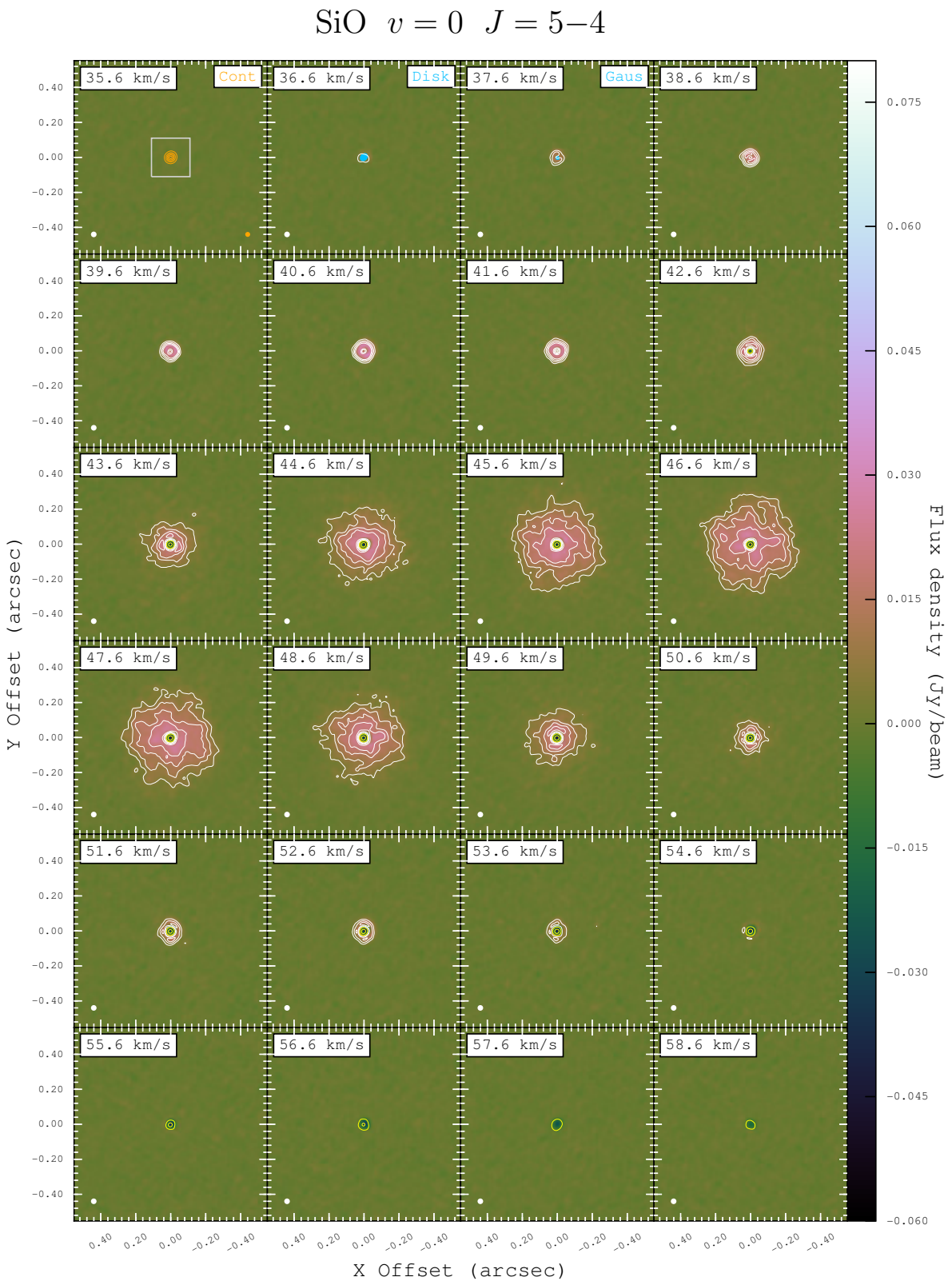

Figure D.6.: Same as Fig. 3.9 for the *simulated* channel maps of post-imaging continuum-subtracted SiO $v = 0$ $J = 5$–4. The white contours represent 6, 12, 18, 24, 48, and 72σ and the yellow contours represent −72, −60, −48, −36, −24, −12, and −6σ, where σ = 0.80 mJy beam^{-1} is the map rms noise in the real data. The LSR velocities are slightly different from those in Fig. 3.9 because of the different velocity grid in our model.

Full data channel maps (without continuum subtraction)

Figures E.1–E.5 show the channel maps without continuum subtraction. As explained in Sects. 3.2 and 3.3.2, we extract from these maps the spectra for our radiative transfer modelling (Sects. 3.3.3 and 3.4) and discussion (Sect. 3.5).

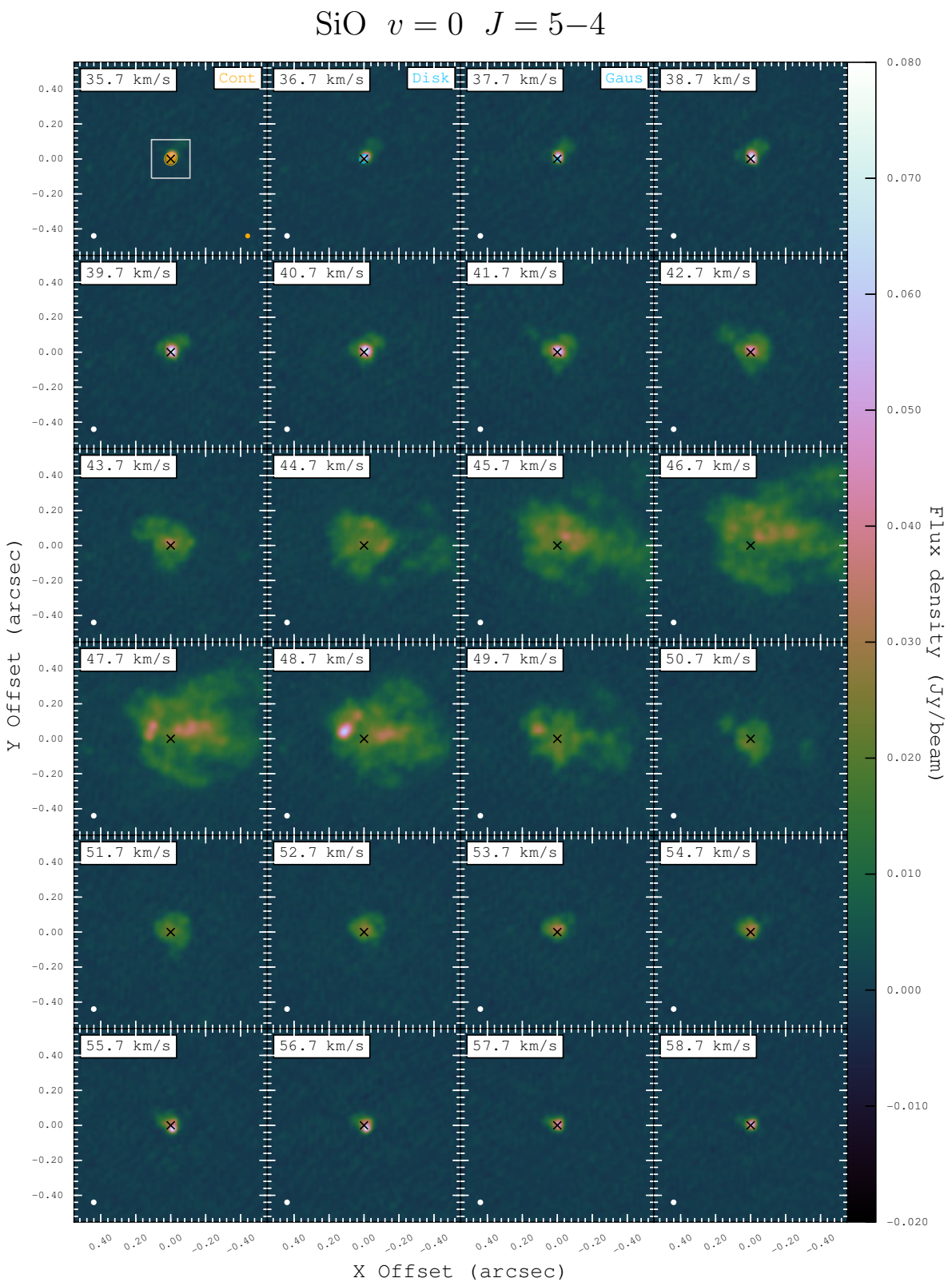

Figure E.1.: Same as Fig. 3.9 for the channel maps, including continuum emission from Mira A, of SiO $v = 0$ $J = 5$–4. The absolute position of Mira A is denoted by a black cross. The map rms noise is 0.80 mJy beam^{-1}. In the first panel of the top row, the white box centred at Mira A indicates the $0''.22 \times 0''.22$ region of the zoomed maps of SiO $v = 0$ (Fig. E.2), $v = 2$ (Fig. E.4), and H_2O $v_2 = 1$ (Fig. E.5).

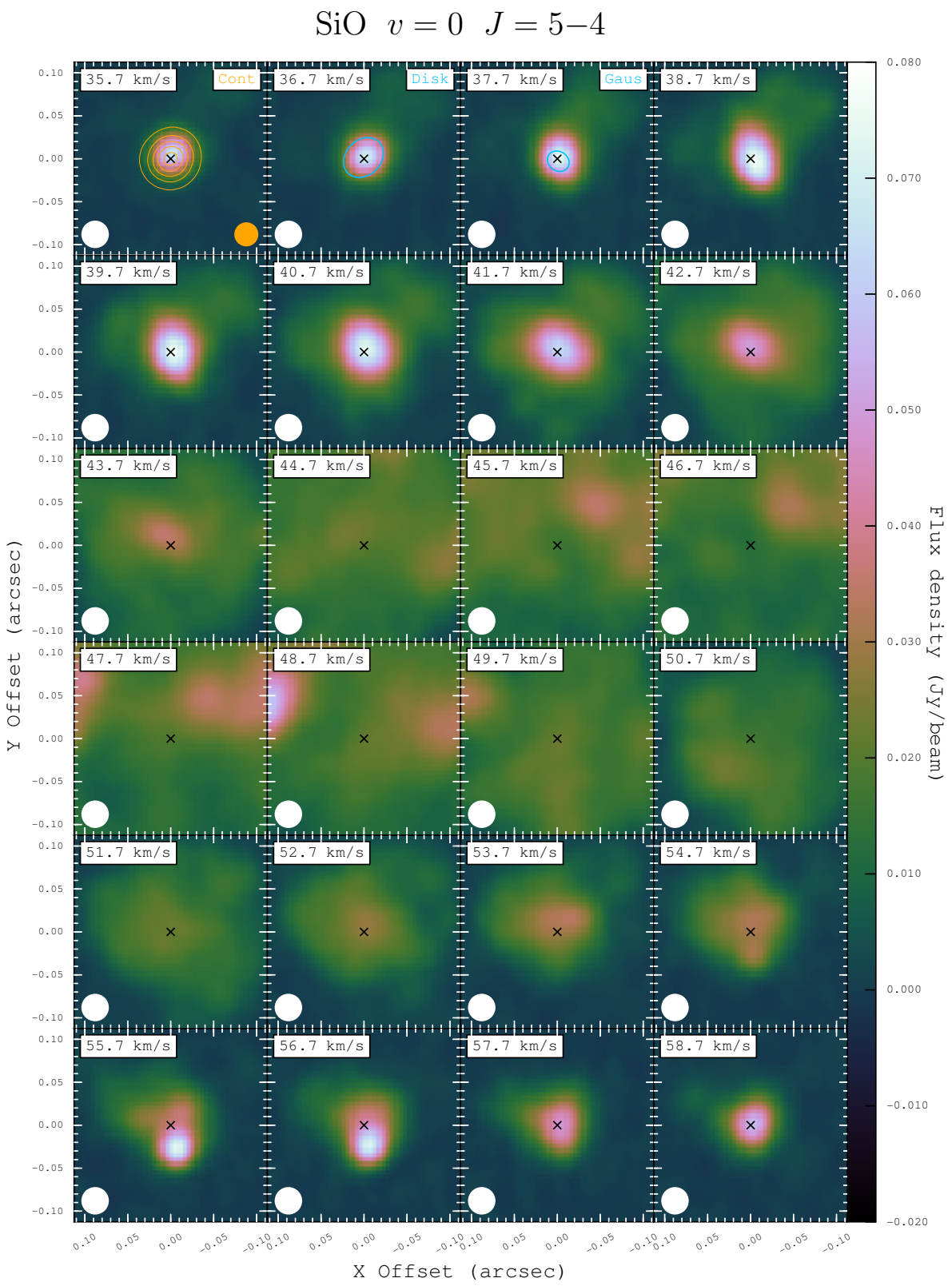

Figure E.2.: Same as Fig. E.1 for the zoomed (0.″22 × 0.″22) channel maps of SiO $v = 0$ $J = 5$–4 including continuum emission from Mira A.

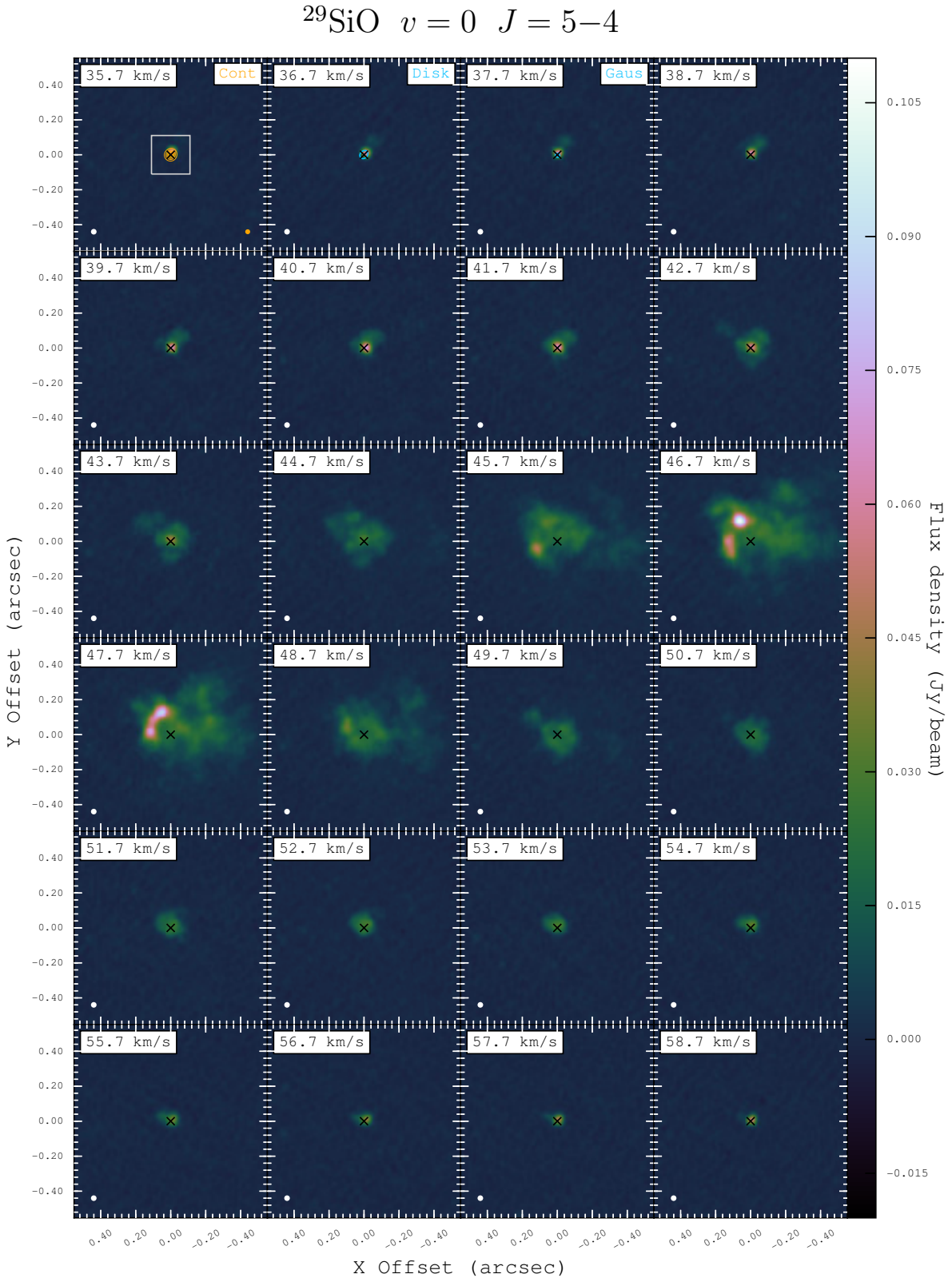

Figure E.3.: Same as Fig. E.1 for the channel maps of ^{29}SiO $v = 0$ $J = 5$–4 including continuum emission from Mira A. The map rms noise is 0.65 mJy beam^{-1}.

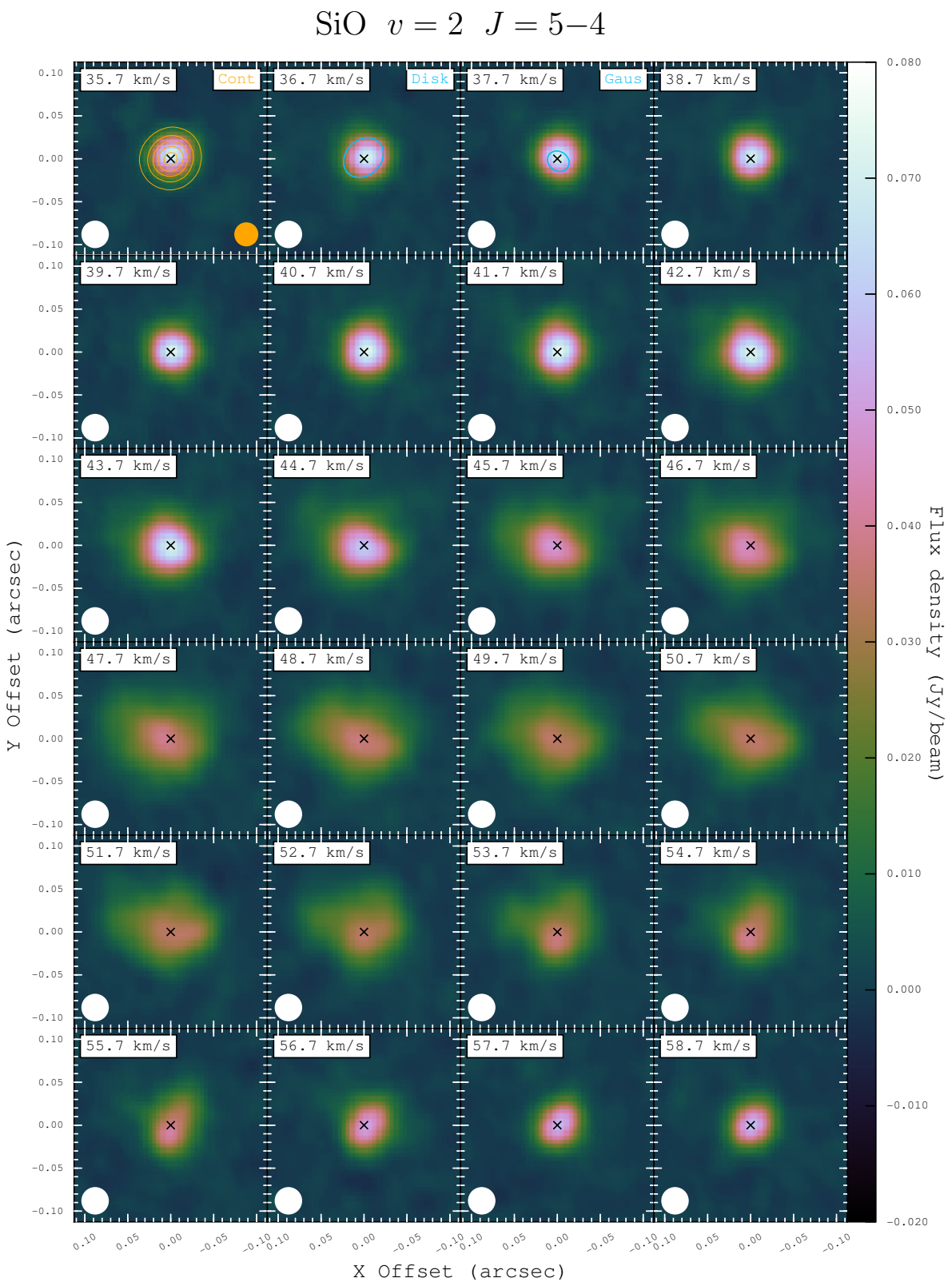

Figure E.4.: Same as Fig. E.1 for the zoomed (0″.22 × 0″.22) channel maps of SiO $v = 2$ $J = 5$–4 including continuum emission from Mira A. The map rms noise is 0.72 mJy beam^{-1}.

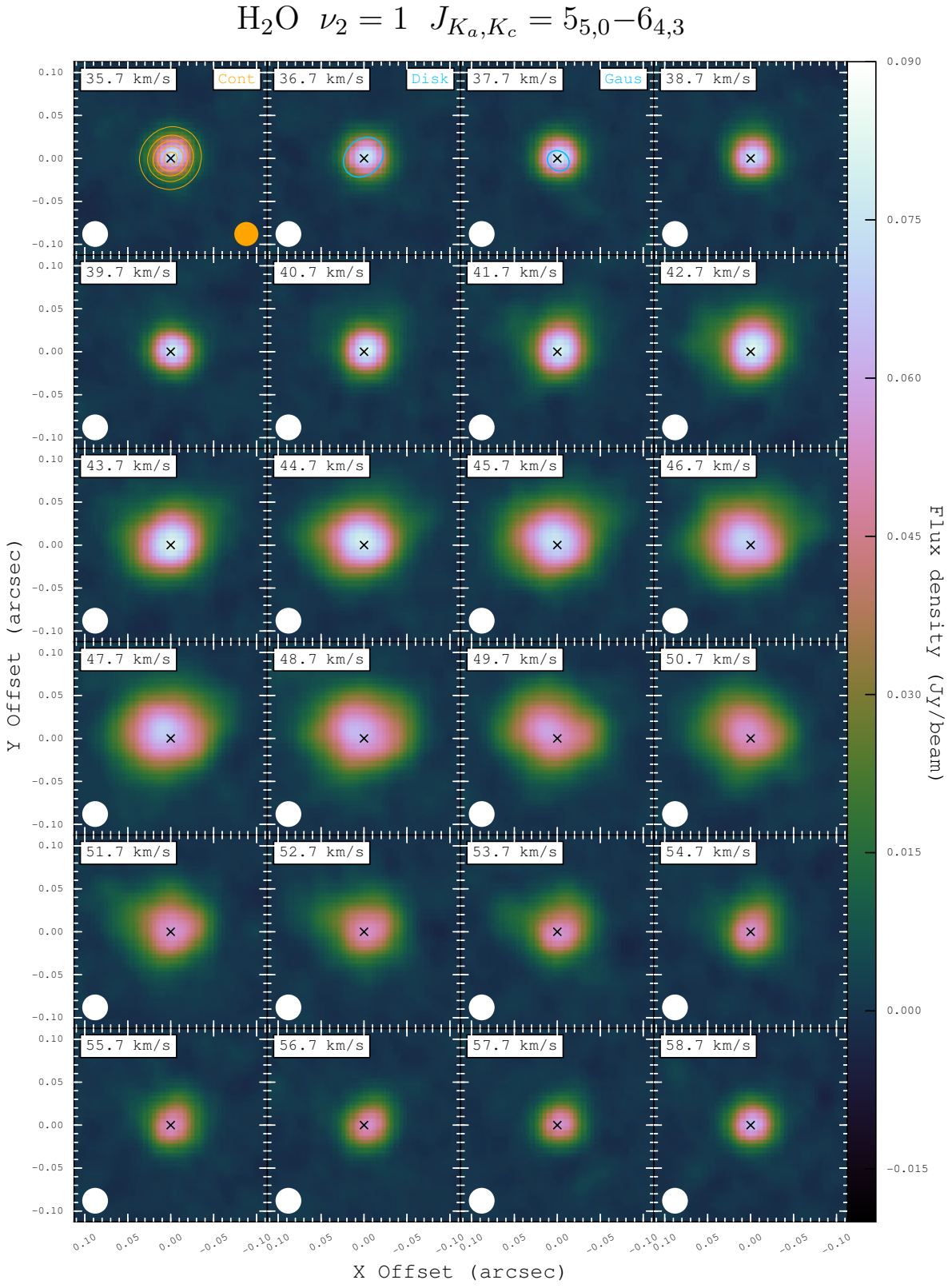

Figure E.5.: Same as Fig. E.1 for the zoomed (0″.22 × 0″.22) channel maps of H_2O $v_2 = 1$ $J_{K_a,K_c} = 5_{5,0}$–$6_{4,3}$ including continuum emission from Mira A. The circular restoring beam of 0″.030 FWHM for the H_2O images is indicated in white in the bottom left corner in each panel. The map rms noise is 0.72 mJy beam^{-1}.

Acknowledgements

I would like to express my deepest gratitude to *Karl Menten* for offering me the opportunity at the MPIfR to work on evolved stars, a research field in which PhD and postdoc positions can be difficult to find. Karl is always so supportive and generous in sharing his insights and experience, in encouraging me to participate in various meetings, schools, and observations, and in helping me to connect with other experts when I encountered difficulties. Thank you, Karl, for being so enthusiastic and meticulous in my work and for inspiring me with all the innovative ideas of research.

I would also like to thank *Norbert Langer* for agreeing to be my second examiner and for his useful advice in the Thesis Advisory Committee meetings.

The contribution from *Tomasz Kamiński* to this work is significant and is very much appreciated. It was his creativity that helped solve a number of issues in the studies presented in this research. A very big thank you to you, Tomek, for reading my manuscripts in great detail and giving me highly useful comments and suggestions.

I am indebted to *Friedrich Wyrowski* for squeezing his limited time to read and comment on my drafts for papers and proposals. He also guided me through the world of GILDAS, radiative transfer, and observations at the APEX Telescope. Without his patience and clear explanations, it would not have been possible for me to grasp the ideas of all these sophisticated systems and complicated concepts.

I am also very grateful to *Helmut Wiesemeyer* for his ideas on radiative transfer modelling, assistance in preparing the IRAM 30m and IRTF observations, and encouragement in the course of my studies.

Furthermore, I would also like to thank *Andreas Brunthaler*, *Jens Kauffmann*, and *Arnaud Belloche* for their time and very helpful guidance on preparing VLA, IRAM, and APEX observations, and also *Thushara Pillai* and *Christian Henkel* for their interest in and comments on my work.

The teaching experience at the University of Bonn helped improve me a lot in many different ways. I am grateful to *Frank Bertoldi* for offering me the opportunity to teach in his ISM course and radio-astronomical experiments. I am also very thankful to the MSc students for bearing with me in the tutorials and the labs. I wish you all the best in your MSc, and perhaps PhD, studies and future career.

In addition, I appreciate the assistance from the administrative staff of MPIfR, IMPRS, BCGS, and IRAM.

Last but not least, thanks so much to all whom I have met, including my officemates, current and past colleagues of the Millimeter and Submillimeter Astronomy Group, fellow PhD students and postdocs at MPIfR, AIfA, Leuven-IvS, and many other places, and my family and friends.

Contributions from many others were also needed to complete the work presented in this thesis

and they are acknowledged in the following.

I am indebted to *D. Gobrecht* for the insightful discussions of the chemical models of IK Tau (Gobrecht et al., 2016).

I thank *M. J. Reid* for a careful reading of the manuscript of Wong et al. (2016) and for the highly useful comments.

I am also grateful to *L. D. Matthews*, *E. W. Greisen*, and the anonymous referee of Wong et al. (2016) for their insightful comments and suggestions, which have inspired some of the tests in Appendix D to address the imaging issues.

The original data files of ortho- and para-NH_3 were kindly provided by *M. R. Schmidt* and allowed me to extend the collisional rate coefficients based on these files.

I would like to thank *A. Faure* for the new collisional rate coefficients of ortho- and para-NH_3 with ortho-H_2, para-H_2, and H (Bouhafs et al., 2017); and for the useful comments of the extrapolation methods of the rate coefficients.

The data reduction and analysis of the IRTF data would not have been possible without the continuous support from *J. H. Lacy* and *T. K. Greathouse*. They were the Visiting Astronomers at the Infrared Telescope Facility, which is operated by the University of Hawaii under contract NNH14CK55B with the National Aeronautics and Space Administration.

I would like to express my gratitude to *M. J. Richter* for the assistance in the preparation of the IRTF proposal and data analysis.

I also thank *M. Scholz*, *M. J. Ireland*, and *P. R. Wood* for kindly providing their model atmospheres from the `o54` series of the Cool Opacity-sampling Dynamic EXtended (CODEX) atmosphere model.

I appreciate the generosity of *R. A. McLaren* and *A. L. Betz* for giving us the consent and IOP Publishing Ltd. for granting us the permission to reproduce the NH_3 spectra as shown in Figs. 1 and 3 of McLaren & Betz (1980).

Telescopes and instruments

This thesis makes use of the following ALMA data: ADS/JAO.ALMA#2011.0.00014.SV. ALMA is a partnership of ESO (representing its member states), NSF (USA) and NINS (Japan), together with NRC (Canada) and NSC and ASIAA (Taiwan), and KASI (Republic of Korea), in cooperation with the Republic of Chile. The Joint ALMA Observatory is operated by ESO, AUI/NRAO and NAOJ.

Herschel is an ESA space observatory with science instruments provided by European-led Principal Investigator consortia and with important participation from NASA. The *Herschel* spacecraft was designed, built, tested, and launched under a contract to ESA managed by the *Herschel*/*Planck* Project team by an industrial consortium under the overall responsibility of the prime contractor Thales Alenia Space (Cannes), and including Astrium (Friedrichshafen) responsible for the payload module and for system testing at spacecraft level, Thales Alenia Space (Turin) responsible for the service module, and Astrium (Toulouse) responsible for the telescope, with in excess of a hundred subcontractors.

HIFI has been designed and built by a consortium of institutes and university departments from across Europe, Canada and the United States under the leadership of SRON Netherlands Institute for Space Research, Groningen, The Netherlands and with major contributions from Germany, France and the US. Consortium members are: Canada: CSA, U.Waterloo; France: CESR, LAB, LERMA, IRAM; Germany: KOSMA, MPIfR, MPS; Ireland, NUI Maynooth; Italy: ASI, IFSI-INAF, Osservatorio Astrofisico di Arcetri-INAF; Netherlands: SRON, TUD;

Poland: CAMK, CBK; Spain: Observatorio Astronómico Nacional (IGN), Centro de Astrobiología (CSIC-INTA). Sweden: Chalmers University of Technology - MC2, RSS & GARD; Onsala Space Observatory; Swedish National Space Board, Stockholm University - Stockholm Observatory; Switzerland: ETH Zurich, FHNW; USA: Caltech, JPL, NHSC.

HCSS / HSpot / HIPE is a joint development (are joint developments) by the Herschel Science Ground Segment Consortium, consisting of ESA, the NASA Herschel Science Center, and the HIFI, PACS and SPIRE consortia.

This research is partly based on observations with ISO, an ESA project with instruments funded by ESA Member States (especially the PI countries: France, Germany, the Netherlands and the United Kingdom) and with the participation of ISAS and NASA.

This research has made use of the NASA/IPAC Infrared Science Archive, which is operated by the Jet Propulsion Laboratory, California Institute of Technology, under contract with the National Aeronautics and Space Administration. The version of the ISO data presented in this article correspond to the Highly Processed Data Product (HPDP) sets called 'Uniformly processed LWS L01 spectra' by C. Lloyd, M. Lerate, and T. Grundy; and 'A uniform database of SWS 2.4–45.4 micron spectra' by G. C. Sloan et al., available for public use in the ISO Data Archive.

This research is partly based on observations carried out under project numbers 216-09, 212-10, and 052-15 with the IRAM 30m Telescope. IRAM is supported by INSU/CNRS (France), MPG (Germany) and IGN (Spain).

This research is partly based on observations at Kitt Peak National Observatory, National Optical Astronomy Observatory (NOAO), which is operated by the Association of Universities for Research in Astronomy (AURA) under cooperative agreement with the National Science Foundation.

Databases and catalogues

I acknowledge with thanks the variable star observations from the AAVSO International Database contributed by observers worldwide and used in this research.

This research has made use of NASA's Astrophysics Data System Bibliographic Services.

This research has made use of the SIMBAD database, operated at CDS, Strasbourg, France.

This research has made use of the VizieR catalogue access tool, CDS, Strasbourg, France. The original description of the VizieR service was published in Ochsenbein et al. (2000). In particular, I would like to thank Velilla Prieto et al. (2016) for the millimetre spectra of IK Tau and Tenenbaum et al. (2010b) for the table of emission lines in VY CMa deposited in the VizieR database. This research has made use of NASA's Astrophysics Data System Bibliographic Services.

Software tools

This research made use of Astropy, a community-developed core Python package for Astronomy (Astropy Collaboration et al., 2013).

PyFITS is a product of the Space Telescope Science Institute, which is operated by AURA for NASA.

Financial support

I was supported for this research through a stipend from the International Max Planck Research School (IMPRS) for Astronomy and Astrophysics at the Universities of Bonn and Cologne.

I was also supported by the Bonn-Cologne Graduate School of Physics and Astronomy (BCGS).

I acknowledge the BCGS Honors Budget which covers the digitisation cost of the Ph.D. thesis of Doel (1990).